Abstract

Utilizing Brillouin Interactions for Optical Control of Bulk Acoustic Waves

Prashanta Kharel

2019

Acoustic-wave devices have become indispensable components of modern technologies with applications ranging from time-keeping to signal processing. Since acoustic waves can store information for extended periods of time in compact mode volumes and mediate interactions between different types of excitations (photons, microwaves, and defect centers), phonons are intriguing resources for emerging quantum technologies.

In order to efficiently utilize mechanical degrees of freedom for both scientific and technological applications ranging from studies of decoherence to precision metrology and quantum information, we seek long-lived phonons that are less sensitive to thermal noise. Often times, this means achieving coherent control of high-frequency mechanical modes that are more decoupled from their thermal environment or operations at cryogenic temperatures.

In this context, bulk acoustic wave (BAW) resonators are crucial resources for both classical and quantum technologies. Since acoustic dissipation within crystalline solids plummets at cryogenic temperatures, BAW resonators, which are formed by shaping the surfaces of pristine crystals, can support long-lived phonon modes. To date, electromechanical coupling has been used to access such long-lived phonons within piezoelectric crystals, enabling various scientific and technological applications ranging from tests of Lorentz symmetry to low-noise oscillators. However, if we could access such bulk acoustic phonons with light, we have an opportunity to access high-frequency phonons in practically any transparent crystal, opening new avenues for sensitive metrology, materials spectroscopy, high-performance lasers, and quantum

information processing.

In this thesis, we demonstrate the optical control of long-lived, high-frequency phonons within BAW resonators. We utilize Brillouin interactions to engineer tailorable coupling between free-space laser beams and high Q-factor phonon modes supported by a plano-convex BAW resonator. Analogous to the Gaussian beam resonator design for optics, we present analytical guidelines, numerical simulations, and novel microfabrication techniques to create stable acoustic cavities that support long-lived bulk acoustic phonons.

For efficient optical control of bulk acoustic phonons, we utilize resonant multi-mode interactions by placing the bulk crystal inside an optical cavity. Resonant interactions permit us to dramatically enhance the optomechanical coupling strength. Utilizing enhanced optomechanical interactions in a system where we can select between Stokes and the anti-Stokes process, we demonstrate cooling and parametric amplification of bulk acoustic modes as a basis for ultra-low-noise oscillators and high-power lasers.

Finally, we enhance the optomechanical coupling strength to be larger than the optical and mechanical decoherence rates, creating hybridized modes that are part light and part sound. Deterministic control of long-lived bulk acoustic phonons with light in this so-called strong coupling regime opens the door to applications ranging from quantum transduction to quantum memories.

Utilizing Brillouin Interactions for Optical Control of Bulk Acoustic Waves

A Dissertation
Presented to the Faculty of the Graduate School
of
Yale University
in Candidacy for the Degree of
Doctor of Philosophy

by
Prashanta Kharel

Dissertation Director: Prof. Peter T. Rakich

December, 2019

Contents

Acknowledgments

I want to express my sincerest gratitude to my advisor, Prof. Peter Rakich, for his tireless guidance and support throughout the last six years. I could not have imagined having a better advisor and mentor. He dedicated an incredible amount of time mentoring us, encouraging us to purse new research ideas, and fostered a very collaborative learning environment. His emphasis on scientific communication and storytelling is something I will value for the rest of my career. Moreover, his passion for learning and positive outlook on everything in life will always be an inspiration for me.

I would like to thank my thesis committee: Prof. Robert Schoelkopf, Prof. Jack Harris, Prof. Steven Girvin, and Prof. Avi Zadok for their mentorship and feedback on the dissertation. I am especially grateful to Prof. Robert Schoelkopf and Prof. Jack Harris for giving me several opportunities to collaborate on groundbreaking research projects with their groups and also for the generous contribution of their time and experimental resources.

Six years is a long time to spend in one place but coming to work was a lot of fun because of my incredible colleagues at Yale: Ryan Behunin, William Renninger, Heedeuk Shin, Yiwen Chu, Vijay Jain, Eric Kittalus, Nils Otterstrom, Shai Gertler, Royce Luo, Yishu Zhou, Naijun Jin, Maggie Pavlovich, and Ruoping Li. I am very grateful to have mentors like Ryan, William, and Yiwen who were very patient when teaching me new theoretical concepts and experimental techniques. I am also very

fortunate to have incredibly talented colleagues: Eric, Nils, and Shai, who grew to become some of my closest friends. They were always available to brainstorm research ideas, provide feedback, and collaborate on research. I will always cherish the friendships that we developed over the years.

Having an incredibly caring and supportive administrative staff: Maria Rao, Theresa Evangeliste, Nuch Graves, and Giselle Maillet from the applied physics department made coming to work so much more enjoyable. I will miss our spontaneous tea-time conversations and am grateful to them for giving me a home away from home.

I also want to thank Mike Power, Chris Tillinghast, Jim Agresta, Yong Sun, Sean Rinehart, and Mike Rooks for their immense help with my fabrication projects. In particular, Mike has been a great mentor and a contributor as we worked on developing new processes in the cleanroom. It is a colossal task to keep shared facilities like the cleanroom and the YINQE running smoothly and this would not have been possible without their hard work.

I am also very grateful to the following funding agents for supporting my Ph.D. work: National Science Foundation (NSF), Lucile Packard foundation, Defense Advanced Research Project Agency (DARPA), the Office of Naval Research (ONR), and the Air Force Office of Scientific Research (AFOSR).

I am where I am today because of my undergraduate research advisor Prof. Randolph Peterson. He spent an enormous amount of time mentoring me and provided numerous research opportunities to help foster my research and academic career. I attribute my success in graduate school partly to a very well-rounded education I received at my undergraduate institutions Sewanee: The University of the South, and Columbia University. In particular, I want to thank Prof. Emily Puckett, Prof. Ben Szapiro, Prof. Reinhard Zachau, Prof. James Davidheiser, Kay Mackenzie for their support and guidance throughout my years at Sewanee. I am also incredibly grateful

to my wonderful host family, Pat Kelly and Connie Kelly, for making Sewanee feel like home to me.

My mother, Sabita Kharel, has always been a source of inspiration for me. She has faced every adversity with an unbelievable amount of grit and often times with a smile. I am thankful to her for fostering my intellectual curiosity and providing me an opportunity to pursue my passions. Lastly, I want to thank my incredible wife Bibhusha Dangol for her love and support throughout my PhD program.

List of Figures

List of Tables

Chapter 1

Introduction

A variety of linear and nonlinear processes occur when light interacts with matter [1]. Such interactions arise from coupling of light to internal degrees of freedom of the solid, resulting in either elastic or ineslatic light scaattering processes. For example, the blue color of the sky is a consequence of elastic (linear) scattering of sunlight due to the electrical polarizability of molecules in the atmosphere [2]. On the other hand, green laser pointers utilize inelastic (nonlinear) light scattering, particularly the mechanism of frequency doubling, to synthesize visible light from infrared laser light [3].

Brillouin scattering is a type of inelastic light scattering that occurs when light waves interact with elastic waves in a medium [4–6]; thermally populated elastic waves (or acoustic phonons) spontaneously scatter an incident light wave to higher and lower frequency sidebands. It is analogous to Raman scattering [7,8], which results from the scattering of light from the vibrational modes (or optical phonons) of the molecules constituting the medium. Typically, the frequency shifts due to Brillouin scattering in most solids is of the order of 10 GHz, which is much smaller than 10s of THz observed for Raman-shifts [1].

Even though Brillouin scattering was experimentally observed almost a century

ago [9], exploration of this scattering mechanism for various scientific and technological applications continues to this day. In the earlier days (1940s-1960s), Brillouin scattering was widely used as spectroscopy tool to measure various properties of solids [10, 11] and liquids [12, 13]. After the invention of lasers in the 1960s [14], Brillouin-based stimulated light scattering processes [15] were used for applications ranging from spectroscopy [16,17] to tunable laser sources [18,19]. In contrast to spontaneous Brillouin scattering, which results from scattering of incident laser light by thermal phonons, stimulated scattereing process occurs because optical forces generated by incident laser fields drive phonons which in turn scatter light into new frequency components. This field saw even more progress after the invention of low loss optical fibers [20, 21] and the demonstration of stimulated Brillouin scattering within such fibers in 1972 [22].

As opposed to light-sound coupling in a bulk medium [15], optical fibers provided a platform where light waves and sound waves could interact over long distances [23,24]. However, this increased nonlinearity within optical fibers has been a major hindrance to fiber-based long-distance optical communication [22,25]. This is because stimulated Brillouin scattering (SBS) causes light propagating within a long fiber-optic cable to backreflect and redshift even at modest (10s of mW) optical powers [25,26]. Therefore, suppression of SBS in an optical fiber remains active area of research even today [27–31]. Nevertheless, increased interaction lengths for nonlinear light-sound interaction within optical fibers has enabled a whole host of technologies including low-threshold Brillouin lasers [32–34], amplifiers [35], sensors [36–38], dynamics gratings [39, 40], and Brillouin-based signal processing devices [41, 42].

More recently, the demonstration of Brillouin scattering within microstructured fibers [43–45] and on-chip waveguides [46–48] has led to a renaissance in the field of Brillouin scattering. By tailoring the overlap between the light and the sound fields, these structures have not only permitted greater control [45, 49] over Brillouin

interactions but also enabled dramatic enhancement [50] in the Brillouin nonlinearity ($10^4 - 10^5$ larger than those in optical fibers). Such engineerable light-sound coupling has led to a plethora of new technologies including opto-acoustic isolators [51–54], low noise lasers [47, 55–58] , microwave synthesizers [58–60], narrowband microwave filters [61–63], pulse storage devices [64, 65], and gyroscopes [58, 66].

While Brillouin scattering can be greatly enhanced by tailoring the acousto-optic overlap within microscale and nanoscale waveguides, large Brillouin nonlinearities can also be achieved within bulk materials by extending acoustic lifetimes. This is because the effective strength of Brillouin coupling increases with the acoustic lifetime. Therefore, achieving control over acoustic lifetimes could provide an alternative approach to tailor Brillouin interactions.

In this context, optical fibers provide a natural platform to guide acoustic waves and mitigate certain acoustic loss channels for enhanced Brillouin interaction. The germanium doped core of a single mode fiber has a slightly lower longitudinal sound velocity compared to that of the cladding, permitting acoustic guiding inside the fiber core [24, 67]. This eliminates extrinsic loss mechanisms such as diffraction losses and provides an opportunity to explore intrinsic acoustic dissipation mechanisms.

Many experiments attempted to reach intrinsic levels of acoustic dissipation in fiber by lowering the system temperature [68, 69]. At low temperatures, thermal phonons, which typically scatter coherent phonons through various nonlinear processes [70], are quenched, leading to a modest ($\sim$ 12 times) lifetime enhancement compared to that at room temperatures [71]. However, this acoustic dissipation trend within silica-based optical fibers–and more generally within amorphous media–reverses (acoustic dissipation increases) at cryogenic temperatures due to the deleterious effect of two-level tunneling states (TLSs) [70, 72, 73].

In this context, crystalline media provide an alternative platform to access low loss phonons as acoustic dissipation plummets more dramatically in crystals at cryogenic

temperatures [74, 75]. A number of theoretical studies [76–78] in the 1930s, which explored fundamental limits to acoustic dissipation in crystalline solids, suggested that astonishingly large Q-factors ($> 10^{11}$) [79] could be achieved within pristine crystalline solids at cryogenic temperatures. Such fundamental limit to acoustic dissipation in a real perfect crystal is a consequence of the anharmonicity of the lattice potential energy; anharmonicity in the lattice potential gives rise to nonlinear acoustic scattering, causing coherent phonons to scatter off of thermal phonons or even vacuum fluctuations, akin to nonlinear wave mixing in optics [80].

Acoustic dissipation due to such phonon-phonon scattering can vary dramatically with crystal structure and crystal cut [81]. Energy conservation and phase matching requirements severely limit which nonlinear acoustic scattering processes can occur [79]; typically, three-phonon scattering is the most dominant source of acoustic loss. Moreover, as a consequence of anisotropy in the elastic constants in crystalline media, coherent phonons can scatter off of only certain polarizations of thermal phonons [74,79,82]. Therefore, the fundamental limit to acoustic dissipation depends strongly on the choice of the crystalline structure and the crystalline axis [81].

A number of experiments in the 1940s-1970s explored temperature dependence of acoustic dissipation in a variety of crystals [74, 83–95]. For example, such measurements in trigonal crystals (such as sapphire, quartz, and lithium niobate) revealed that the acoustic dissipation of high-frequency (9.4 GHz) longitudinal acoustic waves follows a $T^{6.5}$-law at cryogenic temperatures ($\sim$ 20K-100K) [75]. These astonishingly steep acoustic dissipation trends as a function of temperature suggested a great opportunity to access long lived, high-frequency phonons within crystalline solids by further lowering the cryogenic temperature.

However, these attenuation measurements themselves introduced additional acoustic losses [84,87,91], hindering the prospect of harnessing long lived phonons at liquid helium temperatures and below. Such early experiments exploring attenuation of

hypersonic waves relied on piezoelectricity to generate phonons. A microwave cavity with a piezoelectric crystal that was partially inserted inside the cavity walls was used to transduce as well as detect hypersonic waves. Therefore, either piezoelectric films (such as CdS [75, 92]) were deposited on non-piezolectric samples or these samples were bonded with piezoelectric materials using spurious materials (such as indium film [85], resin [96], and epoxy [94]), which introduced additional acoustic loss.

In addition, imperfections in the crystal as well as the crystalline geometry itself severely impacted measurements of intrinsic acoustic attenuation. There was a large variation in crystal quality (i.e. the amount of defects and impurities) within naturally occurring crystalline samples and the technologies for growing ultra-pure synthetic crystalline materials were not as mature as we have today. Moreover, the crystalline samples typically used for such measurements were flat-flat samples, meaning the traveling acoustic waves suffered beam diffraction and scattering as they reflected off the samples surfaces [83].

To access high Q-factor acoustic modes by mitigating extrinsic loss channels for phonons, a new type of piezoelectric resonator was invented in the 1970s [97–99]. These acoustic resonators–also known as BVA resonators–consisted of a plano-convex contoured quartz and they featured a contactless electrode design, permitting transduction of ultrasonic acoustic waves in the 5-100 MHz range [99]. Similar to a plano-concave optical cavity, the plano-convex acoustic resonator supported acoustic modes that were tightly trapped inside the resonator, eliminating acoustic diffraction losses. Moreover, the contactless electrode design mitigated spurious scattering losses by the electrodes themselves.

More recently, using such plano-convex acoustic resonators and paying careful attention to nonidealities in the crystal quality and surfaces, Galliou et al. [100] demonstrated record high Q-factors (8 billion) for 200 MHz acoustic waves in quartz at liquid helium temperatures. Such resonators [100, 101] have had tremendous scientific

and technological impact with applications ranging from tests of Lorentz symmetry [102] to tests of quantum gravity [103].

These remarkable demonstrations of ultra-low loss phonons within quartz bulk acoustic wave resonators spurred a number of questions: How low can we go in terms of acoustic dissipation? Could we access such low loss phonons at GHz frequencies? Could we achieve even lower acoustic losses using other crystalline substrates such as sapphire, silicon, or diamond? Unfortunately, a vast majority of these crystals are not piezoelectric, preventing electromechanical transduction of acoustic waves within such crystals.

Optical access to such long-lived acoustic waves within crystalline solids could enable studies of acoustic dissipation in a wider class of crystals. Unlike piezoelectric effect, photoelastic effect is present in all solids, meaning electrostrictive optical forces can be used to generate and detect elastic waves in practically any transparent crystal. We could then envision using such optomechanical transduction to harness favorable coherence properties of bulk acoustic waves for applications ranging from high-performance oscillators to quantum information processing.

In this context, stimulated Brillouin spectroscopy of tellurium dioxide (TeO_2) crystals at cryogenic temperatures by Ohno et al. [104, 105] revealed new features in the Brillouin spectra due to reflection of traveling acoustic waves at the crystal surfaces. These measurements confirmed that Brillouin scattering can be used to both generate and detect standing-wave phonon modes within crystals at cryogenic temperatures.

1.1 Summary of dissertation

In this dissertation, building upon prior measurements of Brillouin scattering at cryogenic temperatures, we report several advances which enable efficient optical control

of long-lived phonon modes of a bulk acoustic resonator. These advances pave the way for utilizing long-lived bulk acoustic phonons for materials spectroscopy, precision metrology, exploration of new regimes of laser physics, as well as quantum information processing.

- In Chapter 2, we bridge the gap between cryogenic Brillouin physics and mesoscopic optomechanical interactions by engineering bulk acoustic phonon modes and their interaction with free-space laser beams. We use a Hamiltonian based framework to explore optomechanical interactions in this new regime of Brillouin dynamics where discrete standing wave phonon modes mediate interaction between counterpropagating laser fields. This permits us to draw an analogy between our bulk crystalline optomechanical system and a multimode cavity optomechanical system. We develop new optomechanical design principles, simulation techniques, and precision spectroscopy methods to transduce and detect long-lived phonon modes of a macroscopic (cm-scale) bulk acoustic resonator with laser fields, expanding the range of possible optomechanical interactions in bulk crystals. This work is based in Ref. [106] and the theoretical groundwork for exploring such optomechanical interaction was presented in Ref. [107]. These results are presented in chapter 3.

  [106] W. H. Renninger*, P. Kharel*, R. O. Behunin, and P.T. Rakich, "Bulk crystalline optomechanics," *Nature Physics* **14**, 601-607 (2018). * These authors contributed equally.

  [107] P. Kharel, R. O. Behunin, W. H. Renninger, and P. T. Rakich, "Noise and dynamics in forward Brillouin interactions," *Physical Review A* **93**, 063806 (2016).

- In Chapter 4, we report novel design principles and simple microfabrication techniques to create high performance chip-scale bulk acoustic resonators in

variety of crystalline substrates. We developed analytical as well as numerical techniques to understand acoustic beam propagation in anisotropic solids and create stable plano-convex acoustic cavities in practically any crystal. We utilize novel microfabrication techniques to produce chip-scale bulk acoustic resonators in a variety of crystalline substrates (quartz, silicon, GaAs, and sapphire) and demonstrate unprecedented tailorability in the acoustic resonator geometry. By radically reducing the device footprint ($\times$1000 reduction in device volumes), we were able to harness long-lived, high-frequency phonons modes within chip-scale bulk acoustic resonators for classical [108] and emerging quantum technologies [109, 110].

[108] P. Kharel, Y. Chu, M. Power, W. H. Renninger, R. J. Schoelkopf, and P. T. Rakich, "Ultra-high-Q phononic resonators on-chip at cryogenic temperatures," *APL Photonics* **3**, 066101 (2018).

[109] Y. Chu, P. Kharel, W. H. Renninger, L. D. Burkhart, L. Frunzio, P.T. Rakich, and R. J. Schoelkopf, "Quantum acoustics with superconducting qubits," *Science* **358**, 199-202 (2017).

[110] Y. Chu, P. Kharel, T. Yoon, L. Frunzio, P.T. Rakich, and R. J. Schoelkopf, "Creation and control of multi-phonon Fock states in a bulk acoustic-wave resonator," *Nature* **563**, 666-670 (2018).

- In Chapter 5, by placing bulk acoustic resonators inside an optical cavity, we use resonant Brillouin interactions to dramatically increase optomechanical coupling to high-frequency bulk acoustic phonons. We engineer new ways to break symmetry between the Stokes and the anti-Stokes scattering processes, enabling beam-splitter and entanglement interactions necessary for optical control of phonons. By increasing optomechanical coupling through resonant interactions, we achieve large cooperativities ($\sim$700) and use it to demonstrate phonon mode

cooling and parametric amplification. In summary, we realized a versatile cavity optomechanical system to harness long-lived, high-frequency bulk acoustic phonon modes as a basis for applications ranging from high-power oscillators to quantum information storage devices. This work is based in Ref. [111].

[111] P. Kharel, G. I. Harris, E. A. Kittalus, W. H. Renninger, Nils T. Otterstrom, and Jack G. E. Harris, Peter T. Rakich, "High-frequency cavity optomechanics using bulk acoustic phonons," *Science Advances* **5**, eaav0582 (2019).

- In Chapter 6, we demonstrate strong coupling between infrared light and bulk acoustic phonons as a basis for deterministic quantum optical control of bulk acoustic phonons. We enhance the optomechanical interaction rate to be larger than the dissipation rate of both the optical and acoustic modes, pushing our system into the strong-coupling regime. Strong coupling to GHz frequency bulk acoustic modes, having motional masses that are 1-100 million times larger than those of microscale counterparts, opens new avenues for robust ground state control of phonons for quantum applications, including microwave-to-optical conversation and quantum memories. Moreover, by engineering strong coupling between a single optical mode and multiple acoustic modes, we study novel physical phenomena in the previously unexplored regime of cavity optomechanics and utilize non-trivial multimode interactions to protect the hybridized modes from extrinsic dissipation channels. This work is based in Ref. [112].

[112] P. Kharel*, Y. Chu*, E. A. Kittalus, Nils T. Otterstrom, Shai Gertler, and Jack G. E. Harris, "Multimode strong coupling in cavity optomechanics," *arXiv:1812.06202v2* (2019). * These authors contributed equally.

Chapter 2

Stimulated Brillouin Scattering Theory

2.1 Introduction

In this chapter, we begin by deriving the dynamics of stimulated Brillouin scattering at ambient temperatures. We then explore Brillouin dynamics when the acoustic dissipation rate is dramatically reduced at cryogenic temperatures.

Stimulated Brillouin Scattering (SBS) is a nonlinear light scattering resulting from the interaction of traveling wave optical fields with traveling wave elastic fields. The interference between two counterpropagating optical waves in a medium produces a periodic density variation in the medium through electrostriction (Fig. 2.1**a**), which is the property of all dielectric materials to change shape (or develop strain fields) when exposed to electric fields [49]. This periodic variation in density of the medium results in the modulation of refractive index (or dielectric constant) of the medium through the photoelastic effect. Frequency detuning of the optical waves generates a moving interference pattern and consequently a moving refractive index modulation (Fig. 2.1**b**). Dynamical Bragg scattering of light now occurs off this moving refractive

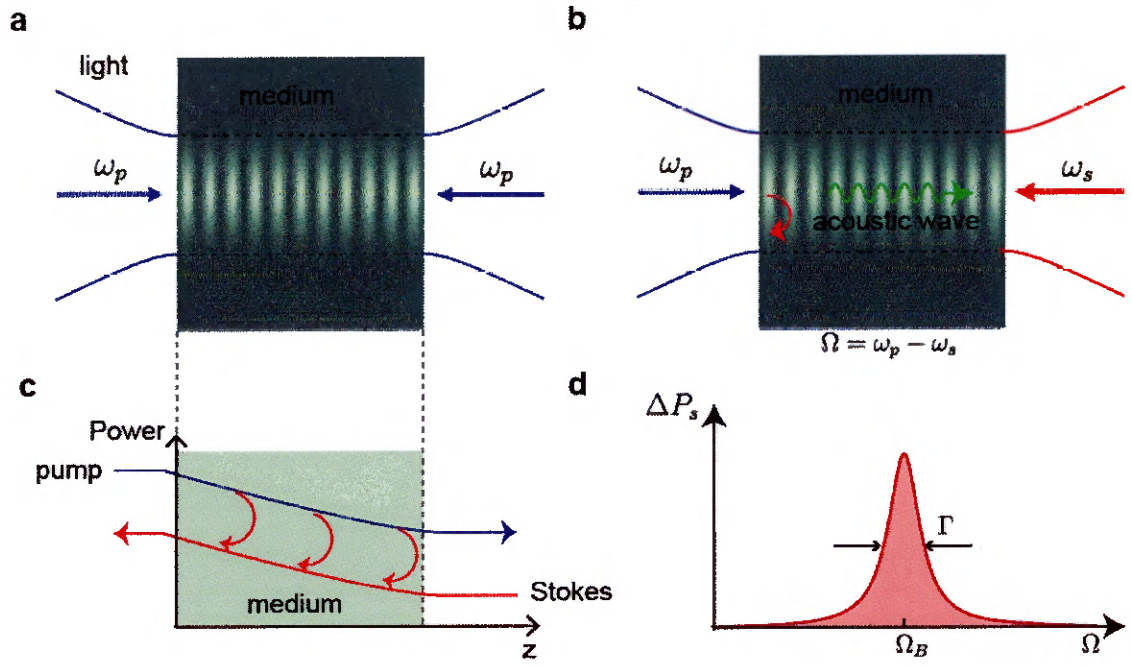

Figure 2.1: **Stimulated Brillouin Scattering.** (**a**) The interference between counter-propagating optical fields generates a period density variation along the medium through electrostriction. This in turn leads to refractive index modulation through photoelastic effect. (**b**) As the counter-propagating optical waves are frequency detuned from each other, the beat pattern moves and essentially acts like a moving Bragg mirror. This scatters and Doppler shifts the incident light at higher frequency ω_p to light at lower frequency ω_s and generates an acoustic wave at frequency $\Omega = \omega_p - \omega_s$. (**c**) Resonant transfer of energy occurs between the counter-propagating beam when the velocity of the acoustic wave matches the longitudinal sound velocity in the medium. (**d**) The energy transfer spectrum (or amplified Stokes light represented by ΔP_s) has a characteristic Lorentzian line shape centered at the Brillouin frequency Ω_B.

index modulation, transferring energy from the higher frequency (pump) optical wave to the lower frequency (Stokes) optical wave (Fig. 2.1**c**). Resonant enhancement of both the acoustic wave and back-scattered light occurs when the frequency detuning between the counter propagating waves is such that the velocity of the interference pattern matches the longitudinal sound velocity in the medium (Fig. 2.1**d**). This characteristic detuning frequency at which the resonant energy transfer occurs is called Brillouin frequency Ω_B. Next we discuss how to determine Ω_B.

In a backward scattering geometry, a forward propagating pump light having

frequency and wavevector $(\omega_p, k(\omega_s))$ is scattered to a backward propagating Stokes light $(\omega_s, -k(\omega_s))$ and a moving acoustic wave $(\Omega, q(\Omega))$. We assume linear dispersion relation $k(\omega) = \omega/v_o(q(\Omega) = \Omega/v_a)$ for both the optical (acoustic) waves, where $v_o(v_a)$ is the velocity and light (sound) in the medium (Fig. 2.2**a**). Since the higher frequency (ω_p) pump light is transferred to lower frequency Stokes light (ω_s) with the excitation of the acoustic wave it must satisfy the following energy conservation requirement (Fig. 2.2**b**):

$$\omega_p - \omega_s = \Omega_{\mathrm{B}} \tag{2.1}$$

Moreover, since the acoustic waves are driven by the interference of the optical waves the acoustic wavevector must also satisfy the following phase matching requirement:

$$k(\omega_p) = -k(\omega_s) - q(\Omega). \tag{2.2}$$

These requirements along with the dispersion relations for optical and acoustic waves (assumed linear for a bulk system) set the frequency for the resonant Brillouin energy transfer:

$$\Omega_{\mathrm{B}} = \frac{2\omega_p v_a}{1 + v_a/v_o} \approx \frac{2\omega_p v_a}{v_o} = \frac{2\omega_p v_a n}{c}, \tag{2.3}$$

c is the speed of light in vacuum and n is the refractive index of the medium. Assuming optical wavelengths of 1.5 μm, one obtains Brillouin frequency in the 10-100 GHz range for most crystalline materials.

For heavily damped phonons, the dynamics of SBS typically gives rise to a non-linear scattering over a finite bandwidth, Γ, around Ω_{B}. This bandwidth, which is typically in the 10-100 MHz [113], is determined by the lifetime $(\tau_{\mathrm{ph}} = 2\pi/\Gamma)$ of the acoustic waves in the bulk medium.

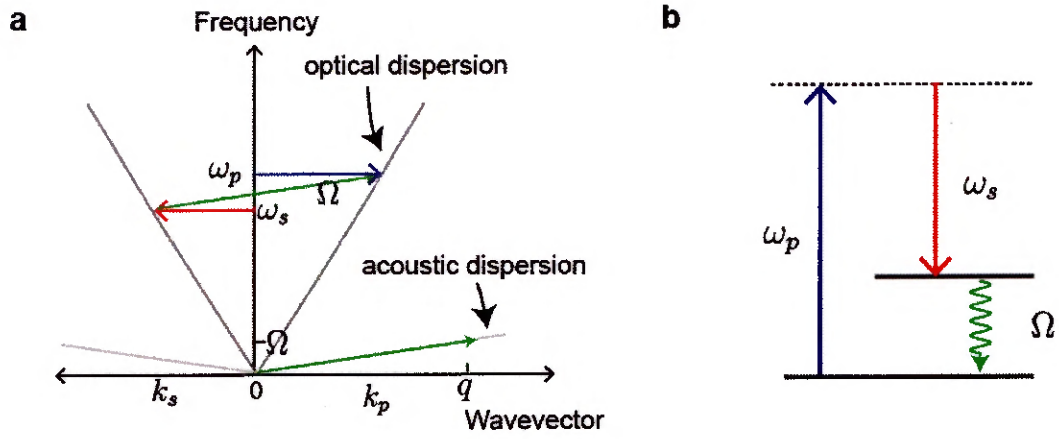

Figure 2.2: **Phase matching and energy conservation requirements.** (**a**) traveling wave optomechanical interaction, the acoustic and optical fields must satisfy phase-matching requirements set by the linear dispersion of the optical and longitudinal acoustic waves in a bulk medium. (**b**) The difference in frequency between the optical waves must match the frequency of the acoustic wave.

To explore such dynamics resulting from the nonlinear coupling of optical and acoustic waves, we start with a simple 1-Dimensional formalism that assumes plane wave optical fields

$$E_p(z,t) = A_p(z,t)e^{i(k_p z - \omega_p t)} + \text{c.c.} \tag{2.4}$$

$$E_s(z,t) = A_s(z,t)e^{i(-k_s z - \omega_s t)} + \text{c.c.} \tag{2.5}$$

interacting with a plane wave acoustic field

$$u(z,t) = B(z,t)e^{i(qz - \Omega t)} + \text{c.c.}, \tag{2.6}$$

where $\Omega = \omega_p - \omega_s$ and $q = k_p + k_s$. The acoustic displacement field obeys the elastic wave equation [114],

$$\rho\ddot{u} = -\eta\dot{u} + C\nabla^2 u + f_{\text{es}}, \tag{2.7}$$

where η is the damping constant, C is the elastic constant and f is the optical force density due to electrostriction. Here, η is related to the Brillouin linewidth as $\Gamma = \eta/\rho$ and C is related to the acoustic velocity as $v_a = \sqrt{C/\rho}$. Note that for our current 1-Dimensional calculation $\nabla = \partial/\partial z$. f_{es}, which is the divergence of the stress σ due to electrostriction, is given by [49]

$$f_{\text{es}}(z,t) = -\nabla \cdot \sigma = -\frac{\partial}{\partial z}\left(-\frac{1}{2}\epsilon_0 n^4 p \left\langle E(z,t)^2 \right\rangle\right) = \frac{1}{2}\epsilon_0 n^4 p \frac{\partial}{\partial z}\left\langle (E_(z,t) + E_s(z,t))^2 \right\rangle . \tag{2.8}$$

Note that $\langle \ldots \rangle$ here denotes time averaged optical fields as the optical frequencies is much faster than the acoustic response of the system. The relevant term of f_{es} that drives the acoustic wave is then given by

$$\begin{aligned} f_{\text{es}}(z,t) &= \frac{1}{2}\epsilon_0 n^4 p \frac{\partial}{\partial z}\left(2A_p(z,t)A_s^*(z,t)e^{i(k_p+k_s)z-(\omega_p-\omega_s)t} + \text{c.c.}\right) \\ &= iq\epsilon_0 n^4 p A_p(z,t)A_s^*(z,t)e^{i(qz-\Omega t)} + \text{c.c.}, \end{aligned} \tag{2.9}$$

where ϵ_0 is the vacuum permittivity, n is the index of refraction and p is the photoelastic constant. Substituting Eqns. (2.6) and (2.9) into the elastic wave equation (2.7) and assuming that the acoustic amplitude varies slowly in space and time, we obtain the following equation

$$-2i\Omega\frac{\partial B}{\partial t} + (\Omega_{\text{B}}^2 - \Omega^2 - i\Gamma\Omega)B - \Gamma\frac{\partial B}{\partial t} - 2iv_a^2 q\frac{\partial B}{\partial z} = \frac{iq\epsilon_0 n^4 p}{\rho}A_p A_s^*. \tag{2.10}$$

Note that the Brillouin frequency $\Omega_B = qv_a$ in the above equation. Typically acoustic waves at GHz frequencies are strongly damped and propagate much smaller distances compared to distance over which the optical driving force varies significantly. Therefore, we ignore the spatial derivative of the acoustic envelope field (i.e. $\partial B/\partial z \to 0$) and derive the following equation of motion for the envelope field B at steady state

in time (i.e. $\partial B/\partial t = 0$)

$$B(z) = \frac{iq\epsilon_0 n^4 p}{\rho} \frac{A_p(z)A_s^*(z)}{(\Omega_B^2 - \Omega^2 - i\Omega\Gamma)}. \tag{2.11}$$

This equation shows that the mechanical response to the optical driving is local. In other words, the phonon envelope, $B(z)$, follows the optical driving term $A_p(z)A_s^*(z)$ at every point in space. We also see that optical forces due to electrostriction can be used to resonantly excite acoustic waves.

The spatio-temporal evolution of the optical fields the wave equation derived from the Maxwell's equations [1]

$$\frac{\partial^2 E_i}{\partial z^2} - \frac{1}{v_o^2}\frac{\partial^2 E_i}{\partial t^2} = \frac{1}{\epsilon_0 c^2}\frac{\partial^2 \mathcal{P}_i}{\partial t^2}, i = \mathrm{p, s}, \tag{2.12}$$

where $\mathcal{P} = \epsilon_0 \Delta\chi E$ is the nonlinear polarization that results from the change in the susceptibility ($\Delta\chi$) of the medium due to the presence of the acoustic fields. The change in susceptibility stems from the refractive index change $\Delta\epsilon = n^4 pS$ due to the photoelastic effect, where $S = \nabla u = \partial u/\partial z$ is the strain field. Therefore, the nonlinear polarization is given by

$$\mathcal{P} = \epsilon_0 n^4 p \left(\frac{\partial u}{\partial z}\right) E. \tag{2.13}$$

The components of P that act as driving terms for the pump field E_p and the Stokes field E_s are

$$\mathcal{P}_p = iq\epsilon_0 n^4 pBA_s e^{i(k_p z - \omega_p t)} + \text{c.c.}, \tag{2.14}$$

$$\mathcal{P}_s = -iq\epsilon_0 n^4 pB^* A_p e^{i(-k_s z - \omega_s t)} + \text{c.c.}, \tag{2.15}$$

respectively. Notice that since the displacement field $u \propto E^2$, $P \propto E^3$, meaning

Brillouin scattering is a type of third-order nonlinear interaction. Now substituting Eqs. (2.4-2.5) and Eqs. (2.14-2.15) into the elastic wave equation 2.12 and assuming the optical envelopes varies slowly in space and time, we obtain the following equations for the optical envelope fields

$$\frac{\partial A_p}{\partial z} + \frac{n}{c}\frac{\partial A_p}{\partial t} = -\frac{q\omega_p n^4 p}{2nc} B A_s, \tag{2.16}$$

$$-\frac{\partial A_s}{\partial z} + \frac{n}{c}\frac{\partial A_p}{\partial t} = \frac{q\omega_s n^4 p}{2nc} B^* A_p. \tag{2.17}$$

Now substituting the solution for B from Eq. (2.11) to these equations we can derive the following coupled mode equations at steady state in time

$$\frac{\partial A_p}{\partial z} = -\frac{iq^2\omega_p\epsilon_0 n^8 p^2}{2nc\rho}\frac{A_p|A_s|^2}{(\Omega_{\mathrm{B}}^2 - \Omega^2 - i\Omega\Gamma)}, \tag{2.18}$$

$$\frac{\partial A_s}{\partial z} = \frac{iq^2\omega_s\epsilon_0 n^8 p^2}{2nc\rho}\frac{A_p|A_s|^2}{(\Omega_{\mathrm{B}}^2 - \Omega^2 - i\Omega\Gamma)}. \tag{2.19}$$

Therefore, defining optical power as $P_i = 2n\epsilon_0 c A_i A_i^* A_{\mathrm{eff}}$, where A_{eff} is the effective transverse cross sectional area of the optical beam, we find these equations from Eqns. (2.18-2.19)

$$\frac{\partial P_p}{\partial z} = -G_{\mathrm{B}} P_p P_s, \tag{2.20}$$

$$\frac{\partial P_s}{\partial z} = -G_{\mathrm{B}} P_p P_s \tag{2.21}$$

where the Brillouin gain $G_B(\Omega)$ is given by

$$G_{\mathrm{B}}(\Omega) = \frac{n^7 p^2 \omega^2}{v_a c^3 \rho \Gamma A_{\mathrm{eff}}}\frac{(\Gamma/2)^2}{(\Omega_B - \Omega)^2 + (\Gamma/2)^2}, \tag{2.22}$$

where we have assumed $\omega_p \simeq \omega_s = \omega$. Assuming undepleted pump (i.e. small energy transfer between the pump and the Stokes light so that I_p is essentially constant), we

can solve Eqn. (2.23) to get

$$P_s(z) = P_s(L)e^{-G_B(\Omega)P_p(L-z)}. \tag{2.23}$$

In the weak signal gain limit, i.e. $G_{\mathrm{B}}(\Omega)P_pL \ll 1$, we can use Eq. (2.23) to obtain the following fractional change in Stokes power over the interaction length L

$$\frac{\Delta P_s}{P_s} = \frac{P_s(0) - P_s(L)}{P_s(L)} \simeq G_B(\Omega)P_pL. \tag{2.24}$$

As explained before the Brillouin gain bandwidth in the weak signal limit is Lorentzian having the linewidth Γ determined by the acoustic dissipation rate. Therefore, energy transfer spectrum can not only be used to characterize $G_B(\Omega_B)$ but also get information about the acoustic damping rate Γ.

Such energy transfer measurements are relatively easy to perform within optical fiber-based systems due to long interaction lengths but are relatively challenging to measure within bulk crystalline solids because of typically weaker coupling strengths and shorter interaction lengths. Assuming a typical value of $G_{\mathrm{B}} \sim 0.5$ $\mathrm{W^{-1}m^{-1}}$ for a silica optical fiber and $P_p = 100$ mW, we see that it is possible to get $\Delta P_s/P_s > 1$ (i.e. large energy transfer from the pump light to the Stokes light) using an optical fiber with $L > 20$m. Therefore, energy transfer measurements to determine G_B is relatively easy in such fiber based systems because long fibers with very low optical losses (~0.2 dB/km [21]) are readily accessible. However, such measurements are significantly challenging within crystalline solids whose lengths are typically in the range of a few millimeters because $\Delta P_s/P_s$ is usually of the order of 10^{-5}. Sensitive measurement technique to measure small Brillouin gain within crystalline materials is discussed in Chapter 3.

In summary, the combination of electrostriction and photoelastic effect gives rise to resonant energy transfer between counter-propagating optical waves as well as

excitation of acoustic waves resulting in a phenomena known as stimulated Brillouin scattering. While we used a simple 1-Dimensional formalism to derive the salient features of Brillouin scattering, a more generalized Hamiltonian treatment will be presented in Section 2.4.

2.2 Conventional Brillouin Limit

In the theoretical treatment above, we assumed that the GHz acoustic waves are strongly damped at ambient temperatures. Typical acoustic dissipation rates ($\Gamma/2\pi$) of 10-100 MHz within most glasses/crystalline solids would correspond to acoustic decay lengths (or coherent lengths, L_{ac}) of 10-100 μm. In this limit of Brillouin interaction when $L_{\text{ac}} \ll L$, which we call the 'Conventional Brillouin Limit', we can ignore the acoustic propagation (i.e. by setting $\partial B/\partial z \rightarrow 0$) while deriving the dynamics of stimulated Brillouin scattering. However, acoustic dissipation rates within crystalline solids can plummet at low temperatures [75]. In such scenarios, the acoustic propagation can no longer be ignored and the response of the acoustic envelope ($B(z)$) at a given position now depends on the optical forcing function throughout the device length, meaning the phonon response to optical driving is non-local in space.

When coherence length of acoustic waves at low temperatures become comparable to the length of a bulk medium, traveling wave treatment with left and right moving acoustic waves (i.e. $B_L(z)$ and $B_R(z)$) with self-consistent boundary conditions could be used to describe stimulated Brillouin interactions. However, when the coherence length of acoustic far exceeds the crystal length, the left and right moving acoustic waves form standing waves or macroscopic discrete acoustic modes. Next, we explore this regime when the acoustic coherence far exceeds the length of the crystal.

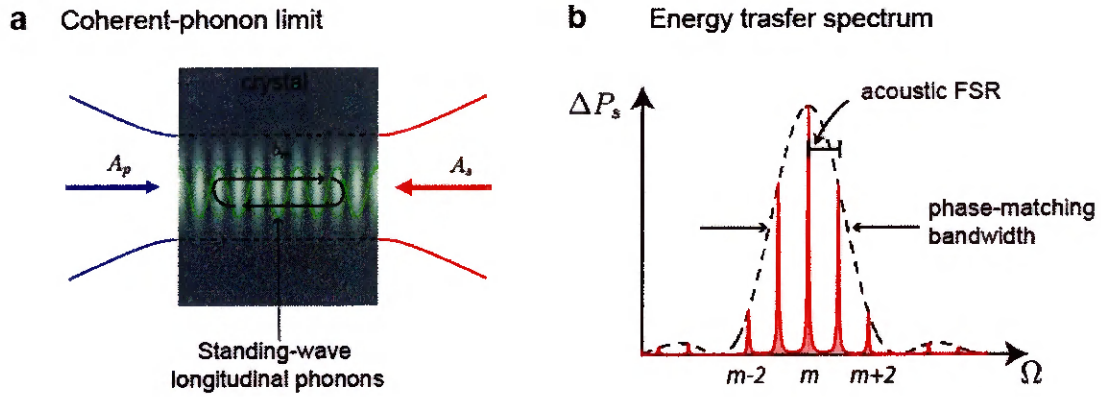

Figure 2.3: **Coherent-phonon limit.** (a) Acousto-optic interaction between traveling wave pump (A_p) and Stokes light (A_s) with discrete standing wave acoustic modes (b_m). (b) Multiple standing wave acoustic modes within the phase-matching bandwidth resonantly scatter energy from the pump waves to the Stokes wave, resulting in a multi-peaked spectrum. Adapted from Ref. [106].

2.3 Coherent-phonon Limit

At low temperatures, the coherence length of GHz frequency acoustic waves within bulk crystalline solids can be many times longer (order of meters) than the length L of the solid (order of cm) [106]. We call this limit of Brillouin interactions when $L_{ac} \gg L$ as the 'Coherent-phonon limit'. As discussed above, the conventional assumption that the mechanical response to optical driving is local is no longer valid. The acoustic waves with long coherence lengths reflect from the planar surfaces of the medium to form standing wave phonon modes much like the optical modes in a Fabry-Pèrot resonator (Fig. 2.3a). In this section, we will show how the character of energy transfer in this new regime of high-coherence for phonons (Fig. 2.3b) differs from that in the Conventional Brillouin limit, where acoustic waves have a relatively short coherence length.

To delineate the salient features of Brillouin interactions in the coherent-phonon limit, we start by looking at the coupled mode equations. An alternate formalism based on Hamiltonian framework to derive such coupled mode equations will be presented in Section 2.4. The interaction of counter-propagating optical fields (traveling

waves)

$$E_p(z,t) = A_p(z,t)e^{i(k_p z - \omega_p t)} + \text{c.c.}, \tag{2.25}$$

$$E_s(z,t) = A_s(z,t)e^{i(-k_s z - \omega_s t)} + \text{c.c.}, \tag{2.26}$$

with the standing wave acoustic modes (q_m, Ω_m)

$$u_m(z,t) = b_m(t)(e^{iq_m z} + e^{-iq_m z})e^{-i\Omega_m t} + c.c. \tag{2.27}$$

is described by the following coupled-amplitude equations

$$\frac{\partial b_m}{\partial t} = -i(\Omega_m - \Omega)b_m - \frac{\Gamma_m}{2}b_m - i\int_0^L \mathrm{d}z\ (g_0^m)^* e^{-i\Delta q_m z} A_s^* A_p, \tag{2.28}$$

$$\frac{\partial A_p}{\partial t} + v_o\frac{\partial A_p}{\partial z} = -i\sum_m g_0^m e^{i\Delta q_m z} A_s b_m, \tag{2.29}$$

$$\frac{\partial A_s}{\partial t} - v_o\frac{\partial A_s}{\partial z} = -i\sum_m (g_0^m)^* e^{-i\Delta q_m z} b_m^* A_p. \tag{2.30}$$

Here, g_0^m represents the strength of Brillouin interaction of the optical fields to a m^{th} standing wave acoustic mode (see Chapter 2.4.3 for details) and $\Delta q_m = q(\Omega_m) - (k(\omega_p) - (-k(\omega_s)) = q_m - k_p - k_s$ is the phase-mismatch between the optical driving and the right moving component of the standing wave acoustic mode. The left moving component does not satisfy the phase-matching requirement for the electrostriction mediated acousto-optic interaction. We assume that Γ_m for each acoustic mode incorporates all forms of acoustic damping mechanisms such as intrinsic losses, scattering at the surfaces, diffraction losses, and other nonidealities of the system. The integral over z in Eq. (2.28) suggests that the acoustic response to optical driving is non-local. The uncertainty in the acoustic wavevector due to the finite length of the bulk medium gives rise in a non-zero phase matching bandwidth. Multiple discrete acoustic modes within the phase-matching bandwidth can mediate Brillouin

coupling between the pump and Stokes light fields (Fig. 2.3**b**). This salient feature of the 'coherent phonon limit' arises due to the integral term in Eq. (2.28).

The actual set of standing wave acoustic modes within the phase-matching bandwidth for the bulk crystalline optomechanical system not only depends on the geometry (i.e., how you shape the boundaries of the bulk medium) but also on the anisotropy of the crystal. We will discuss this problem in greater detail in Chapter 3.2. Nevertheless, frequencies of these standing wave acoustic modes in 1-dimension can be approximated by fitting acoustic half-wavelengths (λ_{ac}) inside the crystal length (L) (i.e. $m\lambda_{\mathrm{ac}}/2 = L$). So the frequency of the m^{th} acoustic mode assuming a linear acoustic dispersion ($q(\Omega) = \Omega/v_a$) is $\Omega_m = 2\pi \times (mv_a)/(2L)$, where v_a is the longitudinal sound velocity.

In the limit of weak signal gain and undepleted pump (i.e. $\Delta P_s(0) \ll P_s(L)$ and $A_p(z) \approx$ constant), we obtain the following equation for the acoustic mode amplitude and the Stokes power change for a crystalline medium of length L

$$b_m \simeq (g_0^m)^* L \frac{A_p(0)A_s^*(L)}{(\Omega - \Omega_m + i\Gamma_m/2)} e^{-i\frac{\Delta qL}{2}} \mathrm{Sinc}\left(\frac{\Delta q_m L}{2}\right), \tag{2.31}$$

$$P_s(0) - P_s(L) \simeq P_p(0)P_s(L) \sum_m \frac{4|g_0^m|^2 L^2}{\hbar\omega_p v_o^2 \Gamma_m} \frac{(\Gamma_m/2)^2}{(\Omega - \Omega_m)^2 + (\Gamma_m/2)^2} \mathrm{Sinc}^2\left(\frac{\Delta q_m L}{2}\right), \tag{2.32}$$

where the phase mismatch $\Delta q_m = q_m - k_p - k_s \simeq \Omega_m/v_a - 2\omega_p/v_o$ to an excellent approximation. Eq. (2.32) shows that the spectrum of the power transfer has multiple Lorentzian resonances with peak amplitudes modulated by a Sinc square envelope (Fig. 2.4**b**). Note that the multi-peaked spectrum obtained in the coherent phonon limit is markedly different from a single Lorentzian response obtained in the low coherence limit (Fig. 2.4**a**).

In summary, stimulated Brillouin scattering measurement in the coherent-phonon

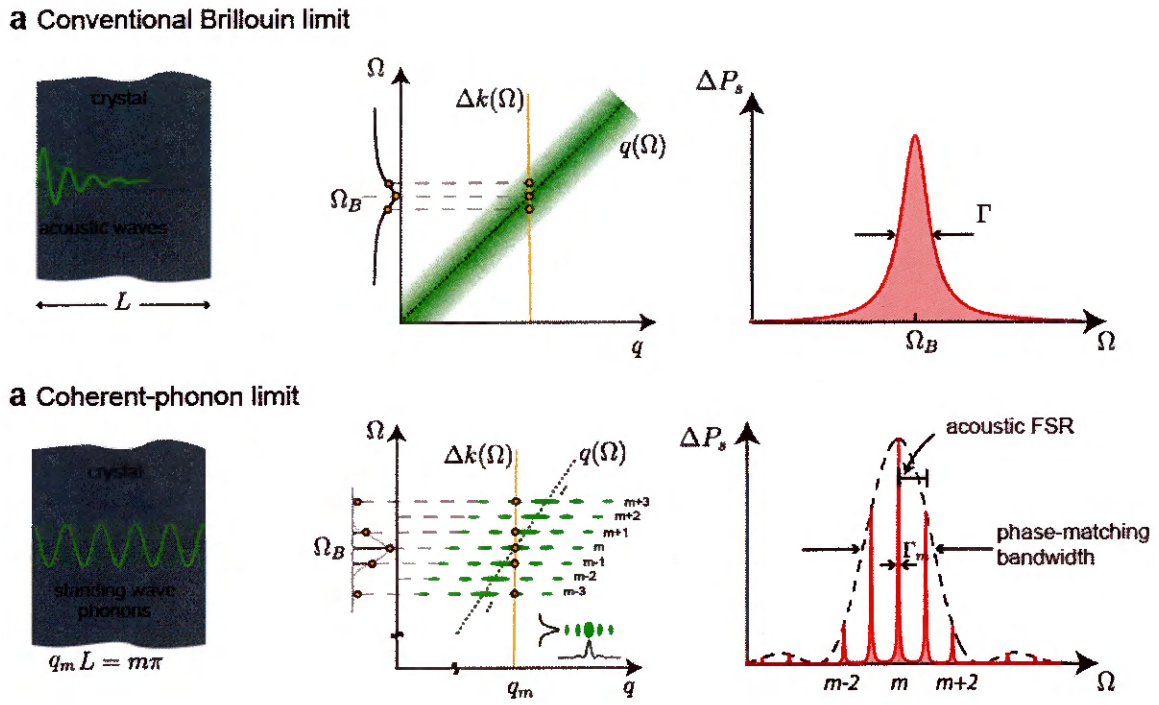

Figure 2.4: **Schematics comparing Conventional Brillouin Limit to Coherent-phonon limit.** (**a**) Sketch comparing acoustic coherence length to the crystal length (L) (left). Acoustic dispersion relation $q(\Omega)$ and the 2D intensity map (green) showing the acoustic response to an applied forcing function (middle). The optical wavevector difference between the pump and the Stokes wave $\Delta k(\Omega)$ is plotted on top of the intensity map and the intersection of this with the acoustic response yields a Lorentzian frequency response (projected left). Since generation of Stokes photons coincides with the generation of acoustic waves, $\Delta P_s(\Omega)$ exhibits the same Lorentzian response (right). (**b**) Sketch showing formation of discrete standing wave acoustic modes when the coherence length is much longer than the crystal length L (left). These acoustic modes are separated by the acoustic free spectral range of $2\pi \times v_a/2L$. Discretized acoustic dispersion relation $q_m(\Omega_m)$ and 2D intensity map (green) showing the acoustic response to an applied forcing function (middle). Each acoustic response has frequency broadening due to acoustic damping and a sinc^2 broadening in wavevector due to the finite length of the crystal. The optical wavevector difference $\Delta k(\Omega)$ that intersects the 2D intensity map of the discretized acoustic response yields a sinc^2 acoustic response (projected left). Since generation of Stokes photons coincides with the generation of acoustic waves, $\Delta P_s(\Omega)$ exhibits the same sinc^2 frequency response. Adapted from Ref. [106].

limit has dynamics and spectral response that is quite different from the Lorentzian Brillouin gain spectrum observed in the conventional Brillouin limit. Since traveling waves optical fields interact with long-lived standing wave acoustic modes (i.e with $L_{\mathrm{ac}} \gg L$) the acoustic response to optical driving in non-local in space. This optomechanical system in which free-space propagating laser beams are used to access Brillouin active acoustic modes is quite different from conventional cavity optomechanical systems that typically have discrete cavity modes for both light and sound. However, it is possible to make analogies between our optomechanical system and conventional cavity optomechanical in some regime of optomechanical interaction by writing down a Hamiltonian and defining parameters such as single-photon coupling strength and cooperativity. We discuss this in detail in the next section.

2.4 Hamiltonian Treatment

In this section, we give a brief overview of the Hamiltonian treatment, which can be used to derive coupled mode equations that describe the dynamics of Brillouin scattering both in the coherent-phonon limit and the conventional Brillouin limit. In the coherent-phonon limit, we can use this generalizable Hamiltonian treatment to define coupling rates, nonlinear susceptibility, and cooperativity, permitting us to make analogies with the more familiar multimode cavity optomechanical systems. Note that the Hamiltonian treatment outlined here closely follows the supplementary section of our manuscript Ref. [106].

The total Hamiltonian H of our optomechanical system

$$H = H^{\mathrm{opt}} + H^{\mathrm{ac}} + H^{\mathrm{int}}, \tag{2.33}$$

where H^{opt}, H^{ac}, and H^{int} is the Hamiltonian of the optical fields, is the Hamiltonian

of the acoustic fields, and is the interaction Hamiltonian, respectively.

$$H^{\text{opt}} = \frac{1}{2\mu_0}\int B^i(\mathbf{r})B^i(\mathbf{r})\mathrm{d}\mathbf{r} + \frac{1}{2\epsilon_0}\int D^i(\mathbf{r})\beta_r^{ij}(\mathbf{r})D^i(\mathbf{r})\mathrm{d}\mathbf{r}, \tag{2.34}$$

where $\mathbf{D}(\mathbf{r})$ is the electric displacement field operator, $\mathbf{B}(\mathbf{r})$ is the magnetic field operator and $\epsilon_r(\mathbf{r}) = 1/\beta_r^{ij}(\mathbf{r})$ is the relative dielectric constant tensor.

$$H^{\text{ac}} = \int \frac{\pi^i(\mathbf{r})\pi^i(\mathbf{r})}{2\rho(\mathbf{r})}\mathrm{d}\mathbf{r} + \int \frac{1}{2}S^{ij}(\mathbf{r})c^{ijkl}(\mathbf{r})S^{ij}(\mathbf{r})\mathrm{d}\mathbf{r}, \tag{2.35}$$

where $\pi(\mathbf{r})$ is the conjugate momentum of the acoustic displacement field operator $\mathbf{u}(\mathbf{r})$, $\rho(\mathbf{r})$ is the density, $c^{ijkl}(\mathbf{r})$ is the elastic constant tensor and $S^{ij}(\mathbf{r}) = 1/2(\partial u^i(\mathbf{r})/\partial r^j + \partial u^j(\mathbf{r})/\partial r^i)$ is the strain operator.

The coupling between light and sound arises in bulk medium arises because $\beta^{ij}(\mathbf{r})$ depends on $\mathbf{u}(\mathbf{r})$. Therefore, $\beta^{ij}(\mathbf{r}, \mathbf{u}(\mathbf{r})) = \beta_r^{ij} + \tilde{\beta}^{ij}(\mathbf{r}; \mathbf{u}(\mathbf{r}))$, where $1/\beta_r$ is the original purely electromagnetic dielectric constant tensor and $\tilde{\beta}^{ij}(\mathbf{r}; \mathbf{u}(\mathbf{r})) = p^{ijkl}S^{kl}(\mathbf{r})$ is the correction to the inverse dielectric constant tensor due to the photoelastic interaction within a bulk medium [115]. The photoelastic constant tensor p^{ijkl} relates changes in the strain to changes in the inverse dielectric constant of the medium due to electrostriction/photoelasticity mediated optomechanical coupling. Therefore, the interaction term is given by

$$H^{\text{int}} = \frac{1}{2\epsilon_0}\int D^i(\mathbf{r})\tilde{\beta}^{ij}(\mathbf{r})D^i(\mathbf{r})\mathrm{d}\mathbf{r}, = \int \frac{1}{2\epsilon_0}D^i(\mathbf{r})D^j(\mathbf{r})p^{ijkl}(\mathbf{r})S^{kl}(\mathbf{r})\mathrm{d}\mathbf{r}. \tag{2.36}$$

This Hamiltonian framework along with appropriate normal mode expansions, optical and acoustic mode normalization, and commutation relations can be used to derive Hamiltonian for both the coherent-phonon limit and the conventional Brillouin limit. Next, we discuss the Hamiltonian for our system in the coherent-phonon limit.

2.4.1 Coherent-phonon Limit

The dynamics of Brillouin scattering in the coherent-phonon limit, where scattering between two counter-propagating optical fields is mediated by a coherent phonon, is reminiscent of a multimode cavity optomechanical system in which a phonon mode mediates interaction between two distinct optical cavity modes. The interaction Hamiltonian for such system is described by $\hbar(g_{12}a_2a_1^\dagger b^\dagger + g_{12}^* a_2^\dagger a_1 b)$, where a_1, a_2, and b are the annihilation operator for the Stokes-photon, pump-photon, and the phonon mode, respectively [116]. However, since free-space optical beams travels directly through our bulk crystalline resonator, no optical cavity modes are formed (for simplicity, we assumed negligible reflections at the surfaces of the bulk crystal). Consequently, each coherent phonon mode (b_m) couples to a continuum of traveling optical waves. Therefore, the total interaction Hamiltonian for the coupling of discrete phonon modes to a continuum of counter-propagating pump and Stokes waves in the coherent-phonon limit is given by

$$H^{\text{int}} = \sum_m \int \frac{\mathrm{d}k\mathrm{d}k'}{2\pi} \hbar g_m(k,k') a_{pk}^\dagger a_{sk'} b_m + \text{H.c.}, \tag{2.37}$$

where $g_m(k,k')$, which we call the geometric coupling rate, characterizes the strength of the optomechanical interaction (see Appendix A). Unlike the case of discrete optical cavity modes with unitless mode amplitude operators, here the mode amplitude operator a_k has units of $\sqrt{\text{Length}}$ and g_m has units of $\sqrt{\text{Length}} \cdot \text{Time}^{-1}$ [107].

The interaction Hamiltonian written as a sum over continuum of optical modes in Eq. (2.37) looks rather complicated. We chose this $k-$space representation to make analogies between our optomechanical system with the more familiar case of a multimode optomechanical system consisting of discrete optical cavity modes. Despite these similarities, coupling to a continuum of traveling-wave optical fields in our system gives rise to different dynamics such as optomechanical coupling that depends

on phase-matching and optical field amplitudes that vary as a function of space within the crystal. For instance, for typical experimental parameters, the Stokes optical field is amplified along the axis of propagation at the expense of pump field. Therefore, it is more natural to formulate the Hamiltonian of our system in real space using mode envelope operators [107, 115]

The interaction between traveling wave pump photon $(\mathbf{D}_p(\mathbf{r}), k_p, \omega_p)$ with counter-propagating Stokes photon $(\mathbf{D}_s(\mathbf{r}), -k_s, \omega_s)$ mediated by a standing wave acoustic wave $(\mathbf{U}_m(\mathbf{r}), q_m, \Omega_m)$ results in the spatiotemporal evolution of the optical fields. For the purpose of deriving the nonlinear susceptibility, we begin by expressing the Hamiltonian of our traveling-wave system as a sum over modes in k-space, as follows:

$$H^{\text{opt}} = \int \mathrm{d}k\ \hbar\omega_p(k) \left(a_{pk}^\dagger a_{pk} + \frac{1}{2}\right) + \int \mathrm{d}k\ \hbar\omega_s(k) \left(a_{sk}^\dagger a_{sk} + \frac{1}{2}\right), \tag{2.38}$$

$$H^{\text{ac}} = \sum_m \hbar\Omega_m \left(b_m^\dagger b_m + \frac{1}{2}\right), \tag{2.39}$$

$$H^{\text{int}} = \sum_m \int \frac{\mathrm{d}k\mathrm{d}k'}{2\pi} \hbar g_m(k, k') a_{pk}^\dagger a_{sk'} b_m + \text{H.c.}. \tag{2.40}$$

We convert this k-space Hamiltonian into an equivalent Hamiltonian over real-space (z) as follows:

$$H^{\text{opt}} = \int \mathrm{d}z\ \hbar \left(A_p^\dagger(z)\hat{\omega}_{p,z} A_p(z) + \frac{1}{2}\right) + \int \mathrm{d}z\ \hbar \left(A_s^\dagger(z)\hat{\omega}_{s,z} A_s(z) + \frac{1}{2}\right), \tag{2.41}$$

$$H^{\text{ac}} = \sum_m \hbar\Omega_m \left(b_m^\dagger b_m + \frac{1}{2}\right), \tag{2.42}$$

$$H^{\text{int}} = \sum_m \int \mathrm{d}z\ \hbar g_0^m(z) e^{i(q_m - k_p - k_s)z} A_p^\dagger(z) A_s(z) b_m + \text{H.c.}. \tag{2.43}$$

Here, our real-space operator $A_j(z)$ is define as $A_j(z) = \int \frac{\mathrm{d}k}{\sqrt{2\pi}}\ a_{jk} e^{i(k-k_j)z}$, for $j = p$ and s, is the mode amplitude operator for pump and Stokes, respectively. In this case, the mode amplitude operators have the units of $1/\sqrt{\text{Length}}$ and the operator $A^\dagger(z)A(z)$ represents photon number per unit length (or photon number density).

Note that in the real-space description, $\hat{\omega}_{p,z} = \omega_p - iv_o\partial_z$ and $\hat{\omega}_{s,z} = \omega_s + iv_o\partial_z$ are spatial operators obtained after Taylor expanding the dispersion relations for the optical fields $\omega_p(k)$ and $\omega_s(k)$ in k-space. $g_0^m(z)$ is the single-photon coupling rate that depends on the transverse mode overlaps of the acoustic and optical fields. For details on this transformation see Appendix A and Appendix B.

2.4.2 Nonlinear optical susceptibility

In this section, we derive the nonlinear optical susceptibility resulting from the acousto-optic interaction in the coherent-phonon limit. Optical susceptibility permits us to relate optomechanical scattering rates to coupling rates and acoustic dissipation rates. We begin by writing down the coupled mode equations derived from the real-space Hamiltonian of our system in Eqns. (2.41-2.43).

Using the Heisenberg equations of motion ($\dot{b}_m(t) = -(i/\hbar)[b_m, H]$, and $\dot{A}_\gamma(z,t) = -(i/\hbar)[A_\gamma, H]$) and commutation relations ($[b_m, b_n^\dagger] = \delta_{mn}$, and $[A_\gamma(z,t), A_{\gamma'}^\dagger(z',t)] = \delta_{\gamma\gamma'}\delta(z-z')$), we can write down the equations of motion for the phonon mode amplitude operator and the optical mode envelope operators as

$$\partial_t b_m = -i\Omega_m b_m - i\int_0^L \mathrm{d}z\ (g_0^m)^* e^{-i\Delta q z} A_s^\dagger A_p - \Gamma_m/2, \tag{2.44}$$

$$\partial_t A_p = -i\hat{\omega}_{p,z} A_p - i\sum_m g_0^m e^{i\Delta q z} A_s b_m, \tag{2.45}$$

$$\partial_t A_s = -i\hat{\omega}_{s,z} A_s - i\sum_m (g_0^m)^* e^{-i\Delta q z} b_m^\dagger A_p. \tag{2.46}$$

Here, $\Delta q = q_m - k_p - k_s$. Recall, that the spatial operators $\hat{\omega}_{p,z} = \omega_p - iv_o\partial_z$ and $\hat{\omega}_{s,z} = \omega_s + iv_o\partial_z$. In Eq. (2.44), we phenomenologically added a phonon dissipation rate $\Gamma_m/2$ so that it models all forms of phonon losses such as intrinsic losses in the bulk medium, losses at the surface due to roughness, losses due to diffraction and so on. Finally, after factoring out the fast-oscillating component by letting $\bar{b}_m(t) =$

$b_m(t)e^{i\Omega t}$, where $\Omega = \omega_p - \omega_s$ is the frequency detuning between the pump and the Stokes fields, and $\bar{A}_\gamma(z,t) = A_\gamma(z,t)e^{i\omega_\gamma t}$, we obtain the following spatiotemporal evolution for the phonon mode amplitude operators and the envelope fields

$$\partial_t \bar{b}_m = -i(\Omega_m - \Omega)\bar{b}_m - \frac{\Gamma_m}{2}\bar{b}_m - i\int_0^L \mathrm{d}z\ (g_0^m)^* e^{-i\Delta qz}\bar{A}_s^\dagger \bar{A}_p, \tag{2.47}$$

$$\partial_t \bar{A}_p + v_o \partial_z \bar{A}_p = -i\sum_m g_0^m e^{i\Delta qz}\bar{A}_s \bar{b}_m, \tag{2.48}$$

$$\partial_t \bar{A}_s - v_o \partial_z \bar{A}_s = -i\sum_m (g_0^m)^* e^{-i\Delta qz}\bar{b}_m^\dagger \bar{A}_p. \tag{2.49}$$

We have assumed negligible optical absorption inside the crystalline medium because the optical crystals are transparent. We also assume that the mode profiles are uniform along z such that g_0^m is a constant. If we now make the undepleted pump approximation ($A_p(z,t) \approx A_p$) and small signal gain approximation ($\Delta P_s(0) \ll P_s(L)$), Eqs. (2.47) and (2.49) result in the following steady-state equations for the phonon mode amplitude and the Stokes field envelope

$$\bar{b}_m \simeq (g_0^m)^* L \frac{\bar{A}_p(0)\bar{A}_s^*(L)}{\left(\Omega - \Omega_m + i\frac{\Gamma_m}{2}\right)} e^{-\frac{i\Delta qL}{2}} \mathrm{sinc}\left(\frac{\Delta qL}{2}\right), \tag{2.50}$$

$$\bar{A}_s(z) = \bar{A}_s(L) - \sum_m \frac{|g_o^m|^2 L}{v_o} \frac{|\bar{A}_p^*(0)|^2 \bar{A}_s(L)}{\left(\Omega - \Omega_m - i\frac{\Gamma_m}{2}\right)} e^{\frac{i\Delta qL}{2}} \mathrm{sinc}\left(\frac{\Delta qL}{2}\right) \frac{\left(e^{-i\Delta qz} - e^{-i\Delta qL}\right)}{\Delta q}. \tag{2.51}$$

Eq. (2.51) can be further simplified to calculate Stokes field envelope at $z = 0$ as

$$\bar{A}_s(0) \approx \bar{A}_s(L) - i\sum_m \frac{|g_0^m|^2 L^2}{v_o} \frac{|\bar{A}_p^*(0)|^2 \bar{A}_s(L)}{\left(\Omega - \Omega_m - i\frac{\Gamma_m}{2}\right)} \mathrm{sinc}^2\left(\frac{\Delta qL}{2}\right). \tag{2.52}$$

Using Eq. (2.52) and the expression for the optical power $P_\gamma^{\mathrm{opt}}(z) = \hbar\omega_\gamma v_o A_\gamma^\dagger(z)A_\gamma(z)$,

the Stokes power exiting the system at $z = 0$ is given by

$$P_s(0) \approx P_s(L) + P_p(0)P_s(L)\sum_m \frac{4|g_0^m|^2 L^2}{\hbar\omega_p v_o^2 \Gamma_m} \frac{(\Gamma_m/2)^2}{(\Omega-\Omega_m)^2+(\Gamma_m/2)^2} \mathrm{sinc}^2\left(\frac{\Delta q L}{2}\right). \tag{2.53}$$

In deriving the above expression, we have ignored higher order terms proportional to $|\bar{g}_o^m|^4 P_p^2 L^4/(\hbar^2\omega^2 v_o^4)$ because we are considering the case of weak signal gain.

2.4.3 Single-Photon Coupling Rate

In a prototypical cavity optomechanical system consisting of a single optical cavity mode interacting with a single mechanical mode, single-photon coupling strength g_0 quantifies the strength of interaction between a single photon and a single phonon. We seek to define a similar quantity in our optomechanical system where a standing wave mechanical mode interacts with counter-propagating free-space optical beams. The Hamiltonian treatment presented earlier naturally allows us to define such a single-photon coupling rate for our system, g_0^m. In our system, optomechanical coupling to a mechanical mode shifts the optical dispersion bands (i.e. $\Delta\Omega = \Delta(\omega_p(k) - \omega_s(k))$). Therefore, g_0^m quantifies this shift in the dispersion bands for the pump and Stokes waves simply due to a single excitation (or a single phonon) of the mechanical mode in our system.

This single-photon coupling rate for the electrostriction mediated optomechanical coupling between counter-propagating free-space optical fields and a standing wave phonon in our system is given by Eqn. (A.20)

$$g_o^m(z) \simeq \frac{\sqrt{\hbar\omega_p\omega_s\Omega_m}}{4\epsilon_0} \int \mathrm{d}\mathbf{r}_\perp (D_p^i(\mathbf{r}))^* D_s^j(\mathbf{r}) p^{ijkl}(\mathbf{r}) \left(\frac{\partial U_m^k(\mathbf{r})}{\partial r^l} + iq_m\delta_{lz}U_m^k(\mathbf{r})\right). \tag{2.54}$$

Since the transverse mode profiles for the traveling wave optical fields inside the crystal (for example, Gaussian laser beams) can vary along the propagation direction,

the coupling rate depends on space. For now, it is instructive to derive an approximate expression for the coupling rate to extract dependencies between the coupling rates and material parameters. To this end, we assume that the transverse mode profiles of both the optical and acoustic waves along the propagating direction (z-direction) remain invariant. This, for instance, is a good approximation for Gaussian optical beams when the crystal length is much shorter than the Rayleigh range (i.e. the beam diffraction is negligible inside the crystal). For simplicity, we also assume that the pump field, $\mathbf{D}_p$, and the Stokes optical field, $\mathbf{D}_s$, are both co-polarized along the x-axis, and the standing wave phonon mode, $\mathbf{U}_m$ is longitudinally polarized along z-axis. In this case we can greatly simplify Eqn. (2.54) to

$$g_0^m \simeq \frac{iq_m}{4\epsilon_o}\sqrt{\hbar\Omega_m\omega_p\omega_s}\int \mathrm{d}\mathbf{r}_\perp \Big(D_p^x(\mathbf{r})\Big)^* D_s^x(\mathbf{r}) p^{1133} U_m^z(\mathbf{r}). \tag{2.55}$$

In deriving the above expression we assumed that the $\partial_x u_m^z, \partial_y u_m^z \ll q_m u_m^z$. The transverse derivatives are small if the transverse acoustic mode profiles (typically $\sim$ tens of microns for our experimental system) are much larger than the wavelength of phonons ($\sim< 1$ μm). The relevant photoelastic constant ($p^{1133} \equiv p_{13}$) depends on the anisotropy of the crystal as well as the crystal axis along which the longitudinal acoustic waves propagate.

Assuming plane-wave optical and acoustic fields with transverse area, A, we can use the normalization conditions in Eqs. (A.13), (A.14), and (A.18) to obtain the following simplified expression for the coupling rate

$$g_0^m \approx i\frac{\omega^2 n^3 p_{13}}{2c}\sqrt{\frac{\hbar}{\Omega_m \rho A L}}, \tag{2.56}$$

where n is the refractive index and ρ is the density of the bulk medium. In deriving the following expression, we assumed $\omega_p \simeq \omega_s \equiv \omega$ and the acoustic wavevector $q_m = k_p + k_s \simeq 2\omega_p n/c$.

Parameters	TeO2	Quartz
L	1 mm	1 mm
A	$\pi \times (20\ \mu\text{m})^2$	$\pi \times (20\ \mu\text{m})^2$
n	2.33	1.55
p_{13}	0.34	0.27
ρ	6040 kgm^{-3}	2648kgm^{-3}
λ	1549 nm	1549 nm
Ω	$2\pi \times 12.2$ GHz	$2\pi \times 12.7$ GHz
$\lvert g_0^m \rvert$	$2\pi \times 720$ Hz	$2\pi \times 250$ Hz

Table 2.1: Calculation of single-photon coupling rate.

As an example calculation, we compute the single-photon coupling rate for z-cut TeO_2 and z-cut Quartz crystal in Table 2.1.

2.4.4 Free-space Cooperativity

In linear cavity optomechanics, cooperativity is a figure of merit that quantifies the strength of optomechanical coupling in presence of optical and acoustic damping. For an optomechanical system having coupling rate g, optical dissipation rate κ, and acoustic dissipation rate Γ_m, the cooperativity C is defined as $C = 4g^2/(\kappa\Gamma_m)$.

The interaction Hamiltonian for a typical cavity optomechanical system is nonlinear and is the form $g_0\hat{a}^\dagger\hat{a}(\hat{b}+\hat{b}^\dagger)$, where g_0 is the single-photon coupling strength and $\hat{a}$ ($\hat{b}$) is the annihilation operator for the optical (acoustic) mode. Using an external optical drive field, this interaction Hamiltonian can be linearized to obtain a bilinear Hamiltonian of the form form $ga^\dagger b^\dagger + \text{H.c.}$ or $gab^\dagger + \text{H.c.}$. Here, $g = \sqrt{\bar{n}_c}g_0$ and n_c is the cavity enhanced coupling rate and $\bar{n}_c$ is the average intracavity photon number due to the external drive field [117]. So it is in this linearized regime that we can define $C = 4g^2/(\kappa\Gamma_m) = 4\bar{n}_c g_0^2/(\kappa\Gamma_m)$.

To make an analogy between our optomechanical system consisting of free-space laser beams instead of optical cavity modes, we seek to define cooperativity in our system. In the earlier section 2.4.1, we derived the interaction Hamiltonian for our

system and discovered that the interaction Hamiltonian, which has a form $g_0 a_p a_s^\dagger b^\dagger$, is analogous to the nonlinear Hamiltonian that of a multimode optomechanical system. However, assuming undepleted pump, it is possible to linearize this system and define what we call 'free-space cooperativity'

$$\mathcal{C}^{\text{fs}} = \frac{P_p L^2 |g_0^m|^2}{\hbar \omega_p v_{gs} v_{gp} \Gamma_m}. \tag{2.57}$$

Here, P_p is the power in the pump optical wave, L is the length of the bulk medium, g_0^m is the single-photon coupling rate, v_{gs} (v_{gp}) is the group velocity of the Stokes (pump) wave and Γ_m is the acoustic damping rate (see Appendix C for a complete derivation of free-space cooperativity). The analogy between the C^{fs} and C becomes apparent if we consider an optical cavity of length L with light only making a single pass. In this case, the standard cavity-optomechanical definition of cooperativity $\mathcal{C} = 4\bar{n}_c |g_0|^2/(\Gamma_m \kappa)$, where $\kappa = 4v_{gs}/L$ and $\bar{n}_c = P_p L/(\hbar \omega_p v_{gp})$ give us the same cooperativity derived in Eq. (2.57). Note that when cooperativity equals 1 the system can undergo self-oscillation.

2.5 Conclusions

In summary, we used a generalizable quantum Hamiltonian treatment to describe the dynamics of optomechanical coupling when free-space laser beams interact with standing-wave acoustic modes within a bulk acoustic medium. We also used this Hamiltonian treatment to define optomechanical coupling rates, cooperativity, and nonlinear optical susceptibility. In Chapter 3, we perform experiments to measure these important figures of merit.

Chapter 3

Brillouin Coupling to Bulk Acoustic Waves using Free-space Laser Beams

3.1 Introduction

Within crystalline medium, acoustic dissipation plummets at low temperatures, leading to the formation of macroscopic standing wave acoustic modes. Using specially engineered cavities made out of crystalline quartz to confine such bulk acoustic modes, Galliou et. al. demonstrated acoustic Q-factors that exceed > 1 billion for 200 MHz acoustic waves at liquid Helium temperatures [100, 101]. Electromechanical coupling was used to access such low-loss phonon modes within quartz, which is piezolectric along certain crystalline axis. This result combined with a number of studies [74, 83–95] of intrinsic acoustic loss mechanisms in a wider variety of non-piezo electric crystals such as diamond, silicon, sapphire, and CaF2, suggested an immense potential for reaching intrinsic levels of acoustic dissipation within bulk crystals. Such low-loss phonons could then be utilized for applications ranging from precision metrol-

ogy [103] to tests of fundamental physics [102]. While piezoelectricity is absent in a wide variety of crystals, photoelasticity is present in every bulk medium. Therefore, optomechanical coupling using Brillouin interaction would allow us to access low-loss phonons within practically any transparent solids as the basis for new technologies and fundamental scientific studies.

In this section, as a first step toward efficient optical control of such low-loss phonons, we demonstrate Brillouin coupling between free-space laser beams and low-loss bulk acoustic modes of a crystalline resonator. Optomechanical coupling to such 'Brillouin-active' phonon modes permits us to perform phonon-mode spectroscopy, allowing us to characterize the mechanical properties of our optomechanical system. We will see in Section 3.5-3.6 that these measurements not only allow us to explore the intrinsic limits of acoustic dissipation but also provide crucial information necessary to create a new breed of cavity optomechanical system that utilizes bulk acoustic phonons.

To efficiently access such low-loss Brillouin-active phonons modes with light, we need to shape the surfaces of the crystal to confine phonons as well to engineer acoustic mode profiles to produce good acousto-optic overlap. Next, we present the design principles used to form such phonon-confining cavities.

3.2 Acoustic Resonator Design

The acoustic beam propagation within our system is reminiscent of optical beam propagation in the paraxial limit. This is because Brillouin-active phonons at high frequencies have wavelengths ($\lambda_{\mathrm{ph}} < 1$ μm) that are much smaller than the system dimensions (mm-scale). Propagating acoustic beams having coherence lengths longer than the crystal dimensions, reflect off the planar surfaces of the crystal to form standing wave acoustic modes. This is analogous to the formation of standing wave

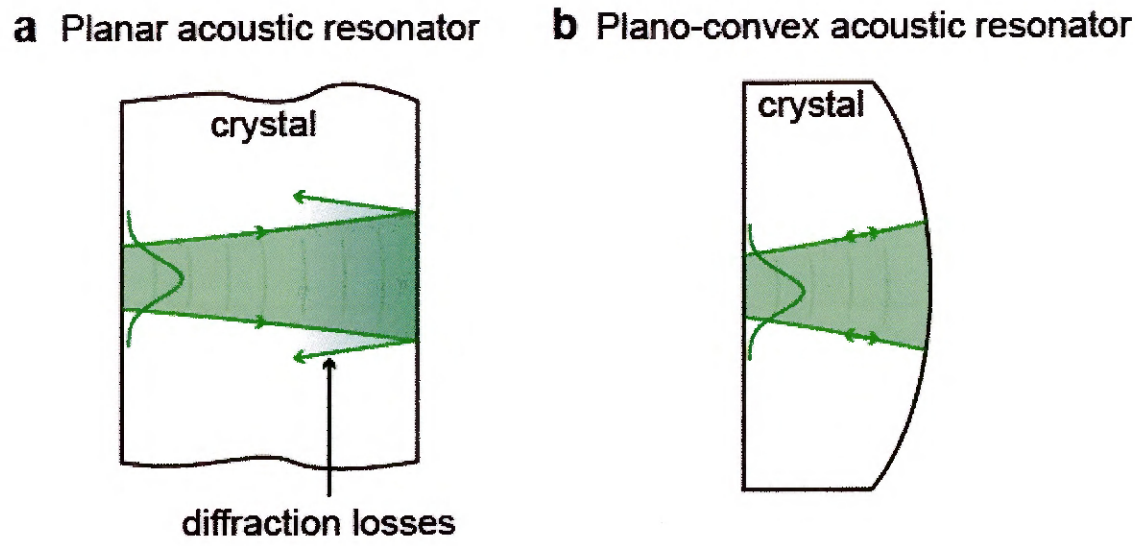

Figure 3.1: **Shaping the surfaces of a crystalline resonator for phonon trapping.** (**a**) Acoustic waves that reflect off the planar surfaces of the crystal suffer acoustic diffraction losses. (**b**) By shaping the acoustic resonator into a plano-convex geometry, we can mitigate diffraction losses to confine phonons laterally and produce stable acoustic cavities that support long-lived phonons. Adapted from Ref. [106].

optical modes within a Fabry-Pérot cavity. Similar to diffraction losses of optical modes within a Fabry-Pérot cavity, the acoustic modes within a flat-flat crystal suffer from losses due to acoustic diffraction (Fig. 3.1**a**). To address this problem, we need to shape the boundary of the crystal to mitigate acoustic diffraction and "trap" phonons in much the same way as using curved mirrors to confine light in an optical Fabry-Pérot resonator (Fig. 3.1**b**).

While the formation of stable cavities to confine light has been well studied in optics [118], to our knowledge, analogous criteria for acoustic beam stability has not been previously explored. Unlike optical beam propagation in vacuum, acoustic beam propagation within crystalline solids, can be nontrivial due to the anisotropy of elastic constants [119]. Nevertheless, by understanding the acoustic beam propagation within anisotropic solids, we show that is is possible to adopt well-known optical design principles used to form stable Gaussian beam resonators to design stable acoustic resonators.

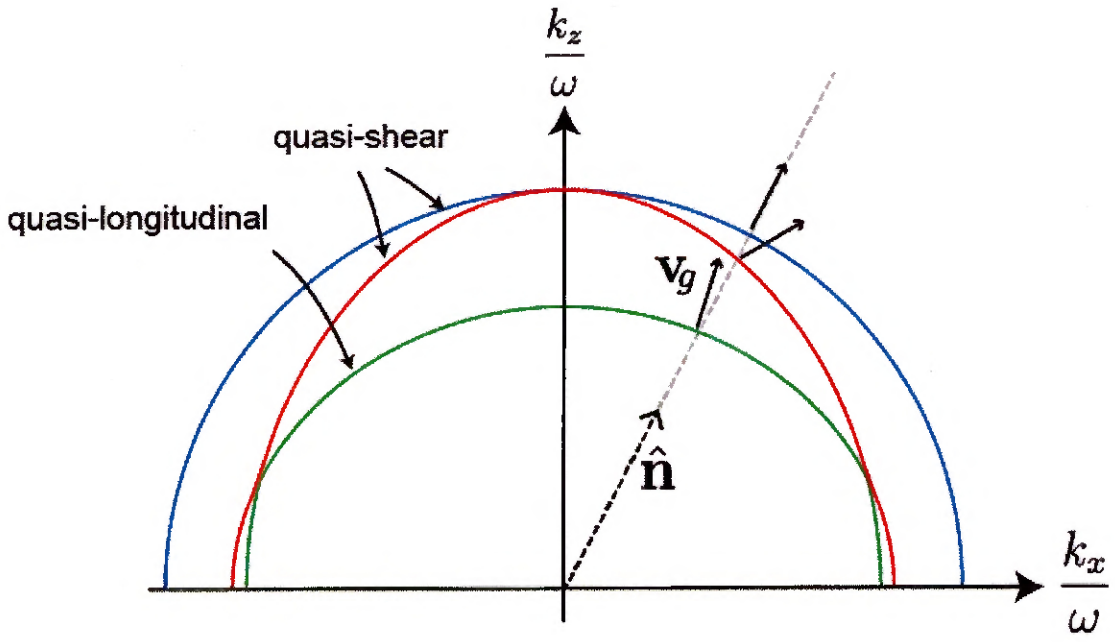

Figure 3.2: **Slowness surface of z-cut TeO_2 in XZ plane.** For an acoustic plane wave propagating along $\hat{\mathbf{n}}$, one obtains three different sound speeds corresponding to three orthogonal polarizations (one longitudinal and two transverse waves) using Christoeffel's equation. The plot of inverse sound speed as a function of the propagation direction yields the slowness surfaces (blue, red and green). Adapted from Ref. [106].

3.2.1 Elastic-wave theory

A rich spectrum of standing wave acoustic modes exists when the boundaries of a crystalline medium are shaped to confine longitudinal acoustic phonons. For such systems, the actual set of standing wave phonon modes for a crystalline medium depends on the geometry (i.e., the shape of boundaries) and also on the cut and anisotropy of the crystal. In this section, we will describe an approach to finding the bulk-acoustic modes in a shaped crystalline medium.

The propagation of elastic waves in solids is described by the elastic wave equation [114, 120]:

$$\rho \frac{\partial u_i}{\partial t^2} = c_{ijlm} \frac{\partial u_m}{\partial x_j \partial x_l}, \tag{3.1}$$

where u_i is the i^{th} component of acoustic displacement vector, c_{ijlm} is the isothermal

elastic constant tensor and ρ is the density of the medium. For a plane wave $\mathbf{u} = \mathbf{u}_0 e^{i(\mathbf{k}.\mathbf{r}-\omega t)}$ propagating in the direction $\hat{\mathbf{n}}$, where $\mathbf{k} = k\hat{\mathbf{n}}$, Eq. (3.1) reduces to the following eigenvalue equation:

$$\left(\frac{c_{ijlm}}{\rho} n_j n_l - v^2 \delta_{im}\right) u_{0m} = 0, \tag{3.2}$$

where $v = \omega/k$ is the phase velocity of the acoustic wave. The nontrivial solutions to the equation above determines the dispersion relation for the acoustic wave in the medium. For each direction $\hat{\mathbf{n}}$, solution to the eigenvalue equation yields three orthogonal eigenvalues and eigenvectors corresponding to the three speeds and polarizations of the acoustic waves. The plot of $1/v$ (or k/ω) as a function of $\hat{\mathbf{n}}$, yields the slowness surface which describes the magnitudes and directions of the phase as well as group velocities (see Fig. 3.2). Group velocity direction points in the direction normal to the slowness surface. When $\hat{\mathbf{n}}$ lies in certain symmetry directions, the group velocity direction is in the same direction as the phase-velocity direction (or direction of $\hat{\mathbf{n}}$). Only in this case we get one longitudinally polarized and two shear polarized acoustic waves. Generally however the waves are quasi-longitudinal ("longitudinal like") or quasi-shear ("shear like").

In piezoelectric crystals elastic wave equation and electromagnetic equations are intimately coupled. This type of piezoelectric coupling affects acoustic propagation in solids because slowness surfaces are modified upon such coupling [114]. We have ignored this effect because the modification to slowness surfaces (corresponding to longitudinal acoustic waves) due to piezoelectric coupling is negligible in the crystals we measured experimentally in Section 3.6.

Starting with the Christoffel equation in Eq.(3.1), we will derive an equation of motion for an elastic wave in the paraxial limit. This equation, which is analogous to paraxial Helmholtz equation for an electromagnetic field, can then be used to show

that plano-convex acoustic resonators support Hermite-Gaussian-like mode families. We can then use adopt the established methods from optics to design stable acoustic cavities; in such stable cavities transverse spatial confinement occurs because the reflections from the resonator surfaces can mitigate the effects of diffraction.

3.2.2 Analytical Stability Criterion and Anisotropy Parameter

Before we discuss design guidelines for acoustic cavities, let us begin by considering the well-known problem of designing stable cavities for light. Within the framework for Gaussian beam optics, we expect only certain radii of curvatures to form stable cavities [121]. For a Fabry-Pérot cavity in vacuum having two mirrors with radii of curvatures R_1 and R_2 that are separated by a distance of L, the stability criteria is given by $0 \leq g_1 g_2 \leq 1$. Here, g_i is the stability parameter for each mirror is defined as $g_i = 1 - L/R_i (i = 1, 2)$.

We seek to formulate similar stability parameters when designing acoustic cavities that support. However, correct formulation of g_1 and g_2 for elastic wave propagation must account for the anisotropy of elastic constants, which lead to nontrivial acoustic beam propagation within crystalline solid. Unlike slowness surfaces for optical waves propagating in free-space, acoustic slowness surfaces are not necessarily symmetric or even parabolic [114, 122, 123]. Nevertheless, in the paraxial limit, it is possible to formulate stability criteria that closely mirror the stability criteria for optical resonators along certain crystalline axes about which the slowness surfaces are parabolic and symmetric. In this case, the stability parameters for an acoustic resonator of length L_{ac} having two convex surfaces with radii of curvatures R_1 and R_2 is given by

$$g_1 = 1 - \frac{L_{\text{ac}}}{\chi R_1}, g_2 = 1 - \frac{L_{\text{ac}}}{\chi R_2}, \tag{3.3}$$

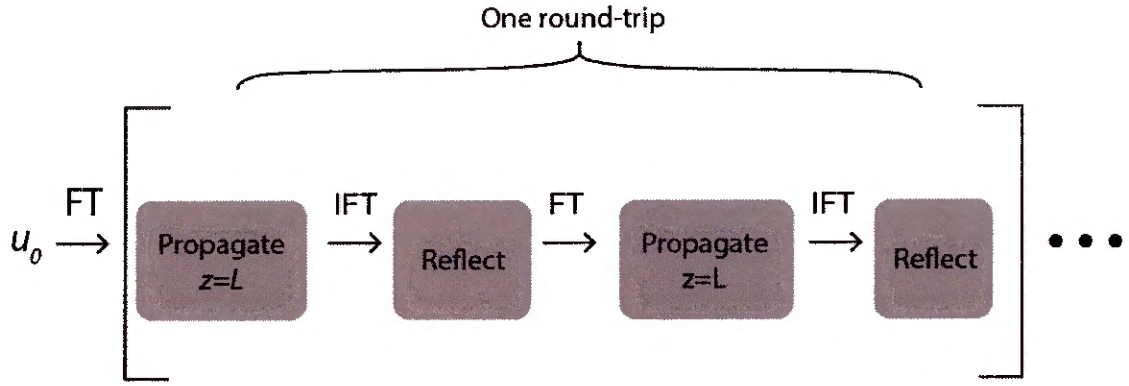

Figure 3.3: **Numerical Beam propagation.** Schematics depicting algorithm used to numerically propagate the beam during a single round trip inside the crystal. Adapted from Ref. [106].

where χ is the "anisotropy-constant" that includes the effect of propagation of acoustic beam in an anisotropic medium. The range of radii of curvatures that can form a stable acoustic cavity is then given by the condition $0 \leq g_1 g_2 \leq 1$ (see Appendix D for the derivation of the stability criterion and anisotropy parameters). Note that these design principles can be used to engineer stable cavities along crystalline axes that produce parabolic and symmetric dispersion surfaces. More generally, one can use numerical beam propagation techniques to design phonon cavities along crystalline axes that produce non-trivial dispersion surfaces, as well be described in the next section.

3.2.3 Numerical Beam Propagation: Finding Stable Acoustic Modes

An acoustic field $\mathbf{u}(x,y,z,t)$ propagating in the z direction, can be written in the plane wave basis as [119]

$$\mathbf{u}(x,y,z,t) = \left(\frac{1}{2\pi}\right)^3 \int_{-\infty}^{\infty} d\omega \int_{-\infty}^{\infty} dk_x \int_{-\infty}^{\infty} dk_y \sum_{i=1}^{3} \phi^n(k_x,k_y,\omega)\hat{d}^n\left(\frac{k_x}{\omega},\frac{k_y}{\omega}\right) \times e^{i(\omega t - k_x x - k_y y - k_z^n z)}. \quad (3.4)$$

where n indexes the three slowness surfaces, $\hat{d}^n\,(k_x/\omega, k_y/\omega)$ is the polarization vector for the plane wave propagating along (k_x, k_y, k_z^n), where k_z^n is determined by the corresponding slowness surfaces, and $\phi^n(k_x,k_y,\omega)$ corresponds to the amplitude for each polarization. For propagation along any other direction than z direction, we rotate the coordinate system (and the elastic tensor) such that the z-axis always corresponds to the direction of beam propagation. To find resonant acoustic modes of a system, we are looking for solutions of the form $\mathbf{u}(x,y,z,t) = \mathbf{u}(x,y,z)e^{i\Omega t}$, where Ω is the frequency of the acoustic mode. Once the slowness surfaces, k_z^n, and the corresponding polarization vectors, d^n, are calculated using Eq. (3.2), we calculate the amplitudes, ϕ^n, for the plane wave decomposition of the input field $\mathbf{u}^0(x,y,z=0)$ at z=0 using the following equation [119]:

$$\phi^{n=1}(k_x,k_y,\Omega) = \frac{\left\{(\mathbf{H}\cdot\hat{d}^1)[1-(\hat{d}^2\cdot\hat{d}^3)^2]+(\mathbf{H}\cdot\hat{d}^2)[(\hat{d}^1\cdot\hat{d}^3)(\hat{d}^2\cdot\hat{d}^3)-(\hat{d}^1\cdot\hat{d}^2)]+(\mathbf{H}\cdot\hat{d}^3)[(\hat{d}^1\cdot\hat{d}^2)(\hat{d}^3\cdot\hat{d}^2)-(\hat{d}^1\cdot\hat{d}^3)]\right\}}{\left\{1+2(\hat{d}^1\cdot\hat{d}^2)(\hat{d}^2\cdot\hat{d}^3)(\hat{d}^3\cdot\hat{d}^1)-(\hat{d}^1\cdot\hat{d}^2)^2-(\hat{d}^1\cdot\hat{d}^3)^2-(\hat{d}^2\cdot\hat{d}^3)^2\right\}} \quad (3.5)$$

where $\mathbf{H}(k_x, k_y, \Omega)$ is the Fourier transform of the initial displacement field at plane $z = 0$ and is given by:

$$\mathbf{H}(k_x, k_y, \Omega) = \int_{-\infty}^{\infty} dt \int_{-\infty}^{\infty} dx \int_{-\infty}^{\infty} dy \; \mathbf{u}^0(x, y, z = 0) e^{i\Omega t} e^{i(-\omega t + k_x x + k_y y)}. \tag{3.6}$$

ϕ^2, and ϕ^3 by obtained similarly by permutation of indices in Eq. (3.5). Once the amplitude coefficients ϕ^n of the input field at $z = 0$ is calculated, field at $z = L$ is calculated using Eq. (3.4). Then a phase-profile corresponding to spherical geometry is applied to each displacement component:

$$\begin{bmatrix} u'_x(x, y, L) \\ u'_y(x, y, L) \\ u'_z(x, y, L) \end{bmatrix} = \begin{bmatrix} u_x(x, y, L) e^{ik_{t1}(x^2+y^2)/R} \\ u_y(x, y, L) e^{ik_{t2}(x^2+y^2)/R} \\ u_z(x, y, L) e^{ik_l(x^2+y^2)/R} \end{bmatrix} \tag{3.7}$$

where $k_{t1} = \Omega/v_{t1}$, $k_{t2} = \Omega/v_{t2}$, and $k_l = \Omega/v_l$ are the wave-vectors of the two shear polarizations and one longitudinal polarization for a plane wave propagating along the z direction. We assume that the spherical surface of the resonator has a radius of curvature given by R. After computing the phase-shift due to the boundary, we re-compute the projection amplitudes and propagate the beam further by a distance of L. As before, we apply a phase profile due to the flat surface (i.e., a constant phase). This results in a displacement profile $\mathbf{u}^{m=1}(x, y, z = 0)$ after one round-trip inside the crystal. For a standing wave acoustic mode, both the phase and the amplitude profile of the displacement field should remain unchanged after a single round-trip inside the crystal (i.e. $\mathbf{u}^1(x, y, z = 0) = \mathbf{u}^0(x, y, z = 0)$). Propagation over multiple round trips can be used to identify both the resonant frequencies and mode profiles. This technique is analogous to "Fox and Li" calculation used to find transverse mode patterns in an optical cavity [124, 125]. We will discuss this in detail next.

To find the resonant mode frequencies, we take an input field $\mathbf{u}^0(x, y, z = 0)e^{i\Omega t}$. k_z^n

is then computed for this particular value of Ω. Using the procedure outline above, we perform multiple round trips of the input field $\mathbf{u}^0$. We then create an interferometric sum of displacement fields after each round trip at $z = 0$:

$$\mathbf{u}_{\text{sum}} = \sum_m \mathbf{u}^m(x, y, z = 0) \tag{3.8}$$

The total intensity in the interfered field is then given by $I = \int dx\ dy |\mathbf{u}_{\text{sum}}|^2$. We then sweep the acoustic frequency Ω and calculate intensity as a function of Ω, $I(\Omega)$. A resonant build-up of intensity occurs at frequencies corresponding to the acoustic modes that remain unchanged after each round-trip (see Fig. 3.4). Once a resonant frequency Ω_m is found, the input field $\mathbf{u}^0(x, y, z = 0)e^{i\Omega_m t}$ is propagated over multiple round-trips and the interferometric sum of displacement fields $\mathbf{u}_{\text{sum}}(x, y, z = 0)$ is computed. This displacement profile, $\mathbf{u}_{\text{sum}}$, is then used as an input to another beam-propagation over multiple round-trips. After several iterations, the interference profile does not change and converges to the mode profiles of the standing wave acoustic modes. We choose a Gaussian profile for the input acoustic field to find resonant acoustic modes because the electrostrictive force produced by the beating of the pump and Stokes light with Gaussian profiles also has a Gaussian shape.The input acoustic field is also off-centered relative to the to crystalline axis to simulate imperfect alignment in our experiment.

We used this general approach to find the acoustic modes accounting for all three slowness surfaces and considering all three polarizations directions in our plano-convex system. For the longitudinal modes of interest we find that only a small amount ($\sim$ 1%) of energy resides on the other polarizations (i.e. u_x and u_y). Assuming all the energy in the polarization other than the z-direction is lost, we find a linewidth of $\sim$ 10 Hz from our simulations, corresponding to a Q-factor of 10^9. For the acoustic modes of our interest we are well within the paraxial limit as the beam profiles varies

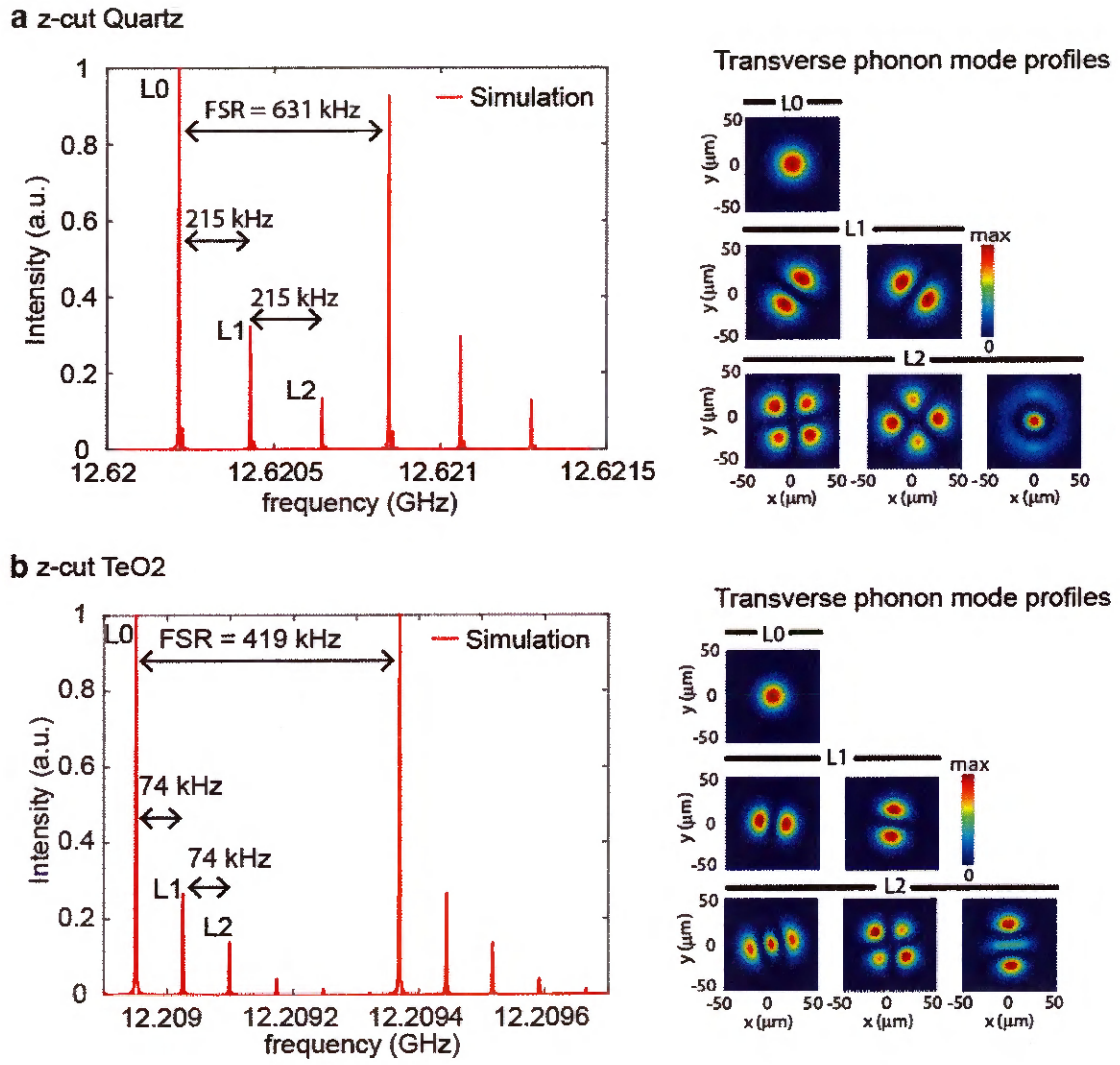

Figure 3.4: **Acoustic mode simulation.** Simulated frequency sweep to identify resonant modes and mode profiles for a plano-convex crystals of 5 mm length and 10 mm radius of curvature. a, Simulation of z-cut Quartz with $\rho = 2648$ kgm^{-3}, $c_{11} = 86.8$ GPa, $c_{12} = 7.04$ GPa, $c_{13} = 11.91$ GPa, $c_{33} = 105.75$ GPa, $c_{44} = 58.20$ GPa, $c_{14} = -18.04$ GPa, and $c_{66} = 39.88$ GPa [126]. b, Simulation of z-cut α-TeO_2 with $\rho = 6040$ kgm^{-3}, $c_{11} = 55.7$ GPa, $c_{12} = 51.2$ GPa, $c_{13} = 21.8$ GPa, $c_{33} = 105.8$ GPa, $c_{44} = 26.5$ GPa, and $c_{66} = 65.9$ GPa [127]. Adapted from Ref. [106].

only in a small range of k_x and k_y. Therefore, we neglect the variation of polarization with propagation direction ($i.e. \hat{d}^n(k_x/\omega, k_y/\omega) = \hat{d}^i(0,0)$) [119]. To calculate longitudinal acoustic modes we can then use the slowness surface corresponding to just the longitudinal polarization (i.e. $u_z(x,y,z)$). This approximation improves the computational speed and allows us to calculates transverse mode profiles for the longitudinal modes show in Figure. 3.4 (**a**)-(**b**) . We compared the mode found using this approximation to the ones found using the general approach (without approximations) and find an excellent agreement.

3.3 Experimental Setup

We characterize the optomechanical coupling in our system through stimulated energy transfer measurements using a pump-probe apparatus as seen in Fig. 3.5. When counterpropagating pump and Stokes light passes through the bulk acoustic resonator, optomechanical interaction produces amplification of Stokes light at the expense of pump light. We measure this change in Stokes light power to determine nonlinear optical susceptibility, and use it to characterize optomechanical coupling rate, acoustic dissipation rate, free-space cooperativity as well as to perform phonon-mode spectroscopy.

Several aspects of our system make these measurements challenging. First, as explained before, the fractional change in Stokes power in mm-length scale bulk crystal is typically quite small (order of 10^{-5} at room temperatures). As a result, the amplified Stokes light that we want to measure is accompanied by a large background signal. Therefore, any small power fluctuation in the Stokes signal would make detection of amplified Stokes signal very challenging. Moreover, this backscattered Stokes light is typically much smaller than the $\sim$4 % back-reflection of the pump light when it passes through the air-quartz interface. Therefore, we must also spectrally separate

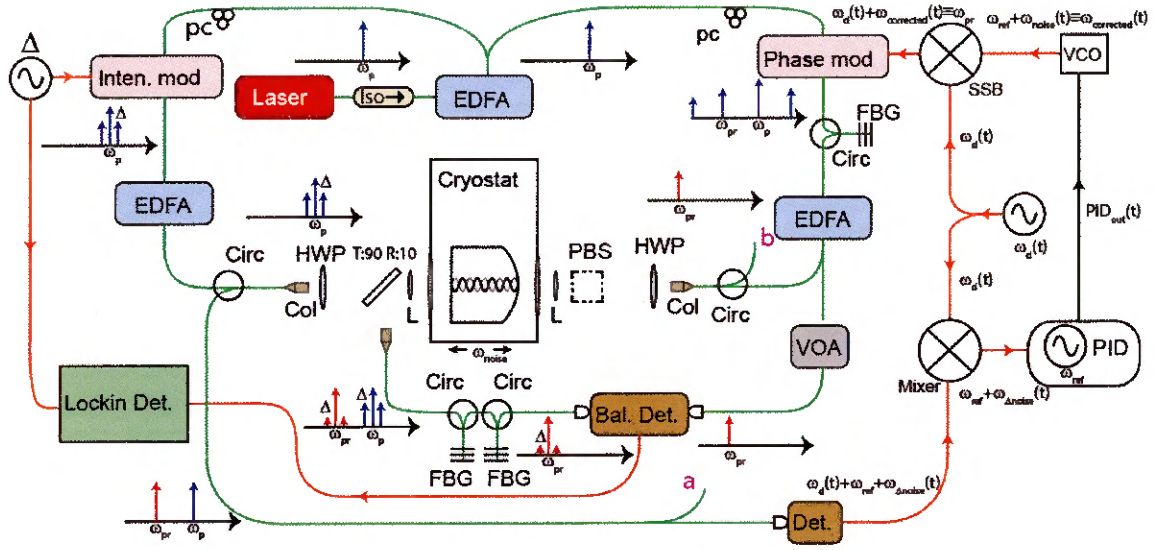

Figure 3.5: **Schematics of the experimental apparatus for sensitive Brillouin spectroscopy at cryogenic temperatures.** Green lines represent optical fiber and orange lines indicated RF cables. pc: polarization controller; col: collimator; iso: isolator; EDFA: erbium-doped fiber amplifier; HWP: half-wave plate; PBS: polarizing beam splitter; L: lens; det: detector; FBG: fiber bragg grating; bal. det.: balanced detector; Inten. mod: intensity modulator; phase mod: phase modulator. Adapted from Ref. [106].

the Stokes light from the pump light. We devised a sensitive measurement technique using lock-in detection and spectral filtering of the back-scattered Stokes signal to get rid of unwanted pump light and perform essentially zero background measurement. In what follows, we present the detail description of the experimental apparatus as outlined in Ref. [106].

The optical setup consists of fiber and free-space sections, with the fiber displayed in green (Fig. 3.5). The counter-propagating pump and probe beams derived from the same laser are coupled to the free-space setup using fiber-optic collimators before being focused into the bulk-crystalline sample. For maximum optomechanical coupling the polarization state of the pump and the probe light are matched using a combination of half-wave plate to rotate the polarization and a polarizing beam splitter to define a polarization axis. The polarizing beam splitter is then removed during measurement to avoid interfering with counter-propagating light. The sample

is mounted on the cold finger of a continuous-flow liquid helium cryostat with a 4-K base temperature and is accessed through two AR-coated fused quartz windows.

The pump and probe beams are both derived from the same amplified narrow-linewidth laser source (PurePhotonics PPCL 300) centered around 1550 nm. The pump tone at frequency ω_p is at the same frequency as the laser source and an erbium-doped fiber amplifier (EDFA) is used to amplify the pump power to 200 mW before it impinges on the crystal. To create the probe light at frequency ω_s, part of the light derived from the laser source is phase modulated using an electro-optic modulator (EOM). Then, a fiber-Bragg grating (FBG) is used to spectrally filter a single sideband out of many sidebands imprinted on the laser light due to electro-optic modulation. When we drive the EOM (EOSPACE Model PM-0S5-20-PFA-PFA) with rf-voltages close to the half-wave voltage ($V\pi \approx 5$ V), we can get appreciable power in the 4th order phase-modulated side-band. Since the phase modulator can be driven with an arbitrary frequency up to 20 GHz, this technique permits us to generate pump-probe frequency detuning as large as 80 GHz. The probe light is amplified using an EDFA and approximately 40 mW impinges on the bulk crystalline sample.

The amplified Stokes signal after passing through the crystal is reflected from a 90:10 free-space beam splitter and collected using a fiber collimator. Since this output collimator also collects the pump light that is back-reflected off the quartz-vacuum interface, two additional fiber Bragg grating (FBG) filters are used to remove this unwanted light. These two FBGs, when placed in series, ensure 50 dB suppression of the pump light. Whereas the Stokes light suffers a modest optical loss of approximately 3 dB in passing through the two FBG filters. Since the pass band of the FBG depends on the temperature, all FBGs are placed within a temperature stabilized housing to achieve stable and robust suppression of pump light over time. This amplified Stokes signal after passing through the FBGs is compared with a reference probe light before amplification using a balanced amplified photodetector (Thorlabs:

PDB450C-AC). This probe reference arm is power matched to the signal arm through the use of a variable optical attenuator (FDK YS-500-155 magneto-optic). The output of the balanced detector is measured with a lock-in amplifier (Zurich Instruments HF2LI).

While we have filtered out the unwanted pump, the amplified Stokes signal stills sits on top of a large background signal. Therefore, to enhance the sensitivity of the apparatus, lock-in measurement is used. For this purpose, the pump light is modulated with an optical intensity modulator (Optilabs IM-1550-3GHz). The frequency generator of the lock-in instrument (at frequency Δ) drives the intensity modulator. The modulated pump light then imparts additional side-bands on the amplified Stokes light due to Brillouin scattering. So, the amplified Stokes light is also modulated at Δ and is easily measured using lock-in detection. This measurement essentially picks out part of Stokes signal that results from optomechanical coupling. For a complete description of how the pump modulation frequency becomes imprinted on the measured amplified probe for the two limits of operation, see Section 3.4.

Neglecting the phase noise canceling circuit (see details regarding this in the next paragraph), the probe frequency is given by $\omega_{\mathrm{pr}} = \omega_p - \Omega$. Ω is repeatedly swept through the optomechanical frequency, Ω_B, at a period, $T_{\mathrm{sweep}} \sim 1$ second. Finally, the lock-in detector output is measured with an oscilloscope triggered with period T_{sweep} and the accumulating swept optomechanical signal is averaged for ~ 1 minute. This signal corresponds to the optomechanical susceptibility of the system.

If the crystal were stationary, the relative frequency between the pump and the probe would be precise. Therefore, the pump and probe tone should have a narrow beat tone with linewidth limited by the linewidth (typically mHz) of the RF generator that drives the EOM. This would then permit measurement of optomechanical response with unprecedented frequency resolution of milli Hz. In practice, however, the crystal is attached to the long arm of a cryostat and is sensitive to the vibrations

in the environment. Therefore, as these vibrations translate to phase noise on the optical tones, they place a lower limit to the measurable linewidths of the optomechanical response. Experimentally, this limit corresponds to ~ 1 kHz for our system. In order to surpass this limit, we developed a phase-noise canceling technique.

Phase noise is accounted by using a feedback loop and a proportional-integral-derivative (PID) controller. The ability to control the noise lies in the fact that the pump light reflecting from the vibrating crystal acquires the same phase noise as the optomechanical response. Therefore, we use the back-reflecting pump light in order to provide an error signal to our PID circuit. The complete circuit is depicted in Fig. 3.5.

The new probe frequency, ω_{pr} consists of a dithering frequency component, $\omega_{\text{corrected}}$, which stabilizes the beat frequency between the pump and the Stokes field inside the crystal. Specifically, a rf single-sideband mixer mixes ω_d with the output of a voltage controlled oscillator (VCO) that is controlled by the PID output. The error frequency for the PID is given by the beat frequency of the backreflected pump and the probe, after mixing with ω_d. This error frequency is compared with a stable reference frequency, ω_{ref}, to generate the phase difference as the error signal for the VCO drive. When the PID loop is activated the new probe has an identical frequency response to that of the backreflected pump. From our detection limited beat frequency between the backreflected pump and the probe, we expect the measurement scheme to have a linewidth resolution of less than 1 Hz.

3.4 Stimulated Brillouin Spectroscopy using Modulated Pump

Through the measurement of the amplified Stokes signal, we can determine both the optomechanical coupling strength, g_0^m, and characterize the mechanical properties of

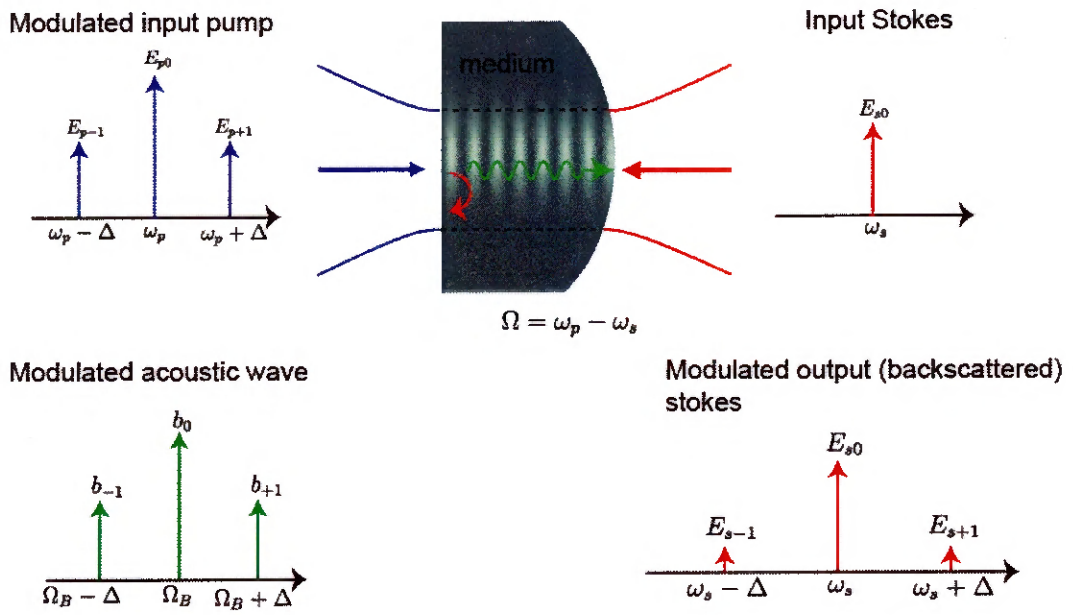

Figure 3.6: **Brillouin spectroscopy at room temperature.** For the measurement of Brillouin gain in the conventional Brillouin limit, we just modulate the input pump field. The interference of pump and Stokes fields results in a modulated phonon field. This modulation is imparted on the back-scattered Stokes light, permitting us to perform sensitive lock-in detection. Adapted from Ref. [106].

our bulk crystalline resonator. However, as explained before, the fractional change in Stokes light due to Brillouin interaction within most crystals is rather small. Therefore, to perform zero background measurement of the small signal gain (fractional change as low as 10^{-6}), we modulate the pump light and use lock-in detection of the modulated Stokes gain signal. The dynamics of the Stokes light when we modulate the pump is quite different in the conventional Brillouin limit (room temperature measurements) and the coherent-phonon limit, which we describe in the next sections.

3.4.1 Dynamics in the Conventional Brillouin Limit

In this section, we explore the dynamics of stimulated Brillouin scattering measurements in the conventional Brillouin limit when the pump light is intensity modulated. In the frequency domain, intensity modulation of the pump light typically gives us two additional side-bands on the carrier. Note that our intensity modulator operates

near the quadrature point, where the power output as a function of driving voltage in linear, giving us weaker sidebands on a large carrier. Therefore, the dynamics of Brillouin scattering in this case can be derived by considering the interaction of three pump waves with a single frequency Stokes wave.

In typical stimulated Brillouin measurements, as explained in section 2.1, a single frequency pump wave (ω_p) interferes with a single frequency Stokes wave (ω_s) to produce a beat tone at the difference frequency ($\Omega = \omega_p - \omega_s$). The resulting optical forcing function at Ω then resonantly drives an acoustic waves when Ω matches the Brillouin frequency Ω_{B}. However, when the modulated pump light, consisting of waves at frequencies ω_p, $\omega_p - \Delta$, and $\omega_p + \Delta$, interferes with a single frequency Stokes wave at ω_s, generating a modulation in the optical forcing function with frequency components at Ω, $\Omega - \Delta$, $\Omega + \Delta$. Here, Δ is the modulation frequency of the intensity modulator, which we assume is much smaller than the Brillouin frequency. All three frequency components of this forcing function resonantly drive a modulated acoustic wave near the Brillouin frequency and scatters pump light not just into the frequency component at ω_s but also into additional new sidebands at $\omega_s \pm \Delta$ as seen in Fig. 3.6. From the coupled mode equations derived from the Hamiltonian treatment presented in Section 2, we obtain the following optical power for the Stokes sidebands at the end of the crystal

$$P_{s-1} = G_B^2 L^2 \left(\frac{\Gamma^2 + \Delta^2}{\Gamma^2 + 4\Delta^2} \right) P_{p0} P_{p-1} P_{s0}. \tag{3.9}$$

Here, Γ is the acoustic damping rate, P_{p0}, P_{p-1}, P_{p+1} is the input power of the pump waves at carrier and sidebands, respectively, and P_{s0} is the input Stokes power. In deriving the above formula we assumed that $P_{p-1} = P_{p+1}$. From Eq. (3.9) we see that P_{s-1} is largest when $\Delta \to 0$. To maximize signal-to-noise ratio at room-temperature, we modulate pump with frequency $\Delta \ll \Gamma_B$(see Fig. 3.7). In this limit, the sideband

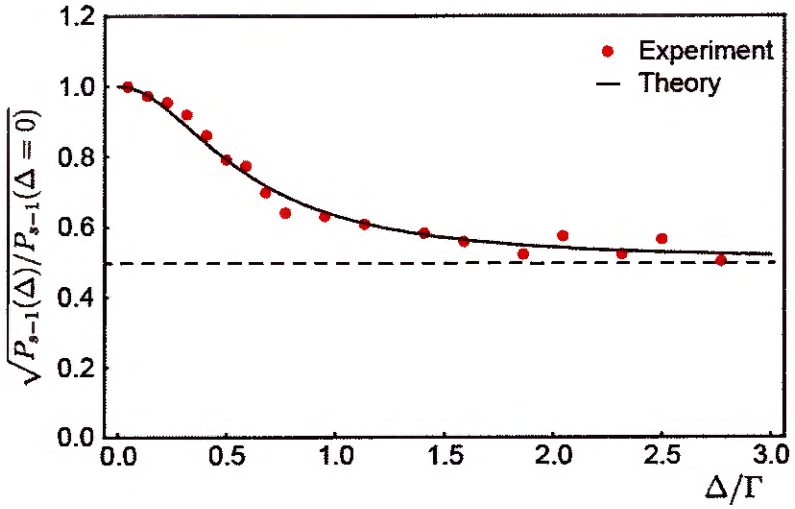

Figure 3.7: **Brillouin gain as a function of modulation frequency (Δ).** Peak gain for energy transfer measurements in TeO_2 at room-temperature measured using the heterodyne lock-in detection as a function of Δ/Γ. $\Gamma \simeq 11$ MHz obtained by fitting Eq. (3.9) agrees well with the independently measured acoustic dissipation rate of 10 MHz in TeO_2. Adapted from Ref. [106].

Stokes power is given by

$$P_{s-1} \simeq G_B^2 L^2 P_{p0} P_{p-1} P_{s0}. \tag{3.10}$$

In experiments, we intensity modulate the pump wave at frequencies of around 400 kHz, which is typically much smaller than the acoustic linewidth of $\sim$ 10 MHz, observed for most crystals at room temperature.

The generation of new sidebands on the Stokes light allows us to perform in theory a zero-background measurement of scattered Stokes signal using lock-in detection. The power measured by an optical detector is proportional to the square of the optical fields (i.e. $P \propto \langle E^* E \rangle$). Therefore, when a Stokes field with two sidebands

(see Fig. 3.6) separated by Δ is measured using a power detector, yielding

$$P_s(\text{detector}) = P_{s0} + P_{s-1} + P_{s+1} + 2\sqrt{P_{s0}P_{s-1}}\text{Cos}(\Delta t) + 2\sqrt{P_{s0}P_{s+1}}\text{Cos}(\Delta t) + 2\sqrt{P_{s+1}P_{s-1}}\text{Cos}(\Delta t). \quad (3.11)$$

In our experiments, $P_{s-1} = P_{s+1} \ll P_{s0}$. Furthermore, in the weak gain limit $\Delta P_{s0}(0) \ll P_{s0}(L)$ is also an excellent approximation. By demodulating the detected power at frequency Δ, we obtain the following expression for the power detected at the lock-in

$$P_s(\text{heterodyne}) = 4\sqrt{P_{s0}P_{s-1}}. \quad (3.12)$$

Now substituting Eq. (3.9) in Eq. (3.12) we obtain the following expression for the power detected in the lock-in measurement

$$P_s(\text{heterodyne}) = 4G_B L P_{s0}\sqrt{P_{p0}P_{p-1}}. \quad (3.13)$$

Therefore, the heterodyne measurement of the zero-background sideband Stokes tone using the lock-in detection gives a direct measure of the coupling strength. Note that in experiments, however, the backreflected pump gives a large noise background because the lock-in detection occurs at the same frequency as the pump modulation. Therefore, we use a FBG filter to suppress the pump light hitting the detector by $\sim$ 50 dB before the lock-in measurement. It may be possible to create a truly zero background measurement without the use of a filter by using an optical local oscillator derived from the same Stokes light. One can take part of the Stokes light shifting it to a new frequency $\omega_{\text{LO}} = \omega_s + \omega_{\text{AOM}}$ using an AOM, and performing the heterodyne measurement between the modulated Stokes signal and the optical local oscillator. The lock-in detected frequency components at $\omega_{\text{AOM}} \pm \Delta$ would permit zero background measurement of the Stokes sidebands without filtering the pump.

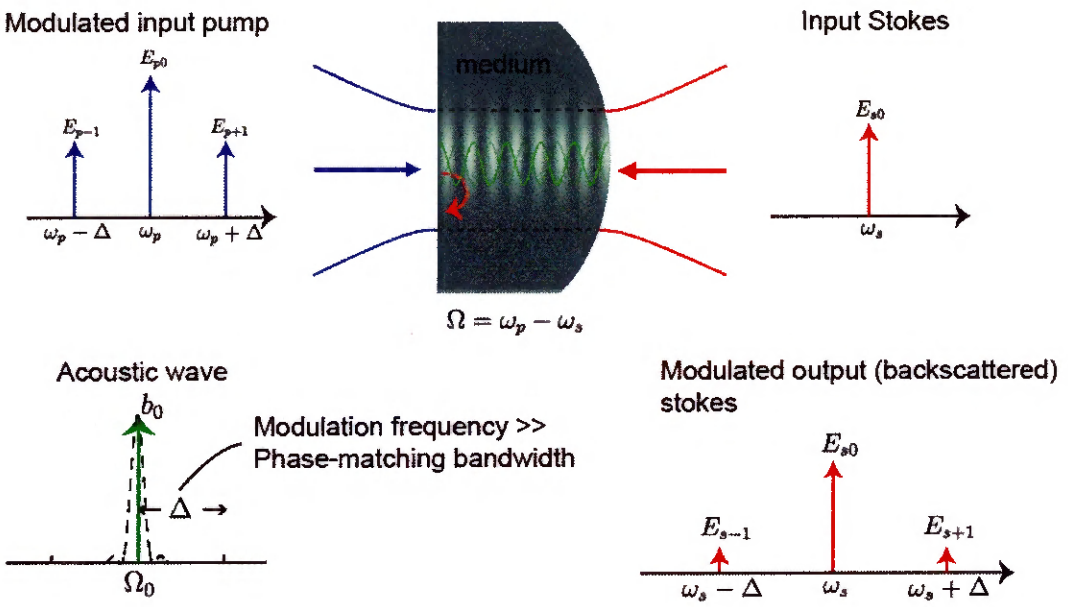

Figure 3.8: **Brillouin spectroscopy at cryogenic temperatures.** For the measurement of Brillouin gain in the coherent-phonon limit, we modulate the input pump field at a frequency much larger than the phase-matching bandwidth. As a result, the side-bands on the acoustic fields are vanishingly small. Adapted from Ref. [106].

3.4.2 Dynamics in the Coherent-phonon Limit

In this section, we discuss the dynamics of stimulated Brillouin scattering in the coherent-phonon limit when the pump light is intensity modulated. For conceptual and experimental simplicity, we consider the case when the modulation frequency, Δ is much larger than the phase matching bandwidth as seen in Fig. 3.8. We do this because modulation within the phase matching bandwidth results in a more complicated spectrum of Stokes scattering that will have overlapping contribution from the three pump tones. In this case, the modulated pump beam interfering with the stokes field drives a modulated optical forcing function. Since the modulation frequency is much larger than the phase matching banding the optical forcing function drives a single acoustic wave at frequency $\Omega = \omega_p - \omega_s$. Each pump sideband scatters off this coherent phonon to then produce stokes sideband at $\omega_s \pm \Delta$. With an additional assumption that the intensity beat length of the pump is much longer than the crys-

tal length ($v_{\rm opt}/\Delta \gg L_{\rm ac}$) we arrive at the following expression for the maximum scattered sideband Stokes power on resonance

$$P_{s-1} \simeq \frac{4|g_0^m|^4 L_{\rm ac}^4}{\hbar^2 \omega^2 v_o^4 \Gamma_m} P_{p0} P_{p-1} P_{s0}, \tag{3.14}$$

where v_o is the optical velocity in the bulk medium (see supplementary section 4.2 of Ref. [106] for details). Finally, using Eq. (3.12) we get the following zero-background heterodyne power for the sideband Stokes signal in the coherent-phonon limit

$$P_s(\text{heterodyne}) = \frac{8}{\hbar \omega v_o^2 \Gamma_m} |g_0^m|^2 L_{\rm ac}^2 \sqrt{P_p P_{p-1}} P_s. \tag{3.15}$$

3.5 Stimulated Brillouin Scattering Measurements at Room Temperatures

We now present the phonon-mediated energy transfer measurements performed at room temperature in a variety of crystal species using the experimental apparatus seen in Fig. 3.5. These energy transfer measurements provide us information about the Brillouin frequencies, acoustic lifetimes, and the nonlinear optical susceptibility of the system.

In Fig. 3.9a-e, we see Stokes energy transfer measurements on z-cut TeO_2, z-cut quartz, x-cut CaF_2, x-cut GaAs, and x-cut Silicon. These crystals were all 5 mm long. These measurements reveal broad Lorentzian lineshapes with Brillouin frequencies that agree well with the predicted resonance frequencies from Eqn. (2.3). The linewidths for most crystals is of the order of 10 MHz at room temperature, corresponding to spatial decay lengths of the order of 100 μm. The fractional change in Stokes power is considerably smaller for Silicon ($\sim$ 1 ppm) due to it's weak photoelastic response. Whereas, in quartz and CaF_2, smaller refractive index results in

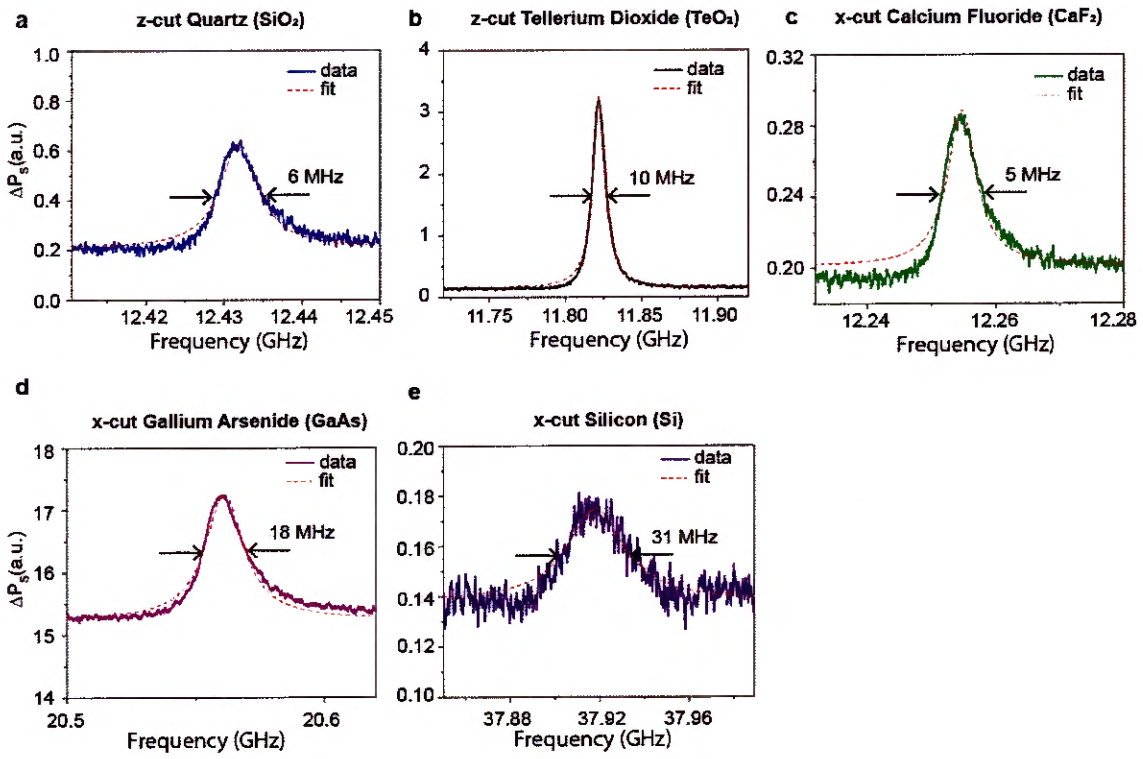

Figure 3.9: **Stimulated Brillouin Scattering measurements: Conventional Phonon limit.** (a-e) Amplified Stokes power ΔP_s as a function of the frequency, $\Omega = \omega_p - \omega_s$, obtained for a variety of crystalline substrates through stimulated Brillouin spectroscopy at room temperature.

a weaker Brillouin response. Finally, we note that the precise values of Brillouin frequencies obtained from these stimulated scattering measurements are crucial pieces of information as we consider utilizing bulk acoustic phonons to make novel Brillouin lasers and high-frequency cavity optomechanical system, which we will discuss in greater detail in Chapter 5.

We performed careful comparison between theoretically predicted Brillouin gain and experimentally observed values for stimulated energy transfer measurements in quartz and TeO_2. To theoretically estimate Brillouin gain (see Eq. (2.22)) for each measurement, we first need to determine the effective acousto-optic area, which we can determine by measuring the mode profiles of the Gaussian optical fields inside each crystal as seen in Fig. 3.10 (see supplementary information of Ref. [106] for details). Since acoustic waves at room temperature decay rapidly (i.e., we do not have formation of discrete standing wave acoustic modes with transverse mode profiles determined by the crystalline geometry), we assume that the acoustic mode profile is just given by the profile of the optical forcing function, which is proportional to the product of the transverse mode profiles of the counterpropagating optical fields. Using measured effective acousto-optic area of $\pi \times (71.1\ \mu m)^2$ ($\pi \times (65.2\ \mu m)^2$) we predict a Brillouin gain of 0.1 $(Wm)^{-1}$ (9.7×10^{-3} $(Wm)^{-1}$) in TeO_2 (quartz). The experimentally measured Brillouin gain of 0.1 $(Wm)^{-1}$ (1.2×10^{-2} $(Wm)^{-1}$) in TeO_2 (quartz) agrees well with the theoretically predicted values calculated above. Note that such small Brillouin gain corresponds to peak fractional change in probe power of 80 ppm (13 ppm) for TeO_2 (quartz).

This weak scattering rate for photons is dramatically enhanced as acoustic dissipation rates plummet at low temperatures. Next we look at how the nonlinear optical susceptibility for photon-phonon coupling is modified at cryogenic temperatures.

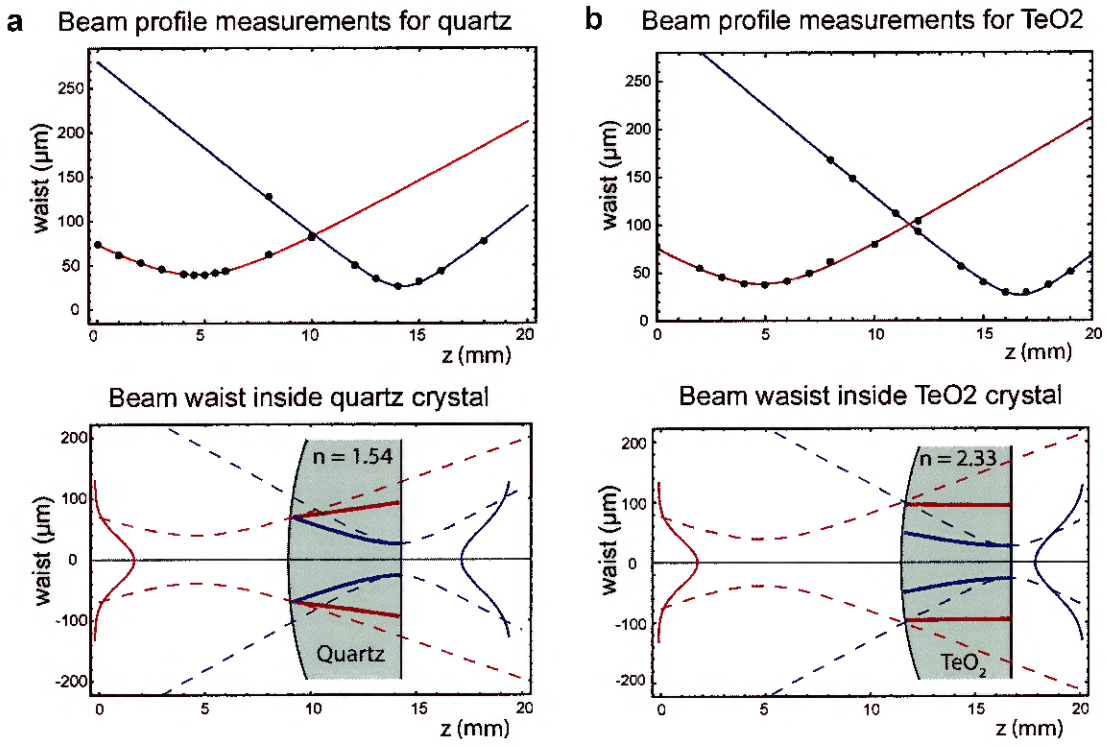

Figure 3.10: **Optical beam profile measurements.** (**a-b**) Measurement of the beam waist of the Gaussian optical beam along with the ABCD law [118] for Gaussian beam propagation is used to determine the optical mode profiles inside the quartz and TeO_2 plano-convex resonator. Adapted from Ref. [106].

3.6 Stimulated Brillouin Scattering Measurements at Cryogenic Temperatures

At cryogenic temperatures of $\sim$ 10 K, our system enters the coherent-phonon limit, leading to the formation to discrete standing-wave phonon modes. As a result, the energy transfer spectrum in this regime shows multiple Lorentzian peaks within a finite bandwidth around the Brillouin frequency.

Fig. 3.11 shows measured stimulated energy transfer spectrum for z-cut quartz crystal at $\sim$ 10 K temperatures. In a wide spectral scan, we see a series of narrow resonances with peak resonance height modulated by a sinc^2 envelope around the Brillouin frequency. We show the calculated phase-matching bandwidth (dashed line), demonstrating that the observed modulation profile agrees well with the predicted geometric bandwidth. We can also perform such stimualted energy transfer measurements for a vareity of crystals at cryogenic temperatures as seen in Fig. 3.13. For some crystals, we observe the modulation profile deviates from the usual sinc^2 response. This occurs when the pump and Stokes beam are not exactly colinear due to misalignment. The non-trivial acousto-optic overlap resulting from this misalignment then gives rise to a more complicated modulation profile [105]. Note that due to changes in elastic and optical properties of these crystals at cryogenic temperatures, the Brillouin frequency of these crystals shifts at cryogenic temperatures.

These stimulated scattering measurements allow us to perform a type of phonon mode spectroscopy. For example, the regularly spaced resonances in quartz (Fig. 3.11 (**b**)) reveals three acoustic mode families (color-coded). The observed spacing of 630 kHz between each mode families is consistent with the acoustic free spectral range ($v_a/(2L)$) for the standing waves acoustic modes within quartz. Elastic-mode simulations as seen in Fig. 3.11 (**c**) show that this mode structure is consistent with coupling to the fundamental (L0) and higher order transverse (L1, L2) modes

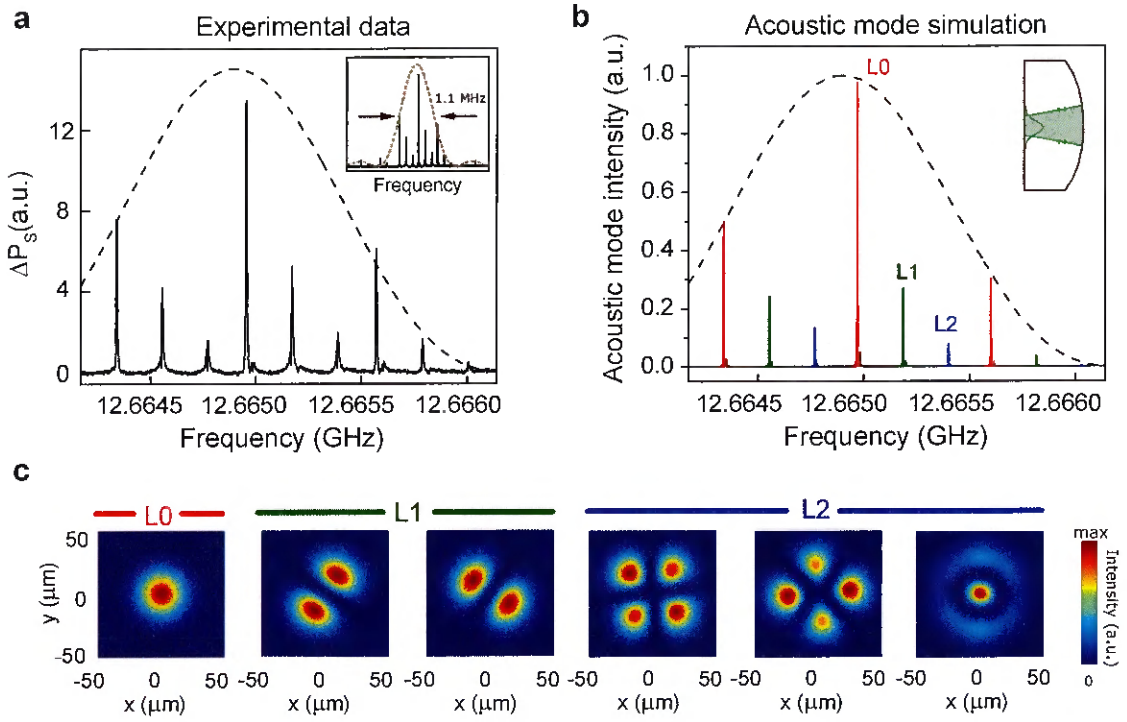

Figure 3.11: **Comparison of experimental data to acoustic mode simulations.** (a) Stimulated Stokes scattering measurement of a plano-convex bulk acoustic resonator in z-cut quartz crystal at cryogenic temperature. The optical beams are misaligned from the acoustic cavity to enhance the response from the higher-order transverse acoustic modes. The wider frequency span in the inset reveals a sinc^2 spectral response and the dashed lines indicate the geometrically imposed phase-matching bandwidth. (**b**) Simulated acoustic mode spectrum of the plano-convex acoustic resonator accounting for the anisotropy in the elastic constants. Three separate spatial mode families identified by different colors with red corresponding to the fundamental mode (L0), green to the near-degenerate 1st higher-order modes (L1), and blue to the near-degenerate 2nd higher-order modes (L2). We seed the simulation with an input acoustic beam that is shifted 10 μm horizontally and 15 μm vertically from the axis of the resonator to couple to higher-order spatial modes for comparison with experiment. (**c**) Normalized acoustic mode intensity profile of the higher-order spatial modes (L0, L1, and L2) at the planar surface of the acoustic resonator. Adapted from Ref. [106].

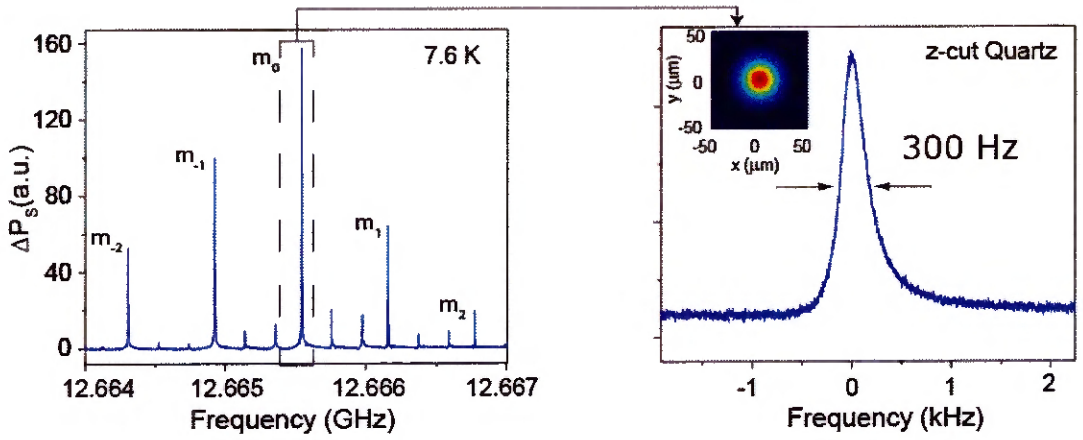

Figure 3.12: **Acoustic Q-factor at cryogenic temperature (7.6 K).** High resolution measurement of a 12.67 GHz fundamental Gaussian acoustic mode in z-cut plano-convex quartz reveals a narrow linewidth of 300 Hz. This corresponds to an acoustic Q-factor of 42 million. Adapted from Ref. [106].

supported by the plano-convex acoustic resonator. The spectrum of the resonator modes obtained from the elastic-wave simulation matches well with the observed mode structure in all the crystals that we have measured experimentally.

The energy transfer spectrum also provides information about the acoustic damping rate. So, the high resolution spectra of the fundamental L0 cavity mode for quartz as seen in Fig. 3.12, reveals a linewidth, $\Gamma_m/2\pi$, of 300 Hz. This corresponds to acoustic Q-factor of 42 million or energy decay time of 0.53 ms for 12.7 GHz acoustic mode. These long lived phonons, with an unprecedented $f \cdot Q$ product of 0.5×10^{18}, have coherence lengths L_{ac} of $\sim$ 3 m that is considerably larger than the crystal length of 5 mm. $f \cdot Q$-product is an important figure of merit for our optomechanical system because the number of coherent oscillations an oscillator can have in presence of thermal decoherence is proportional to $f \cdot Q$ (i.e. $Q/(\Gamma_m n_{\text{th}}) \propto f \cdot Q$) [117].

Acoustic Q-factors for the various crystals that we measured are tabulated in Table 1. A variety of extrinsic and intrinsic acoustic damping mechanisms could limit acoustic lifetimes. To achieve ultra long-lived phonons, extrinsic loss mechanisms such as diffraction losses and anchoring losses must be eliminated. In our system,

the plano-convex geometry produces tightly confined acoustic phonons (beam waists of $< 60\mu$m) that have negligible diffraction and anchoring losses, as the transverse mode size is more than a hundred times smaller than the crystal radius (6.35 mm).

A variety of acoustic loss mechanisms scatter energy from the longitudinal mode of interest as the acoustic waves reflects of the crystal surface. For example, there is a non-negligible amount of polarization mode conversion. Accounting for this polarization mode conversion but ignoring material dissipation and device imperfections, the acoustic mode simulations suggest that the Q-factor due to the fundamental mode should exceed 10^9 in z-cut quartz. Acoustic waves also encounter scattering losses at the crystal surfaces. From the measured root mean square surface roughness of approximately 1 nm, we expect Q-factor limit of 200 million due to surface scattering [100]. This is still a factor of 5 larger than the measured Q-factor, suggesting that the measured Q-factor of 42 million is likely dominated by other intrinsic loss mechanisms due to impurities/defects or dislocations in the crystal. Upon further studies of various quartz wafers, we found out that the crystal quality and in particular the aluminum impurity, which we measured using a Fourier Transform Infrared Spectroscopy, was a strong predictor of the phonon linewidth at low temperatures. Hence, through further improvements in the crystal quality to minimize crystal impurities and device imperfections, it may be possible to increase the Q-factor for 12.7 GHz phonons in quartz by another order of magnitude.

The dramatically increased Q-factor at cryogenic temperatures also greatly enhances the nonlinear optical susceptibility. Since the peak susceptibility scales inversely with the acoustic dissipation rate (see Eqn. 2.22), the stimulated scattering rates are enhanced by 10^4 (10^2) in quartz (TeO_2) over their room temperature values. From the measured optical susceptibility we determine zero point coupling rates ($g_0^m/2\pi$) of 31 and 82 Hz for quartz and TeO_2 respectively. These values agree well with the theoretically predicted values of 36 Hz and 71 Hz for the coupling rates in

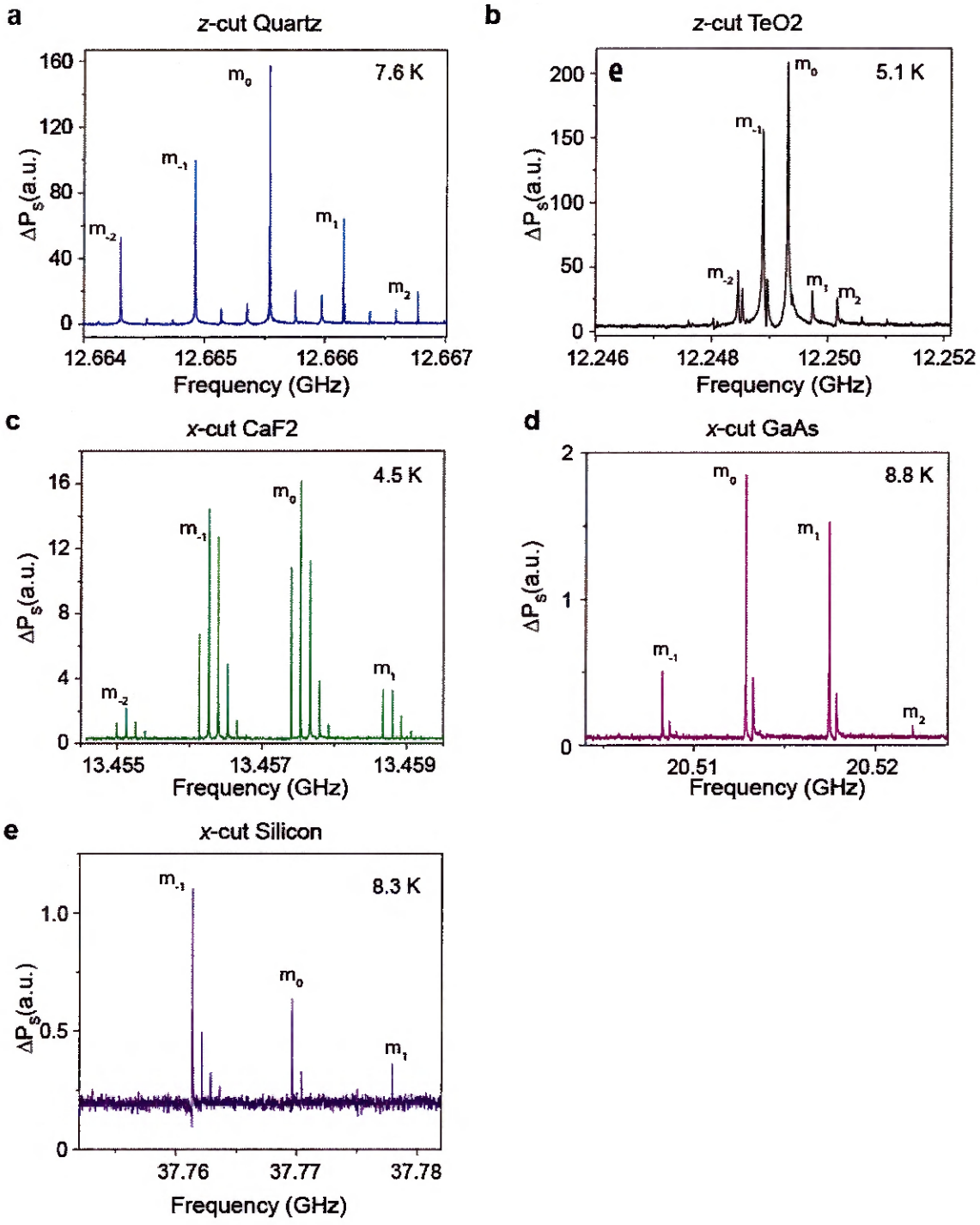

Figure 3.13: **Brillouin spectroscopy at cryogenic temperatures.** Stimulated Stokes scattering measurements in plano-convex (a) z-cut quartz resonator having a length $L = 5$ mm and radius of curvature, $R = 10$ mm at 7.6 K (b) z-cut TeO_2 resonator with $L = 5$ mm and $R = 10$ mm at 5.1 K (c) x-cut CaF_2 resonator with $L = 3$ mm and $R = 40$ mm at 4.5 K(d) x-cut GaAs resonator with $L = 0.5$ mm and $R = 16$ mm at 8.8 K(e) x-cut Silicon resonator with $L = 0.5$ mm and $R = 13.3$ mm at 8.3 K.

quartz and TeO_2 using known material parameters and device geometry.

The Hamiltonian framework that we developed in Chapter 2 can now be used to interpret optomechanical cooperativity for photon-phonon coupling in our system. For example, within quartz crystal, an acoustic dissipation rate of $2\pi \times 300$ Hz and an incident pump power of ~ 250 mW corresponds to the free space cooperativity $C^{\text{fs}} = P_p|g_0^m|^2 L_{\text{ac}}^2/(\Gamma_m \hbar \omega_p v_{gp} v_{gs}) \approx 0.03$. While it is possible to achieve unity cooperativity values required for phonon mode-cooling or regenerative self-oscillations by simply increasing the incident pump power, we see in Chapter 5 that it is possible to dramatically enhance the cooperativity of our system by resonantly enhancing both the pump and the Stokes light by placing the bulk crystal inside the optical cavity.

3.7 Conclusions and Outlook

In this chapter, we have shown how electrostriction mediated traveling-wave optomechanical interaction, also called stimulated Brillouin scattering, can be used to access bulk acoustic waves at high frequencies within practically any transparent crystalline media. We observed that various features of such measurements were transformed at cryogenic temperatures. Through such measurements, we demonstrated how the lifetimes of the bulk acoustic waves within crystalline solids at cryogenic temperatures are enhanced by orders of magnitude when compared to room temperature values. This leads to formation of macroscopic (cm-scale) standing waves acoustic modes. We shaped the surfaces of the crystal to form long-lived phonon modes that are tightly confined, permitting efficient coupling to free space laser beams. By adapting the optical design principles to the case of elastic wave propagation in anisotropic crystals, we demonstrated stable plano-convex resonators. For example, high frequency (12.7 GHz) phonons within plano-convex quartz crystal have high Q-factors (42 million) and also yield appreciable single-photon optomechanical coupling rate (31 Hz).

The bulk crystalline optomechanical system offers a powerful ways for probing cryogenic phonon physics in transparent crystalline media. Despite tremendous progress in the field of optomechanics, eletro-mechanics and quantum-phononic systems, it remains unclear which material platform could provide access to long-lived phonons at high-frequencies. While electromechanical transduction has been used to extensively study cryogenic phonon physics in piezoelectric crystals such as quartz [101], such techniques cannot be easily adapted to study other promising non-piezoelectric crystals such as CaF_2, Diamond, and Silicon. Since, photoelastic coupling is present in all media, Brillouin spectroscopy provides a non-invasive approach to explore phonon dissipation in a wide variety of transparent crystals.

Optomechanical coupling to bulk acoustic phonons using free-space laser beams represents an important first step towards utilizing bulk acoustic phonon for cavity optomechanics. Once we precisely know the Brillouin frequency through stimulated energy transfer measurements, we can design a multimode cavity optomechanical system by placing the bulk acoustic resonator inside an optical cavity. This high frequency cavity optomechanical system, with dramatically enhanced coupling rates, can be used to realize a new class of 'phonon lasers' [128] and compact Brillouin lasers [57]. We will discuss such high-frequency cavity optomechanical systems for classical as well as quantum applications in greater detail in Section 5 and Section 6.

Chapter 4

Bulk Acoustic Resonators on Chip

4.1 Introduction

In the previous chapter, we saw how a variety of crystalline materials at cryogenic temperatures can support long-lived acoustic waves at high-frequencies. Phonons within such crystalline bulk acoustic resonators (BAW) can become coherent carriers of information and can be utilized for a variety of classical and quantum applications ranging from novel 'phonon lasers' to devices for quantum information storage and transduction. However, for many such applications we seek high performance acoustic resonators that offer a path towards chip-scale integration.

Historically, confocal bulk acoustic resonators, which support long-lived phonons with $f \cdot Q$ products as high as 1.8×10^{18} [100], were designed for operation at relatively low frequencies (5-100 MHz) [99]. As a consequence, these resonators have been relatively large; confinement of such low-frequency acoustic waves requires a resonator with cm-scale later dimensions. Fortunately, as we scale these resonators to operate at higher frequencies (tens of GHz), smaller acoustic wavelengths permit dramatic size reduction. Such high frequency phonons are less sensitive to thermal decoherence mechanisms, making them a valuable resource for quantum applications. Despite

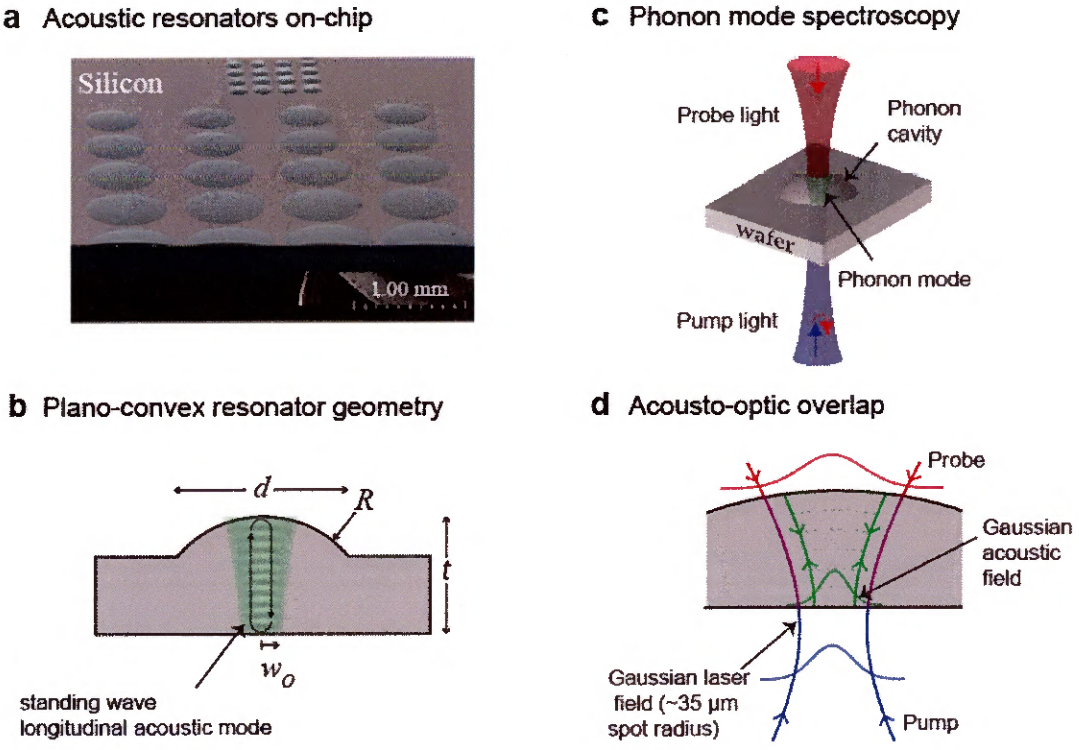

Figure 4.1: **On-chip acoustic resonator design.** (a) Plano-convex resonators microfabricated on a silicon wafer. (**b**) Schematics shows standing wave longitudinal mode with waist radius w_o supported by a plano-convex resonator with thickness, t, radius of curvature, R, and diameter, d. (**c**) Brillouin spectroscopy as cryogenic temperatures can be used to perform a type of laser-based phonon mode spectroscopy. (**d**) For sensitive spectroscopy, we enhance the light-sound interaction by tailoring the acoustic resonator geometry to produce good overlap between the acoustic and the optical fields. Adapted from Ref. [108].

this opportunity for size reduction, our initial efforts to engineer Brillouin coupling to bulk acoustic phonons relied on confocal macroscopic resonators. The reason for the relatively large size of these first systems was one of convenience; using commercially available optical polishing services, we could shape a variety of crystals into confocal resonators having larger (cm-scale) sizes. However, we realized that reaching record high lifetimes for acoustic waves required us to pay attention to crystal quality as well as possible defects and damage induced by mechanical polishing at the surface. This motivated us to develop our own fabrication techniques to shape confocal resonators. Micro-fabrication would not only allow us to precisely control the surfaces, utilize a large class of high-purity wafers as substrates to fabricate arrays of phononic resonators, permitting us to perform systematic studies of cryogenic phonon physics. Moreover, this approach would enable us to create chip-scale resonators that can be integrated with emerging quantum phononic systems [109, 110, 129, 130].

In this chapter, we present novel design principles used to fabricate miniaturized BAW on-chip. These devices have volumes that are more than 1000 times smaller than that of the cm-scale BAW resonators presented in the earlier chapter. To achieve such size reduction, we developed simple microfabrication techniques that allows us to create high-performance BAW resonators of a wide array of crystalline substrates. By performing laser-based phonon spectroscopy of high-frequency Brillouin-active phonon modes with such on-chip resonators, we demonstrate performance comparable to the best cm-scale BAW resonators. Finally, we show how such non-invasive laser spectroscopy of an array of on-chip BAW resonators could be used to explore fundamental limits of phonon dissipation at cryogenic temperatures.

4.2 On-chip Resonator Design

Creating high-performance bulk acoustic wave resonators within a small package presents a unique set of challenges. First and foremost, we seek to eliminate extrinsic losses to achieve long phonon lifetimes. The longitudinal waves which reflect from the top and bottom surfaces of the crystalline wafer can suffer from diffraction losses. To mitigate such extrinsic loss channels for phonons, we shape one of the surfaces of the crystal to create a plano-convex resonator, which produces tight confinement of acoustic energy in the transverse direction (beam waist or radius of $<$ 40 μm). As discussed in section 3.2, we must first determine the range of radii of curvatures, R, of the convex surface that would result in a stable cavity for phonons. Assuming one surface in planar, the stability condition is simply given by $R \geq t/\chi$, where t is the thickness of the substrate and χ is the anisotropy parameter.

In addition to forming stable acoustic modes, we must engineer the acoustic mode to couple efficiently to light. Since Brillouin coupling depends on the overlap integral between the optical and acoustic modes [131], we seek to maximize the optomechanical coupling to the fundamental Gaussian acoustic mode by matching the acoustic mode waist to the Gaussian optical beam having spot sizes of $\sim$ 35 μm. Note that one can also also change the optical beam size to match the acoustic beam waist. We chose to change the acoustic mode waist through fabrication because this is relatively easier than changing free-space components to vary the optical beam size. The following expression relates R to the acoustic mode waist, w_o, at the planar surface (see Appendix D for details)

$$w_o^2 = \frac{t\lambda_{\text{ph}}}{\pi\chi}\sqrt{\frac{g_1 g_2(1-g_1 g_2)}{(g_1+g_2-2g_1 g_2)^2}}. \tag{4.1}$$

Here, λ_{ph} is the wavelength of the acoustic mode, and the stability parameters $g_1 = 1$ for the planar surface and $g_2 = 1 - t/(\chi R)$ for the convex surface. For instance, if we

were to fabricate a plano-convex BAW resonator in a 1 mm thick z-cut quartz wafer, it would support a 12.66 GHz acoustic mode ($\lambda_{\text{ph}} = 497$ nm) having an acoustic waist $\omega_o = 39.6$ μm. Typically, the resonators that we fabricate on variety of crystalline substrates (silicon, quartz, sapphire, GaAs) have radii of curvatures on the order of 10s of mm.

Finally, we design the phonon cavity such that anchoring losses are negligible. We minimize anchoring losses by setting the diameter, d, of the convex surface to be much larger than the acoustic mode waist, w_o, ensuring that the only vanishingly small component of the acoustic mode feels the edges of the convex resonator. Since almost all of the acoustic energy resides within the plano-convex mode volume, this leads to negligible anchoring losses. For example, if we were to fabricate a resonator in quartz such that $d/w_o = 5$ and assume that all the energy outside the convex surface is lost to anchoring losses, we still find that the Q-factor limit due to this loss mechanism would be 7×10^9 [108]. Therefore, BAW resonators fabricated on 1 mm thick quartz having acoustic waist of 39.6 μm that we considered earlier, it is possible to almost completely eliminate anchoring losses in resonators with diameters as small as 200 μm. We usually fabricate resonators with diameters of the order of 1 mm. We will see in the next section that our fabrication approach provides an elegant way of changing the radius of curvature, R, by simply changing the diameter d of the lens. A typical resonator with a diameter of the order of 1 mm fabricated on a 0.3-1 mm thick wafers, representing more than 1000-fold reduction in device volume when compared to the 5 mm thick confocal resonators with half-inch diameters.

4.3 Fabrication

We developed simple microfabrication techniques to create plano-convex resonators on-chip by adapting existing techniques used to fabricate optical micro-lenses [132–

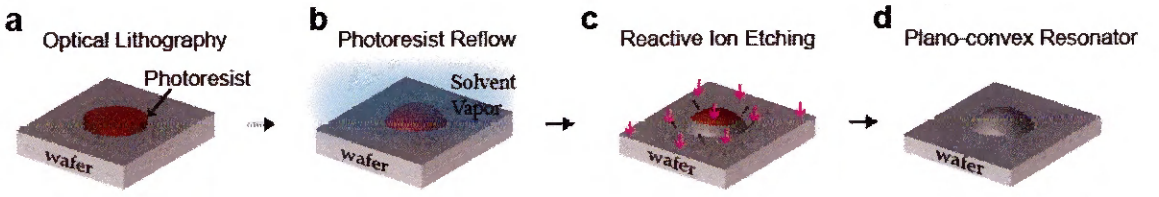

Figure 4.2: **Microfabrication steps.** (a) Standard optical lithography is used to define a circular photoresist pattern having finite thickness (i.e. a photoresist cylinder). (b) When the photoresist is placed in a chamber containing its constituent solvent, it absorbs the solvent, becomes less viscous, and reflows into a hemispherical shape. The resist hardens and retains its hemispherical shape after a post-bake following the reflow process. (c) This hemispherical surface is used as a mask during a slow reactive ion etching process. (d) After completely etching away the photoresist, the hemispherical surface profile is transferred onto the substrate, yielding a plano-convex acoustic resonator. Adapted from Ref. [108].

137]. We optimized the fabrication steps for each crystalline substrate so it yielded resonators with excellent surface roughness necessary to achieve long phonon lifetimes.

In this fabrication process, standard optical lithography is first used to define circular photoresist patterns. These photoresist cylinders are subsequently reflowed into photoresist hemispheres using the solvent vapor reflow technique [138–140]. When the circular photoresist cylinders are exposed to solvent vapor, the photoresist becomes less viscous, allowing surface tension to turn them into hemispherical surfaces having excellent surface roughness (order of 1 nm). Unlike more widely used thermal reflow techniques used to fabricate optical micro-lenses, solvent vapor reflow permits us to create hemispheres with very small contact angle and achieve large radii of curvatures (tens of mm) needed to form stable acoustic cavities. Another important advantage of using solvent reflow technique is that this technique is essentially substrate independent. For example, the center height of the reflowed photoresist hemisphere only depends on the initial thickness of the photoresist and is not dependent on the substrate materials (i.e. same contact angle for a fixed diameter photoresist for every substrate). In contrast, contact angle varies dramatically with substrates during thermal reflow ,and the reflow process needs to be optimized for each substrate. In

the solvent vapor reflow, the center height of the photoresist is also relatively insensitive to the photoresist diameter, meaning we can independently change the radius of curvature of the convex surface by simply changing the diameter of the photoresist cylinders.

Reactive ion etching is then used to transfer the hemispherical surface profile onto the substrate by completely etching away the photoresist material using a reactive ion etch. The reactive ion etching parameters must be developed for each substrate material and optimized to ensure excellent surface finish after etching. The ratio of etching rate of the photoresist to the etching rate of the substrate, also called etch selectivity, can be varied, providing another independent way to control the final radius of curvature of the convex surface. Typically, we perform slow reactive ion etching (etch rates of 10-100 nm/min), meaning that etching of ~10 μm thick photoresist hemispheres takes 1-3 hours. Therefore, one must try to minimize any contaminants that could form inside the etching chamber during such a long etch process by performing an extensive conditioning run. The detailed fabrication steps for producing acoustic resonators on a variety of crystalline substrates are presented in Appendix F.

4.4 Phonon mode spectroscopy of on-chip resonators

We probe the lifetimes of high-frequency acoustic waves in microfabricated plano-convex bulk acoustic resonators at cryogenic temperatures using laser-based optomechanical spectroscopy. As explained before, electrostriction and photo-elasticity mediated optomechanical coupling permits us to both generate and detect phonons over a finite bandwidth near Brillouin frequency, Ω_B (see Section 2-3). Since the coupling bandwidth due to the phase matching constraints is approximately twice the acoustic free spectral range (FSR) of $v_a/2t$ (typically 1-50 MHz), this laser spectroscopy per-

mits us to determine the longitudinal mode spectrum of plano-convex phononic cavity. This measurement is performed by illuminating the resonator with both pump and probe laser beams. As the frequency detuning between the pump and probe waves are varied, stimulated energy transfer mediated by these Brillouin-active phonon modes permits us to perform high-frequency phonon mode spectroscopy.This technique is very versatile; we can readily probe the performance of an array of such chip-scale resonators fabricated on the same chip by laterally translating the laser beam across the chip.

In the experimentally measured energy transfer spectrum seen in Fig. 4.3**b-d**, we observe multiple resonances corresponding to the standing wave longitudinal phonon modes centered about the Brillouin frequency of 12.66 GHz, 20.51 GHz, and 37.78 GHz for BAW resonators microfabricated in z-cut Quartz, x-cut GaAs and x-cut Silicon wafers, respectively. Specifically, we identify family of narrow resonances that are separated by the acoustic FSR of 3.13 MHz, 4.61 MHz, and 8.27 Mhz, as expected for 1-mm-thick z-cut quartz, 0.5-mm-thick x-cut GaAs, and 0.5-mm-thick x-cut silicon wafer, respectively.

A high-resolution measurement of modes within a single mode family as seen in Fig. 4.3 reveals multiple equally spaced resonances separated by 154 kHz, 398 kHz, and 761 kHz in quartz, GaAs, and silicon. These resonances (L1, L2, L3, and so on) are Hermite-Gaussian-like higher order transverse acoustic modes of the plano-convex geometry. We observe coupling to such higher order acoustic modes when the Gaussian laser beams are not perfectly mode matched to the fundamental Gaussian mode of these acoustic resonators or when the laser beams are slightly misaligned.

The frequency spacing for these higher order modes shows good agreement with both the analytically and numerically calculated mode spacing. Assuming paraxial wave propagation and parabolic acoustic dispersion surfaces, the analytical calculation gives mode spacing of 155 kHz, 410 kHz, and 731 kHz, which agrees well with

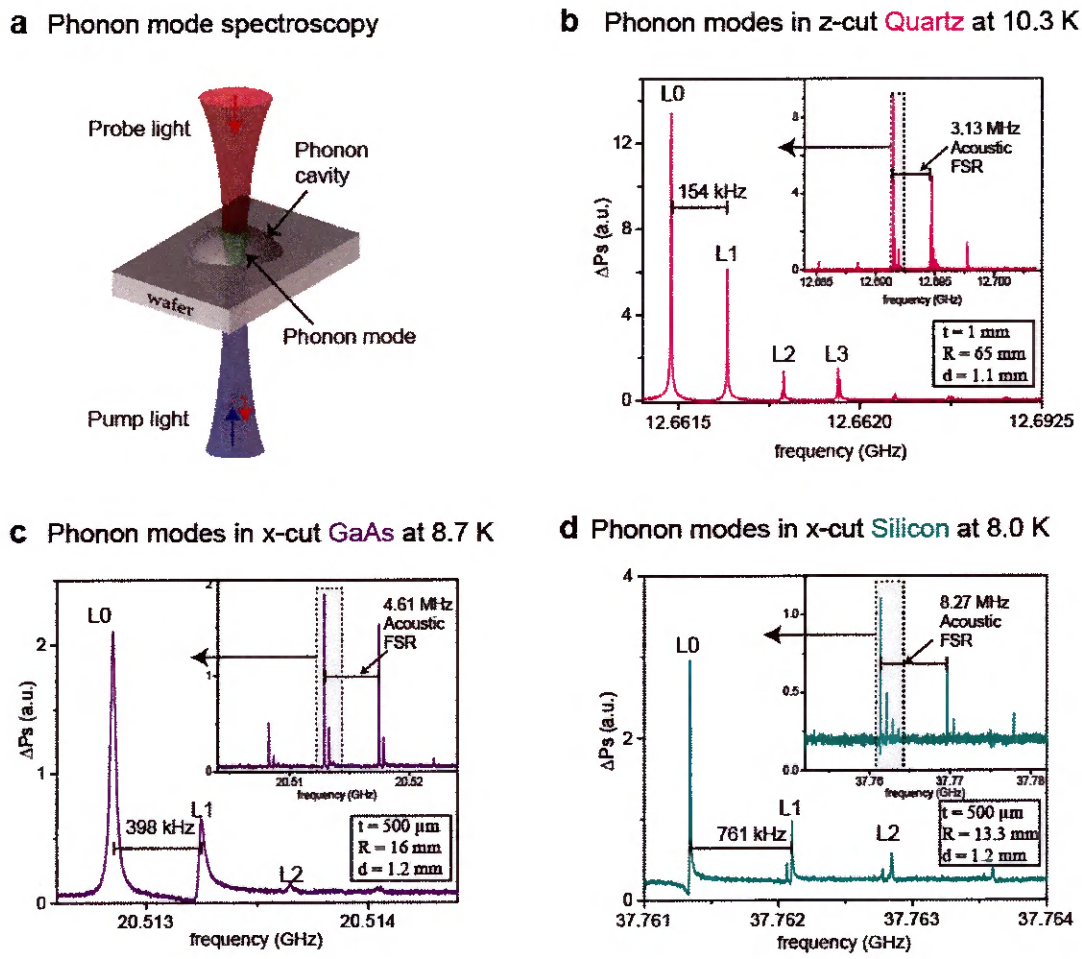

Figure 4.3: **Laser-based spectroscopy of the acoustic modes** (a) Pump-probe spectroscopy and energy transfer measurements at cryogenic temperatures (discussed in Chapter 3.6) is used to probe the frequency spectrum and dissipation rates of the standing wave longitudinal acosutic modes within a chip-scale bulk acoustic resonator. (a) Longitudinal phonon-mode spectrum of a plano-convex resonator fabricated on a 1 mm thick z-cut quartz wafer shows a fundamental mode (L0) and series of equally spaced higher-order transverse modes (L1, L2, L3, and so on) seperated by 154 kHz. A zoomed out spectrum shows families of such modes separated by longitudinal acoustic free spectral range of 3.13 MHz. (**c-d**) Mode spectrum of plano-convex resonators fabricated on x-cut GaAs and x-cut Silicon wafer, respectively. Adapted from Ref. [108].

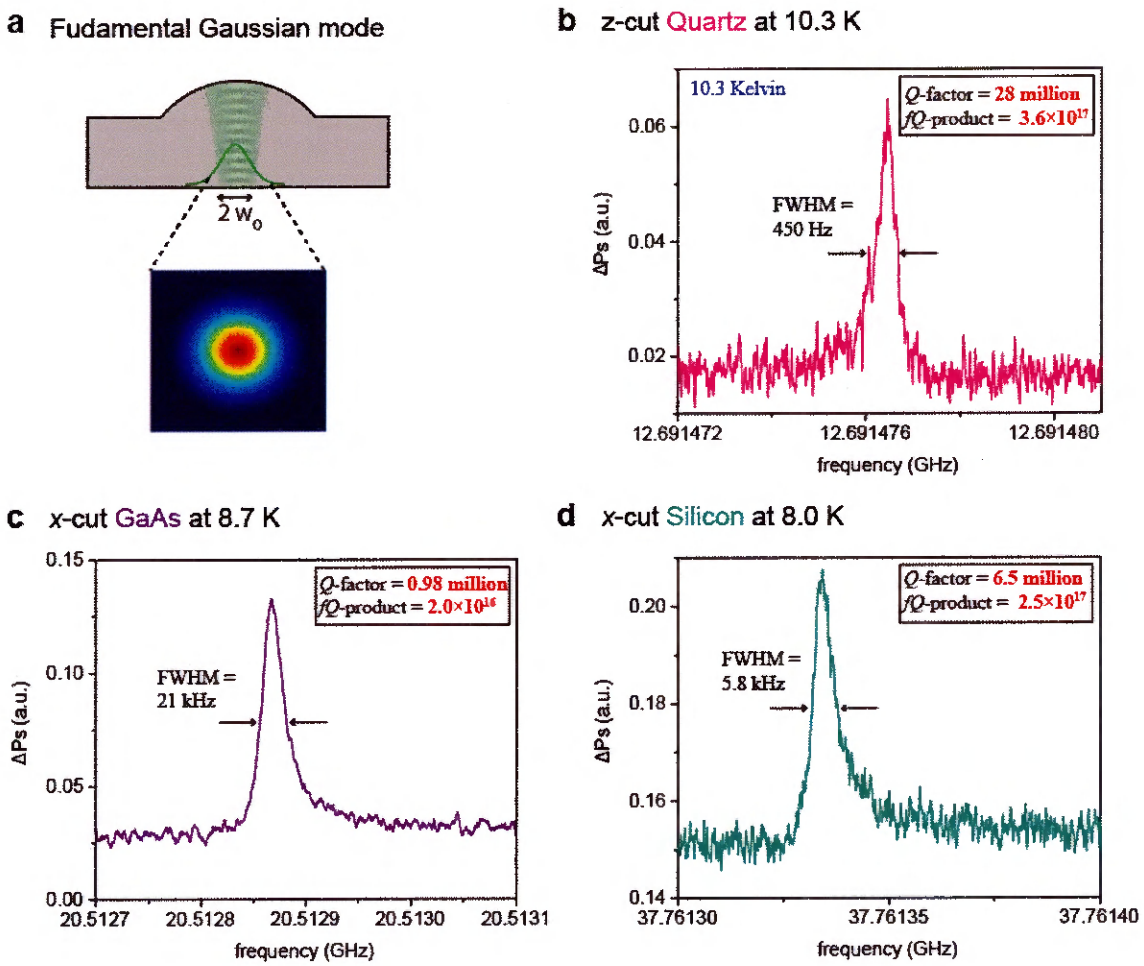

Figure 4.4: **Acoustic Q-factors at cryogenic temperatures** (**a**) We perform high-resolution spectroscopy of fundamental Guassian acoustic modes (L0) within chip-space resonators (**a-d**) This measurement reveals Q-factors of 2.8×10^7, 0.98×10^6, and 6.5×10^6 in quartz, GaAs, and Silicon, respectively. Adapted from Ref. [108].

the experiments (see Appendix D).

The numerical simulations also provides insights into the observed frequency splitting ($\sim$ tens of kHz) of the higher order transverse modes in quartz and silicon. We observe similar resonance splittings in simulation when the shape of the microfabricated surface has some asymmetry about its axis. This small asymmetry was confirmed independently by measuring surface profiles of these microfabricated cavities. Typically, we find that resonators that are larger than 1 mm in diameter start to exhibit this type of axial asymmetry during the reflow process.

The linewidth of the resonances observed during the energy transfer measurements is determined by the acoustic dissipation rate $\Gamma_m/2\pi$, permitting us to calculate Q-factors of such Brillouin active phonon modes. To explore the performance of such microfabricated bulk acoustic resonators, we compare the Q-factor for the fundamental Gaussian acoustic mode (L0), which typically exhibits the lowest diffraction and anchoring losses. We perform these measurements over a range of optical powers to identify the intrinsic acoustic linewidth. Since the steady state phonon numbers can be quite large ($10^{10} - 10^{13}$) during such stimulated energy transfer measurements, we reduce the optical powers to avoid possible line-shape distortions that may arise from acoustic nonlinearities. Moreover, other nonlinear optical effects like free carrier-induced absorption and refractive index change that can leads to Fano line-shapes in silicon (see Fig. 4.3**d**), can also be minimized at low optical powers. Measurement of the linewidth at low optical powers (order of 10 mW for pump and 1 mW for Stokes light) as seen in Fig. 4.4 revealed a linewidth of 450 Hz, 21 kHz, and 5.8 kHz corresponding to a Q-factor of 2.8×10^7, 0.98×10^6, 6.5×10^6 for 12.66 GHz, 20.51 GHz, and 37.78 GHz acoustic mode in on-chip resonators in quartz, GaAs, and silicon. Note that we obtain large $f \cdot Q$-products of 3.6×10^{17} and 2.5×10^{17} for resonators in quartz and silicon that are comparable to the $f \cdot Q$-products obtained in cm-scale bulk crystalline resonators.

4.5 Conclusions and Outlook

In conclusion, the analytical guidelines, numerical techniques, and microfabrication techniques presented in this chapter could be used to perform studies of acoustic dissipation in a broad class of crystalline solids. Moreover, these techniques can be used to miniaturize high performance BAW resonators for applications ranging from oscillators to on-chip Brillouin lasers.

As for quantum applications, we have been able to couple on-chip plano-convex resonators of the type discussed here to superconducting qubits. Coherent control of long-lived phonon modes supported by on-chip BAW resonators using superconducting qubits have already yielded creation of non-classical mechanical states such as the number states.

Beyond optomechanics and quantum information, the microfabrication techniques presented here can also be utilized to produce high-finesse optical cavities on-chip. Through microfabrication of parabolic surfaces, we have an opportunity to fabricate on-chip optical cavities with excellent surface finish (roughness $\sim$ 0.1 nm) and radii of curvatures ranging from 0.1 mm to 10 m. Miniaturization and microfabrication of high-finesse optical resonators has a potential to impact fields ranging from spectroscopy to time-keeping.

Chapter 5

High-frequency Cavity Optomechanics using Bulk Acoustic Waves

5.1 Introduction

The field of cavity optomechanics has successfully harnessed coupling between light and mechanical motion to perform precision measurements [141, 142], create nonclassical mechanical states [143–145], and develop new technologies [146]. Building on these achievements, cavity optomechanical systems aim to harness optical control of mechanical motion for the exploration of fundamental physics and for classical as well as quantum applications ranging from state-of-the-art microwave oscillators [59] to efficient microwave-to-optical conversion [147–150].

For many of these lofty goals of cavity optomechanics, it is desirable to have optical control of long-lived mechanical modes at high frequencies [117]. High frequencies (GHz) phonon modes can be initialized deep in their quantum ground state using standard refrigeration techniques, opening doors to synthesis of more complex quantum

states of mechanical motion. Long-lived phonons can preserve coherent information for extended periods of time, enabling robust control and storage of information in the mechanical modes.

A variety of micro/nanoscale optomechanical systems [151–154] already exists to manipulate mechanical motion at GHz frequencies. These systems have enabled ground state cooling [155], quantum control at the single phonon level [144], and remote entanglement between mechanical resonators [145]. However, these microscopic structures, having large surface-to-volume ratios and pico-gram scale motional masses, are particularly sensitive to the effect of spurious laser heating [156], complicating the prospects for robust ground state operation.

In this context, bulk acoustic resonators offer a number of favorable properties that make them enticing resources for cavity optomechanics. Since acoustic dissipation plummets in crystalline media at cryogenic temperatures, bulk acoustic phonons even at high frequencies exhibit very long lifetimes [75, 106]. For example, in Chapter 4, we demonstrated acoustic Q-factors as high as 42×10^6, corresponding to lifetimes of 0.53 ms, for 12.7 GHz bulk acoustic phonon modes in quartz at $\sim$ 10K. Moreover, such long-lived phonon modes can be accessed in practically any transparent crystalline substrate. So, we can choose our material platform to minimize acoustic as well as optical losses or to add new functionality to our optomechanical system such as engineering coupling to defect centers. These modes of the bulk acoustic resonators live primarily in the bulk are less sensitive to surface interactions. The motional masses ($\sim$20μg) [106, 111] of these acoustic modes are more than 1-100 million times larger than those of comparable GHz frequency microscale and nanoscale optomechanical systems, permitting bulk acoustic resonators to support large occupation numbers for both photons and phonons. Such large motional masses might also be particularly useful when studying decoherence phenomena in macroscopic objects. In addition, a single bulk acoustic resonator can support a multitude of long-lived phonon modes

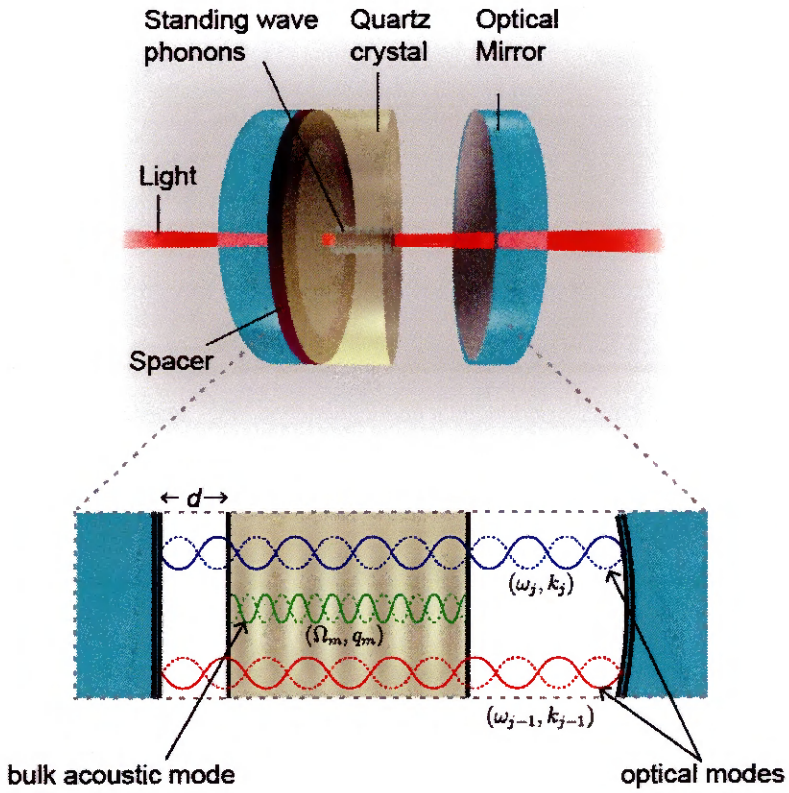

Figure 5.1: **Cavity optomechanical system using bulk acoustic phonons** Schematic of a cavity optomechanical system formed by placing a bulk acoustic resonator inside a Fabry-Pérot optical cavity. Brillouin interactions permit resonant inter-modal coupling between two distinct standing wave modes of the optical cavity at frequencies ω_j and ω_{j+1} is mediated by a standing wave acoustic mode at frequency Ω_m formed within the bulk acoustic resonator (i.e. the quartz crystal). Adapted from Ref. [112] and Ref. [111].

over a wide range (1-100 GHz) of frequencies, which could be harnessed for applications ranging from low-noise microwave oscillators to quantum memories.

In the previous chapter, we have shown that we can access these Brillouin-active phonon modes using free-space laser beams at cryogenic temperatures. However, the optomechanical interaction strength for this process is rather weak because each laser beam passes through the crystal only once. Alternatively, it should be possible to access these phonons more efficiently by placing the bulk acoustic mode inside an optical cavity. This new system would not only permit us to dramatically increase the optomechanical interaction strength but also leverage the well-developed cavity optomechanical techniques to harness bulk acoustic phonons for applications ranging from high-power lasers and oscillators to efficient quantum transducers.

In this chapter, we describe a novel cavity optomechanical system that utilize high-frequency modes of a bulk acoustic resonator. We design our system so that the free-spectral range of the optical cavity matches the Brillouin frequency of the bulk crystalline resonator. We show that high-frequency bulk acoustic phonons then mediate resonant coupling between two distinct modes of an optical cavity through Brillouin coupling. Resonant driving of an optical mode within this multimode cavity optomechanical system permits large coupling strengths ($\sim$ 10 MHz) and high cooperativities (>700) as required for efficient control of phonons using light.

In the linearized interaction regime, breaking the symmetry between Stokes and the anti-Stokes processes in our optomechanical system can yield beam-splitter and two-mode squeezing Hamiltonian as a basis for quantum protocols ranging from state-transfer to generation of non-classical mechanical states. In the next section, we discuss how we engineer the optical mode spectrum to break the symmetry between the Stokes and anti-Stokes scattering process.

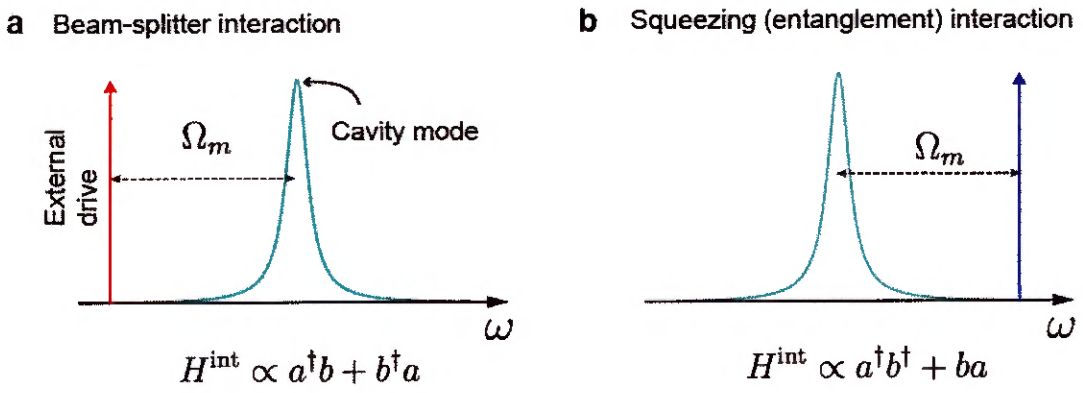

Figure 5.2: **Linearized Hamiltonian of a protyptical cavity optomechanical system.** (a) In a single-mode optomechanical system, a red-detuned control laser produces a "beam-splitter" interaction [117], which can be used to transfer quantum states from light to mechanics or vice versa. (b) On the other hand, a blue-detuned control laser produces a "two-mode squeezing" Hamiltonian, which can be used to entangle light with mechanical motion.

5.2 Asymmetric Cavity Mode Spacing

In a prototypical cavity optomechanical system, consisting of a single optical mode coupled to a single mechanical mode, a variety of linearized interactions can be engineered by simply choosing the detuning of the laser drive with respect to the optical cavity mode (see Fig. 5.2). By comparison, in our multimode optomechanical system, the external field is typically on resonance with an optical mode, permitting large intracavity photon numbers and hence large optomechanical coupling strengths (see Section 6 for more details). However, such resonant driving of the optical cavity mode presents a problem in the case of a Fabry-Pérot cavity with regular mode spacing. This is because a Brillouin active phonon mode, having frequency ($\Omega_\mathbf{m}$) that matches the optical FSR, will resonantly scatter pump light at frequency ω_j to both cavity modes at ω_{j-1} and ω_{j+1} with nearly equal probabilities (see Fig. 5.3a). Therefore, to break the symmetry between the Stokes and anti-Stokes scattering rates, we need to tailor the optical mode spectrum so that one of the scattering process (say anti-Stokes) is no longer resonant (see Fig. 5.3b).

Fortunately, the introduction of a bulk crystalline resonator inside an optical cav-

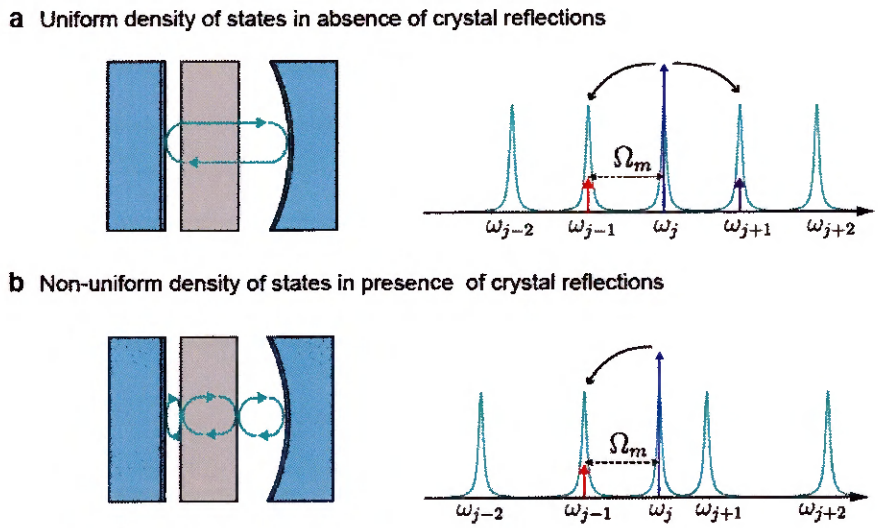

Figure 5.3: **Tailoring the optical mode spectrum.** (**a**) For a Fabry-Pérot optical cavity, the standing wave longitudinal optical modes are equally spaced. (**b**) The additional optical reflections at the surfaces of the quartz crystal causes dispersive shifts of the cavity resonances. Adapted from Ref. [111].

ity provides an elegant strategy to engineer the optical mode spectrum. Even modest optical reflections at the surfaces of the bulk acoustic resonator can shift the modes of the Fabry-Pérot cavity by an amount that is much larger than the linewidth of the optical modes. As a result, the mode spectrum of the Fabry-Perot cavity is no longer uniform. Using this non-uniform mode spacing, we can select a pair of optical modes (ω_{j-1} and ω_j) having frequency difference matching the phonon frequency (Ω_m) and achieve high-selectivity between Stokes or anti-Stokes process, even when the external field is directly on resonance with an the optical mode.

To explore the modification to the optical mode spectrum in detail, we consider the case of a planar quartz crystal (bulk acoustic resonator) that is placed inside a nearly hemispherical optical cavity having high-reflectivity (98%) mirrors. We can use the scattering/transmission matrix [118] to calculate the mode spectrum of the optical cavity with the quartz crystal placed in between the two mirrors. We will show how the introduction of the quartz crystal causes the mode spectrum to change dramatically as a function of optical mode number as well as the position of the

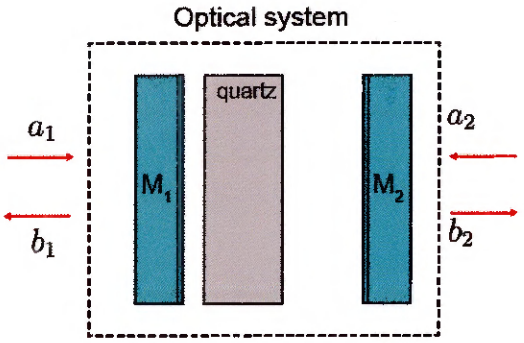

Figure 5.4: **Transmission matrix treatment to determine optical mode spectrum.** The introduction of bulk crystal inside the optical cavity modifies the reflection/transmission spectrum of the optical cavity, which can be explored using the scattering/transmission matrix treatment. Adapted from Ref. [111].

crystal inside the optical cavity.

In what follows, we use a 1-dimensional model of a Fabry-Pérot cavity, which consists of optical mirrors having power reflectivities of R_1 and R_2 and transmission of T_1 and T_2. We assume no absorption losses in the mirrors so that $R_i + T_i = 1$, where $i = 1, 2$. The power reflectivity at each crystal face, R_0, is given by $(1-n)^2/(1+n)^2$, where n is the refractive index of the quartz crystal. For simplicity, we assume plane wave optical fields ($E = \mathrm{Re}\{ae^{i(kz-\omega t)}\}$). The phase shift ϕ acquired by an optical field after propagating a distance z in a medium with refractive index n is given by $\phi = kz = n\omega z/c$, where c is the speed of light in vacuum.

To calculate the reflection and transmission spectrum of this cavity, we start by defining a transmission matrix ($\mathcal{T}$) which relates the input field amplitudes a_1, a_2 to the output field amplitudes b_1, b_2 (see Fig. 5.4) as follows:

$$\begin{bmatrix} b_1 \\ a_1 \end{bmatrix} = \mathcal{T} \begin{bmatrix} b_2 \\ a_2 \end{bmatrix}. \tag{5.1}$$

Using the transmission matrices for a lossless mirror and for propagation in space are given by we can determine the total transmission matrix ($\mathcal{T}$) for our optical system,

which is given by

$$\mathcal{T} = \mathcal{T}_{mirror1} \cdot \mathcal{T}_{propVacuum} \cdot \mathcal{T}_{mirrorQuartz} \cdot \mathcal{T}_{propQuartz} \tag{5.2}$$

$$\cdot \mathcal{T}_{mirrorQuartz} \cdot \mathcal{T}_{propVacuum} \cdot \mathcal{T}_{mirror2}$$

$$= \frac{-i}{t_1}\begin{bmatrix} -1 & r_1 \\ -r_1 & 1 \end{bmatrix} \cdot \begin{bmatrix} e^{i\phi_1} & 0 \\ 0 & e^{-i\phi_1} \end{bmatrix} \cdot \frac{-i}{t_0}\begin{bmatrix} -1 & r_0 \\ -r_0 & 1 \end{bmatrix} \cdot \begin{bmatrix} e^{i\phi_2} & 0 \\ 0 & e^{-i\phi_2} \end{bmatrix}$$

$$\cdot \frac{-i}{t_0}\begin{bmatrix} -1 & -r_0 \\ r_0 & 1 \end{bmatrix} \cdot \begin{bmatrix} e^{i\phi_3} & 0 \\ 0 & e^{-i\phi_3} \end{bmatrix} \cdot \frac{-i}{t_2}\begin{bmatrix} -1 & r_2 \\ -r_2 & 1 \end{bmatrix}. \tag{5.3}$$

Here, $r_1 = \sqrt{R_1}, r_2 = \sqrt{R_2}, r_0 = (1-n)/(1+n), \phi_1 = \omega d/c, \phi_2 = n\omega L_{\rm ac}/c$, $\phi_3 = \omega(L_{\rm opt} - L_{\rm ac} - d)/c$, and d is separation between the crystal and the planar mirror. The normalized reflection ($P_r(\omega)$) and transmission spectrum ($P_t(\omega)$) of our optical system can then be calculated from $\mathcal{T}$ as follows

$$P_r(\omega) = \left|\frac{\mathcal{T}_{12}}{\mathcal{T}_{22}}\right|^2 \text{ and } P_t(\omega) = \left|\frac{1}{\mathcal{T}_{22}}\right|^2. \tag{5.4}$$

While the analytical expressions for P_r and P_t can be derived in a straightforward way from Eqn. (5.2), they are quite cumbersome to display here. Using this analytical expression for P_r along with the known geometrical parameters (d= 0.15 mm, $L_{\rm ac}$ = 5.19 mm, $L_{\rm opt}$= 9.13 mm, and n= 1.55), we compare the cavity mode spectrum with and without the quartz crystal inside the optical cavity near experimentally relevant wavelength (1550 nm or $\omega/2\pi \sim$ 194 THz). For the case without the crystal, we simply set n=1 and the analytical calculation reveals equally spaced cavity modes separated by the optical FSR ($c/(2L_{\rm opt})$). However, with the introduction of the quartz crystal the optical path length increases and we observe that on average the spacing between the optical modes gets narrower. However, we also see a undulation in the free spectral range (i.e., change in the spacing between adjacent optical modes)

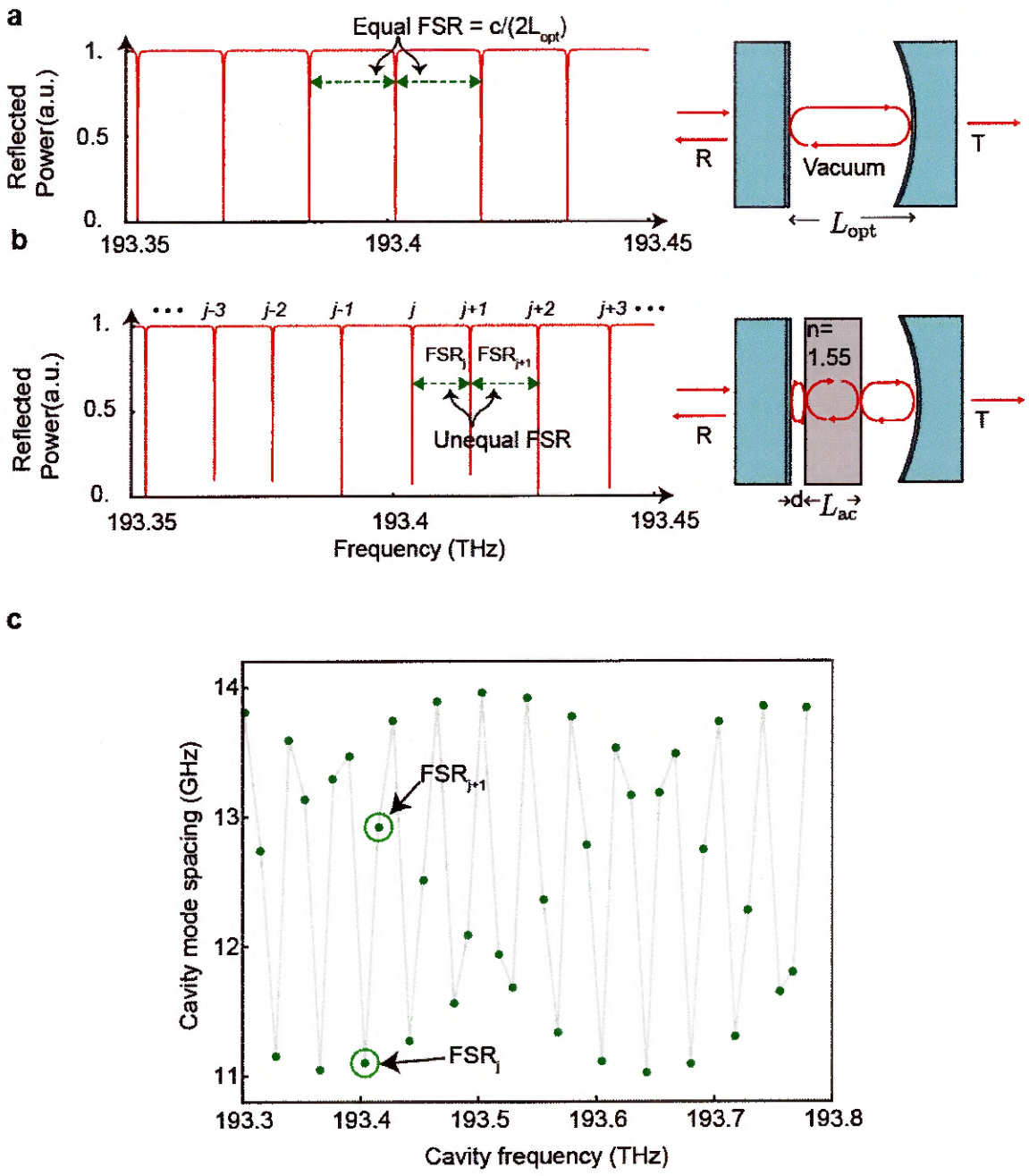

Figure 5.5: **Undulation in the optical mode spectrum due to the bulk crystal.** (a) For a Fabry-Pérot, the standing wave cavity modes are spaced equally by the optical free spectral range (FSR) given by $c/2L_{\text{opt}}$. (b) This mode spectrum changes dramatically when a medium with refractive index n is placed in between the two mirrors. In addition to the overall decrease in the FSR because of increase in the optical path length, the small-optical reflections ($\sim 4\%$) on the quartz-vacuum interface shift the modes of the Fabry-Perot cavity. (c) This gives rise to a large ($\sim 20\%$) variation in optical FSR as a function of frequency. Adapted from Ref. [111].

as a function of cavity frequency. This variation in FSR ($(\omega_{j+1} - \omega_j)/2\pi$) can be as large as 2.94 GHz between 1548 nm and 1552 nm (see Fig. 5.5**c**). Furthermore, the difference in FSR between adjacent optical modes ($\Delta\omega = \omega_{\mathrm{FSR}}^{j+1} - \omega_{\mathrm{FSR}}^{j}$) can be as large as 2.47 GHz; the parameter $\Delta\omega$ is important because it quantifies the degree of asymmetry between the Stokes and the anti-Stokes scattering processes. Additionally, since the FSR variation is periodic as a function of cavity frequency, it is relatively easy to find several pairs of cavity modes having FSRs that match Brillouin frequency.

The location of the crystal inside the cavity can be used as another knob to tune the cavity mode spectrum. For instance, we observe periodic variations in cavity mode frequencies for each mode number j (see Fig. 5.6**b**) as we change the position of the crystal from d to $d + \Delta d$. This variation in cavity frequency was $\lambda/2$ periodic, where λ is the wavelength of the light; this is a result of crystal surfaces passing through the nodes and anti-nodes of the standing wave optical cavity modes. Therefore, we can change the displacement of the crystal to match the optical FSR to Brillouin frequency.

Now, we compare experimental measurement of the cavity mode spacing with the analytical calculations. We perform cavity mode spectroscopy at cryogenic temperatures by sweeping the laser wavelength between 1548 nm and 1552 nm and recording the back-reflected power (see Fig. 5.7 **a**). We use this reflection spectrum to identify the resonant mode frequencies, $\omega_j/2\pi$ and calculate the cavity mode spacing (i.e., $\mathrm{FSR}_j = (\omega_{j+1} - \omega_j)/2\pi$). As expected from analytical calculations, we observed periodic variation in cavity mode spacing (see Fig. 5.7**b**). However, because of the uncertainties in the geometrical parameters (such as a exact crystal position d) we took the exact crystal location as a free parameter. For $d = 152.52$ μm, we see a good agreement between the experimentally determined cavity mode spacing (black dots) and the theoretically calculated values (green dots) in Fig. 5.7c. With the quartz crystal inside the optical cavity, the maximum FSR variation of 2.6 GHz obtained

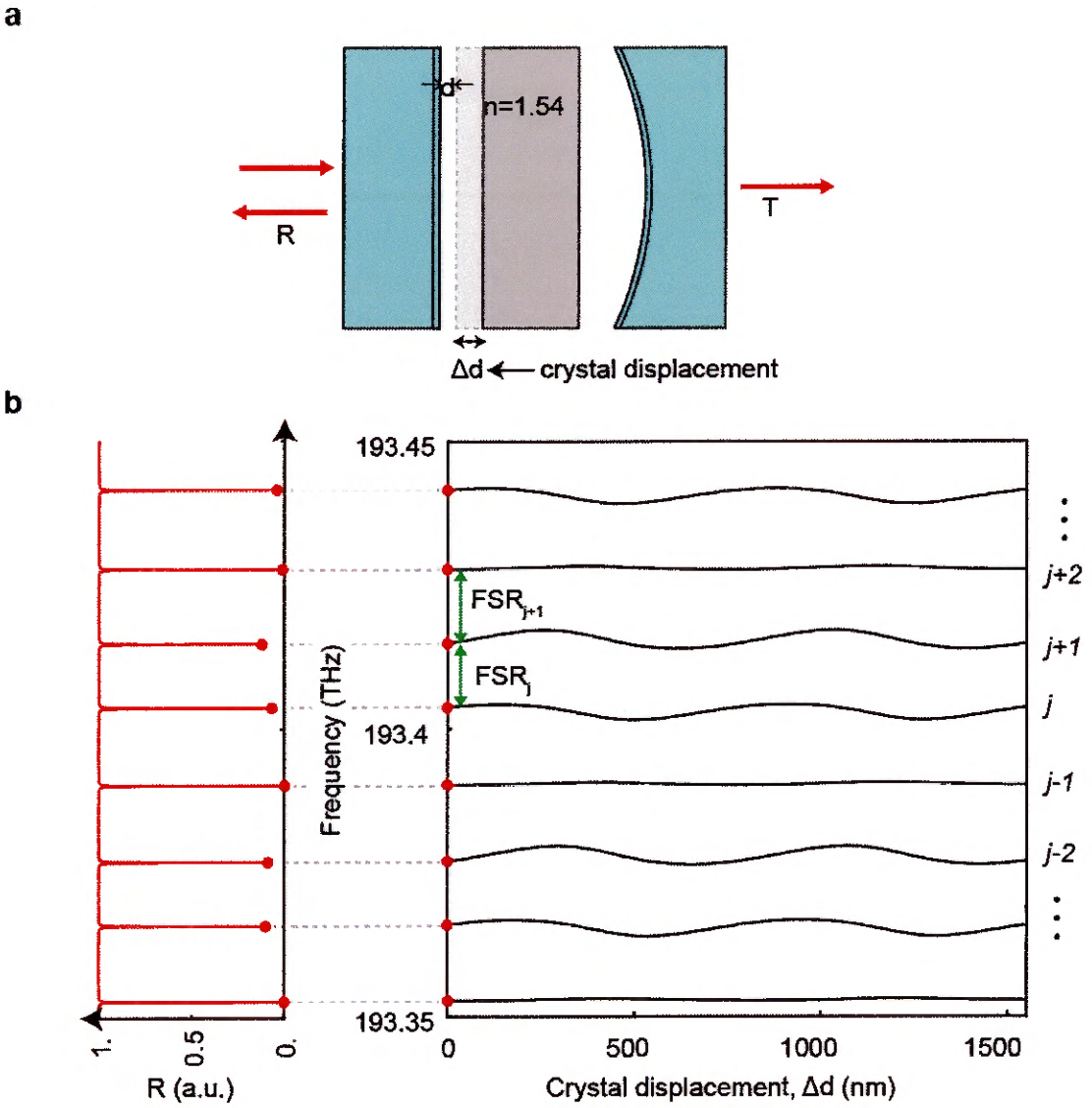

Figure 5.6: **Variation in the optical mode spectrum as a function of crystal position (d).** (a) A schematic showing how the crystal is displaced from its original location d to $d + \Delta d$. (b) Plot of the optical mode frequencies (ω_j) (near 193 Thz or 1550 nm wavelength) as a function Δd. This plot reveals period variation in the optical mode frequency with a periodicity that is equal to half the wavelength of light, which corresponding to crystal moving through the nodes and the anti-nodes of the standing wave optical cavity modes. Adapted from Ref. [111].

experimentally agrees well with the predicted value of 2.94 GHz.

As a consequence of this large ($\sim$ 20%) undulation in the optical FSRs, we can achieve $> 10^3$-fold difference in scattering rates between the Stokes and the anti-Stokes process. In a single-mode cavity optomechanical, such large asymmetry in the scattering rates is produced by far-detuning the drive. However, this reduces the intracavity photon number of the external drive field. In contrast, our multimode optomechanical system permits greatly enhanced intracavity photon numbers since the external drive field is directly on resonance with an optical mode. The relative strength of the Stokes/anti-Stokes scattering rates in the case of resonant driving is determined by the ratio $(2\Delta\omega/\kappa)^2$, where $\Delta\omega$ is the difference in the FSR between then adjacent optical modes and κ is the optical cavity linewidth. Because $\Delta\omega$ is well-resolved from the linewidth (i.e., $2\Delta\omega/\kappa \simeq 36$ for optical cavities having mirrors with 98% reflectivity) we can virtually eliminate the Stokes or anti-Stokes interaction by resonantly driving the lower or higher frequency optical mode.

Symmetry breaking between the Stokes and anti-Stokes process allows us to simply consider the resonant coupling between two optical modes mediated by bulk acoustic phonons. We develop a Hamiltonian formulation to explore such Brillouin mediated optomechanical coupling in the next section.

5.3 Hamiltonian Treatment

In this section, we derive the total Hamiltonian for our multimode system in which a single bulk acoustic mode at frequency Ω_m mediates interaction between two optical cavity modes at frequencies ω_j and ω_{j+1}. We begin by deriving the Hamiltonian for the optical and acoustic fields and eventually add an interaction term that characterizes the electrostriction mediated optomechanical coupling.

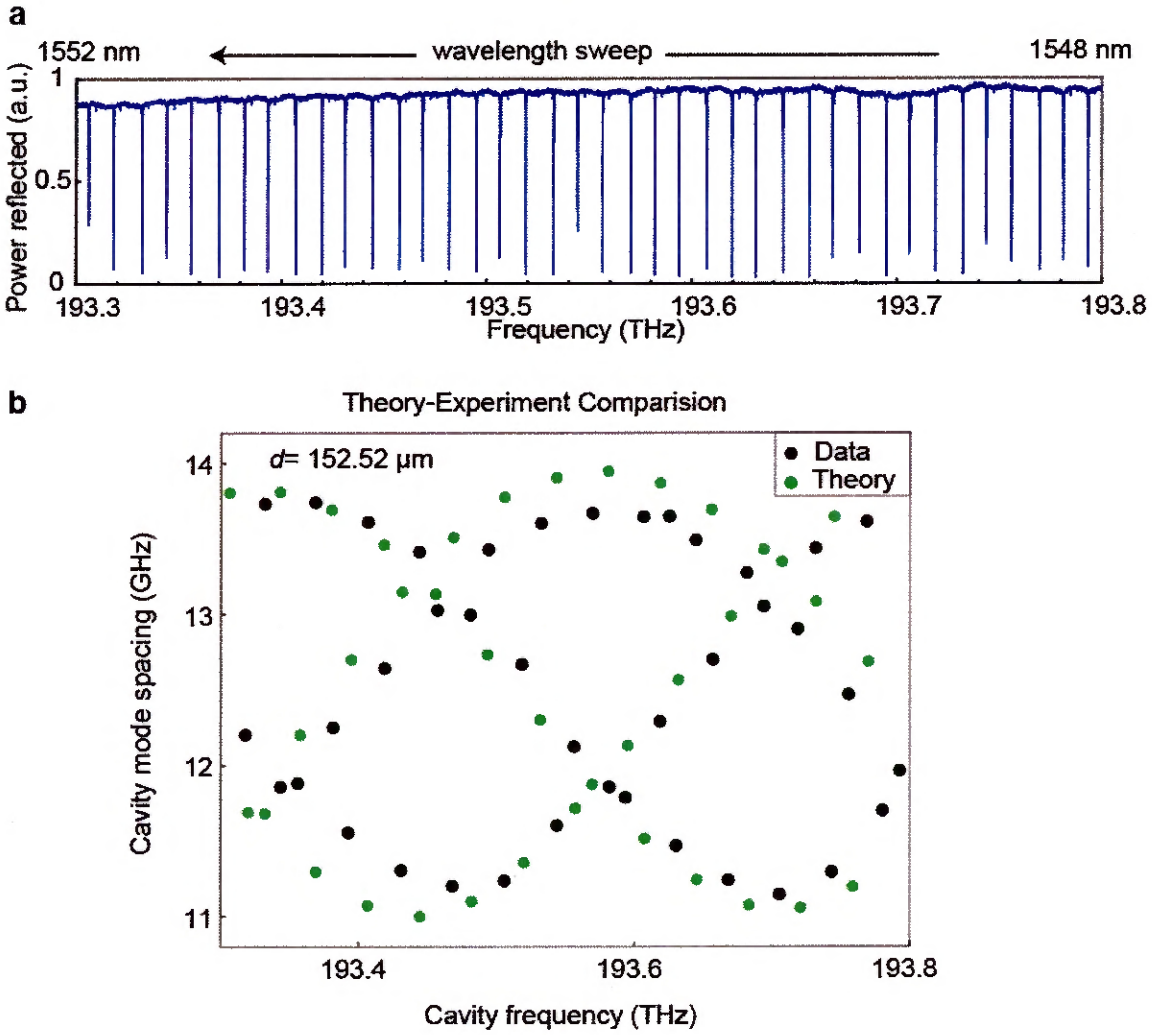

Figure 5.7: **Measured reflection spectrum at cryogenic temperatures.** (a) Reflection spectrum obtained by sweeping the laser from 1548 to 1552 nm, revealed narrow optical resonances corresponding to longitudinal cavity modes. (b) The observed undulation in the FSR as a function of the cavity frequency (or mode number j) matches well with the theoretically predicted values. Adapted from Ref. [111].

5.3.1 Hamiltonian of the Electromagnetic Fields

We consider the case of an electromagnetic field having a single polarization ($\hat{x}-$direction) that is subjected to the boundary conditions defined by the two mirrors. For simplicity, we assume that the electric field vanishes at the location of the left mirror ($z = 0$) and the right mirror ($z = L_{\text{opt}}$). Hence, when we expand the electric field into the normal modes (standing waves) of the optical cavity

$$E_x(z,t) = \sum_j E_j \sin(k_j z)(\hat{a}_j(t) + \hat{a}_j^\dagger(t)), \tag{5.5}$$

where $\hat{a}_j$ is the normal mode amplitude, $k_j = \omega_j/c$, with j = 1, 2, 3, ..., and the zero-point amplitude of the electric field is

$$E_j = \sqrt{\frac{\hbar\omega_j}{\epsilon_0 \epsilon_r^{\text{eff}} A_{\text{opt}} L_{\text{opt}}}}, \tag{5.6}$$

where ω_j is the frequency of the normal mode, ϵ_r^{eff} is the effective relative permittivity of the optical cavity, A_{opt} is the effective transverse area of the optical mode, and L_{opt} is the optical cavity length. The zero-point fluctuation of the electric field was obtained knowing that the total electromagnetic energy per mode for the ground state is $\hbar\omega_j/2$. Starting with the Hamiltonian for the electromagnetic fields

$$\hat{H}^{\text{opt}} = \frac{1}{2}\int_V dV\ (\epsilon E^2 + \mu_o H^2) \tag{5.7}$$

and substituting the normal mode expansions for the electromagnetic fields, we obtain the quantized version of the electromagnetic Hamiltonian given by

$$\hat{H}^{\text{opt}} = \sum_j \hbar\omega_j \left(\hat{a}_j^\dagger \hat{a}_j + \frac{1}{2}\right). \tag{5.8}$$

Note that the mode amplitude operators satisfy the commutation relations $[\hat{a}_j, \hat{a}_{j'}^\dagger] = \delta_{j,j'}$ and $[\hat{a}_j, \hat{a}_j'] = [\hat{a}_j^\dagger, \hat{a}_{j'}^\dagger] = 0$.

5.3.2 Hamiltonian of the Acoustic Fields

For the quantization of acoustic fields, we consider a longitudinally polarized ($\hat{z}$-direction) acoustic field subject to free boundary conditions at the surfaces of the crystal, which forms an acoustic Fabry-Pérot cavity. As a starting point, we assume that the separation between the mirror and the crystal face (d) is vanishingly small (i.e., the crystal is flush with the mirror). We expand the acoustic displacement field into the normal modes (standing waves) of the Fabry-Pérot acoustic cavity

$$u_z(z,t) = \sum_m U_m \cos(q_m z)(\hat{b}_m(t) + \hat{b}_m^\dagger(t)), \tag{5.9}$$

where $\hat{b}_m$ is the normal mode amplitude, $q_m = m\pi/L_{ac}$, with $m = 1, 2, 3, \ldots$, and the zero-point amplitude of the acoustic displacement field

$$U_m = \sqrt{\frac{\hbar}{\rho A_{\mathrm{ac}} L_{\mathrm{ac}} \Omega_m}}. \tag{5.10}$$

Here Ω_m is the frequency of the acoustic mode, ρ is the density of the medium, A_{ac} is the effective transverse area of the acoustic mode, and L_{ac} is the thickness of the acoustic Fabry-Pérot cavity. The zero-point fluctuation of the acoustic field was calculated knowing that the total acoustic energy (kinetic plus potential) per mode for the ground state is $\hbar\Omega_m/2$. We start with the acoustic Hamiltonian

$$H^{\mathrm{ph}} = \frac{1}{2}\int_V dV \left(\rho \dot{u}^2 + C\left(\frac{\partial u}{\partial z}\right)^2\right), \tag{5.11}$$

where $C = v_{ac}^2 \rho$ is the elastic coefficient and substitute the normal mode expansion to obtain the quantized version of the acoustic field

$$\hat{H}^{\text{ph}} = \sum_m \hbar \Omega_m \left(\hat{b}_m^\dagger \hat{b}_m + \frac{1}{2} \right). \tag{5.12}$$

Note that the mode amplitude operators satisfy the commutation relations $[\hat{b}_m, \hat{b}_{m'}^\dagger] = \delta_{m,m'}$ and $[\hat{b}_m, \hat{b}'_m] = [\hat{b}_m^\dagger, \hat{b}_{m'}^\dagger] = 0$.

5.3.3 Interaction Hamiltonian

To calculate the interaction Hamiltonian, we consider the interaction energy $H^{\text{int}} = -\int_V dV \sigma \cdot S$ for electrostriction mediated coupling between light and sound fields, where σ is the electrostrictively induced stress and S is the phonon mode's strain field. For the simple case of coupling between longitudinal acoustic waves propagating in the $\hat{z}$-direction with linearly polarized electromagnetic field in the $\hat{x}$-direction, the dominant stress component is given by $\sigma \equiv \sigma_z = -(1/2)\epsilon_0 \epsilon_r^2 p_{13} E_x(z)^2$ [49], where ϵ_0 (ϵ_r) is the vacuum (relative) permittivity of the optical cavity, p_{13} is the relevant photoelastic constant of the crystalline medium, and E_x is the electric field of the optical cavity mode. Similarly, the relevant strain component $S \equiv S_z = \partial u_z / \partial z$, where u_z is the displacement field of the phonon mode. So, the interaction Hamiltonian for the optomechanical coupling is given by

$$\hat{H}^{\text{int}} = \frac{1}{2} \int_V dV \ \epsilon_0 \epsilon_r^2 p_{13} E_x^2 \frac{\partial u}{\partial z}. \tag{5.13}$$

We now substitute the normal mode expansions for the electric field and the acoustic displacement field from eqn. (5.5) and eqn. (5.9) into this interaction Hamiltonian

and using the rotating wave approximation to obtain

$$\hat{H}^{\text{int}} = -\sum_{j,j',m} \int dV\ \epsilon_0 \epsilon_r^2 p_{13} q_m U_m E_j E_{j'}\ \sin(k_j z)\sin(k_{j'} z)\sin(q_m z)\ (\hat{a}_j^\dagger \hat{a}_{j'} \hat{b}_m + \hat{a}_j \hat{a}_{j'}^\dagger \hat{b}_m^\dagger). \tag{5.14}$$

The term $\hat{a}_j^\dagger \hat{a}_{j'} \hat{b}_m$ in the interaction Hamiltonian represents the annihilation of an optical mode at frequency $\omega_{j'}$ and a phonon mode at frequency Ω_m to create a photon mode at higher frequency $\omega_j = \omega_{j'} + \Omega_m$ (also called the anti-Stokes process). The other term $\hat{a}_j \hat{a}_{j'}^\dagger \hat{b}_m^\dagger$ represents the conjugate process, whereby a photon at lower frequency $\omega_{j'}$ and a phonon at frequency Ω_m are created from the annihilation of photon at ω_j (Stokes process). Here, g_0^m is the single-photon coupling rate, which we discuss in greater detail in the next section.

5.3.4 Single-Photon Coupling Rate

In a single mode optomechanical system, the single-photon coupling rate is a measure of the optical frequency shift due to the single excitation in the mechanical mode (or single phonon). In our multimode optomechanical system, this single-photon coupling rate describes the change in the frequency spacing between the two optical modes resulting from the dynamical modulation of the refractive index of the crystal produced by a single excitation of the mechanical mode.

Expressing the interaction Hamiltonian in Eqn. (5.14) as $-\sum_m \hbar g_0^m (a_j^\dagger a_{j'} b_m + a_j a_{j'}^\dagger b_m^\dagger)$, we see that the single-photon coupling rate g_0^m for inter-modal optomechanical coupling between two optical modes (ω_j, k_j) and (ω_{j+1}, k_{j+1}) mediated by a phonon mode (Ω_m, q_m) is given by

$$g_0^m = \frac{1}{\hbar} \int dV\ \epsilon_0 \epsilon_r^2 p_{13} q_m U_m E_{j+1} E_j\ \sin(k_{j+1} z)\sin(k_j z)\sin(q_m z). \tag{5.15}$$

From this equation, we see that g_0^m depends on the spatial overlap of the optical and acoustic fields inside the crystal. Using a trigonometric identity,

$$\sin(\mathrm{A}) \cdot \sin(\mathrm{B}) \cdot \sin(\mathrm{C}) = 1/4(\text{-}\sin(\mathrm{A\text{-}B\text{-}C})+\sin(\mathrm{A+B\text{-}C})+\sin(\mathrm{A\text{-}B+C})\text{-}\sin(\mathrm{A+B+C})), \tag{5.16}$$

we see that non-zero spatial overlap and, hence, a non-zero coupling rate occurs when the phase-matching requirement ($q_m = k'_{j+1} + k'_j$) is satisfied. Note that the finite integral volume in Eqn. (5.15) means that this phase-matching condition is relaxed and more than one-phonon modes near the Brillouin frequency yield non-zero optomechanical coupling rate.

Note that, up until this point, we assumed that the crystal face is flush with the planar mirror (i.e. $d = 0$). However, the position of the crystal inside the optical cavity can affect the overlap integral of the acoustic and optical fields (Fig. 5.8**a**). For example, the nodes of the strain profile could line up with the anti-nodes of the optical forcing function, resulting in zero optomechanical coupling.

If we now account for the separation (d) between the crystal and the mirror and substitute the zero-point amplitudes of the electric and acoustic fields we obtain

$$g_0^m = A\epsilon_0\epsilon_r^2 p_{13} q_m \sqrt{\frac{\hbar}{\rho A L_{\mathrm{ac}} \Omega_m}} \frac{\sqrt{\omega_j \omega_{j+1}}}{\epsilon_0 \epsilon_r^{\mathrm{eff}} A L_{\mathrm{opt}}} \times \int_d^{d+L_{\mathrm{ac}}} dz \, \sin\left(k'_{j+1}\left(z - d + \frac{d}{n}\right)\right) \sin\left(k'_j\left(z - d + \frac{d}{n}\right)\right) \sin\left(q_m(z-d)\right). \tag{5.17}$$

The phase factors for the sine functions come from the appropriate boundary conditions on the electric and acoustic fields at the crystal and mirror surfaces. For simplicity we have assumed $A_{\mathrm{ac}} = A_{\mathrm{opt}} \equiv A$. Here, $k'_j = nk_j$ denotes the wavevector of the optical modes inside the crystal.

From this equation we see that the maximum coupling rate to a single acoustic

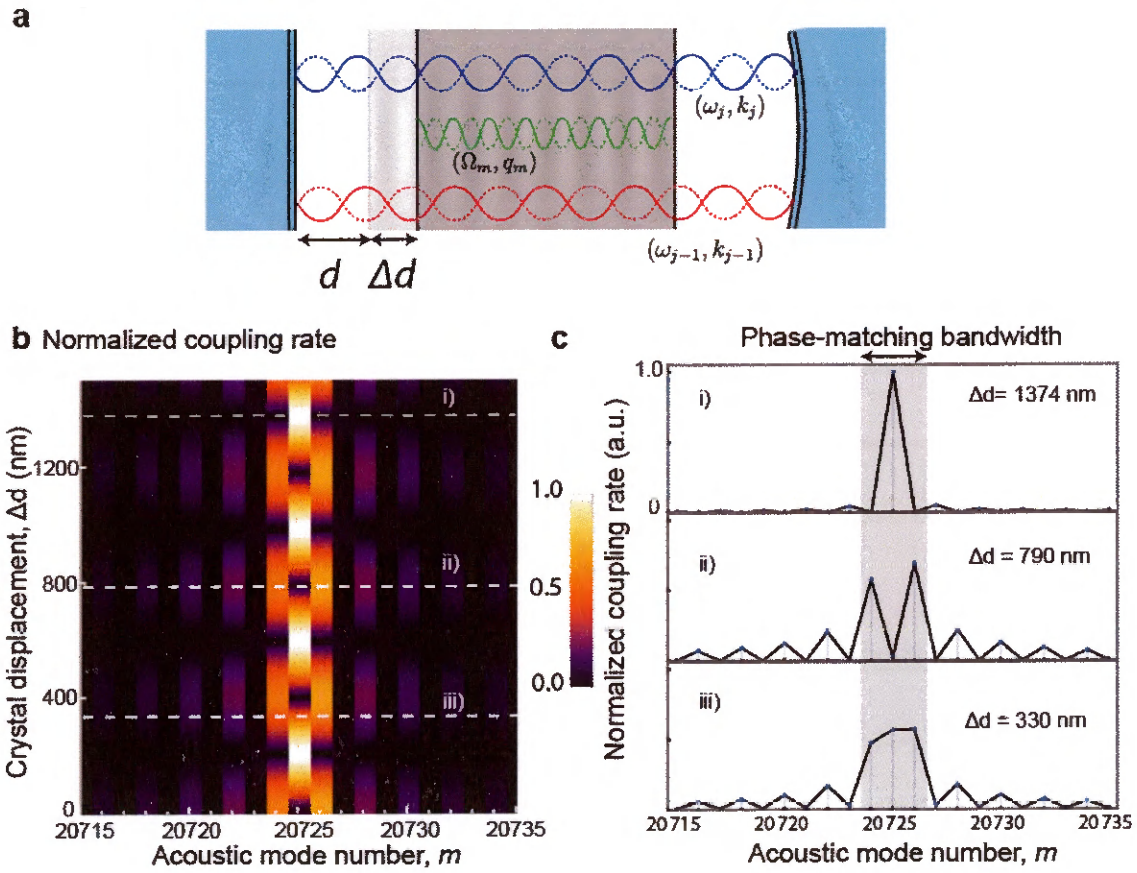

Figure 5.8: **Variation in the coupling rate as a function of the crystal position** (d). A schematic showing the displacement of the bulk acoustic resonator inside the optical cavity. (**b**) Optomechanical coupling occurs to a small set of phonon modes (indexed by longitudinal mode number m) near the Brillouin frequency. For an arbitrary crystal displacement, we still have appreciable coupling at least one phonon mode. Coupling to an individual phonon mode (say $m = 20725$) is periodic as a function. (**c**) Line cuts to this plot (in **b**) shows how it is possible to engineer coupling to primarily one (inset i), two (inset ii) or three phonon modes (inset iii) by changing the crystal displacement. Adapted from Ref. [111].

mode occurs when the crystal positions is such that the nodes (anti-nodes) of the strain profile line up with the nodes (anti-nodes) of the optical beat tone. This maximum coupling rate can be determined from Eqn. (5.17) and is given by

$$\tilde{g}_0 \approx \frac{\omega_j^2 n^5 p_{13}}{2cn_{\text{eff}}^2}\sqrt{\frac{\hbar}{\rho A L_{\text{ac}}\Omega_m}}\frac{L_{\text{ac}}}{L_{\text{opt}}}, \tag{5.18}$$

where n_{eff} is the effective refractive index of the optical mode, and we assumed $\omega_{j+1} \simeq \omega_j$, so that $q_m = k'_{j+1} + k'_j \approx 2n\omega_j/c$. Note that the simplified derivation presented above, we did not account for the variation in the transverse mode area ($\sim$ 30 %) of the Gaussian optical and acoustic beams. To calculate the coupling rate within our actual system, we perform acousto-optical overlap integral in Eq. (5.15), taking into account the actual mode profiles of the optical and acoustic fields (see Fig. 5.9). This calculation for optical modes near 1551.0335 nm that are separated by $\Omega_m = 2\pi \times 12.645$ GHz, yields a maximum coupling rate $g_0^m/2\pi \simeq 24$ Hz in our system. Note that we used these experimentally relevant geometric and material parameters for the calculation of g_0^m: $p_{13} = 0.27$, $n = 1.55$, $\rho = 2648$ kg/m^3, $v_a = 6327$ m/s, $L_{\text{ac}} = 5.19$ mm, and $L_{\text{opt}} = 9.13$ mm.

A density plot in Fig. 5.8**b** reveals how optomechanical coupling rate changes with acoustic mode number and the crystal displacement. We see that appreciable optomechanical coupling occurs to a few modes near the Brillouin frequency ($\Omega_m = m \times v_a/2L \approx 12.645$GHz). The bandwidth of coupling ($\Delta\nu_B = 1.76v_a/2L_{\text{ac}}$) is $\sim$ 1.1 MHz in our system. For an individual phonon mode (say m= 20725), coupling rate is periodic in the crystal displacement (see Fig. 5.8**b**) and as explained before it can be zero at certain crystal positions (see Fig. 5.8**b**.ii). Fortunately, for any arbitrary crystal position, we still obtain an appreciable optomechanical coupling to least one phonon mode. This is a consequence of the finite length of the crystal, which relaxes the phase-matching condition. Therefore, as long as the linewidth of

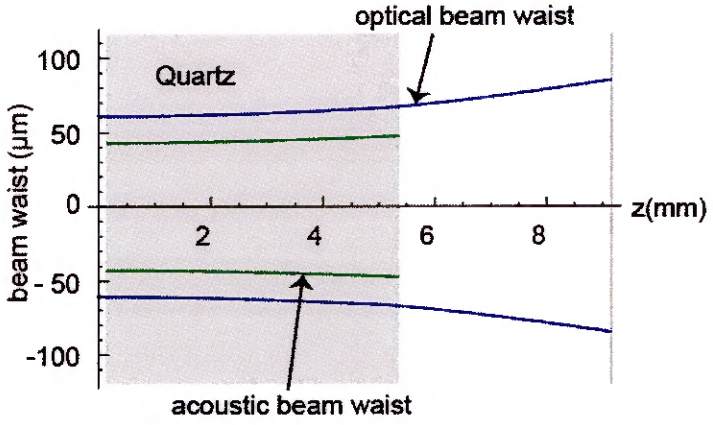

Figure 5.9: **Optical and acoustic mode profiles.** We use ABCD matrix for Gaussian beam propagation to determine optical mode waist inside the optical cavity. Since, acoustic modes in a planar crystal are not confined laterally (or in the transverse direction), we assume that the transverse mode profile is simply given by the profile of the forcing function, which is proportional to the square of the optical field. Adapted from Ref. [111].

the optical mode ($\kappa/2\pi$) is greater than the phase-matching bandwidth ($\Delta\nu_B$), we observe appreciable optomechanical coupling to at least one phonon mode irrespective of the crystal position.

Changing the position of the crystal inside the cavity offers one approach to tailoring the coupling rate to one or more phonon modes (Fig. 5.8c). Alternatively, we can change acousto-optic overlaps by changing the wavevector of the optical fields by moving to a different pair of optical resonances having frequency difference matching the Brillouin frequency. Initially, we chose this approach as it avoids the experimental complexity of adding a piezo-actuator in our optomechanical system. However, piezo-actuation would provide a more controllable way to vary the coupling strength and we are currently in the process of upgrading our optomechanical system to allow such in situ control.

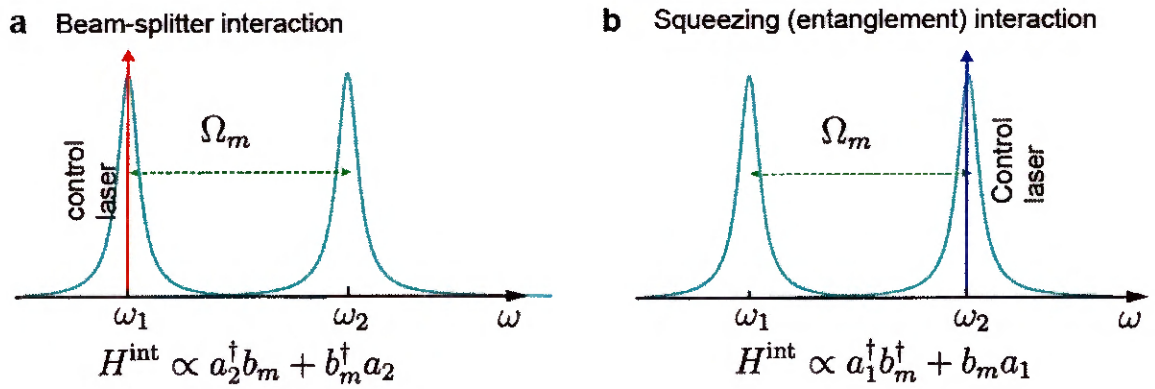

Figure 5.10: **Bilinear interaction Hamiltonian** (a-b) An external control laser which is on resonance with the lower (higher) frequency optical mode produces a "beam-splitter" ("two-mode squeezing") interaction within our multimode system. Since the laser is directly on resonance with a cavity mode, we can dramatically enhance the coupling rates for such interactions.

5.4 Optomechanical coupling in the linearized regime

In the earlier section, we saw that Brillouin interactions (i.e. $H^{\text{int}} \propto g_o^m(a_{j+1}^\dagger a_j b_m +$ H.c.)) yield intrinsically nonlinear coupling between optical and acoustic fields. This nonlinearity plays a crucial role in a variety of experiments in the classical regime such as parametric instability of a mechanical mode. However, to exploit this nonlinearity for applications in the quantum regime such as deterministic preparation of non-classical mechanical states, we need to achieve single-photon coupling strength (g_0^m) that is larger than the dissipation rates of both the optical (κ) and acoustic modes (Γ_{m}). It would be very difficult to access this regime in our optomechanical system since $g_0^m \ll (\kappa, \Gamma_{\text{m}})$. Nevertheless, by using a external laser drive, we can transform our intrinsically nonlinear coupling into a linearized interaction and use it to dramatically enhanced optomechanical interaction strength. Despite sacrificing intrinsic nonlinearity to obtain large coupling strengths, we can use single-photon sources or single-photon detection and post-selection to add nonlinearity in our system.

Next, we describe the linearized Hamiltonian of our system in presence of an external laser drive. Let's consider the case when the laser field is on resonance with

the lower frequency optical mode (ω_1) as seen in Fig. 5.10 **a**. The total Hamiltonian of our system in presence of the external laser drive is given by

$$\hat{H} = \hbar\omega_1 a_1^\dagger a_1 + \hbar\omega_2 a_2^\dagger a_2 + \hbar\Omega_m b_m^\dagger b_m - \hbar g_0^m (a_2^\dagger a_1 b_m + b_m^\dagger a_1^\dagger a_2) + \hat{H}_{\text{drive}}, \tag{5.19}$$

where the Hamiltonian for the drive field is given by $\hat{H}_{\text{drive}} = i\hbar\sqrt{\kappa_1^{\text{ext}}}\alpha_{\text{in}} a_1^\dagger e^{-i\omega_1 t} +$ H.c., κ_1^{ext} is the external coupling rate of the optical mode, and α_{in} is the input laser amplitude. The input laser field is normalized such that the input laser power $P = \hbar\omega_1 \langle\alpha_{\text{in}}^\dagger \alpha_{\text{in}}\rangle$. This external drive field causes resonant build-up of photons in the mode ω_1. To calculate this average coherent amplitude $\langle a_1\rangle$, we assume a strong control laser; within this undepleted pump approximation we assume that the dynamics of the mode at frequency ω_1 is not influenced by the optomechanical coupling (i.e. $g_0^m \to 0$). Then, we arrive at the following equation of motion from the Hamiltonian in Eqn. (5.19)

$$\dot{a}_1(t) = \left(-i\omega_1 - \frac{\kappa_1}{2}\right) a_1 + \sqrt{\kappa_1^{\text{ext}}}\alpha_{\text{in}} e^{-i\omega_1 t}, \tag{5.20}$$

where the optical dissipation rate $\kappa_1 = 2\kappa_1^{\text{ext}} + \kappa_1^0$, κ_1^{ext} is the loss rate at each cavity mirror and k_1^0 is the loss rate inside the cavity. Since we are focused on the classical average quantities, we have the noise term in writing down the above equation of motion. From eqn. (5.20), we obtain the following steady state solution for mode a_1

$$\langle a_1\rangle = \sqrt{N_1} e^{-i\omega_1 t} = \frac{2\sqrt{\kappa_1^{\text{ext}}}}{\kappa_1} |\alpha_{\text{in}}| e^{-i\omega_1 t}, \tag{5.21}$$

where N_1 is the average intracavity photon number for mode a_1.

In the undepleted pump regime, we substitute $\langle a_1\rangle$ in eqn. (5.19) to derive the following linearized Hamiltonian for the interaction between the optical mode a_2 and

the phonon mode b_m

$$H = \hbar\omega_2 a_2^\dagger a_2 + \hbar\Omega_m b_m^\dagger b_m - \hbar g_0^m \sqrt{N_1}(a_2^\dagger b_m e^{-i\omega_1 t} + b_m^\dagger a_2 e^{i\omega_1 t}).$$

By working in the rotating frame of $H_0 = \hbar\omega_1 a_2^\dagger a_2$ (i.e., $a_2(t) \to a_2(t)e^{-i\omega_1 t}$), we obtain an effective Hamiltonian

$$H_{\text{eff}} = \hbar\Delta a_2^\dagger a_2 + \hbar\Omega_m b_m^\dagger b_m - \hbar g_m(a_2^\dagger b_m + b_m^\dagger a_2) \tag{5.22}$$

where $\Delta = \omega_2 - \omega_1$ and $g_m = g_0^m\sqrt{N_1}$ is the cavity-enhanced coupling rate.

In this way, resonant driving of the lower frequency optical mode in our optomechanical system produces beam-splitter type interaction Hamiltonian given by $-\hbar g_m(a_2^\dagger b_m + b_m^\dagger a_2)$. Since $N_1 \propto |\alpha_{\text{in}}|^2$, g_m can be greatly enhanced by increasing the strength of the laser drive field. Time dependent control of $g_m(t)$, could then be used to perform deterministic state swaps between photons and phonons once we reach the optomechanical strong coupling regime. We will discuss this in greater detail in Chapter 6.

For the case when the external laser drive is on resonance with the higher frequency optical mode ω_2, we can follow an approach similar to the one outline above to derive the following effective optomechanical Hamiltonian

$$H_{\text{eff}} = -\hbar\Delta a_1^\dagger a_1 + \hbar\Omega_m b_m^\dagger b_m - \hbar g_m(a_1 b_m + b_m^\dagger a_1^\dagger). \tag{5.23}$$

Therefore, resonant driving of the higher-frequency optical mode produces two-mode squeezing interaction that can be used for parametric application of both the optical (a_1) and the acoustic mode (b_m). In addition, such interactions can be used to generate entanglement between light and mechanics and single-photon detection and postselection can be used to generate nonclassical mechanical states [144].

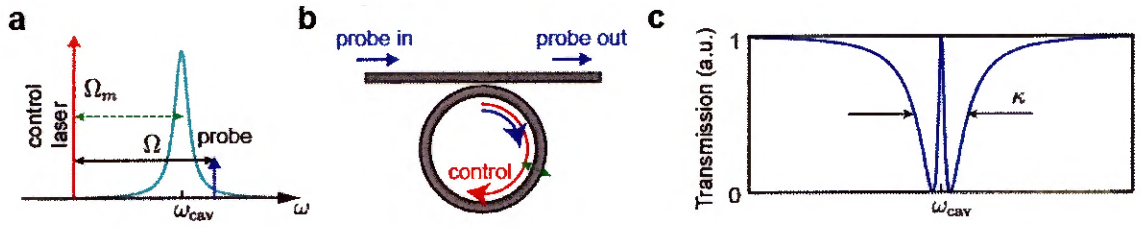

Figure 5.11: **Optomechanically induced transparency in a single-mode optomechanical system.** (a) Schematic showing a "control" laser that is red-detuned from an optical cavity mode by Ω_m. A weak laser then probes the transmission spectrum of the optical mode. (b) Within a ring resonator geometry, the probe light inside the cavity destructively interferes with the anti-Stokes light generated from optomechanical scattering. (c) As a result, the optical transmission spectrum develops a narrow transmission band at $\omega_{\rm cav}$.

5.5 Coherent Optomechanical response

To explore the optomechanical coupling in our system (i.e., to characterize g_m, κ, and Γ_m), we use a weak probe laser in addition to a strong control laser, which gives rise to two well-known coherent phenomena called Optomechnically Induced Amplification (OMIA) and Optomechanically Induced Transparency (OMIT) [157–159]. We outline a theoretical framework to understand such coherent phenomena in the next two sections.

5.5.1 Optomechanically Induced Transparency (OMIT)

In a conventional single mode optomechanical system, when a strong control laser is red-detuned from a cavity response, the cavity response for a weak probe develops a narrow transparency window (see Fig. 5.11). This phenomena occurs as a result of destructive interference between the intracavity probe field and the anti-Stokes field generated through the optomechanical interaction. In an optomechanical system consisting of a ring-resonator-type optical cavity, the transmission spectrum for the probe light in presence of a strong red-detuned control laser becomes non-zero in a narrow band around the optical resonance. Therefore, this phenomena is analogous to

electromechanically induced transparency, in which the optical absorption spectrum of a three-level atom develops a transparency dip due to interaction with coherent laser fields.

The destructive interference between intracavity probe field and the anti-Stokes light, which we refer to as OMIT, also occurs in our optomechanical system when the control laser is on-resonance with the lower-frequency optical mode ω_1. However, since we are using a Fabry-Perot-type optical cavity, the transmission spectrum for the probe light develops a narrow dip, which looks like absorption. Therefore, to avoid any confusion due to the naming convention, we just focus on the dynamics of the intracavity probe field.

To derive the dynamics of the intracavity probe field for a more general and experimentally relevant case, we assume that the optical mode spacing does not exactly match the phonon frequency ($\omega_2 - \omega_1 \approx \Omega_m$) and the control laser is also slightly detuned from the lower-frequency (ω_1) optical mode. The Hamiltonian of our optomechanical system that accounts for the external drive fields (i.e., the control laser and the probe laser) is given by

$$\begin{aligned} H = {} & \hbar\omega_1 a_1^\dagger a_1 + \hbar\omega_2 a_2^\dagger a_2 + \hbar\Omega_m b_m^\dagger b_m - \hbar g_0^m (a_2^\dagger a_1 b_m + b_m^\dagger a_1^\dagger a_2) \\ & + i\hbar\sqrt{\kappa_1^{\text{ext}}}\alpha_l (a_1^\dagger e^{-i\omega_l t} - a_1 e^{i\omega_l t}) + i\hbar\sqrt{\kappa_2^{\text{ext}}}\alpha_p (a_2^\dagger e^{-i\omega_p t} - a_2 e^{i\omega_p t}). \end{aligned} \tag{5.24}$$

Here, α_l (α_p) is the input control (probe) laser amplitude. Note that we normalize the incident optical power launched into the cavity such that $P_l = \hbar\omega_l \langle \alpha_l^\dagger \alpha_l \rangle$ and $P_p = \hbar\omega_l \langle \alpha_p^\dagger \alpha_p \rangle$. We assume a strong control laser and a weak probe; assuming undepleted pump approximation, we can derive the following steady state coherent amplitude for mode a_1

$$\langle a_1 \rangle = \sqrt{N_1} e^{-i\omega_l t} = \left| \frac{\sqrt{\kappa_1^{\text{ext}}}\alpha_l}{i\Delta_1 + \kappa_1/2} \right| e^{-i\omega_l t}, \tag{5.25}$$

where N_1 is the control laser driven intracavity photon number for mode a_1, and $\Delta_1 = \omega_1 - \omega_l$. (see Fig. 5.12 **a**). In the undepleted pump regime, we substitute $\langle a_1 \rangle$ in eqn. (5.19) to derive the following linearized Hamiltonian for the interaction between the optical mode a_2 and the phonon mode b_m

$$H = \hbar\omega_2 a_2^\dagger a_2 + \hbar\Omega_m b_m^\dagger b_m - \hbar g_0^m \sqrt{N_1}(a_2^\dagger b_m e^{-i\omega_l t} + b_m^\dagger a_2 e^{i\omega_l t}) + i\hbar\sqrt{\kappa_2^{\text{ext}}}\alpha_p(a_2^\dagger e^{-i\omega_p t} - a_2 e^{i\omega_p t}). \tag{5.26}$$

From this Hamiltonian, by rotating in the frame of $H_0 = \hbar(\omega_p - \omega_l)b_m^\dagger b_m + \hbar\omega_p a_2^\dagger a_2$ (i.e. $a_2(t) \rightarrow a_2(t)e^{-i\omega_p t}$ and $b_m(t) \rightarrow b_m(t)e^{-i(\omega_l - \omega_p)t}$), we obtain an effective Hamiltonian

$$H_{\text{eff}} = -\hbar\delta b_m^\dagger b_m - \hbar(\delta + \Delta_2)a_2^\dagger a_2 - \hbar g_m(a_2^\dagger b_m + b_m^\dagger a_2) + i\hbar\sqrt{\kappa_2^{\text{ext}}}\alpha_p(a_2^\dagger - a_2), \tag{5.27}$$

where $\delta = \Omega - \Omega_m = \omega_p - \omega_l - \Omega_a$, and $\Delta_2 = \Omega_a + \omega_l - \omega_2$, and the cavity field-enhanced coupling rate $g_m = g_0^m\sqrt{N_1}$. The Heisenberg equations of motions derived from this Hamiltonian,

$$\dot{a}_2(t) = \left(i(\delta + \Delta_2) - \frac{\kappa_2}{2}\right)a_2 + ig_m b_m + \sqrt{\kappa_2^{\text{ext}}}\alpha_p, \tag{5.28}$$

$$\dot{b}_m(t) = \left(i\delta - \frac{\Gamma_m}{2}\right)b + ig_m a_2, \tag{5.29}$$

can be used to derive steady state values for the phonon and photon numbers

$$b_m = \frac{-ig_m}{\left(i\delta - \frac{\Gamma_m}{2}\right)}a_2, \tag{5.30}$$

$$a_2 = \frac{-\sqrt{\kappa_2^{\text{ext}}}\alpha_p}{i(\delta + \Delta_2) - \frac{\kappa_2}{2} + \frac{g_m^2}{i\delta - \Gamma_m/2}}. \tag{5.31}$$

Once we know the intracavity photon number for mode a_2, we can use input-output formalism for a symmetric Fabry-Pérot cavity, assuming laser fields incident only on

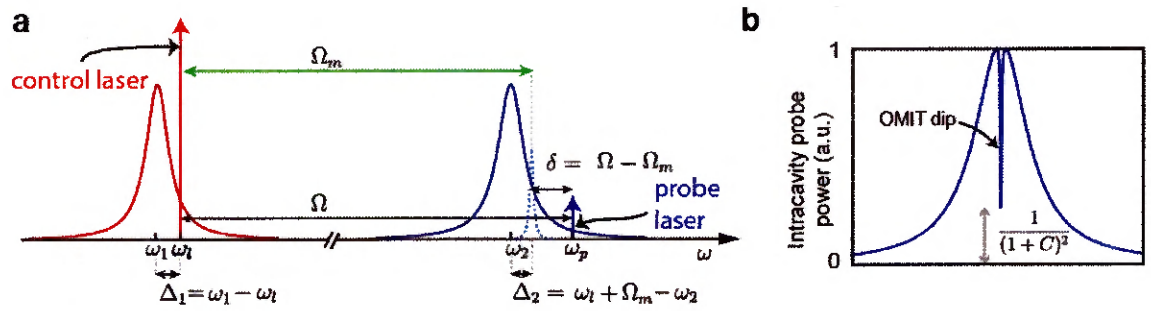

Figure 5.12: **Optomechanically induced transparency in a multimode optomechanical system.** (a) A strong red-detuned control laser at frequency ω_l is on resonance with a lower-frequency optical mode at ω_1 while a weak probe at ω_p is swept near the higher frequency optical mode at ω_2. (b) A sharp dip on the transmission spectrum as a result of destructive interference between the intracavity probe field and the anti-Stokes field generated through the optomechanical interaction. Adapted from Ref. [111].

one of the mirrors, to obtain the transmitted light field

$$a_{2,\text{out}} = \sqrt{\kappa_2^{\text{ext}}} a_2 = -\frac{\kappa_2^{\text{ext}} \alpha_p}{i(\delta + \Delta_2) - \frac{\kappa_2}{2} + \frac{g_m^2}{i\delta - \Gamma_m/2}}. \tag{5.32}$$

In experiments, we use heterodyne detection of the transmitted probe light to measure the intracavity photon number. The power spectrum of this heterodyne signal at the detector is given by

$$P_d(\delta) \propto \langle a_{2,\text{out}}^\dagger a_{2,\text{out}} \rangle = \left| \frac{\kappa_2^{\text{ext}}}{i(\delta + \Delta_2) - \frac{\kappa_2}{2} + \frac{g_m^2}{i\delta - \Gamma_m/2}} \right|^2. \tag{5.33}$$

To highlight the salient features of this power spectrum, we consider the simpler case when the frequency difference between the optical modes is exactly equal to the Brillouin frequency ($\omega_2 - \omega_1 = \Omega_m$) and the control laser is directly on resonance with the optical cavity mode a_1 ($\Delta_2 = 0$), we can use eqn. (5.31) to derive a simple expression for the intracavity field

$$a_2 = \frac{-\sqrt{\kappa_2^{\text{ext}}} \alpha_p}{i\delta - \frac{\kappa_2}{2} + \frac{g_m^2}{i\delta - \Gamma_m/2}}. \tag{5.34}$$

Since $\Gamma_m \ll \kappa_2$ in our experiments, we get the following spectrum for the intracavity anti-Stokes (a_2) near the phonon resonance (i.e., $\Omega \approx \Omega_m$)

$$a_2(\delta) \simeq \frac{2(i\delta - \Gamma_m/2)\sqrt{k_2^{\text{ext}}}/\kappa_2\alpha_p}{i\delta - \frac{\Gamma_m}{2}(1+C)},$$
$$a_2(\Omega) = \frac{2(i(\Omega-\Omega_m) - \Gamma_m/2)\sqrt{k_2^{\text{ext}}}/\kappa_2\alpha_p}{i(\Omega-\Omega_m) - \frac{\Gamma_{\text{eff}}}{2}}, \tag{5.35}$$

where $C = 4|g_0^m|^2 N_1/(\kappa_2\Gamma_m)$ is the cooperativity, and $\Gamma_{\text{eff}} = \Gamma_m(1+C)$ is effective acoustic dissipation rate.

Without optomechanical coupling (i.e. $g_m = 0$), we see that the peak intracavity field is given by

$$a_2'(\Omega_m) = 2\frac{\sqrt{\kappa_2^{\text{ext}}}}{\kappa_2}\alpha_p. \tag{5.36}$$

However, with optomechanical coupling the intracavity field on resonance is given by

$$a_2(\Omega_m) = 2\frac{\sqrt{\kappa_2^{\text{ext}}}}{\kappa_2(1+C)}\alpha_p \tag{5.37}$$

Therefore, the relative dip in the OMIT spectrum, which is given by

$$\left|\frac{a_2(\Omega_m)}{a_2'(\Omega_m)}\right|^2 = \frac{1}{(1+C)^2}, \tag{5.38}$$

can be used to directly measure the value of cooperativity (C) in our optomechanical system.

5.5.2 Optomechanically Induced Amplification (OMIA)

When a strong control laser is on-resonance with the higher-frequency optical mode ω_2, amplification of the intracavity probe field occurs as a result of constructive interference between the intracavity probe field and the Stokes field generated through

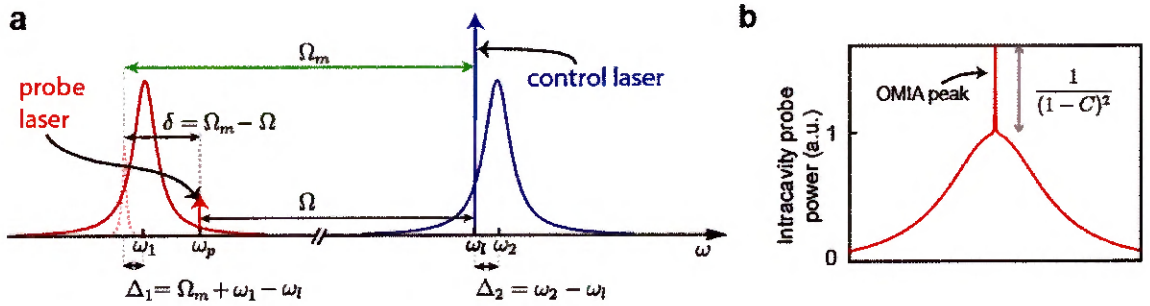

Figure 5.13: **Optomechanically induced amplification in a multimode optomechanical system.** (a) A strong blue-detuned control laser at frequency ω_l is on resonance with a higher-frequency optical mode at ω_2 while a weak probe at ω_p is swept near the lower frequency optical mode at ω_1. (b) A sharp peak on the transmission spectrum as a result of destructive interference between the intracavity probe field and the Stokes field generated through the optomechanical interaction. Adapted from Ref. [111].

the optomechanical process (see Fig. 5.13). Following an approach similar to the one outlined in Section 5.5.1, we can derive the following steady state amplitude for the optical mode a_1

$$a_{1,\mathrm{out}} = \sqrt{\kappa_1^{\mathrm{ext}}} a_1 = -\frac{\kappa_1^{\mathrm{ext}} \alpha_p}{i(\delta - \Delta_1) - \frac{\kappa_1}{2} + \frac{g_m^2}{-i\delta + \Gamma_m/2}}. \tag{5.39}$$

In experiments, we use heterodyne detection of the transmitted probe light to measure the intracavity photon number. The power spectrum of this heterodyne signal at the detector is given by

$$P_d(\delta) \propto \langle a_{1,\mathrm{out}}^\dagger a_{1,\mathrm{out}} \rangle = \left| \frac{\kappa_1^{\mathrm{ext}}}{i(\delta - \Delta_1) - \frac{\kappa_1}{2} + \frac{g_m^2}{-i\delta + \Gamma_m/2}} \right|^2. \tag{5.40}$$

If we assume that the frequency difference between the optical modes is exactly equal to the Brillouin frequency ($\omega_2 - \omega_1 = \Omega_m$) and the control laser is directly on resonance with the optical cavity mode a_2 ($\Delta_2 = \Delta_1 = 0$), we can derive a simple

expression for the intracavity field

$$a_1 = \frac{-\sqrt{\kappa_1^{\text{ext}}}\alpha_p}{i\delta - \frac{\kappa_1}{2} + \frac{g_m^2}{-i\delta+\Gamma_m/2}}. \tag{5.41}$$

Since $\Gamma_m \ll \kappa_1$ in our experiments, we get the following spectrum for the intracavity Stokes (a_1) near the phonon resonance (i.e., $\Omega \approx \Omega_m$)

$$\begin{aligned} a_1(\delta) &\simeq \frac{2(i\delta - \Gamma_m/2)\sqrt{k_1^{\text{ext}}}/\kappa_1\alpha_p}{i\delta - \frac{\Gamma_m}{2}(1-C)}, \\ a_1(\Omega) &= \frac{2(i(\Omega_m - \Omega) - \Gamma_m/2)\sqrt{k_1^{\text{ext}}}/\kappa_1\alpha_p}{i(\Omega_m - \Omega) - \frac{\Gamma_{\text{eff}}}{2}}, \end{aligned} \tag{5.42}$$

where $C = 4N_2|g_0^m|^2/(\kappa_1\Gamma_m)$ is the cooperativity, and $\Gamma_{\text{eff}} = \Gamma_m(1-C)$ is effective acoustic linewidth.

Without optomechanical coupling (i.e. $g_m = 0$), we see that the peak intracavity field is given by

$$a_1'(\Omega_m) = 2\frac{\sqrt{\kappa_1^{\text{ext}}}}{\kappa_1}\alpha_p. \tag{5.43}$$

However, with optomechanical coupling the intracavity field on resonance is given by

$$a_1(\Omega_m) = 2\frac{\sqrt{\kappa_1^{\text{ext}}}}{\kappa_1(1-C)}\alpha_p \tag{5.44}$$

Therefore, the relative peak height of the OMIA spectrum

$$\left|\frac{a_1(\Omega_m)}{a_1'(\Omega_m)}\right|^2 = \frac{1}{(1-C)^2}, \tag{5.45}$$

can be used to directly measure the value of cooperativity (C) in our optomechanical system.

5.6 Experimental Setup

In this section, we describe the experimental apparatus used to perform OMIT and OMIA measurements. Before, we can perform such measurements, we first need to identify a pair of optical modes having frequency spacing that matches the Brillouin frequency. Therefore, we begin by describing the experimental apparatus used to select an optical mode pair suitable for resonant Brillouin interaction.

5.6.1 Selecting an optical mode pair

Bulk acoustic modes at high-frequencies mediate resonant inter-modal coupling between two distinct optical modes when energy conservation and phase-matching requirements are both satisfied (for details see Ref. [111]). As discussed before, such requirements yield a characteristic 'Brillouin frequency' Ω_B. For optical wavelengths near 1.55 μm, we expect acoustic modes near $\Omega_B \simeq 2\pi \times 12.6$ GHz to mediate such phase-matched Brillouin interactions. Since the longitudinal sound velocity in quartz depends on temperature, Brillouin frequency changes (by about 200 MHz) as we cool our crystal from room temperature to cryogenic temperatures. This change is typically much larger than the optical cavity linewidth, which of the order of 1-100 MHz. However, stimulated Brillouin measurements using free-space laser beams (i.e. without the optical cavity) presented in Chapter 3 can be used to precisely determine Ω_B at cryogenic temperatures.

To identify a pair of optical resonances that match the Brillouin frequency, we measure the reflection spectrum of the optical cavity using a setup as shown in Fig. 5.14**a**. The output of a continuously-tunable laser (Agilent 8164B) is split into two arms. Light in one arm is coupled into the optical cavity through a fiber-optic collimator, a free-space polarizer, a mirror, and a lens. Light back-reflected from the optical cavity is collected using the same collimator, separated from the input light

using a fiber circulator, and measured using a photodetector (Thorlabs PDA10CS2). Light in the other arm is coupled to a fiber Fabry-Pérot (FFP) cavity formed by a length of single mode fiber that is imperfectly coupled at one end. The back-reflected light from this FFP cavity is separated from the input light using a fiber circulator and detected using a photodetector (PDA10CS2). Small ($\sim$ 4%) reflections at the fiber-air surfaces, results in a sinusoidal reflection spectrum. Agilent laser sweeps the wavelength continuously at a speed of 2 nm/sec. However, since the wavelength sweep is not perfectly linear as a function of time, we use the reflection spectrum of the FFP cavity as a frequency ruler for our swept measurements. This allows us to rapidly determine optical free-spectral ranges (FSR) ($\sim$ 13 GHz) with an accuracy of $\sim$ 1 MHz for wavelength scans over several nanometers.

From the reflection spectrum obtained by scanning the wavelength from 1556 to 1558 nm as seen in Fig. 5.14**b**, we determine the optical FSRs as a function of laser frequency. Such measurements, an example of which is shown in Fig. 5.14**c**, reveal a significant ($\sim$ 20%) modulation in the FSRs. Due to the modulation in the FSR, we can easily find several pairs of optical modes having FSRs close to the Brillouin frequency. We can also tune to cavity FSR by slightly changing the length of the invar holder that holds the mirrors and the bulk crystal using slight thermal tuning of the cryostat temperature. We use a proportional-integral-derivative (PID) controller (Cryocon 22C) to control the cryostats' temperature, permitting us to precisely match the optical FSR to the Brillouin frequency.

5.6.2 Probing the coherent response

To perform OMIT and OMIA measurements, we derive both the control and probe laser from the same tunable laser source (Purephotonics PPCL 300). The laser output at frequency ω_l is intensity modulated intensity-modulated at a variable frequency Ω using a microwave signal generator (Agilent E8257D), generating additional optical

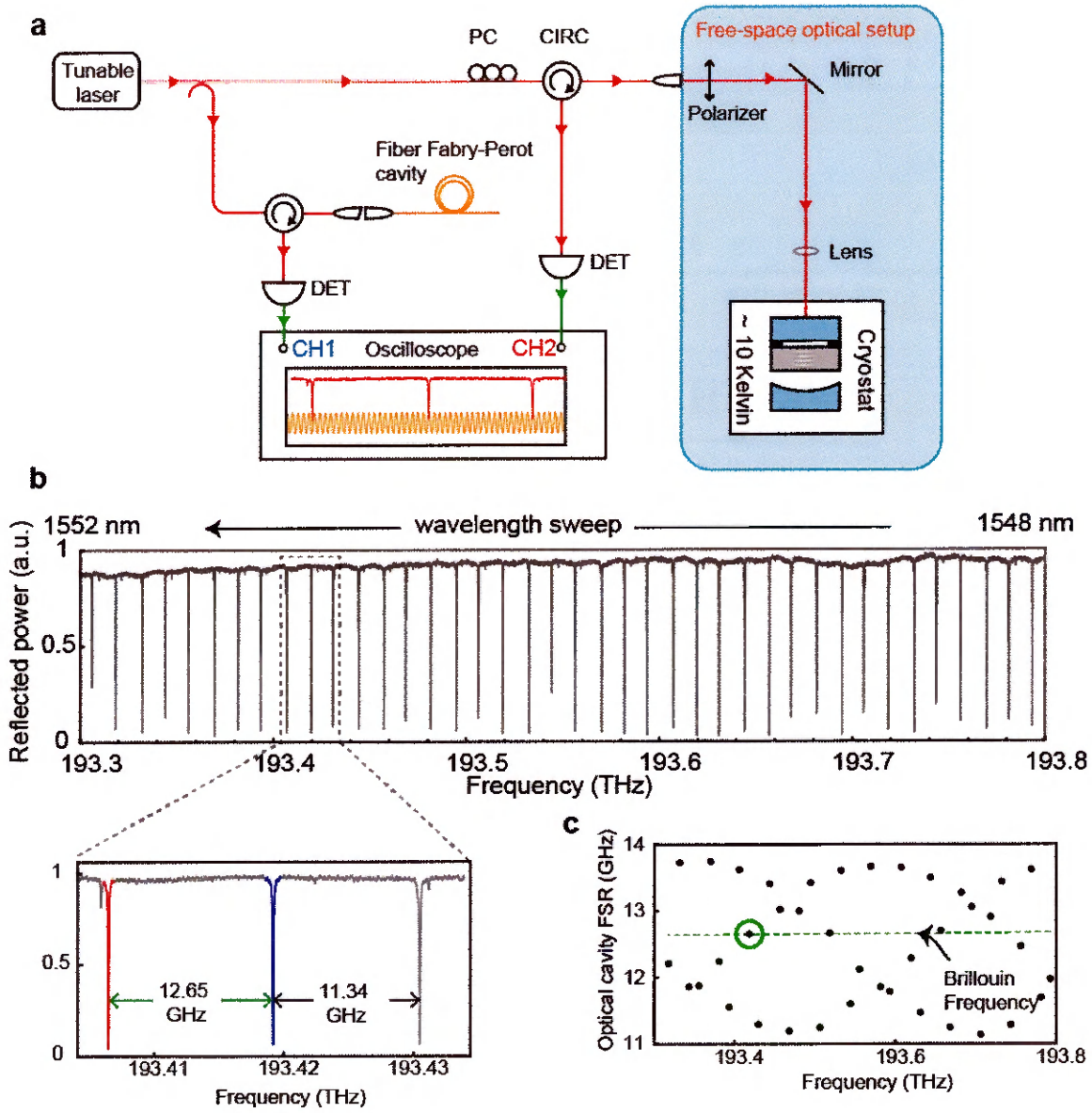

Figure 5.14: **Finding an optical mode pair to match Brillouin frequency.** (a) Schematic of the measurement apparatus used to find optical mode pairs to match Brillouin frequency. Light from a tunable laser source is continuously swept and the back-reflection power from the optical cavity (with bulk crystal) is measured as a function of time. Since this frequency sweep is not perfectly linear as a function of time, we use a separate Fiber Fabry-Pérot cavity to calibrate the frequency axis. (b) Measured back-reflected power obtained by sweeping the laser from 1548 to 1552 nm. High resolution spectra near 193.42 THz shows unequal free-spectral ranges due to the introduction of quartz crystal inside the optical cavity. (c) This variation in optical FSR as a frequency of optical mode frequency allows us to relatively easily find multiple pairs of optical resonances that match the Brillouin frequency. Adapted from Ref. [111].

side-bands at $\omega_l \pm \Omega$. For OMIT (OMIA) measurements, the tone at frequency ω_l serves as a strong control laser, whereas the weak tone at $\omega_l + \Omega$ ($\omega_l - \Omega$) serves as a probe laser. The other side-band at $\omega_l - \Omega$ ($\omega_l + \Omega$) is irrelevant during OMIT (OMIA) measurements, as it is not resonant with any optical cavity modes because of the unequal optical FSRs. the The intensity-modulated light is amplified using an erbium-doped fiber amplifier (EDFA) and coupled into the optical cavity using a fiber-optic polarization controller, a collimator, a free-space polarizer(or a polarizing beam splitter cube), a mirror, and a lens. The fiber-optic variable optical attenuator placed after the EDFA is used to vary control laser power incident on the cavity.

The free-space polarizer allows us to select polarization of the input light. We chose uniaxial z-cut quartz crystal so that the light propagating along the optical axis sees the same refractive index regardless of the transverse polarization of the optical beam. However, when we put the crystal inside the optical cavity and the invar holder, the optical cavity develops a very slight birefringence ($\Delta n \sim 10^{-7}$). This leads to optical mode splittings typically on the order of 10s of MHz. Therefore, the free-space polarizer allows us to selectively couple to one of these two orthogonal polarization modes.

The light back-reflected from the cavity is separated from the incident light using a circulator. This back-reflected light is monitored to ensure that the control laser is on resonance with an optical mode throughout the measurements. Light transmitted through the optical cavity is collected using a free-space lens, a mirror, and a fiber optic collimator. This light is then detected using a photoreceiver (Nortel Networks PP-10G) that is connected to a radio-frequency (RF) spectrum analyzer (Agilent N9030 A). The spectrum analyzer monitors the beat-note between the transmitted control laser and the transmitted probe laser by tracking the frequency (Ω) of the microwave signal generator (Agilent E8257D). Heterodyne detection of the probe light transmitted through the optical cavity provides a direct measurement of the

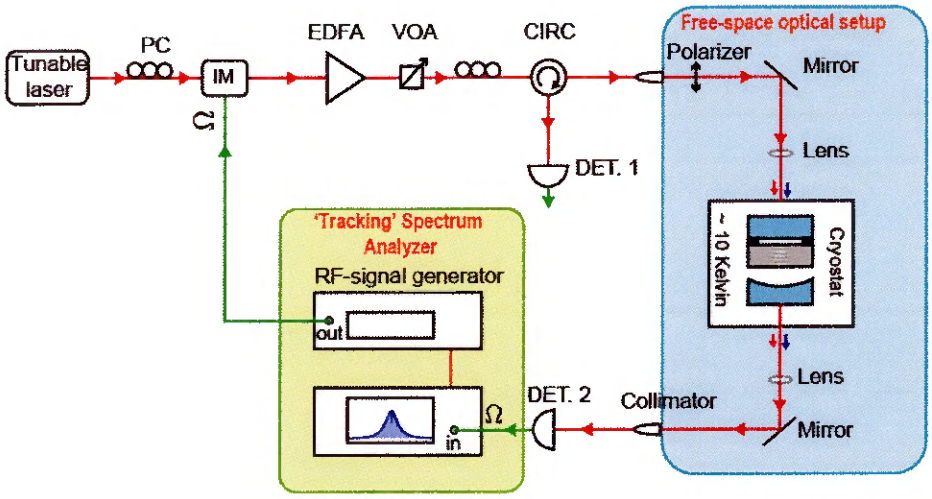

Figure 5.15: **Schematic of the experimental setup used to perform OMIT/OMIA measurements.** A strong control laser and a weak probe laser are synthesized from the same laser source using an intensity modulator. The control laser is on resonance with an appropriately chosen optical mode whereas the weak probe laser is swept through the other optical cavity mode. To determine the coherent-response of the intracavity probe field due to optomechanical interaction, we measure the transmitted probe light using heterodynme detection. Adapted from Ref. [111].

intracavity probe power.

5.7 Measurements of OMIA/OMIT

In this section, we use both OMIA and OMIT measurements to determine optical dissipation rate (κ), mechanical dissipation rates (Γ), and the single-photon coupling strength (g_0^m).

We begin by selecting a pair of optical modes (see Fig. 5.14 **b**) with mode spacing of 12.65 GHz, which matches the Brillouin frequency. For the OMIA (OMIT) measurements, the control laser is placed directly on resonance with the higher (lower) frequency optical mode at ω_2 (ω_1) and the weak probe laser at $\omega_l \mp \Omega$ is swept through the optical mode at ω_1 (ω_2) as seen in Fig. 5.15. Heterodyne detection of transmitted probe light revealed an optical cavity resonance of linewidth $\kappa_2 \simeq 2\pi \times 71$ MHz and

$\kappa_2 \simeq 2\pi \times 81$ MHz, consistent with the mirror's reflectivity of 98%. This modulation in the optical cavity linewidth occurs when a dielectric medium is introduced inside the optical cavity when the dielectric medium introduces additional losses (for instance, due to tilt of the crystal relative to the optical cavity axis) [160].

Near the center of the optical resonance, we find a narrow OMIA peak (OMIT dip) resulting from optomechanical coupling to a phonon mode at 12.645 GHz. From the derivation in Section 5.5, we know that the effective optomechanical Hamiltonian predicts a relative OMIA peak height (OMIT dip) of $1/(1 \mp C)^2$, when $\Omega = \Omega_m$. Moreover, the linewidth of this OMIA peak (OMIT dip) is given by $\Gamma_{\text{eff}} = (1 \mp C)\Gamma_m$. So, to determine g_0^m and Γ_m, we varied the control laser power and measured relative heights and the linewidths of the OMIA peaks and OMIT dips (see Fig. 5.16). As expected from theory, the measured values of cooperativity varied linearly with control laser power (P_{in}) as we varied it from 7.8 mW to 118 mW. Moreover, the Γ_{eff} for the OMIA peaks (OMIT dips) decreased (increased) linearly with P_{in}. Extrapolating the linear fit in Fig. 5.17**a** to zero input power (i.e. $C \to 0$), gives $\Gamma_m \simeq 2\pi \times 86$ kHz. This corresponds to an acoustic Q-factor of 1.5×10^5. Note that the acoustic Q-factor in this system is dominated by diffraction losses and is analogous to diffraction losses within an Fabry-Pérot optical cavity. Finally, using C, κ, and Γ_m, obtained from these measurements, along with intracavity photon number N_2 calculated by measuring the input control laser power P_{in} gives a values of $g_0^m \approx 2\pi \times 18$ Hz. This value of g_0^m is consistent with the theoretically predicted value of $2\pi \times 24$ Hz. Note that for the calculation of N_2 we assumed critical coupling and negligible internal losses.

It is also possible to configure our system, so the optomechanical coupling is mediated by more than one phonon modes. As explained in Section 5.3, we change the optical wavelength and select a different pair of optical resonances to tune coupling to one or more phonon modes. A typical OMIA spectrum in which the optomechan-

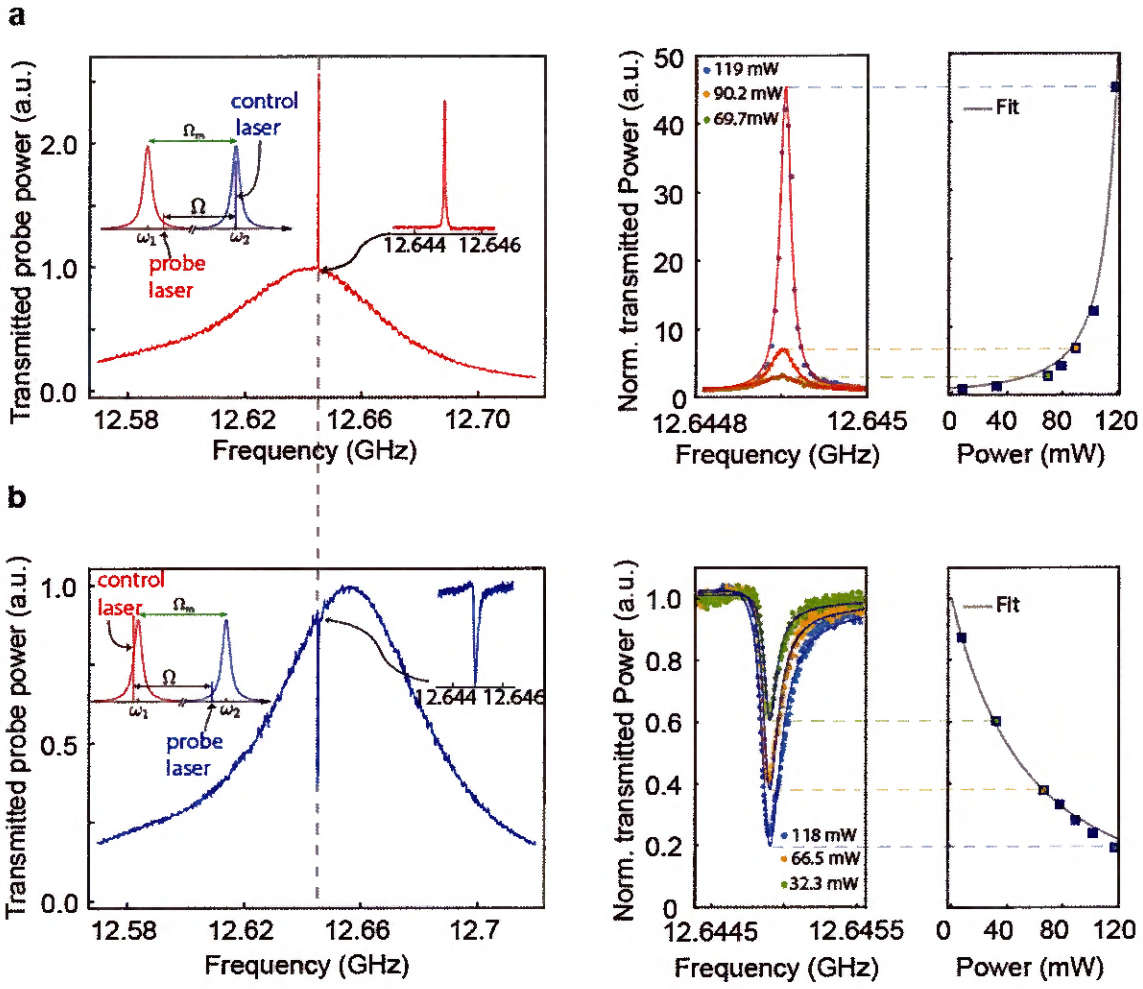

Figure 5.16: **OMIT/OMIA measurements.** (a)We engineer our system to couple primarily to a single phonon mode at 12.645 GHz and perform OMIA measurements. We measure OMIA peak heights as a function of input control laser power. We observe that the peak height increases non-linearly with control laser power. (**b**) We perform OMIT measurements by simply red-detuning the control laser. The OMIT dip is not exactly at the center of the optical resonance because the control laser is not exactly on resonance with the lower frequency optical mode. We observe that the OMIT dip decreases non-linearly with control laser power. Adapted from Ref. [111].

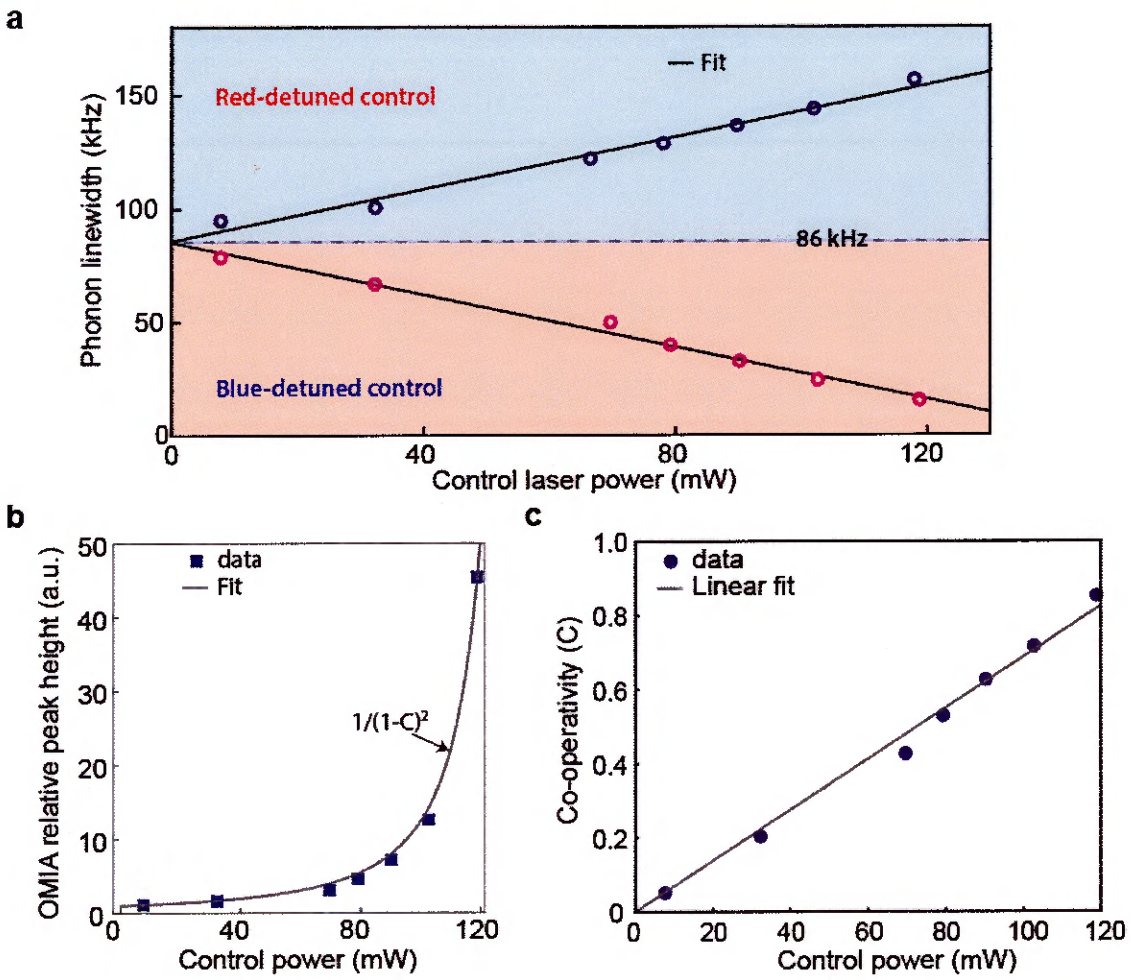

Figure 5.17: **Characterizing Γ_m and g_0^m.** (**a**) From the OMIT (OMIA) measurements in Fig. 5.16, we obtain effective acoustic linewidth as a function of control laser power by measuring the linewidth of the OMIT dip (OMIA peak). By extrapolating the effective phonon linewidths to zero input power, we obtain $\Gamma_m = 86$ kHz. (**b**) The relative peak height of the OMIA signal matches well with the theoretically predicted $1/(1-C)^2$ dependency. (**c**)We use the measured relative peak height of the OMIA signal to calculate cooperativity C as a function of input control laser power. Linear fit to this graph, along with the measured values of κ, Γ_m, and N_2, was used to determine $g_0^m \approx 2\pi \times$ 18 Hz. Adapted from Ref. [111].

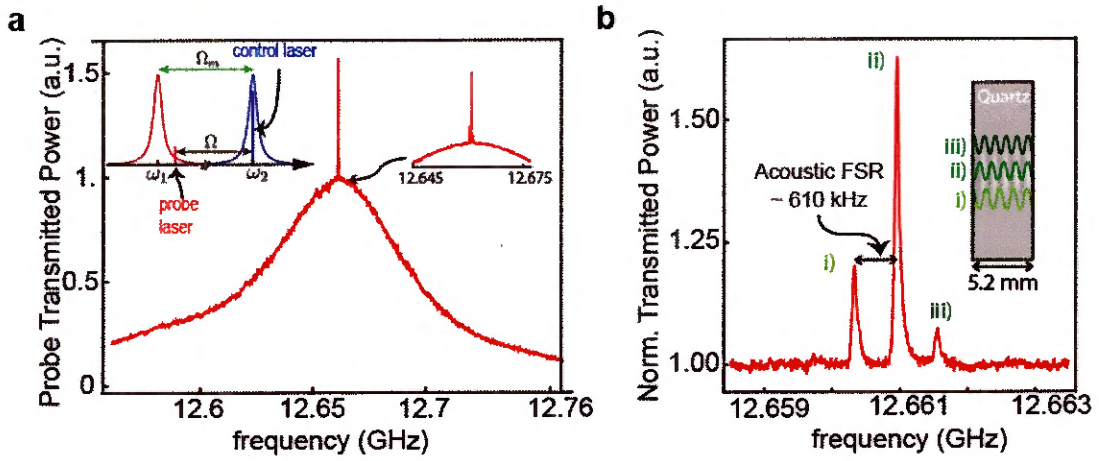

Figure 5.18: **Optomechanical coupling to multiple bulk acoustic phonon modes.** (a) By selecting a different pair or optical modes (i.e. changing optical wavelength) we can tailor coupling to couple to more than one phonon modes. (b) High resolution OMIA measurement near the near the center of the optical resonance reveals three high-frequency acoustic modes around 12.661 GHz with frequency spacing of ~ 610 kHz, which is consistent with the acoustic free spectral range of $v_a/2L_{\rm ac}$. Adapted from Ref. [111].

ical coupling is mediated by more than one phonon modes is shown in Fig. 5.18. Near the center of the transmission spectrum, we observe multiple narrow resonances corresponding to standing wave longitudinal phonon modes near $\Omega_B \approx 12.661$ GHz. These OMIA peaks are spaced equally by ~ 610 kHz, consistent with the acoustic FSR of $v_a/(2L_{\rm ac})$.

So far, we have probed the coherent response of our optomechanical system and used it to determine g_0^m, κ, and Γ_m. However, even in absence of the probe laser, the control laser can spontaneously scatter into Stokes and anti-Stokes sideband due to thermal fluctuations in the mechanical modes. We explore this in greater detail in the next two sections.

5.8 Thermal Fluctuations and Phonon Lasing

When the control laser in on resonance with the higher frequency optical mode (ω_2), a thermally populated phonon mode (Ω_m) mediates scattering of incident control

photons from frequency ω_2 to $\omega_1 = \omega_2 - \Omega$ through Stokes process.

To derive the power spectrum of such spontaneously scattered Stokes light, we begin by considering the effective optomechanical Hamiltonian in Eqn. (5.23),

$$H_{\text{eff}} = -\hbar\Omega_m a_2^\dagger a_2 + \hbar\Omega_m b_m^\dagger b_m - \hbar g_m (a_1 b_m + b_m^\dagger a_1^\dagger), \tag{5.46}$$

where we assumed that the optical mode spacing exactly matches the phonon mode frequency (i.e. $\Delta = \omega_2 - \omega_1 = \Omega_m$), $g_m = \sqrt{N_2} g_0^m$, and N_2 is the intracavity photon number of mode a_2. The Heisenberg-Langevin equations of motion derived from this effective Hamiltonian are given by

$$\dot{a}_1 = \left(i\Omega_m - \frac{\kappa_1}{2}\right) a_1 + i g_m b_m^\dagger, \tag{5.47}$$

$$\dot{b}_m = \left(-i\Omega_m - \frac{\Gamma_m}{2}\right) b_m + i g_m a_1^\dagger + \sqrt{\Gamma_m}\tilde{b}_{\text{in}}, \tag{5.48}$$

where $\tilde{b}_{\text{in}}(t)$ is the input thermal fluctuation that drives the phonon mode. We assume a Markovian noise process (see Ref. [161]) such that

$$\langle \tilde{b}_{\text{in}}^\dagger(t) \tilde{b}_{\text{in}}(t') \rangle = n_{\text{th}} \delta(t - t'), \tag{5.49}$$

$$\langle \tilde{b}_{\text{in}}(t) \tilde{b}_{\text{in}}^\dagger(t') \rangle = (n_{\text{th}} + 1) \delta(t - t'). \tag{5.50}$$

Here, $\langle \ldots \rangle$ represents an ensemble average, and $n_{\text{th}} = (e^{\hbar\Omega_m / k_B T} - 1)^{-1}$ denotes the average number of thermal phonons of angular frequency Ω_m at temperature T. For instance, at a temperatures of 10 Kelvin, $n_{\text{th}} \simeq 16$ for 12.645 GHz phonon modes. In contrast, the optical fields have essentially zero thermal occupation even at room temperatures since they are at much higher frequencies ($\sim$ 200 THz). Therefore, we ignore thermal fluctuations of the optical field in our calculations. Furthermore, we assume that the externally driven laser source is a pure coherent tone (no added noise from the laser itself), which is a good approximation for our experiments.

We now use Fourier-transform (defined as $f(\Omega) = \int_{-\infty}^{+\infty} dt\ f(t)e^{i\Omega t}$) to solve eqns. (5.47-5.48) in frequency space, which are given by

$$a_1(\Omega) = \frac{-ig_m}{i(\omega + \Omega_m) - \kappa_1/2} b_m^\dagger(\Omega) \tag{5.51}$$

$$b_m(\Omega) = \frac{i\sqrt{\Gamma_m}}{(\omega - \Omega_m + i\Gamma_m/2 + \Sigma(\Omega))} \tilde{b}_{\rm in}(\Omega), \tag{5.52}$$

where we define

$$\Sigma(\Omega) = \delta\Omega_m(\Omega) - i\frac{\Gamma_{\rm opt}(\omega)}{2} = \frac{ig_m^2}{i(\Omega - \Omega_m) - \kappa_1/2}. \tag{5.53}$$

Here, $\delta\Omega_m(\Omega) = {\rm Re}\{\Sigma(\Omega)\}$ gives us the frequency shift of the phonon mode and $\Gamma_{\rm opt}(\Omega) = -2{\rm Im}\{\Sigma(\Omega)\}$ gives us the optomechanical amplification rate. While $\Sigma(\Omega)$ is frequency dependent, for weak coupling ($g_m \ll \kappa_1$), we can just evaluate $\delta\Omega_m(\Omega)$ and $\Gamma_{\rm opt}(\Omega)$ at $\Omega = \Omega_m$ (see Ref. [15]). This calculation gives $\delta\Omega_m = 0$ and $\Gamma_{\rm opt} = 4g_m^2/\kappa_1$. So, we can re-write eqn. (5.52) as

$$b_m(\Omega) = \frac{i\sqrt{\Gamma_m}}{(\omega - \Omega_m + i\Gamma_m^{\rm eff}/2)} \tilde{b}_{\rm in}(\Omega), \tag{5.54}$$

where $\Gamma_m^{\rm eff} = \Gamma_m - \Gamma_{\rm opt} = \Gamma_m - 4g_m^2/\kappa_1$.

We can use $b_m(\Omega)$ in eqn. (5.54) along with the noise correlations in eqns.(5.49)-(5.50) to calculate the power spectrum of laser driven mechanical mode, $S_{bb}(\Omega)$, which is defined as

$$S_{bb}(\Omega) = \int_{-\infty}^{+\infty} \langle b^\dagger(t)b(0)\rangle\, e^{i\Omega t} dt \tag{5.55}$$

$$= \frac{\Gamma_m n_{\rm th}}{(\Omega + \Omega_m)^2 + (\Gamma_m^{\rm eff}/2)^2}. \tag{5.56}$$

From this derivation we see that the power spectrum has a linewidth determined by the effective damping rate $\Gamma_m^{\rm eff} = \Gamma_m(1 - \Gamma_{\rm opt}/\Gamma_m)$. Therefore, when the optomechan-

ical amplification rate equals the cold cavity linewidth ($\Gamma_{\text{opt}} = \Gamma_m$ or $C = \Gamma_{\text{opt}}/\Gamma_m = 1$), a threshold condition is achieved. When $\Gamma_m^{\text{eff}} < 0$ (i.e. when $C > 1$), parametric instability initially causes thermal fluctuations to grow exponentially in time and eventually saturate to reach coherent self-sustained oscillations. This phenomenon is well studied in many optomechanical systems [128, 162] and is also commonly known as "phonon lasing" [117].

Below the lasing threshold, we can calculate the intracavity power spectrum of the Stokes light using Eqns. (5.51-5.52). The power spectrum, $S_{a_1 a_1}(\omega)$, is given by

$$\begin{aligned} S_{a_1 a_1}(\Omega) &= \int_{-\infty}^{+\infty} \langle a_1^\dagger(t) a_1(0) \rangle \, e^{i\omega t} dt \\ &= \frac{g_m^2 \Gamma_m (n_{\text{th}} + 1)}{((\Omega - \Omega_m)^2 + (\kappa_1/2)^2)\left((\Omega - \Omega_m)^2 + (\Gamma_m^{\text{eff}}/2)^2\right)}. \end{aligned} \tag{5.57}$$

Since $\Gamma_m \ll \kappa$ in our system, we can further simplify this equation to obtain the following power spectrum for the Stokes light near $\Omega \approx \Omega_m$

$$\begin{aligned} S_{a_1 a_1}(\Omega) &= \int_{-\infty}^{+\infty} \langle a_1^\dagger(t) a_1(0) \rangle \, e^{i\omega t} dt \\ &= \frac{4 g_m^2 \Gamma_m (n_{\text{th}} + 1)}{\kappa_1^2 \left((\Omega - \Omega_m)^2 + (\Gamma_m^{\text{eff}}/2)^2\right)}. \end{aligned} \tag{5.58}$$

From this equation, we see that the power spectrum of the Stokes light is Lorentzian when $C < 1$, and the linewidth of this spectrum is determined by the effective damping rate of the mechanical mode. We also see that, even at zero temperature (i.e. when $n_{\text{th}} = 0$), non-zero spontaneous Stokes scattering occurs due to vacuum fluctuations of the mechanical mode.

We perform such spontaneous scattering measurements as a function as a function of the input control laser power (see Fig. 5.19). First, the measurement of total backscattered light from the cavity using a power meter as a function of the input control laser power reveals a clear threshold of 137 mW. This threshold input control

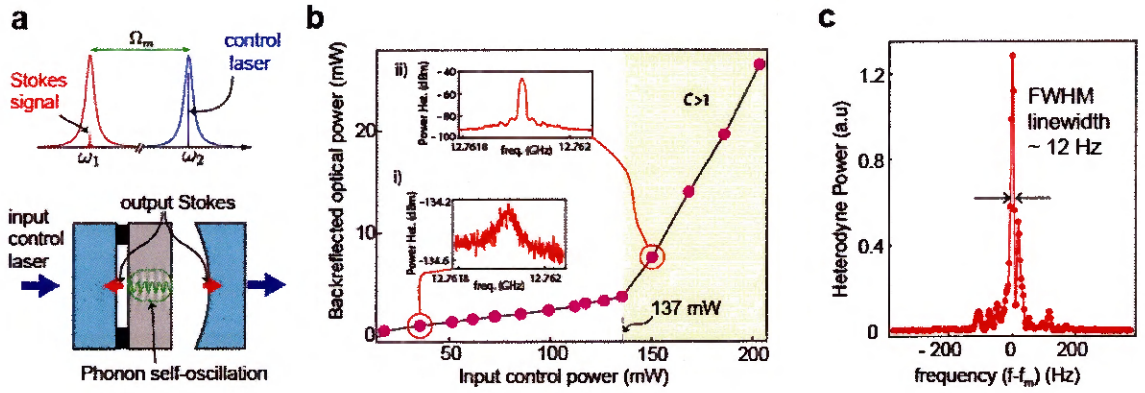

Figure 5.19: **Thermal fluctuations and mechanical self-oscillation.** (a) We tune a strong control laser directly on-resonance with the high-frequency optical mode at ω_2 to observe thermal fluctuations of a mechanical mode. The thermally-populated phonon mode spontaneously scatters light from the higher energy optical mode at ω_2 to the lower energy optical mode at ω_1 (Stokes field). (**b**) The measurement of back-reflected optical power as a function of the input control laser power reveals a clear threshold behavior at 137 mW. This occurs because of regenerative self-oscillation of the phonon mode when $C > 1$. Note that linear increase in backreflected optical power before the threshold occurs due to imperfect coupling of the control laser to the optical mode at ω_2. Once self-oscillating, coherent phonons scatter a large fraction of the input control laser into Stokes light, leading to a dramatic increase in the backreflected optical power. Moreover, above threshold, we observe a significant line narrowing of the heterodyne beat-tone of scattered Stokes light with the frequency shifted version of the input control laser. (**c**) Once the control laser is locked on resonance with the optical mode at ω_2 using Pound-Drever-Hall technique, we observed 12 Hz linewidth for the heterodyne beat tone. Adapted from Ref. [111].

laser power is consistent with the threshold ($\sim$ 140 mW) predicted from the measured values of g_0^m, κ, and Γ_m. Before threshold, a small ($\sim$ 2.6%) backreflection results from imperfect coupling of the control laser to the optical mode at ω_2. Once self-oscillating, phonons scatter a large fraction of the input control laser into Stokes light, which exits the optical cavity through both forward and backward direction, leading to a significant increase in the backreflected optical power. Measuring both the backreflected and total transmitted light, we can determine the total output Stokes power as a function of the input control laser power. This measurement reveals a slope efficiency of $\sim$ 62%, which is consistent with the theoretically predicted value of 57% (see supplementary section S6 of Ref. [111] for details).

In addition to such power measurements, we perform heterodyne detection of the transmitted light to measure the power spectrum ($S_{a_1 a_1}(\Omega)$) of the spontaneously scattered Stokes light (see inset i of Fig. 5.19**b**). As expected from Eqn. (5.57), we observe a Lorentzian spectrum with an effective linewidth that is narrower than Γ_m. Slight asymmetry in this spectrum is a result of the slight mismatch between the cavity mode spacing and the phonon-mode frequency (i.e. $\omega_2 - \omega_1 \approx \Omega_m$).

As the control laser power is increased beyond the lasing threshold of 137 mW, we observe a sharp increase in the magnitude of the scattered Stokes light as well as dramatic spectral narrowing of the heterodyne beat tone. Note that our earlier measurements of the heterodyne beat tone (or equivalently the phonon linewidth) were much wider ($\sim$ 20kHz) as seen in inset ii) of Fig. 5.19**b**. However, once the control laser was locked on resonance with the higher frequency optical mode at ω_2 using a Pound-Drever-Hall locking technique, we observed a dramatic narrowing of the heterodyne beat tone. We observed linewidths of the order of 10 Hz, which was limited by the resolution bandwidth of the RF-spectrum analyzer. Similar to fundamental (quantum) limit (also well known as Schawlow-Townes limit) for the linewidth a conventional laser, the fundamental quantum backaction limited linewidth of phonon

lasers (within optomechanical systems) is also described by Schawlow-Townes-type relation [163, 164].

5.8.1 Phonon Laser Linewidth

Next we estimate the quantum-backaction-limited linewidth and phase noise of our phonon laser. At the highest input control laser power of 204 mW, we achieve large cavity-enhanced coupling rate of $g_m = \sqrt{N_2} g_0^m = 2\pi \times$ 1.5 MHz, where $N_2 = 6.3 \times 10^9$ and $g_0^m = 2\pi \times$ 18 Hz. Moreover, from the measurement of backreflected optical power, we estimate total scattered output Stokes power of P_s = 42 mW (see Fig. 5.19**b**) when P_{in} = 204mW. Knowing the scattering rate of Stokes light per phonon, $\gamma_{\text{OM}} = 4G^2/\kappa$, we can calculate the steady state coherent phonon number as

$$\bar{n}_{\text{ph}} = \frac{P_s}{\hbar\omega\gamma_{\text{OM}}} = 4.2 \times 10^{11}. \tag{5.59}$$

In this case, the quantum-backaction-limited Schawlow-Townes linewidth (see Ref. [164]) for our phonon laser is given by

$$\Delta\Omega = \frac{\Gamma_m}{2\bar{n}_{\text{ph}}}(n_{\text{th}} + 1) = 2\pi \times 1.7 \text{ μHz}, \tag{5.60}$$

where $n_{\text{th}} = 16$ at 10 Kelvin temperatures. Such ultra-narrow linewidth would result in a phase noise of -147 dBc/Hz at 10 kHz offset for a 12.6 GHz optomechanical oscillator. Such low noise performance may be possible in our system because the macroscopic bulk acoustic resonator can support very large phonon occupation numbers ($\sim 10^{12} - 10^{13}$).

Dramatic improvement in the quantum-backaction-limited phase noise performance is possible within this quartz optomechanical system by using a plano-convex acoustic resonator having intrinsic phonon dissipation rate $\Gamma_m = 2\pi \times 300$ Hz (see Chapter 3). For similar control input laser powers of 204 mW, we obtain a large

steady state phonon population of 2×10^{12}. This would result in a Schawlow-Townes narrowed linewidth of $\Delta\Omega = 2\pi \times 0.5$ nHz at 4 Kelvin temperature. Such highly coherent oscillator would have a phase noise of -173 dBc/Hz at 10 kHz offset for a 12.6 GHz optomechanical oscillator. However, a number of technical noise sources such as fluctuation in the input control laser power, optical absorption, and refractive index and sound velocity change with minute temperature fluctuations affect the measured linewidth of the phonon laser. Hence, it would be necessary to manage these technical noise sources before such performance is achievable in practice.

5.9 Phonon mode cooling

When the control laser in on resonance with the lower frequency optical mode (ω_1), a thermally populated phonon mode (Ω_m) mediates scattering of incident control photons from frequency ω_1 to $\omega_2 = \omega_1 + \Omega_m$ through anti-Stokes process. This anti-Stokes process can be used to produce phonon mode cooling. In what follows, we develop the formalism to describe and characterize this cooling process.

Similar to the derivation in Section 5.8, using the Heisenberg-Langevin equations of motion derived from the effective Hamiltonian in Eqn. (5.22)

$$H_{\text{eff}} = \hbar\Delta a_2^\dagger a_2 + \hbar\Omega_m b_m^\dagger b_m - \hbar g_m (a_2^\dagger b_m + b_m^\dagger a_2), \tag{5.61}$$

we obtain the following power spectrum for the spontaneously scattered anti-Stokes light,

$$S_{a_2 a_2}(\Omega) \simeq \frac{4 g_m^2 \Gamma_m \bar{n}_{\text{th}}}{\kappa^2 \left((\Omega - \Omega_m)^2 + (\Gamma_m^{\text{eff}}/2)^2\right)}, \tag{5.62}$$

where g_{m} is the optomechanical coupling rate, Γ_m is intrinsic mechanical decay rate, κ is the linewidth of the optical mode at ω_2 and $\Gamma_m^{\text{eff}} = \Gamma_m(1 + C)$ is the effective

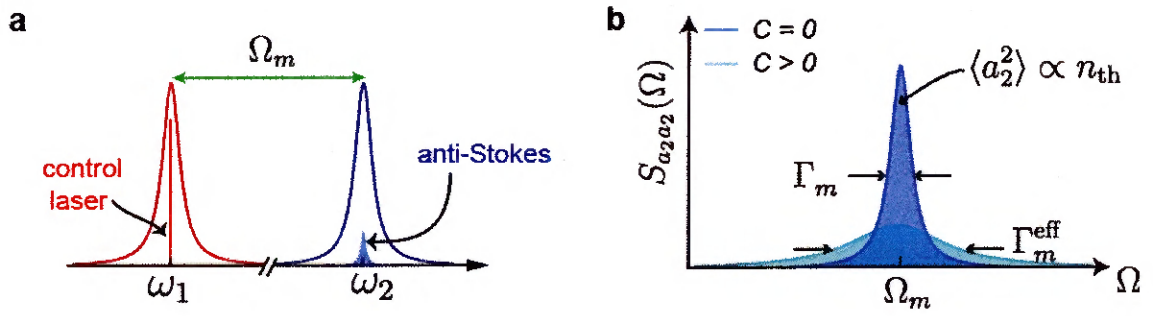

Figure 5.20: **Thermal fluctuations and phonon mode cooling.** (a)We tune a strong control laser directly on-resonance with the lower-frequency optical mode at ω_1 to observe thermal fluctuations of a mechanical mode. The thermally-populated phonon mode spontaneously scatters light from the lower energy optical mode at ω_1 to the higher energy optical mode at ω_2 (anti-Stokes field). (**b**) At $C > 0$, anti-Stokes scattering increases the effective damping rate ($\Gamma_m^{\rm eff}$) of the phonon mode.

damping rate of the acoustic due to the optomechanical coupling. As before, we assumed $\kappa \gg \Gamma_{\rm m}$ while deriving Eq. (5.62).

The linewidth of the anti-Stokes power spectrum given by $\Gamma_m^{\rm eff}/2\pi$, broadens as the cooperativity is increased as seen in Fig. 5.20**b**. This broadened noise spectrum (or larger effective dissipation rate) and reduction in thermal fluctuations is related to the lowering of the effective temperature of the phonon mode [165, 166]. Hence, when the control laser is on resonance with the lower frequency optomechanical mode (ω_1), we can perform phonon mode cooling. We explore this in greater detail below.

The total intracavity spontaneous scattering rate due to thermal fluctuations is given by

$$\Gamma_{\rm opt} = \frac{1}{2\pi}\int_{-\infty}^{\infty} {\rm d}\Omega\ S_{a_2a_2}(\Omega) = \frac{4g_{\rm m}^2\Gamma_{\rm m}\bar{n}_{\rm th}}{\kappa^2\Gamma_{\rm m}^{\rm eff}}. \tag{5.63}$$

Since $a_{2,\rm out} = \sqrt{\kappa^{\rm ext}}a_2$, the total optical power ($P_{\rm t}$) in the spontaneously scattered signal transmitted through the optical cavity is

$$P_{\rm t} = \hbar\omega\kappa^{\rm ext}\Gamma_{\rm opt} \tag{5.64}$$

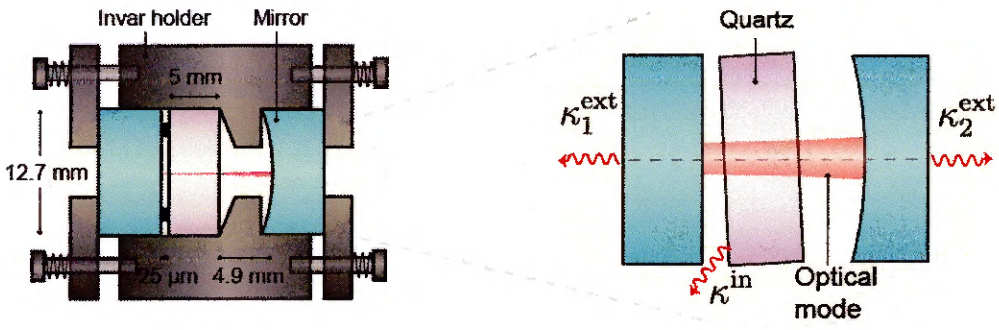

Figure 5.21: **Internal losses** (a) Schematic shows how the tilt of the quartz crystal with respect to the optical cavity axis can introduce additional internal losses for photons. Adapted from Ref. [112].

The total spontaneously scattered power at the detector $P_{\rm d} = \eta P_{\rm t}$, where η is the system detection efficiency resulting from optical losses and detector response. The total spontaneously scattered power can be written in terms of the effective occupation number for the phonon mode $\bar{n}_{\rm eff} = \Gamma_m \bar{n}_{\rm th}/\Gamma_{\rm m}^{\rm eff}$ as

$$P_{\rm d} = \eta P_{\rm t} = \frac{4\eta\hbar\omega\kappa^{\rm ext} g_{\rm m}^2}{\kappa^2}\frac{\Gamma_m n_{\rm th}}{\Gamma_{\rm m}^{\rm eff}} = \frac{4\eta\hbar\omega\kappa^{\rm ext} g_{\rm m}^2}{\kappa^2}\bar{n}_{\rm eff}. \tag{5.65}$$

Since $\bar{n}_{\rm eff} = \Gamma_{\rm m}\bar{n}_{\rm th}/\Gamma_{\rm m}^{\rm eff} = \bar{n}_{\rm th}/(1+C)$, $\bar{n}_{\rm eff}$ decreases as we increase C by increasing the input control. Therefore, increasing the control laser power effectively cools the phonon mode.

We determine $P_{\rm d}$ through spontaneous measurements and $g_{\rm m}$, κ, and $\Gamma_{\rm m}$ through OMIT measurements (see Fig. 5.22). After measuring η, we determine $n_{\rm eff}$ as a function C. For an accurate measurement of thermal occupation number, we also need to determine $\kappa^{\rm ext}$. The addition of the crystal inside our Fabry-Perot optical cavity gives rise to an asymmetry in the external coupling rates for the input and output mirrors and also introduces additional intrinsic loss channels for the optical cavity modes. Nevertheless, by using a combination of reflection as well as transmission measurements of the optical cavity response, we can determine the internal loss rate

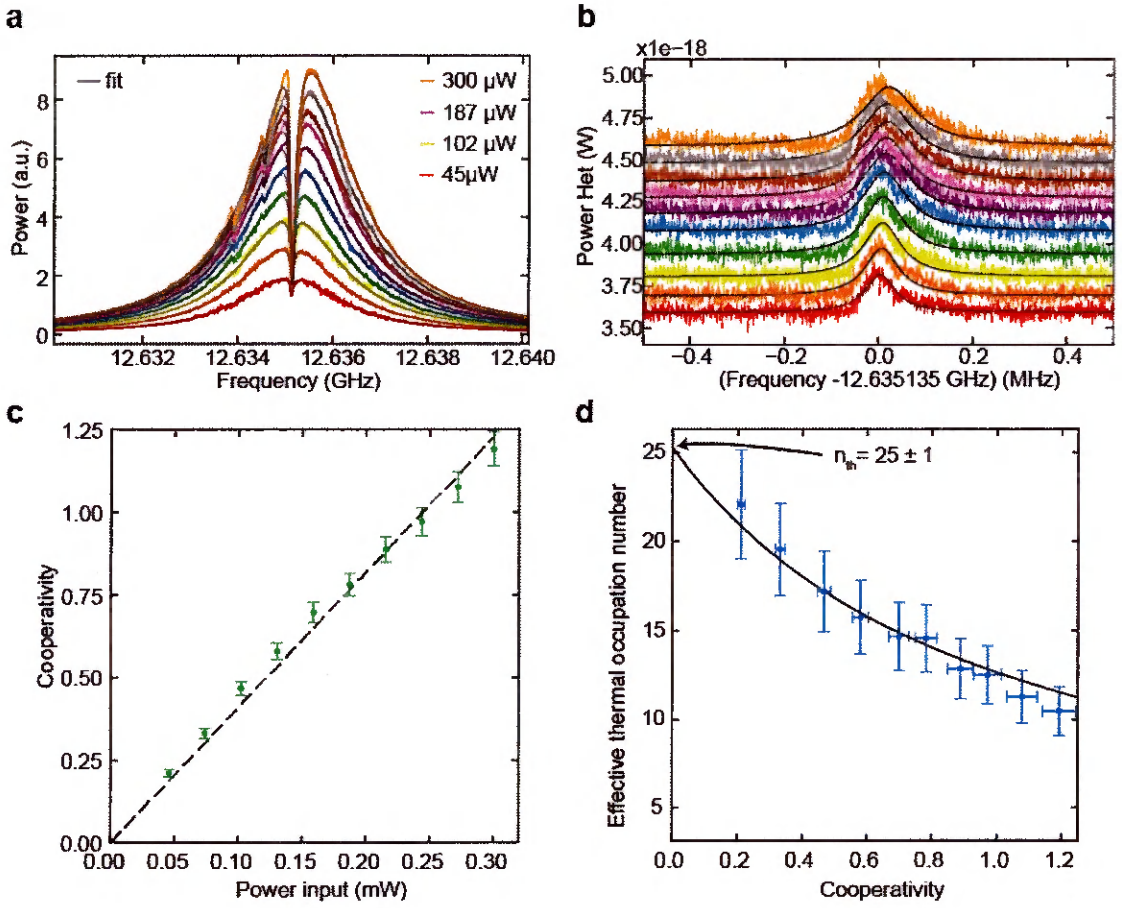

Figure 5.22: **Thermometry of the acoustic mode.** (**a**) OMIT measurements as a function of control laser power (P_{in}) is used to determine κ, Γ_m, and g_m. (**b**) Measurement of the spontaneously spectra at various control laser power (**c**) Cooperativity as a function of P_{in}). (**d**) Extracted effective phonon number n_{eff} as a function of C. From a theoretical fit to this data, we obtain $n_{\text{th}} \approx 25 \pm 1$. Adapted from Ref. [112].

as well as asymmetry in the external coupling rate for an accurate measurement of n_{th}.

We performed such spontaneous mode cooling measurements by using a higher finesse (~ 5000) optical cavity (i.e. using mirrors with 99.9% reflectivity). Note that because the anti-Stokes scattering scales rapidly with the decay rate of the optical cavity (i.e., $S_{a_2a_2}(\Omega) \propto 1/\kappa^2$), we did not have enough signal-to-noise to observe anti-Stokes scattering using the lower finesse (~ 170) optical cavity with low reflectivity (98%) mirrors. We recorded both the OMIT spectra and the spontaneously scattered

signal as we varied the control laser power. We measured $\eta = 0.37 \pm 0.05$, $\kappa = 2.54$ MHz, and $\kappa_2^{\text{ext}} = 2\pi \times (0.92 \pm 0.03)$ MHz to obtain a calibrated measurement of n_{eff} as a function of C (see Fig. 5.22**d**). A fit to n_{eff} as a function of C then allows us to determine the following value of $n_{\text{th}} = 25 \pm 1$, which corresponds to a bath temperature of 15.6 ± 0.7 K for the 12.6 GHz acoustic mode. Note that this temperature is slightly higher than the independently measured Invar temperature of 11.2 K suggesting a non-negligible thermal resistance between the quartz and the Invar holder.

5.10 Conclusion and Outlook

In this chapter, we have demonstrated a new type of cavity optomechanical system that uses Brillouin interactions to harness high-frequency bulk acoustic waves. Unlike most strategies that rely on nanoscale and microscale structural control (i.e. miniaturization) to access GHz-frequency phonons, we have utilized phase-matched Brillouin interactions to couple to massive ($\sim$ 20μg) of a bulk acoustic resonator without any size reduction. Since our acoustic resonator has a very simple device geometry (i.e. a planar crystal), the experimental techniques and theoretical framework delineated in this chapter can be used to transform practically any transparent crystalline substrates into a high-frequency cavity optomechanical system.

The versatility our optomechanical systems should lend itself to new types of low noise and high-power handling acoustic oscillators as well as optical Brillouin lasers. Since these macroscopic optomechanical devices can support large occupation numbers for both photons and phonons, we showed how they can be used to make low-noise oscillators in the regime when the intrinsic mechanical dissipation rate is much narrower than the optical dissipation rate (i.e. $\Gamma_m \ll \kappa$). This regime of phonon lasing is accessible in most crystalline materials at cryogenic temperatures.

In the reverse dissipation regime ($\Gamma_m \gg \kappa$), which is typically accessible at room temperature within most crystals, we can use this same system to achieve Brillouin lasing. Such Brillouin lasers have a potential to be highly efficient (slope efficiency $> 80\%$) and handle large powers (1-100 W output powers). Moreover, because they can handle large intracavity photon number, they have a potential for ultra-low phase-noise performance.

The quartz based optomechanical system demonstrated here is a promising platform for quantum cavity optomechanics and presents new opportunities for robust control of phonons at the quantum level. Operation of our high-frequency optomechanical system at temperatures below 0.9 K should allow access to the quantum ground state of the mechanical resonator. Once initialized to the quantum ground state, probabilistic schemes for heralding and readout of non-Gaussian mechanical states are feasible in our optomechanical system due to the possibility for achieving sub-phonon-level counting sensitivity; In addition to having large mechanical frequencies, which is desirable for such schemes, resonant driving of an optical mode within this multimode system offers an unique opportunity for finesse squared improvement of the phonon-counting sensitivity (see Supplementary Note S8 of Ref. [111]). This may be a surprising advantage, as phonon counting sensitivity is independent of finesse in single-mode optomechanical systems. Such probabilistic protocols for quantum optical control of macroscopic phonons have a potential to be more robust against deleterious effects of optical absorption. This is because the greatly reduced surface-to-volume ratios for both light and sound mitigate the opportunity for laser heating. Moreover, the geometry of our mechanical resonator could enable excellent thermal anchoring.

Beyond probabilistic schemes, our multimode optomechanical system presents opportunities for deterministic quantum control of phonons. Even using the planar bulk acoustic wave resonator geometry, which is non-optimal for the production of high

phononic $f \cdot Q$ products, there is a clear path towards quantum-coherent regime of optomechanical interaction. It is relatively straightforward to decrease the optical decay rate by using higher reflectivity mirrors. We already showed in this chapter how we could improved the finesse from the current value of ($\mathcal{F} \approx 160$) to $\mathcal{F} \approx 5000$ should allow access to the strong-coupling regime ($\Omega_c = 2g_m > \kappa, \Gamma_m$) at relatively modest ($\sim$ 10 mW) control laser powers while operating at $\sim$ 4 K temperatures. Moreover, we can drastically improve the performance of our system through phononic resonator design. By shaping the bulk acoustic resonator into a plano-convex geometry it is possible to achieve mechanical Q-factors as large as 0.5×10^8 for phonons at 13 GHz, as demonstrated in Chapter 3. Optical control of such long-lived, high-frequency phonons at cryogenic temperatures could offer a path towards using bulk-acoustic wave resonators as quantum transducers and as quantum memories.

Chapter 6

Strong Coupling between Light and Bulk Acoustic Waves

6.1 Introduction

In the previous chapter, we demonstrated a new type of cavity optomechanical system in which high-frequency acoustic modes of a bulk acoustic resonator mediate resonant coupling between two distinct optical modes of a Fabry-Perot cavity. We showed that resonant driving of an optical mode within this system permits dramatic enhancement of the optomechanical coupling strength. When the optomechanical coupling rate is larger than the dissipation rate of both the optical and the acoustic mode, we reach the regime of optomechanical strong coupling. For a mechanical oscillator operating in the quantum regime, optomechanical strong coupling can be used for deterministic transfer of quantum states between the optical field and the mechanical oscillator or vice versa [117]. For this reason, reaching the strong coupling regime of optomechanical interaction has remained an intriguing area of research in cavity optomechanics.

So far, only a handful of cavity optomechanical systems [167–169] have demon-

strated strong coupling due to a variety of technical challenges associated with realizing a low-loss system that can also support high coupling rates. Within micromechanical oscillators radiation pressure has been used to demonstrate optomechanical strong coupling between MHz-frequency mechanical oscillators and optical fields. While, in principle, optomechanical cooling can be used to initialize such low frequency (1-100 MHz) mechanical oscillators in their quantum ground states for future experiments in the quantum regime, optomechanical cooling inevitability increases the effective mechanical dissipation rate and it complicates the prospect for storage of complex quantum states. Therefore, achieving optomechanical strong coupling to long-lived high-frequency (GHz) phonon modes, which can be initialized deep in their quantum ground states using standard bulk refrigeration techniques, has remained an important challenge in cavity optomechanics.

A variety of frequency microscale and nanoscale cavity optomechanical systems [151–154] have been realized in order to harness coupling to GHz frequency phonons. In this context, optomechanical crystals [151], which use sub-wavelength structural control to confine photons and phonons, have emerged as a popular platform. Demonstrations ranging from ground state cooling [155] to remote entanglement [145] within such systems have undoubtedly pushed cavity optomechanics in the quantum regime.

Despite these advances, it has proven difficult to achieve strong coupling in such nano-optomechanical systems as a basis for deterministic protocols for coherent control of mechanical motion. Spurious laser heating even at minute optical powers has placed a practical limit on the number of intracavity photons [170], and hence the cavity-enhanced optomechanical coupling strength. Moreover, since these resonators are typically fabricated in materials like silicon in which optically generated free-carriers not only affect the optical power handling but also introduces additional loss channels for phonons at cryogenic temperatures [170].

As an alternative approach, we have seen how phase-matched Brillouin interac-

tions can permit coupling to high-frequency (>10 GHz) phonons within bulk systems independent of the size of those systems. Moreover, resonant intermodal coupling permits dramatic enhancement of the coupling rate. More recently, Brillouin interactions have been used to demonstrate strong coupling to 11.6 GHz-frequency mechanical modes within a whispering gallery mode resonator. While large intracavity photon numbers due to relatively low optical absorption in silica enables this system to enter the regime of strong coupling, it is difficult to achieve low-acoustic dissipation rates in glasses are cryogenic temperatures. In particular, two-level tunneling states which are intrinsic to amorphous materials (silica) produce excess noise and dissipation at cryogenic temperatures [73,171] making such high-frequency phonons not suitable for applications such as quantum transduction and memories.

In this chapter, we demonstrate robust strong coupling between infrared light and long-lived, high-frequency phonons of a bulk acoustic resonator. This system solves the challenge of achieving strong optomechanical coupling in a versatile platform that support low-loss optical as well as mechanical modes. Moreover, we configure our system to enter the multimode strong coupling, in which a single optical mode simultaneously couples to multiple modes of the bulk acoustic resonators. Finally, utilizing nontrivial mode hybridizations in this multimode strong coupling regime, we study a surprising phenomenon of radiative cancellation of extrinsic loss channels for phonons.

6.2 Dyanmics of Light-Sound interaction in the Strong Coupling Regime

To explore the dynamics of light-sound coupling in the strong coupling regime, we begin by considering a simpler case of a single optical mode coupled to a single acoustic mode in the linearized interaction regime [117].

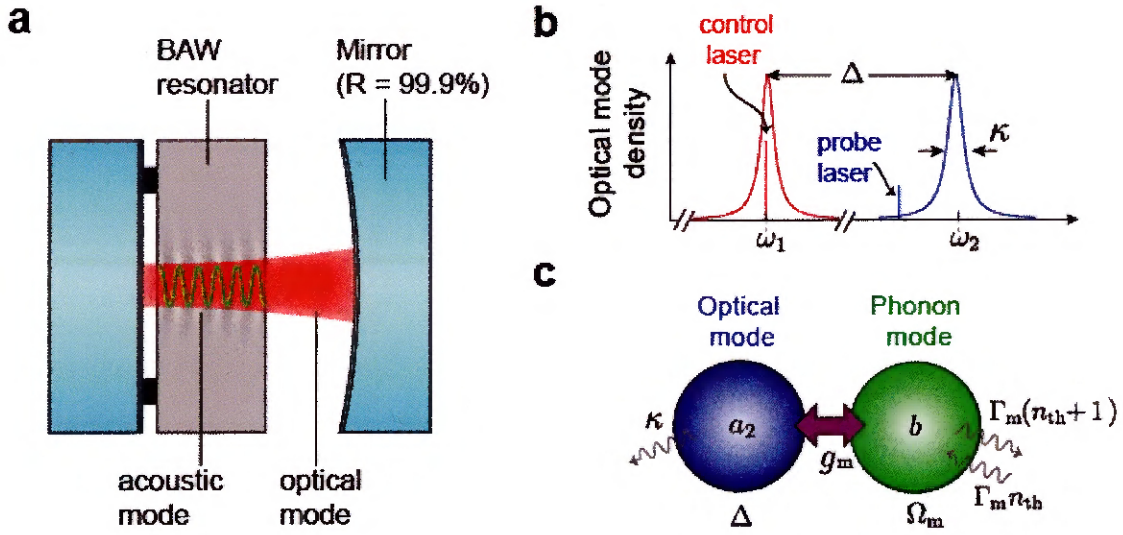

Figure 6.1: **Linearized interaction regime.** (**a**) Schematic of the bulk acoustic resonator inside a high finesse optical cavity consisting of mirrors having high (99.9%) reflectivity. (**b**) A control laser is on resonance with the lower frequency (ω_1) optical mode to enhance the optomechanical coupling rate and a weak probe probes the transmission spectrum of the higher frequency (ω_2) optical mode. (**c**) Under stiff pump approximation, we can eliminate the dynamics of the low frequency (ω_1) optical mode to obtain linear coupling between higher frequency optical mode, a_2, and the phonon mode, b. Adapted from Ref. [112].

As seen in Section 5.5, the Hamiltonian of our optomechanical system when an external control laser is driven on resonance with the lower frequency optical mode a_1 (see Fig. 6.1) is given by

$$H_{\text{eff}} = \hbar\Delta a_2^\dagger a_2 + \hbar\Omega_m b_m^\dagger b_m - \hbar g_m (a_2^\dagger b_m + a_2 b_m^\dagger). \tag{6.1}$$

Here $g_m = \sqrt{N_1} g_0^m$ is the cavity-enhanced coupling rate, N_1 is the intracavity photon number of mode a_1, and $\Delta = \omega_2 - \omega_1$ is the frequency spacing between the two optical modes. Note that we obtained this Hamiltonian by moving to the rotating frame of mode a_1. The interaction term $g_m(a_2^\dagger b_m + a_2 b_m^\dagger)$ describes the coherent exchange of energy between an optical mode a_2 and the phonon mode b_m.

If we ignore the dissipative terms in the Hamiltonian (i.e. assume $\kappa, \Gamma_m \to 0$), the linearized Hamiltonian of Eqn. (6.1) can be written in the matrix form in the basis of a_2 and b_1 as

$$H_{\text{eff}} = \begin{bmatrix} \Delta & -g_m \\ -g_m & \Omega_m \end{bmatrix}. \tag{6.2}$$

This Hamiltonian can be easily diagonalized, yielding two eigenmodes that are symmetric and anti-symmetric superposition of the optical (a_2) and the acoustic modes (b_m) with frequencies given by

$$\omega_\pm = \frac{\Omega_m + \Delta}{2} \pm \sqrt{g_m^2 + \left(\frac{\Delta - \Omega}{2}\right)^2}. \tag{6.3}$$

From this equation we see that, when these two coupled oscillators are on resonance (i.e. $\Delta = \Omega_m$), $\omega_\pm = \Omega_m \pm g_m$. Therefore, we obtain an energy splitting of $\omega_+ - \omega_- = 2g_m$ between the two eigenmodes. Moreover, on resonance, the eigenmodes are equal part light and sound, are given by $A_\pm = (a_2 \pm b_m)/\sqrt{2}$. When the oscillators are far from resonance (i.e. $\Delta \neq \Omega_m$), the eigenmodes are more light like or more sound like.

So far, we ignored dissipation terms in the effective Hamiltonian and just consid-

ered a the limiting case when $g_m \gg (\kappa, \Gamma_m)$. More generally, we can write down the following effective interaction Hamiltonian to account for the decay rate of the optical mode (κ) as well as acoustic mode (Γ_m) [117]

$$H_{\text{eff}} = \begin{bmatrix} \Delta - i\frac{\kappa}{2} & -g_m \\ -g_m & \Omega_m - i\frac{\Gamma_m}{2} \end{bmatrix}, \tag{6.4}$$

From this effective Hamiltonian we obtain the following complex eigenfrequencies

$$\omega_{\pm} = \frac{(\Omega_m + \Delta)}{2} - i\frac{\Gamma_m + \kappa}{4} \pm \sqrt{g_m^2 + \left(\frac{\Delta - \Omega_m}{2} + i\frac{\Gamma_m - \kappa}{4}\right)^2} \tag{6.5}$$

As before if we look at the specific case when the two oscillators are on resonance (i.e, $\Omega_m = \Delta$), we get

$$\omega_{\pm} = \Omega_m - i\frac{\Gamma_m + \kappa}{4} \pm \sqrt{g_m^2 - \left(\frac{\Gamma_m - \kappa}{4}\right)^2} \tag{6.6}$$

Therefore, the two eigenmodes, which are separated by $2\sqrt{g_m^2 - (\Gamma_m - \kappa)^2/16}$, each inherit dissipation rate of both the optical and the acoustic mode and the dissipation rate of the each of these hybridized modes of light and sound is given by $(\Gamma_m + \kappa)/2$ (see Fig. 6.2). Assuming the optical linewidth is much larger than the acoustic linewidth (i.e. $\kappa \gg \Gamma_m$), we see that when $g_m > \kappa/4$, the splitting between the modes $2\sqrt{g_m^2 - (\kappa/4)^2}$ becomes real-valued, and we obtain two well-resolved resonances corresponding to the transition to the strong coupling regime.

So far, we explored the frequency response of our system in the strong coupling regime by just looking at the eigenfrequencies derived from the effective Hamiltonian in Eqn. (6.4). We will see in Section 6.4 that we can measure such frequency response using a weak probe to measure the transmission spectrum of the higher frequency optical mode (a_2). Alternatively, we can also measure the time dynamics of our

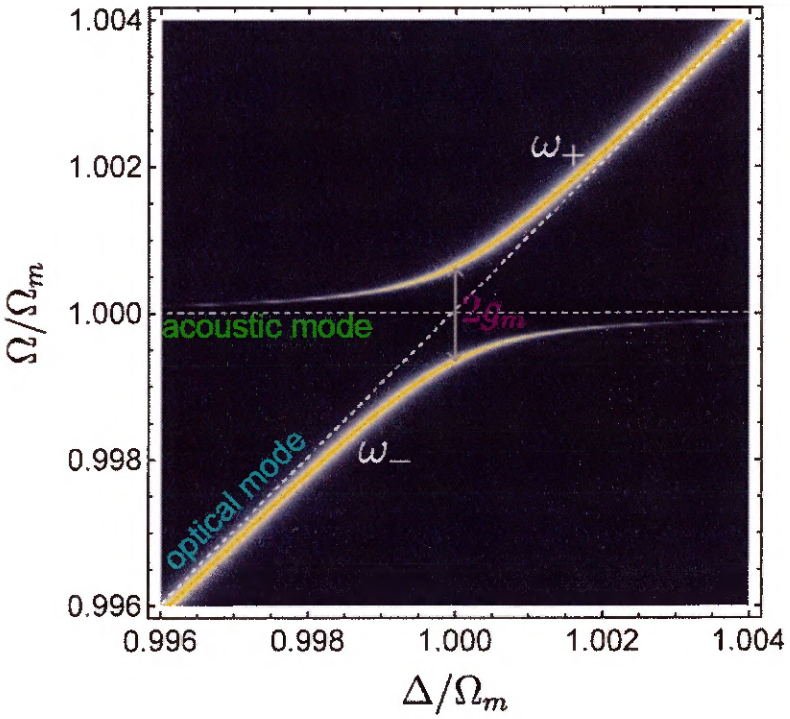

Figure 6.2: **Optomechanical strong coupling.** In the strong coupling regime, the optical and acoustic modes form collective excitation (symmetric and anti-symmetric superpositions) that are part light and part sound. So, as we sweep the frequency of the optical mode (a_2) and bring it on resonance with the acoustic mode (b_m), we expect an avoided crossing in the optical transmission spectrum. The energy difference between such eigenmodes is exactly equal to $2g_m$ when $\Delta = \Omega_m$.

system by using a weak probe excitation at a single frequency.

To explore the time dynamics of our system, for simplicity, we start by assuming that a strong external control laser is directly on resonance with the optical mode a_1. We assume a weak excitation field $\alpha_p(t)$ at frequency $\omega_p = \omega_1 + \Omega$ that excites the higher frequency optical mode (see Fig. 6.3). The effective Hamiltonian of this system by transforming to the frame rotating at ω_p for the optical mode (i.e. $a_2(t) \rightarrow a_2(t)e^{-i\omega_p t}$) and at Ω for the phonon mode ($b_m(t) \rightarrow b_m(t)e^{-i\Omega t}$), we obtain the following effective Hamiltonian

$$H_{\text{eff}} = \hbar(\Delta - \Omega)a_2^\dagger a_2 + \hbar(\Omega_m - \Omega)b_m^\dagger b_m - \hbar g_m(a_2^\dagger b_m + b_m^\dagger a_2) + i\hbar\sqrt{\kappa^{\text{ext}}}(\alpha_p(t)a_2^\dagger - \alpha_p^*(t)a_2), \tag{6.7}$$

where $\Delta = \omega_2 - \omega_1$, κ^{ext} is the mirror's output coupling rate, $\alpha_p(t)$ is normalized such that the incident power in the probe light $P_p = \hbar\omega_p \langle \alpha_p^* \alpha_p \rangle$. The Heisenberg-Langevin equations of motion derived from this Hamiltonian are given by

$$\dot{a}_2(t) = -i(\Delta - \Omega)a_2(t) - \frac{\kappa}{2}a_2(t) + ig_m(t)b_m(t) + \sqrt{\kappa^{\text{ext}}}\alpha_p(t) + \sqrt{\kappa}\tilde{a}_{\text{in}}, \tag{6.8}$$

$$\dot{b}_m(t) = -i(\Omega_m - \Omega)b_m(t) + -\frac{\Gamma_m}{2}b_m(t) + ig_m(t)a_2(t) + \sqrt{\Gamma_m}\tilde{b}_{\text{in}}, \tag{6.9}$$

where $\tilde{b}_{\text{in}}$ ($\tilde{a}_{\text{in}}$) is the thermal fluctuations that drives the phonon (optical) mode.

For now, let's ignore the noise terms since we are using a coherent probe field to probe the time dynamics of our system. From the solution to Eqns. (6.8-6.9) in the strong coupling regime, we observe energy sloshing back and forth between the optical mode (a_2) and acoustic mode (b_m) in Fig. 6.3**a**. The energy exchange occurs at the rate of $2g_m$ (or period of $1/2(g_m/2\pi) \equiv \pi/g_m$. Since the optical excitation is equal part light and sound, the lifetime of the excitation is given by $1/((\kappa+\Gamma_m)/2) \approx 2/\kappa$. Note that for the simulations shown in Fig. 6.3**b**, we assumed that the probe

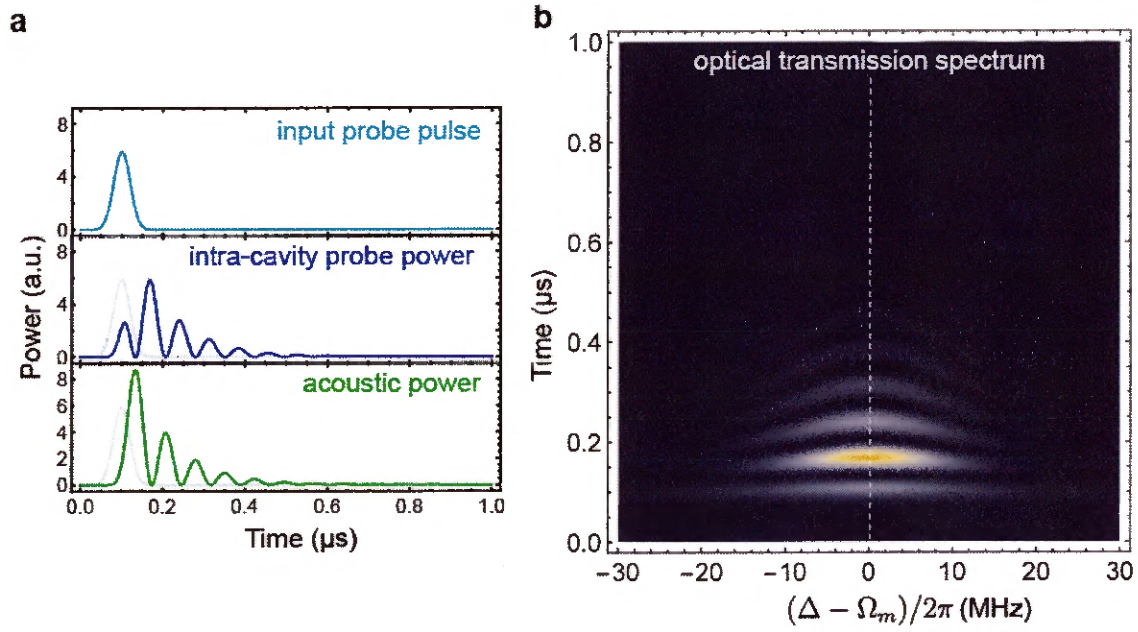

Figure 6.3: **Coherent energy exchange between the optical and the acoustic mode.** (**a**) In the strong coupling regime, if we were to excite our system with a weak probe pulse, we expect the energy to slosh back and forth between the optical and the acoustic modes. On resonance, $\Omega_m = \Delta$, the energy exchange occurs at rate $2g_m$. However, this energy exchange rate changes when the optical and acoustic modes are not on resonance as seen in (**b**).

laser is on resonance with the phonon mode (i.e. $\Omega = \Omega_m$) and that the coupling strength is constant in time ($g_m(t) = \text{constant}$). However, by making the coupling time dependent ($g_m(t)$), it is possible to control the optomechanical interaction and use it to swap energy between the optical and acoustic domain (or vice versa). When such swap-operation is implemented using a single-photon (or more generally non-classical optical states), it is possible to deterministically produce a single-phonon state (or non-classical states) of a mechanical oscillator [117].

6.3 Experimental Setup

In this section, we describe the experimental apparatus used to measure frequency and time-domain response of our system in the strong coupling regime.

6.3.1 Frequency Domain Measurement

We used optomechanically induced transparency (OMIT) to probe the coherent frequency response of our optomechanical system [157] (see Chapter 5.5 for details). This measurement is performed by using a control laser that is on-resonance with the lower-frequency optical mode at ω_1 as seen in Fig. 6.4**a**. A probe laser synthesized from the same laser is swept through the higher-frequency optical mode at ω_2. The transmitted probe light is measured as a function of probe laser detuning $\Omega = \omega_\text{p} - \omega_1$ using heterodyne detection.

Laser light from a tunable laser (Pure Photonics PPCL300) is locked on-resonance to the optical cavity mode at ω_1 using the Pound-Drever-Hall (PDH) locking technique as seen in Fig. 6.4**c**. This light at ω_1 is also intensity-modulated at a variable frequency Ω using a microwave signal generator (Agilent E8257D). This generates additional side-bands at $\omega_1 \pm \Omega$. The tone at frequency ω_1 serves as a strong control laser, whereas the weak tone at $\omega_1 + \Omega$ serves as a probe laser. The side-band at

$\omega_1 - \Omega$ is irrelevant, as it is not resonant with any optical cavity mode due to the unequal FSRs. The intensity-modulated light is amplified using an erbium-doped fiber amplifier (EDFA) and coupled into the optical cavity using a fiber-optic polarization controller, a collimator, a free-space polarizer, a mirror, and a lens. Note that a fiber-optic variable optical attenuator placed after the EDFA is used to vary control laser power incident on the cavity. The light back-reflected from the cavity is separated from the incident light using a circulator. A portion of this back-reflected light is used for the PDH lock.

Light transmitted through the optical cavity is collected using a free-space lens, a mirror, and a fiber-optic collimator and detected using a fast photoreceiver (Nortel Networks PP-10G). The spectrum analyzer monitors the heterodyne signal at Ω resulting from the beat-note of the transmitted probe laser and the transmitted control laser. The same spectrum analyzer also controls the frequency of the microwave signal generator, permitting us to track the heterodyne beat-note as a function of Ω.

6.3.2 Time Domain Measurement

To probe the time dynamics of our system, we use a control laser with a large, constant amplitude that is on-resonance with the optical mode at frequency ω_1 and a weak probe pulse derived from the same laser that is on-resonance with the optical mode at ω_2 as seen in Fig. 6.4**b**. Heterodyne detection of the probe signal transmitted through the cavity as a function of time is used to determine the time dynamics in our system.

A weak excitation pulse is generated by intensity-modulating the laser output using a pulsed microwave drive at frequency Ω_m (see Fig. 6.4**c**); to generate such pulsed microwave drive, RF-output from a microwave signal generator (Berkeley Nucleonics 845-M) at $\Omega_m + \omega_{IF}$ is mixed with a pulsed output of an arbitrary waveform generator (Tektronix AWG5014C) at ω_{IF} using a single-sideband mixer. The control laser and

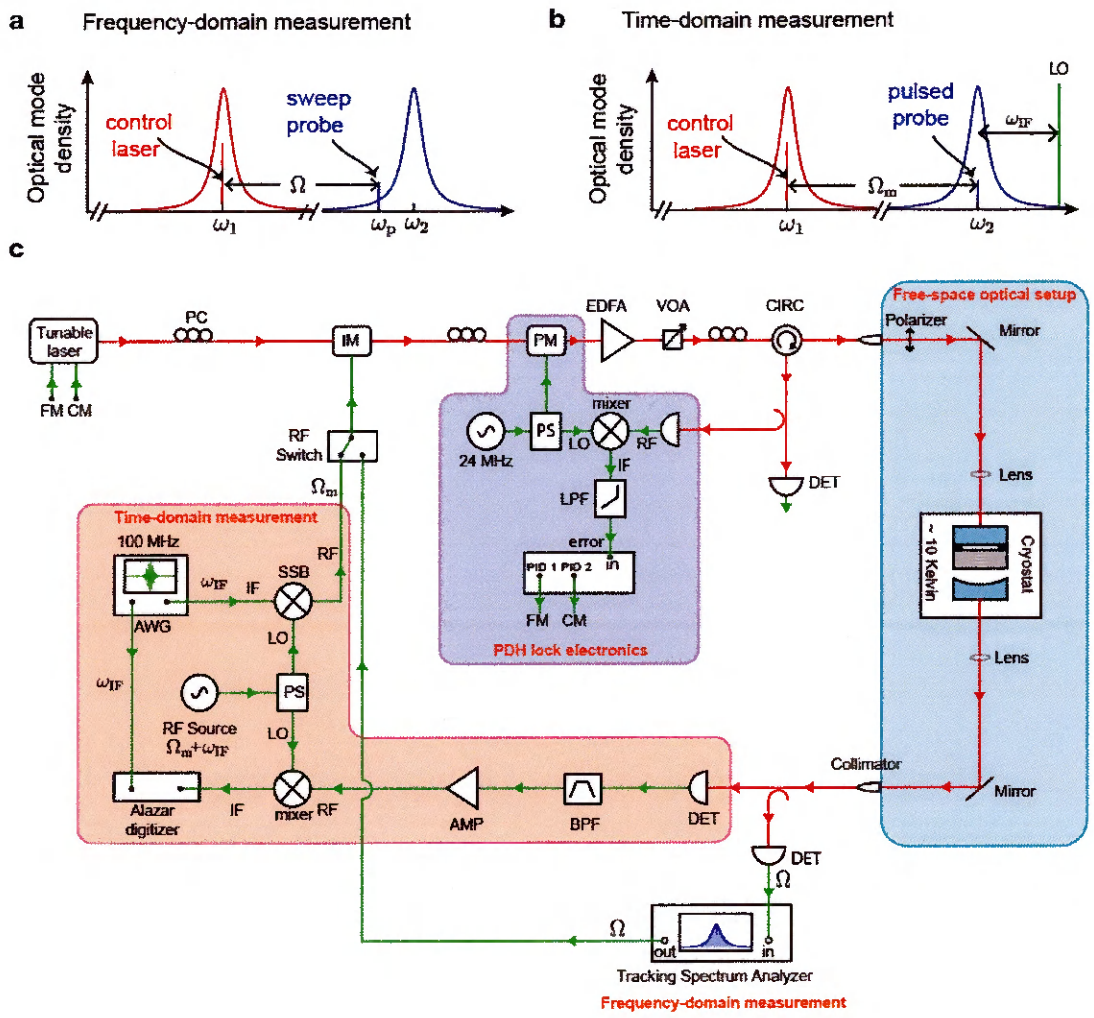

Figure 6.4: **Schematic of the measurement apparatus** (a) We measure the frequency response of the higher frequency optical mode (ω_2) by sweeping a probe laser through the resonance. **b**) The time domain measurement is performed by pulsing a weak probe, which is on resonance with the mechanical mode. (**c**) The control as well as the probe laser light are dervied from the same laser using an intensity modulator. A Pound-Derver-Hall locking technique is used to lock the control laser on resonance with the lower frequency (ω_1) optical mode. An arbitrary waveform generator (AWG) is used to synthesize a pulse probe. The transmitted probe light is detected using sensitive heterodyne technique for both frequency and time-domain measurements. PC: polarization controller, LO: local osciallator, SSB: single sideband mizer, IF: intermediate frequency, PS: power splitter, DET: optical detector, BPF: bandpass filter, LPF: low-pass filterAMP: rf amplifier, CIRC: fiber circulator, VOA: voltage controlled attenuator, LPF, FM: frequency modulation, CM: Clean measurement, IM: intensity modulator, and PID: proportional-integral-derivative controller. Adapted from Ref. [112].

the excitation pulse are both coupled into and out of the optical cavity through a combination of fiber-optic collimators and free-space optics described in the previous section. A part of the light transmitted through the cavity is detected using a fast photoreceiver, generating a RF beat-note at Ω_{m}. This heterodyne signal, resulting from transmitted pump light beating with the transmitted probe light, is filtered, amplified, and demodulated using the RF-output (at $\Omega_{\mathrm{m}} + \omega_{\mathrm{IF}}$) of the microwave source. The demodulated RF-signal along with the reference RF-output of the AWG (both at ω_{IF}) are recorded as a function of time using a digital oscilloscope (AlazarTech ATS9870). Comparing the demodulated signal with the AWG output allows us to measure both the phase and amplitude response of our optomechanical system.

6.4 Observation of Strong coupling to a single acoustic mode

For simplicity, we start by configuring our system so that a single optical mode (a_2) couples predominantly to a single acoustic mode (Γ_m) in the linearized regime of optomechanical interaction. As discussed in Chapter 5, we achieve this by choosing optical mode pairs that produce appropriate acousto-optic overlaps.

Before we push our optomechanical system into the strong coupling regime, we performed several OMIT measurements at low input control laser powers ($< 300\ \mu W$) to characterize coupling rates and dissipation rates within our optomechanical system. We determine g_{m}, Γ_{m} and κ by fitting experimentally obtained OMIT spectrum to Eq. (5.40). Even though the optical mode weakly couples to many acoustic modes, OMIT spectra measured at low input control laser powers are described well by considering coupling to just 3 acoustic modes (see Fig. 6.5**a**). From the values of g_{m} obtained for the 3 acoustic modes (see Fig. 6.5**b**) as a function of input control laser power P_{in}, we determine that the coupling strength to the acoustic mode directly

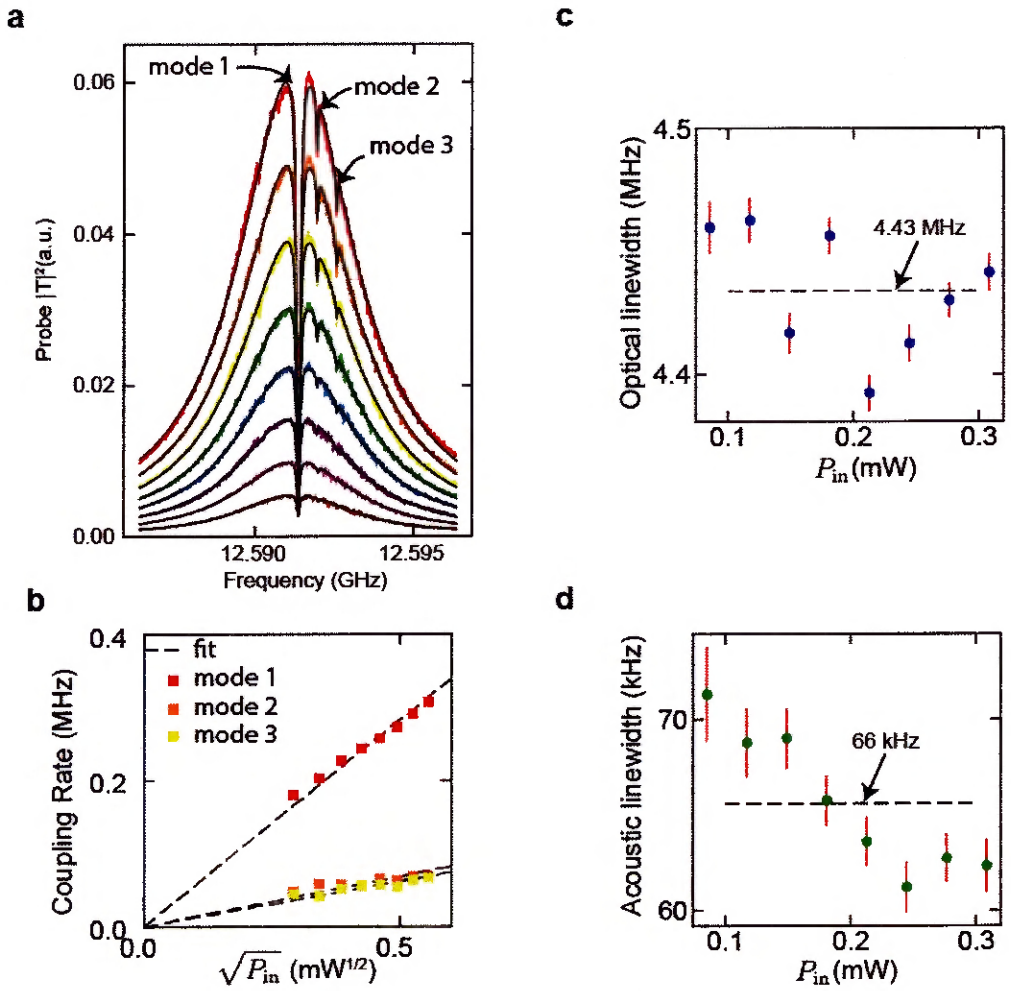

Figure 6.5: **Coupling to a single acoustic mode.** (a) OMIT measurements at low powers (86μW to 309μ W) when coupled primarily to a single acoustic mode. (b)-(d) Such spectra at low powers can be used to extract g_m, κ, and Γ_m. Adapted from Ref. [112].

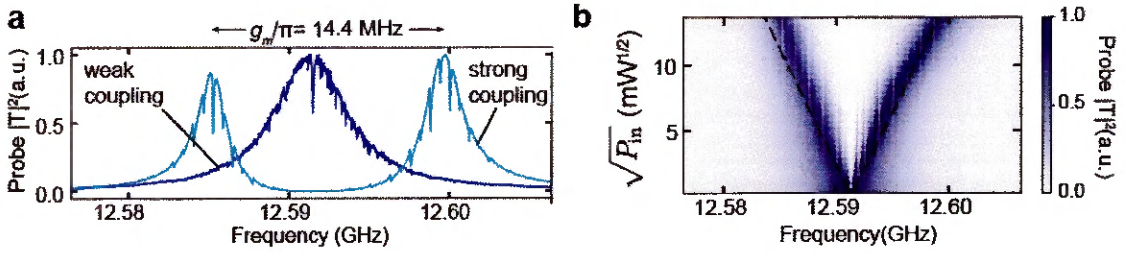

Figure 6.6: **Enhancing the optomechanical coupling rate.** (**a**) As we push our system into the strong coupling regime by enhance g_m, we observe the formation of two hybridized modes that are part light and part sound. (**b**) The energy splitting between these two eigenmodes is given by $2g_m$, which increases proportional to $\sqrt{P_{\rm in}}$ as expected from theory. Adapted from Ref. [112].

on resonance (red) with the optical cavity mode is about 5 times larger than that for the other weakly coupled acoustic modes (yellow and orange). From fits to the OMIT spectrum (see Fig. 6.5**c-d**), we also find that $\kappa = 2\pi \times (4.43 \pm 0.02)$ MHz and $\Gamma_{\rm m} = 2\pi \times (66 \pm 3)$ kHz. Note that we assumed equal intrinsic mechanical damping rate ($\Gamma_{\rm m}$) for the three longitudinal acoustic modes having nearly equal frequencies. Since $g_{\rm m} = \sqrt{N_1} g_0^{\rm m}$, we use the experimentally measured $g_{\rm m}$ along with intracavity photon number (N_1) determined from $P_{\rm in}$ to obtain the single photon coupling rate $g_0^{\rm m} = 2\pi \times (23 \pm 1)$ Hz. Note that $g_0^{\rm m}$ obtained experimentally agrees well with with the theoretically predicted value of $\sim 2\pi \times 24$ Hz (see Chapter 5).

To enter the strong coupling regime, we enhance g_m by increasing the intracavity photon number of mode a_1. OMIT spectra as seen in Fig. 6.6a reveals a clear normal-mode splitting resulting from the hybridization of the acoustic mode (b_m) with the optical mode (a_2). We observe a normal-mode splitting ($2g_m$) that increases proportional to $\sqrt{P_{\rm in}}$ (see Fig. 6.6b). This is expected from theory since $g_m \propto \sqrt{N_1} \propto \sqrt{P_{\rm in}}$. At the highest input optical power $P_{\rm in} = 187$ mW used in our experiments, we observe a normal-mode splitting $2g_m = 2\pi \times 14.4$ MHz. Note that we are able to reach such large coupling rates because the loss loss optical cavity that uses pristine quartz crystal supports a very large intracavity photon number $N_1 \simeq 1.1 \times 10^{11}$. This intracavity photon number is more than 7 order of magnitude larger than those

supported by comparable GHz-frequency optomechanical systems [170].

In addition to large optomechanical coupling rates, our system support low loss optical and acoustic modes. For this reason, we can readily push our system in the regime of strong coupling. From our measurements, we find that the coherent coupling rate far exceeds the dissipation rates of both the optical mode ($2g_{\rm m}/\kappa \simeq 3$) and the acoustic mode ($2g_{\rm m}/\Gamma_{\rm m} \simeq 220$), indicating that our system is in the strong coupling regime. In fact, even though our system operates at ~ 10 K temperatures ($n_{\rm th} \simeq 25$), we find that the coherent coupling rate, $2g_m$, far exceeds the mechanical thermal decoherence rate, $\gamma_m = n_{\rm th}\Gamma_m$ ($2g_m/\gamma_m \simeq 9$). This means that our system meets the more stringent criteria of quantum-coherent coupling necessary for quantum control of mechanical motion [168].

To demonstrate characteristic anti-crossing feature in the strong coupling regime, we vary the frequency (Δ) of the optical mode to bring it on resonance with the acoustic mode. Since the optical FSR, Δ, depends on the temperature, T, of our system, we can readily tune Δ to match the acoustic mode frequency, $\Omega_{\rm m}$. At the highest control laser power, we measure transmission spectra of the optical mode (a_2) as we vary T. The measurements seen in Fig. 6.7**a** reveals a clear anti-crossing at $T = 7.6$ K when $\Delta \simeq \Omega_{\rm m}$, which agrees well with our predictions. Note that dashed black line in Fig. 6.7**a**, shows how Δ changes with T, which we obtained by fitting the spectra to theoretical expression for probe transmission (see Eqn. 5.33).

In addition to these frequency domain measurements, we performed time-domain measurements of strong-coupling. These measurements permits us to study the fundamental origins of acoustic dissipation and noise in pristine crystalline solids and explore technological potential of acoustic systems for quantum information storage. Moreover, time dependent control of our system is a stepping stone towards utilizing our optomechanical interactions for deterministic quantum state transfer between light and mechanics. To time-dynamics of our system, we pulsed a weak probe light

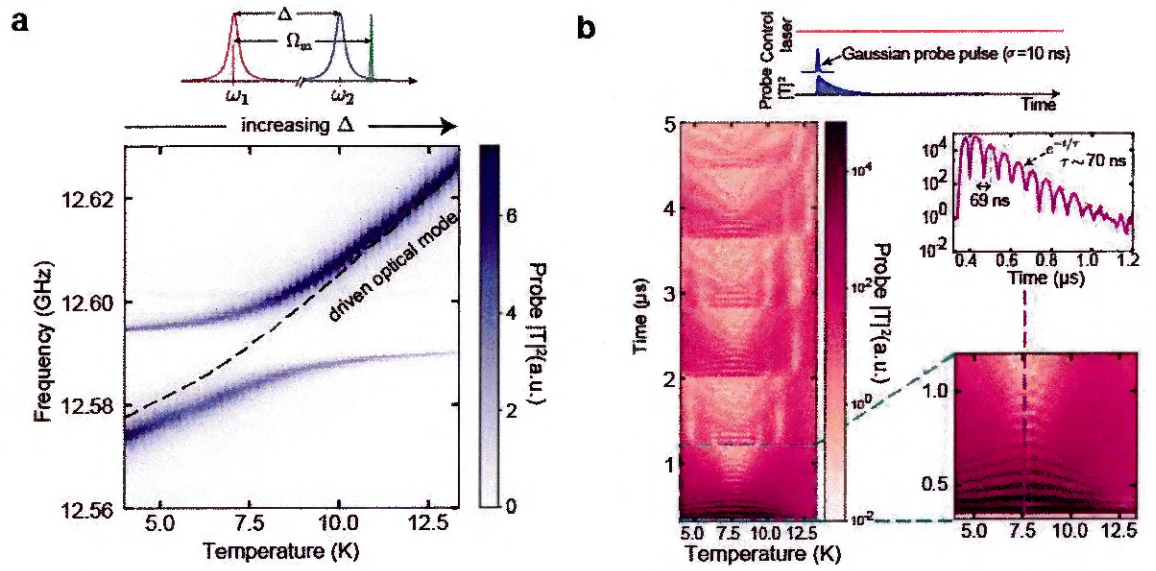

Figure 6.7: **Frequency and time-domain dynamics in the strong coupling regime.** (a) We observe an avoided crossing as we bring the optical mode (Δ) in resonance with the optical mode. Since the optical FSR changes with temperature, we tune Δ by changing the cryostat's temperature. (b) Time-domain response of the system taken at the same set of temperatures as in (a). Probe transmission spectrum after a pulse probe is turned on reveals oscillations at every 69 ns $\sim 2\pi/2g_m$ and exponential decay at timescale $\tau \sim 70$ ns $\sim 2/\kappa$. Additional revivals in the time-domain data is a consequence of weak coupling to a multitude of acoustic modes outside the Brillouin gain bandwidth. Adapted from Ref. [112].

(ω_2) while maintaining a strong continuous drive at ω_1 (see Fig. 6.7**b**). As explained in Section 6.3, a heterodyne signal resulting from the interference between the control and the probe light transmitted through the cavity provides phase-sensitive detection of the probe light as a function of time. These time-domain measurements as seen in Fig. 6.7**b**, were performed at the same temperatures as the frequency-domain measurements shown in Fig. 6.7**a**, showed charactristic Rabi oscillations when two resonators coherently exchange energy in the strong coupling regime [109]. As expected from theory (see Fig. 6.3), we observe increasing frequency of such oscillations when the optical mode is far detuned form the acoustic mode. At $T = 7.6$ K (when $\Delta \simeq \Omega_{\rm m}$), we observe coherent oscillations with a period of 69 ns ($\equiv 1/14.5$ MHz), which is consistent with the normal-mode splitting $2g_{\rm m} = 2\pi \times 14.4$ MHz extracted from frequency domain measurements. As seen in Fig. 6.7**b**, the time constant τ for this energy decay is 70 ns ($\equiv 1/(2\pi \times 2.27$ MHz)), which agrees well with the energy decay rate of $(\kappa + \Gamma_{\rm m})/2 \approx \kappa/2 = 2\pi \times 2.22$ MHz of the hybridized modes.

Surprisingly, we observe revivals of the coherent oscillations even after $t \gg \tau$ (see Fig. 6.7**a**). These nontrivial features appear because the spectrally-broad probe pulse excites not just a single strongly coupled acoustic mode but many weakly coupled acoustic modes outside the phase-matching bandwidth. Due to the modulation in the coupling strength produced by the phase matching conditions, $g_0^{\rm m}$ is suppressed for alternating acoustic mode numbers m outside the phase matching bandwidth (see Fig. 5.8**c**). For this reason, the observed revivals have a period of 0.82 μs, corresponding to a frequency of 1.2 MHz, which is approximately twice the acoustic free-spectral range of 610 kHz. Since the lifetimes of such weakly coupled modes approach the intrinsic mechanical decay time of the uncoupled system, $1/\Gamma_{\rm m} \simeq 2.4$ μs, the revivals are sustained for $t \gg \tau$.

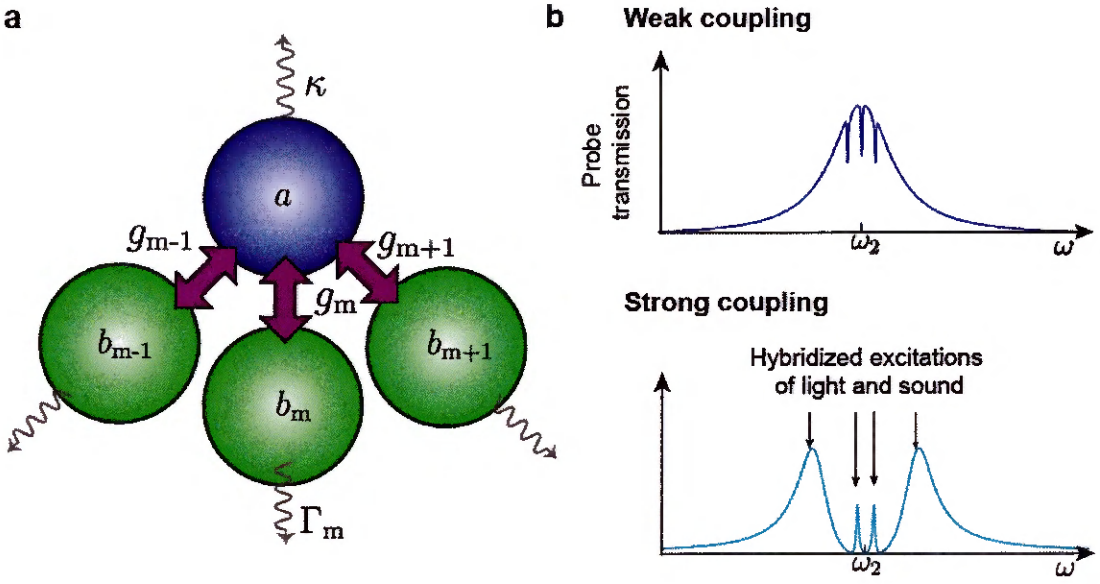

Figure 6.8: **Multimode strong coupling** (**a**) We reconfigure our optomechanical system so that one optical mode couples strongly to three acoustic modes. (**b**) In this regime, we expect four hybridized modes that are part light and part sound. Adapted from Ref. [112].

6.5 Observation of strong coupling to multiple acoustic modes

In the earlier section, we saw how weak coupling to a multitude of phonon mode led to nontrivial time dynamics in our optomechanical system. To further explore such multimode dynamics in the strong coupling regime, we tailor our optomechanical system so that a single optical mode strongly couples to three phonon modes. As explained in chapter 5, we accomplish this by changing the optical wavelength to select a different pair of optical modes whose acousto-optic overlap permits efficient coupling to more than one phonon mode.

We begin by performing OMIT measurements at low input control laser powers ($< 496\mu$W) to characterize coupling rates and dissipation rates. The OMIT spectra taken at low power (see Fig. 6.9**a**) reveals three OMIT dips, corresponding to coupling to three phonon modes separated by the acoustic FSR ($\delta/2\pi$) of 610 ± 10 kHz. This

measured acoustic FSR agrees well with the theoretically predicted FSR $v_a/2L_{ac}$ = 630 kHz. To determine coupling rates to these three acoustic modes near 12.684 GHz, we fit the experimentally obtained OMIT spectra to the following equation [111]

$$P_d(\Omega) \propto a^{\dagger}_{2,out} a_{2,out} = \left| \frac{\kappa_{ext}}{i(\Omega - \Delta) - \frac{\kappa}{2} + \sum_m \frac{g_m^2}{-i(\Omega - \Omega_m + \Gamma_m/2)}} \right|^2, \tag{6.10}$$

where $\Omega = \omega_p - \omega_1$ is the pump-probe detuning, $\Delta = \omega_2 - \omega_1$ is the optical FSR, g_m is the coupling rate to acoustic mode at frequency Ω_m having a intrinsic dissipation rate of Γ_m, κ (κ_{ext}) is the decay rate (output coupling rate) of the optical mode at ω_2. A plot of the coupling rates as a function of $\sqrt{P_{in}}$ as seen in Fig. 6.9**b** shows the expected linear dependence. This linear dependence can be used to extrapolate the following values for the coupling rates $g_m/2\pi$ at the highest input control laser power (P_{in}= 152 mW): $g_1 = 2\pi \times (4.9 \pm 0.1)$ MHz, $g_2 = 2\pi \times (4.0 \pm 0.1)$ MHz and $g_3 = 2\pi \times (3.7 \pm 0.1)$ MHz. From the fits to the OMIT spectra, we find $\kappa = 2\pi \times (2.52 \pm 0.08)$ MHz and $\Gamma_m = 2\pi \times (67 \pm 10)$ kHz. Since $g_1, g_2, g_3 > \kappa/2 \gg \delta \gg \Gamma_m/2$, this system is in the multimode strong coupling regime.

Before we consider coupling of a single optical mode to three phonon modes, let us use the Hamiltonian formulation presented in section 6.2, to understand the salient features of multimode strong coupling regime. To do this, let us consider a simpler case of a single optical mode (a_2) coupled strongly to just two phonon modes two phonon modes (b_1, b_2). We also assume that the modes are separated by 2δ, where δ is the acoustic free spectral range. Furthermore, we assume that $g_1 = g_2 \equiv g$, $\Gamma_1 = \Gamma_2 \equiv \Gamma$, and $\Omega_{1,2} = \Delta \mp \delta$. The Hamiltonian of this three coupled oscillator system in the basis of a_2, b_1, and b_2 is given by

$$H_{eff} = \begin{bmatrix} \Delta - i\kappa/2 & -g & -g \\ -g^* & \Omega_1 - i\Gamma/2 & 0 \\ -g^* & 0 & \Omega_2 - i\Gamma/2 \end{bmatrix}. \tag{6.11}$$

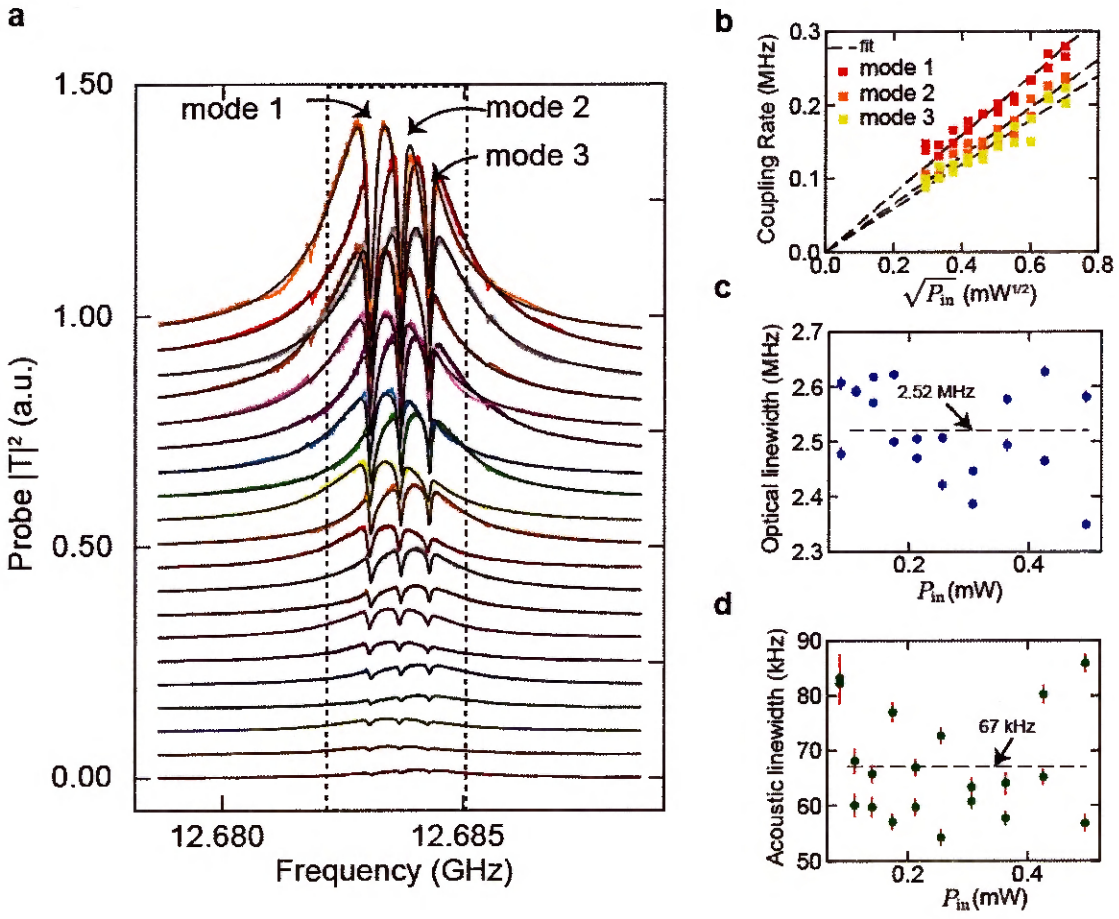

Figure 6.9: **Coupling to a three acoustic modes.** (a) OMIT measurements at low powers (86μW to 496μW) when coupled almost equally to three acoustic modes. (b)-(d) Such spectra at low powers can be used to extract g_m, κ, and Γ_m. Adapted from Ref. [112].

We can diagonalize this Hamiltonian to obtain three eigenmodes of the hybridized system. In the limit of large g, these eigenmodes become two "bright modes" $B_{\pm} = \frac{1}{\sqrt{2}}a_2 \pm \frac{1}{2}(b_1 + b_2)$ at frequencies $\omega_{\pm} = \Delta \pm \sqrt{2}g$ with dissipation rates $\kappa_{\pm} = \kappa/2$ and one "dark mode" $D = \frac{1}{\sqrt{2}}(b_1 - b_2)$ at frequency $\omega_{\mathrm{D}} = \Delta$ with a dissipation rate $\kappa_{\mathrm{D}} = \Gamma$. The bright modes are formed from the superposition of both the optical and the acoustic modes whereas the dark mode lacks an optical mode component, meaning that it does not couple to light. The dynamics of such a system, and the existence of such bright and dark modes, has been explored in an electromechanical system using a GHz frequency microwave resonator strongly coupled to two MHz frequency micromechanical oscillators [172]. However, this regime of coupling has not been previously accessible for optomechanical systems.

In the strong coupling regime, we observe four distinct peaks in the transmission spectrum of mode a_2, representing hybridization of a single optical mode with (a_2) with three phonon modes (b_1, b_2, and b_3). From a straightforward generalization of the effective Hamiltonian in Eq. 6.15 to the case of 3 phonon modes, given by

$$H_{\mathrm{eff}} = \begin{bmatrix} \Delta - i\kappa/2 & -g_1 & -g_2 & -g_3 \\ -g_1^* & \Omega_1 - i\Gamma/2 & 0 & 0 \\ -g_2^* & 0 & \Omega_2 - i\Gamma/2 & 0 \\ -g_3^* & 0 & 0 & \Omega_3 - i\Gamma/2 \end{bmatrix}. \tag{6.12}$$

we now expect four eigenmodes of the hybridized system seen in Fig. 6.10**b**. Of these eigenmodes, the two broad peaks correspond to the bright modes, whereas the two narrow peaks correspond to the dark modes.

We expect the decay rates of these dark modes to approach the mechanical decay rate $\Gamma_{\mathrm{m}} = 2\pi \times$ 67 kHz. However, high-resolution measurements of such modes at the highest control laser powers revealed decay rates $\Gamma_{\mathrm{d2}} = 2\pi \times 14$ kHz and $\Gamma_{\mathrm{d3}} = 2\pi \times 15$ kHz, which are approximately 5 times smaller than the original

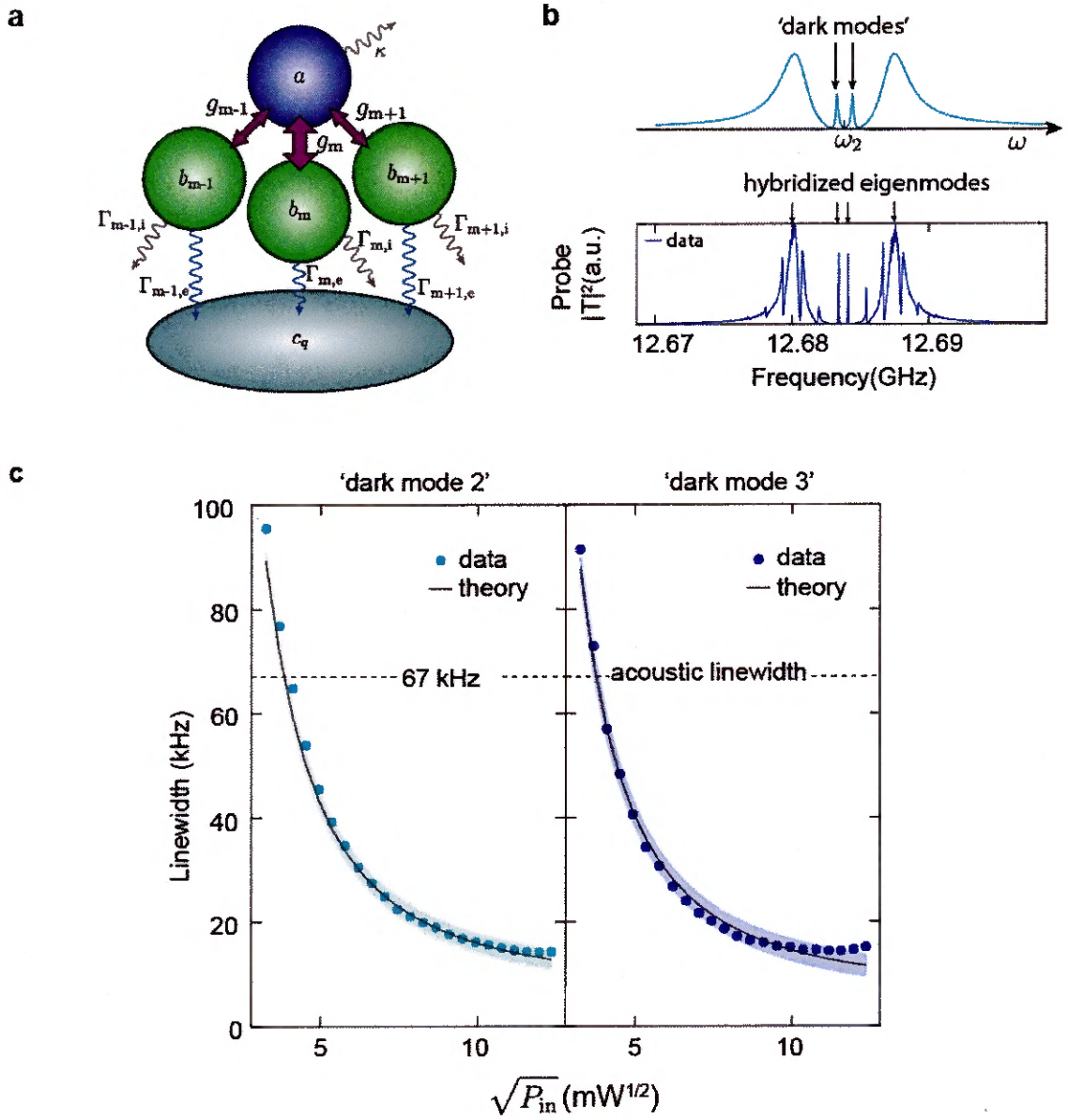

Figure 6.10: **Interference of decay channels in the multimode strong coupling regime.** (a) Schematics showing three acoustic modes decaying into a common bath. (b) Observation of four hybridized eigenmodes in the strong coupling regime. The two narrow resonance in the probe transmission spectrum correspond to optical 'dark modes', meaning the optical component of these eigenmodes vanishes for large g_m. c) Radiative decay channels for the acosutic modes can destructively interfere when the acoustic modes share a common decay channel. As a consequence, these dark modes have lifetimes that are about 5 times longer than those of the uncoupled acoustic modes. Adapted from Ref. [112].

acoustic dissipation rate Γ_m. Time-domain ring-down measurements using probe pulses with a narrow spectral bandwidth centered around each dark mode confirmed their long-lived nature. The measured decay time of $\tau_d \sim 10.9$ μs for both modes is consistent with the linewidths. This linewidth-narrowing phenomena is surprising because these eigenmodes, which are hybridized excitations of light and sound, have decay rates that are smaller than the optical and the mechanical decay rates of the uncoupled system.

6.6 Line-narrowing Phenomena and Interference of Dissipation Channels

Qualitatively, this line-narrowing phenomena for the eigenmodes in our optomechanical system can be described as a result of interference of dissipation pathways when the acoustic modes decay into a common bath. The acoustic loss in our system is dominated by radiative loss mechanisms such as beam diffraction and beam walk-off. As a result, the longitudinal acoustic modes, which have nearly identical Gaussian transverse mode profiles, decay into a common continuum of higher order transverse modes (i.e. the bath modes) that span the entire crystal. Since a dark modes is anti-symmetric superposition of two acoustic modes that decay into a common bath modes, the dissipation pathways can destructively interfere and lead to line-narrowing beyond that of the linewidth of the uncoupled system, which is dominated by radiative loss mechanisms. This phenomena is analogous to the linewidth narrowing observed for anti-symmetric supermode formed by coupling two identical (same frequency) ring resonators to a single optical waveguide.

6.6.1 Dissipative Coupling Mediated by a Common Reservoir

This interference of dissipation pathways for the acoustic modes can be described more quantitatively by including "dissipative coupling" terms of the form $H_{mn} = -i(\Gamma_{mn}/2)b_m^\dagger b_n$ in the Hamiltonian of the system [173, 174]. Here, Γ_{mn} represents the dissipative coupling rate between two acoustic modes b_n and b_m mediated by the bath and it is related to the extrinsic (or radiative) dissipation rate by the following relation

$$\Gamma_{mn} = \sqrt{\Gamma_{m,e}\Gamma_{n,e}} \tag{6.13}$$

Please refer to the Appendix E for more details on how modes decaying into common bath gives rise to such dissipative coupling terms H_{mn}.

To understand the line-narrowing phenomena and obtain analytical expressions for linewidth of the dark mode as we push our system deeper into the multimode strong coupling regime, we begin by considering the simplest case of two acoustic modes (b_1 and b_2) coupled to a single optical mode (a_2). We also assume that the modes are separated by 2δ, where δ is the acoustic free spectral range. Furthermore, we assume that $g_1 = g_2 \equiv g$, $\Gamma_1 = \Gamma_2 \equiv \Gamma$, and $\Omega_{1,2} = \Delta \pm \delta$. The Hamiltonian of this system including the dissipative coupling terms in the basis of a_2, b_1, and b_2 is given by

$$H_{\text{eff}} = \begin{bmatrix} \Delta - i\frac{\kappa}{2} & -g & -g \\ -g^* & \Omega_1 - i\frac{\Gamma}{2} & -i\frac{\Gamma_{12}}{2} \\ -g^* & -i\frac{\Gamma_{12}}{2} & \Omega_2 - i\frac{\Gamma}{2} \end{bmatrix}. \tag{6.14}$$

Working on the rotating frame of the optical mode (a_2) we can further simplify this Hamiltonian to get

$$H'_{\text{eff}} = \begin{bmatrix} -i\frac{\kappa}{2} & -g & -g \\ -g^* & \delta - i\frac{\Gamma}{2} & -i\frac{\Gamma_{12}}{2} \\ -g^* & -i\frac{\Gamma_{12}}{2} & -\delta - i\frac{\Gamma}{2} \end{bmatrix}. \tag{6.15}$$

By defining symmetric ("bright"), $B = (b_1 + b_2)/\sqrt{2}$, and anti-symmetric ("dark"), $D = (b_1 - b_2)/\sqrt{2}$, superpositions of the acoustic modes we can rewrite our effective in the basis of a_2, B, and D as

$$H''_{\text{eff}} = \begin{bmatrix} -i\frac{\kappa}{2} & \sqrt{2}g & 0 \\ \sqrt{2}g & -i\frac{\Gamma+\Gamma_{12}}{2} & \delta \\ 0 & \delta & -i\frac{\Gamma-\Gamma_{12}}{2} \end{bmatrix}. \tag{6.16}$$

In this basis, we already see that the effective dissipation rate for the dark mode is given by $(\Gamma - \Gamma_{12})$. We also see from this Hamiltonian that only the bright mode directly couples to the optical mode, while dark mode is coupled to the bright mode by δ. The final basis transformation involves forming the hybridized states of a and B to give $B_\pm = (a + B)/\sqrt{2}$. If we also make the approximation that $\kappa \gg \Gamma, \Gamma_{12}$, the Hamiltonian in the basis of B_+, B_-, and D is given by

$$H'''_{\text{eff}} \simeq \begin{bmatrix} \sqrt{2}g - i\frac{\kappa}{4} & -i\frac{\kappa}{4} & \frac{\delta}{\sqrt{2}} \\ -i\frac{\kappa}{4} & -\sqrt{2}g - i\frac{\kappa}{4} & -\frac{\delta}{\sqrt{2}} \\ \frac{\delta}{\sqrt{2}} & -\frac{\delta}{\sqrt{2}} & -i\frac{\Gamma-\Gamma_{12}}{2} \end{bmatrix}. \tag{6.17}$$

From this Hamiltonian we can see that the dark rate has a dissipation rate given by

$$\Gamma_D = (\Gamma - \Gamma_{12}) + \frac{\kappa\delta^2}{2g^2} \tag{6.18}$$

Note that the first term on the right hand side of this equation comes from the interference of the decay pathways (or the coupling mediated by the bath cancels

the radiative decay channels for phonons). Whereas the second term comes from the coupling of the dark state, D, to the two bright modes B_+ and B_-, each of which has a decay rate of $\kappa/2$.

From Eqn. (6.18), we see that the linewidth of the dark mode decrease proportion to $1/g^2$, and for large g, $\Gamma_D \rightarrow (\Gamma - \Gamma_{12})$. This makes sense because at large g, the optical component of the Dark mode vanishes and the only contribution to its dissipation comes from the acoustic modes themselves.

When g is large and the acoustic dissipation rate for the acoustic modes were entirely due to radiative losses then $\Gamma_{12} = \sqrt{\Gamma_{1,e}\Gamma_{2,e}} = \sqrt{\Gamma^2} = \Gamma$, meaning $\Gamma_D \rightarrow 0$. However, as explained in Appendix E, in addition to the extrinsic dissipation channels we have considered so far, acoustic resonators also have intrinsic sources of dissipation such as scattering and absorption, where the phonon modes do not share common bath. In this case $\Gamma_D \rightarrow \Gamma_i$, where $\Gamma_i = \Gamma - \Gamma_e$ is the intrinsic acoustic dissipation rate. This intrinsic acoustic dissipation rate (Γ_i) is typically much smaller than acoustic linewidth (Γ) within pristine crystalline solids at cryogenic temperatures. So, we expect the lifetimes of these dark modes to be significantly longer than the lifetime of the uncoupled acoustic mode.

Analogously, to understand the experimentally observed line-narrowing phenomena when couple a single optical mode to three acoustic modes, we take the effective Hamiltonian of Eqn. 6.12 and include the dissipative coupling terms

$$H_{\text{eff}} = \begin{bmatrix} \Delta - i\frac{\kappa}{2} & -g_1 & -g_2 & g_3 \\ -g_1^* & \Omega_1 - i\frac{\Gamma}{2} & -i\frac{\Gamma_{12}}{2} & -i\frac{\Gamma_{13}}{2} \\ -g_2^* & -i\frac{\Gamma_{21}}{2} & \Omega_2 - i\frac{\Gamma}{2} & -i\frac{\Gamma_{23}}{2} \\ -g_3^* & -i\frac{\Gamma_{31}}{2} & -i\frac{\Gamma_{32}}{2} & \Omega_3 - i\frac{\Gamma}{2} \end{bmatrix}. \tag{6.19}$$

From the OMIT measurements at low power, we measured the coupling rates (g_1, g_2, and g_3), the dissipation rates (κ and Γ), phonon mode frequencies ($\Omega_1, \Omega_2, \Omega_3$),

and the optical mode spacing (Δ). We then numerically diagonalize the effective Hamiltonian in Eqn. (6.19) while adjusting $\Gamma_{12} = \Gamma - \Gamma_i$ by hand to obtain the theoretical dissipation rate curves in Fig. 6.10**c**. We see that the linewidth of the dark modes as a function of power, agrees well with the theoretical description of the system discussed above. Here, we only took $\Gamma_i = 2\pi \times 5$ kHz as the fit parameter, and this value is consistent with the independent measurements of the acoustic damping in quartz crystals at cryogenic temperatures [108].

Finally, we emphasize that our experiment combines three crucial ingredients that are necessary to observe the effect of linewidth narrowing beyond that of the bare acoustic modes. First, the extrinsic loss has to be dominant. Second, the multimode strong coupling to the optical mode effectively eliminates the frequency difference between the acoustic modes so that their extrinsic dissipation channels can interfere. Finally, the bath coupling that leads to this dissipation is approximately equal and in-phase so that this interference is destructive for the dark state that is decoupled from the optical mode in the limit of large g.

6.7 Conclusions and Outlook

In summary, we utilized resonant Brillouin interactions to dramatically increase the optomechanical coupling strength, permitting us to engineer strong coupling between optical photons ($\sim$ 200 THz) and high-frequency ($\sim$10 GHz) mechanical modes of a bulk acoustic resonator. Since such resonators provide access to a multitude of long-lived, high-frequency phonons, we strongly coupled a single optical mode to more than one phonon modes as a basis for more sophisticated control of mechanical motion. Using non-trivial mode hybridizations in this so-called multimode strong coupling regime, we created eigenmodes that had lifetimes that significantly ($\sim 5\times$) longer than those of the modes the uncoupled system. We developed a theoretical framework

to understand such lifetime enhancement by considering dissipative couplings between acoustic modes that share a common bath.

Even though our system is in the quantum-coherent strong coupling regime necessary to observe quantum effects [168], we need to make a number of improvements to our system to achieve robust ground state control of phonons for aforementioned applications. First, we need to initialize our mechanical system deep in its quantum ground state. Since the thermal occupation number, $n_{\mathrm{th}} < 0.1$ for 12.6 GHz phonons at temperatures < 250 mK, we can reach quantum ground state of mechanical motion by using a standard dilution refrigerator.

For operation at mK temperatures, we need to reduced input optical powers and pay careful attention to optical scattering losses. Decreasing κ by improving mirror reflectivity to 99.99 % and utilizing low-loss crystalline substrates with larger Brillouin gain (such as TeO_2) could enable access to the strong coupling regime at < 100 μW input powers. These improvements, along with low duty-cycle pulsed operation of the control laser with micro-Watt average powers could make operation in dilution refrigerators feasible.

These improvements could offer new opportunities for harnessing bulk acoustic phonons for future applications ranging from quantum information to precision metrology. Through time dependent control of the coupling rate in the strong coupling regime, it should be possible to deterministically swap quantum states between the optical domain and the acoustic domain for quantum transduction and quantum information storage (i.e. quantum memories). If the input fields are quantum states (such as single photons), it should also be possible to harness optomechanical strong coupling to deterministically create non-classical mechanical states and explore quantum phenomena within macroscopic objects [175]. More generally, it has been shown that acoustic waves within BAW resonators couple strongly to a variety of other quantum systems such as superconducting qubits [110], defect centers [176],

and microwave fields [177]. Therefore, deterministic control of bulk acoustic waves using light in the strong coupling regime could be a valuable tool for connecting various quantum systems. Last but not least, multimode strong coupling between light and mechanical modes of a BAW resonator could be used to probe intrinsic phonon loss mechanisms on practically any transparent crystal.

Chapter 7

Conclusions and Outlook

In this dissertation, we presented an alternative strategy that relies on phase-matched Brillouin interactions, rather than wavelength-scale structural control, to optically access GHz frequency mechanical modes within macroscopic crystalline solids. Exploration of stimulated Brillouin scattering within crystalline solids at cryogenic temperatures yielded surprisingly long lifetimes for high-frequency phonon modes and new dynamics for light-sound coupling.

To access such long-lived phonons modes, we shaped the surfaces of the crystals to create stable acoustic cavities that mitigate extrinsic losses. Analogous to Gaussian resonator design in optics, we formulated novel analytical design guidelines, numerical techniques, and microfabrication techniques to create stable plano-convex acoustic cavities and permitted phonon mode engineering. Beyond optomechanics, these findings were crucial to creating emerging hybrid quantum systems in which a superconducting qubit is coupled to a high-frequency bulk acoustic wave resonator.

Through the theoretical treatment developed to understand the dynamics of Brillouin scattering at low temperatures, we bridged the gap between cryogenic Brillouin physics and cavity optomechanical systems. As a result, bulk acoustic phonons within practically any transparent crystalline solid can now be harnessed to create ro-

bust high-frequency cavity optomechanical systems. Leveraging the well-established framework of optomechanics, we were then able to engineer strong interaction between light fields and bulk acoustic wave as a basis for deterministic quantum control of phonons.

With these demonstrations, one can envision utilizing optical control of bulk acoustic waves a variety of classical technologies, including new types of lasers and oscillators. At cryogenic temperatures, when the acoustic dissipation rate is significantly smaller than the optical dissipation rate, we demonstrated regenerative self-oscillation of the mechanical mode. However, we can also engineer our system so that the optical dissipation rate is much smaller than the acoustic dissipation rate to achieve Brillouin lasing. Brillouin lasing within our optomechanical system has a potential to be highly efficient (slope efficiency $> 80\%$), avoid cascading, handle large powers (1-100 W output powers), and have sub-Hz linewidth. Moreover, by adapting the microfabrication techniques developed in this dissertation to make on-chip optical lenses, it may be possible to demonstrate high-performance Brillouin lasers on-chip.

Optomechanical systems utilizing bulk acoustic phonons are promising platforms for experiments in the quantum regime. Operation of our high-frequency optomechanical system at temperatures < 250 mK should allow access to the quantum ground state of the mechanical resonator. Once initialized to the quantum ground state, probabilistic schemes for heralding and readout of non-Gaussian mechanical states are feasible in our optomechanical system because it is possible to achieve sub-phonon-level counting sensitivity [111, 178]. Such probabilistic protocols for quantum optical control of macroscopic phonons have a potential to be more robust against deleterious effects of optical absorption.

Beyond probabilistic schemes, our multimode optomechanical system presents opportunities for deterministic quantum control of phonons. Some early experimental measurements suggest that it is possible to further increase the finesse of our opti-

cal cavity from the current value of 5000 to 30000, which would allow us to access the strong coupling regime at < 100 μW input powers. These improvements, along with low duty-cycle pulsed operation of the control laser with micro-Watt average powers could make operation in dilution refrigerators feasible. Deterministic optical control of such long-lived, high-frequency phonons at cryogenic temperatures could offer a path towards efficient quantum transducers and quantum information storage devices.

Appendix A

Hamiltonian Treatment: More details

For a system of finite mode volume, we can use the following normal mode expansion to write

$$\mathbf{D}(\mathbf{r}) = \sum_{\gamma} \sqrt{\frac{\hbar\omega_{\gamma}}{2}} a_{\gamma}(t)\tilde{\mathbf{D}}_{\gamma}(\mathbf{r}) + \text{H.c.} \tag{A.1}$$

$$\mathbf{u}(\mathbf{r}) = \sum_{\Lambda} \sqrt{\frac{\hbar\Omega_{\Lambda}}{2}} b_{\Lambda}(t)\tilde{\mathbf{u}}_{\Lambda}(\mathbf{r}) + \text{H.c.} \tag{A.2}$$

where $\tilde{D}_{\gamma}(\mathbf{r})$ is the eigenmode obtained by solving the Maxwell's equation, a_{γ} is the optical mode amplitude operator and ω_{γ} is the optical mode frequency. $\tilde{u}_m(\mathbf{r})$ is the acoustic mode obtained by solving the elastic-displacement equation, b_{Λ} is the acoustic mode amplitude operator, and Ω_{Λ} is the phonon frequency. Note that γ and Λ are collective mode indices. The optical and acoustic modes are normalized such

that

$$\frac{1}{\epsilon_0}\int \mathrm{d}^3r\ \beta_r(\mathbf{r})\tilde{\mathbf{D}}^*_\gamma(\mathbf{r})\cdot\mathbf{D}_{\gamma'}(\mathbf{r}) = \delta_{\gamma,\gamma'} \tag{A.3}$$

$$\int \mathrm{d}^3r\ \rho(\mathbf{r})\Omega_\Lambda\Omega_{\Lambda'}\tilde{\mathbf{u}}^*_\Lambda(\mathbf{r})\cdot\tilde{\mathbf{u}}_{\Lambda'}(\mathbf{r}) = \delta_{\Lambda,\Lambda'} \tag{A.4}$$

The mode amplitude operators satisfy the following commutation relations:

$$[a_\gamma, a_{\gamma'}] = 0,\ [a_\gamma, a^\dagger_{\gamma'}] = \delta_{\gamma,\gamma'}, \tag{A.5}$$

$$[b_\Lambda, b_{\Lambda'}] = 0,\ [b_\Lambda, b^\dagger_{\Lambda'}] = \delta_{\Lambda,\Lambda'}. \tag{A.6}$$

Using the normal mode expansion, the normalizations and the commutation relations we can write down the optical, acoustic and interaction Hamiltonian in terms of the mode amplitude operators as

$$H^{\mathrm{ph}} = \sum_\Lambda \hbar\Omega_\Lambda(b^\dagger_\Lambda b_\Lambda + 1/2) \tag{A.7}$$

$$H^{\mathrm{opt}} = \sum_\gamma \hbar\omega_\gamma(a^\dagger_\gamma a_\gamma + 1/2) \tag{A.8}$$

$$H^{\mathrm{int}} = \sum_{\gamma,\gamma',m}\int \mathrm{d}\mathbf{r}\ \tfrac{1}{2\epsilon_0}\sqrt{\tfrac{\hbar\omega_\gamma\hbar\omega_{\gamma'}\hbar\Omega_m}{8}}p^{ijkl}\left(a_\gamma\tilde{D}^i_\gamma(\mathbf{r})+\mathrm{H.c.}\right)\left(a_{\gamma'}\tilde{D}^j_{\gamma'}(\mathbf{r})+\mathrm{H.c.}\right)\left(b_m\tilde{s}^{kl}_m(\mathbf{r})+\mathrm{H.c}\right) \tag{A.9}$$

This treatment is valid for any system with finite size having discrete optical and acoustic modes. However, we are interested in looking at the interaction between traveling wave pump photons with mode profile, wave-vector, and frequency given by $(\mathbf{D}_p(\mathbf{r}), k_p, \omega_p)$ with the Stokes wave photons with mode profile, wave-vector, and frequency $(\mathbf{D}_s(\mathbf{r}), -k_s, \omega_s)$ mediated by phonons. Therefore, the optical eigenmodes of our interest, ignoring small reflections at the crystal end facets, are traveling-waves

of infinite extent in z (equivalent to a system with length $l \to \infty$)

$$\tilde{\mathbf{D}}_\gamma(\mathbf{r}) \mapsto \mathbf{D}_\gamma(\mathbf{r})e^{ikz}. \tag{A.10}$$

Therefore, using the following normal mode expansion

$$\mathbf{D}(\mathbf{r}) = \int \frac{\mathrm{d}k}{\sqrt{2\pi}}\sqrt{\frac{\hbar\omega_p(k)}{2}}a_{pk}(t)\mathbf{D}_p(\mathbf{r})e^{ikz} + \int \frac{dk}{\sqrt{2\pi}}\sqrt{\frac{\hbar\omega_s(k)}{2}}a_{sk}(t)\mathbf{D}_s(\mathbf{r})e^{ikz} + \text{H.c.} \tag{A.11}$$

to write the optical Hamiltonian as

$$H^{\text{opt}} = \int \mathrm{d}k\ \hbar\omega_p(k)a_{pk}^\dagger a_{pk} + \int \mathrm{d}k\ \hbar\omega_s(k)a_{sk}^\dagger a_{sk}. \tag{A.12}$$

It is important to note that we have assumed that the eigenmode profiles $\mathbf{D}_p(\mathbf{r})$ and $\mathbf{D}_s(\mathbf{r})$ for the pump and Stokes traveling waves in a narrow band about their respective carrier wave-vector remains unchanged. Here, the mode amplitude operators a_k have units of $\sqrt{[\text{Length}]}$. The optical mode profiles are normalized at each point in z such that

$$\frac{1}{\epsilon_o}\int \mathrm{d}\mathbf{r}_\perp\ \beta_r(\mathbf{r})\mathbf{D}_p^*(\mathbf{r})\cdot\mathbf{D}_p(\mathbf{r}) = 1 \tag{A.13}$$

$$\frac{1}{\epsilon_o}\int \mathrm{d}\mathbf{r}_\perp\ \beta_r(\mathbf{r})\mathbf{D}_s^*(\mathbf{r})\cdot\mathbf{D}_s(\mathbf{r}) = 1. \tag{A.14}$$

Extended coherence length of the phonons and the formation of discrete standing wave cavity modes for acoustic waves results in markedly different nonlinear optical susceptibility in the coherent-phonon limit. We will explore this in the next subsection.

In the coherent-phonon limit, where the coherence lengths of acoustic waves are much longer than crystal length ($L_{\text{ac}} \gg L$), acoustic waves can form standing wave

cavity modes that extend throughout the crystal. Therefore, the modes of our interest are of the form

$$\tilde{\mathbf{u}}_\Lambda(\mathbf{r}) \mapsto \mathbf{U}_m(\mathbf{r})(e^{iq_m z} + e^{-iq_m z})/\sqrt{2} \tag{A.15}$$

where the standing wave acoustic modes have discrete wavevector $q_m = 2\pi m/L$, for any integer m, and $\mathbf{U}_m(\mathbf{r})$ is the mode profile that varies slowly in z compared to the carrier wavevector. Since we have discrete acoustic modes in the coherent-phonon limit, the acoustic Hamiltonian is

$$H^{\text{ph}} = \sum_m \hbar\Omega_m b_m^\dagger b_m, \tag{A.16}$$

where we have used the following normal mode expansion for the acoustic displacement field

$$\mathbf{u}(\mathbf{r}) = \sum_m \sqrt{\frac{\hbar\Omega_m}{2}} b_m \frac{\mathbf{U}_m(\mathbf{r})}{\sqrt{2}}(e^{iq_m z} + e^{-iq_m z}) + \text{H.c.} \tag{A.17}$$

and acoustic mode profiles are normalized so that

$$\int \mathrm{d}^3 r\ \Omega_m^2 \rho(\mathbf{r})\mathbf{U}_m(\mathbf{r})^* \cdot \mathbf{U}_m(\mathbf{r}) = 1. \tag{A.18}$$

We can now use Eq. (A.9) along with the the normal mode expansion in Eq. (A.17) and Eq. (A.11) to write down the following interaction Hamiltonian in the coherent-phonon limit

$$H^{\text{int}} = \sum_m \int \frac{\mathrm{d}k\mathrm{d}k'}{2\pi} \int \mathrm{d}z\ \hbar g_o^m(z) e^{i(k'-k+q_m)z} a_{pk}^\dagger a_{sk'} b_m + \text{H.c.} \tag{A.19}$$

where $g_o^m(z)$ that characterizes the single-photon coupling rate is

$$g_o^m(z) \simeq \frac{\sqrt{\hbar\omega_p\omega_s\Omega_m}}{4\epsilon_0}\int \mathrm{d}\mathbf{r}_\perp (D_p^i(\mathbf{r}))^* D_s^j(\mathbf{r}) p^{ijkl}(\mathbf{r}) \left(\frac{\partial U_m^k(\mathbf{r})}{\partial r^l} + iq_m\delta_{lz}U_m^k(\mathbf{r})\right). \tag{A.20}$$

As before, we have assumed that the coupling rate in the narrow band of wavevectors around the carrier wavevectors for pump and Stokes remains unchanged. This coupling rate between traveling wave photons and a discrete phonon mode has dimensions of Hz. Note that the wavevector k and k' for photons are continuous variables whereas the wavevector q_m for a phonon mode is discrete.

Appendix B

Hamiltonian transformed into real-space:coherent-phonon limit

Traveling wave acousto-optic interaction results in the spatial evolution of optical fields in z. In k-space this amounts to increasing occupation numbers for the mode amplitude operators around their respective carrier wavevectors. To transform the Hamiltonian of our system into real-space description, we define the following mode envelope operators for the optical fields

$$A_p(z) = \int \frac{\mathrm{d}k}{\sqrt{2\pi}}\, a_{pk} e^{i(k-k_p)z}, \tag{B.1}$$

$$A_s(z) = \int \frac{\mathrm{d}k}{\sqrt{2\pi}}\, a_{sk} e^{i(k+k_s)z}. \tag{B.2}$$

Taking the Fourier transform to write a_{pk} and a_{sk} in terms of $A_p(z)$ and $A_s(z)$ we can write Eq. (A.12) in terms of the mode envelope operators as [107, 115, 179]

$$\begin{aligned} H^{\mathrm{opt}} = &\int \mathrm{d}z\ \hbar\omega_p A_p^\dagger(z) A_p(z) - i \int \mathrm{d}z\ \hbar v_o A_p^\dagger(z) \partial_z A_p(z) \\ &+ \int \mathrm{d}z\ \hbar\omega_s A_s^\dagger(z) A_s(z) + i \int \mathrm{d}z\ \hbar v_o A_s^\dagger(z) \partial_z A_s(z), \end{aligned} \tag{B.3}$$

where we have assumed linear dispersion for optical waves in a bulk medium (i.e $\omega_p(k) = \omega_p(k_p) + v_o(k - k_p)$ and $\omega_p(k) = \omega_p(k_p) - v_o(k - (-k_s))$).Finally, the real-space optical Hamiltonian in Eq. (B.3) can be written succinctly in terms of the mode envelope operators as

$$H^{\text{opt}} = \int \mathrm{d}z\ \hbar A_p^\dagger(z)\hat{\omega}_{p,z}A_p(z) + \int \mathrm{d}z\ \hbar A_s^\dagger(z)\hat{\omega}_{s,z}A_s(z), \tag{B.4}$$

where the spatial operators $\hat{\omega}_{p,z} = \omega_p - iv_o\partial_z$ and $\hat{\omega}_{s,z} = \omega_s + iv_o\partial_z$. Note that the electric displacement field in Eq. (A.11) can be expressed in terms of the mode envelope operators as

$$\mathbf{D}(\mathbf{r}) \simeq \sqrt{\frac{\hbar\omega_p}{2}}\mathbf{D}_p(\mathbf{r})A_p(z)e^{ik_pz} + \sqrt{\frac{\hbar\omega_s}{2}}\mathbf{D}_s(\mathbf{r})A_s(z)e^{-ik_sz} + \text{H.c.}. \tag{B.5}$$

Finally, the interaction Hamiltonian in Eq. (A.19) can be written in real space in terms of the mode envelope operators as

$$H^{\text{int}} = \sum_m \int \mathrm{d}z\ \hbar g_0^m(z)e^{i(q_m - k_p - k_s)z}A_p^\dagger(z)A_s(z)b_m + \text{H.c.}. \tag{B.6}$$

Appendix C

Free-space cooperativity

For the derivation of free-space cooperativity, we use an alternate definition of cooperativity, which is equivalent to the definition of cooperativity in the main text. Cooperativity is also a figure of merit that compares the ratio of optical contribution to the mechanical damping and the intrinsic mechanical damping. We follow a derivation of cooperativity similar to that in cavity optomechanics [117,161,180] by finding an effective mechanical susceptibility in presence of the optomechanical interaction.

We look at the cooperativity for a phonon mode labeled by index m. We start by considering the coupled mode equations derived from the Hamiltonian in Appendix A with optical dissipation rate $\kappa/2$ and acoustic dissipation rate $\Gamma_m/2$ added phenomenologically as

$$\dot{a}_{sk} = \left(-i\omega_s(k) - \frac{\kappa}{2}\right) a_{sk} - i\int \frac{\mathrm{d}k'}{2\pi}\, g_m^*(k',k) a_{pk'} b_m^\dagger, \tag{C.1}$$

$$\dot{a}_{pk} = \left(-i\omega_p(k) - \frac{\kappa}{2}\right) a_{pk} - i\int \frac{\mathrm{d}k'}{2\pi}\, g_m(k,k') a_{sk'} b_m, \tag{C.2}$$

$$\dot{b}_m = \left(-i\Omega_m - \frac{\Gamma_m}{2}\right) b_m - i\int \frac{\mathrm{d}k\mathrm{d}k'}{2\pi} g_m^*(k,k') a_{sk'}^\dagger a_{pk} + f_{\mathrm{ext}}(t). \tag{C.3}$$

We have phenomenologically added external force $f_{\mathrm{ext}}(t)$ in the equation of motion for the phonon field to derive the effective mechanical susceptibility under optomechan-

ical coupling. In our system, we assume that the crystalline medium is essentially transparent to the traveling wave optical beams. The optical beams experience negligible loss inside the crystal. We will eventually take the limit of zero optical loss to derive our cooperativity.

We derive cooperativity in the limit of weak coupling and assuming undepleted pump. It is convenient to work in an interaction frame that is rotating at ω_p (i.e. $a_{sk}(t) \rightarrow \bar{a}_{sk}(t)e^{-i\omega_p t}$ and $a_{pk}(t) \rightarrow \bar{\alpha}_{pk}e^{-i\omega_p t}$). Note that the pump field is freely evolving and not changing in time. Hence, $\bar{\alpha}_{pk}$ is just a constant. So, we arrive at these equations of motion for Stokes and the phonon field

$$\dot{\bar{a}}_{sk}(t) = \left(-i\omega_s(k) + i\omega_p - \frac{\kappa}{2}\right)\bar{a}_{sk}(t) - i\int \frac{\mathrm{d}k'}{2\pi}\, g_m^*(k',k)\bar{\alpha}_{pk'}b_m^\dagger(t), \tag{C.4}$$

$$\dot{b}_m(t) = \left(-i\Omega_m - \frac{\Gamma_m}{2}\right)b_m - i\int \frac{\mathrm{d}k\mathrm{d}k'}{2\pi} g_m^*(k,k')\bar{a}_{sk'}^\dagger(t)\bar{\alpha}_{pk} + f_{\text{ext}}(t). \tag{C.5}$$

Now we make the undepleted pump approximation, so that $\bar{\alpha}_{pk} = \bar{\alpha}_{k_p}\delta(k-k_p)$ is a delta function that is peaked at the wavevector k_p. It is important to note that because $\delta(k-k_p)$ has units of L and our mode amplitude operators $\bar{\alpha}_{pk}$ has units of $\sqrt{L}$, $\bar{\alpha}_{k_p}$ has units of $1/\sqrt{L}$. Now, we perform the integrals in k-space in Eqs. (C.4) and (C.5) to obtain

$$\dot{\bar{a}}_{sk}(t) = \left(-i\Delta(k) - \frac{\kappa}{2}\right)\bar{a}_{sk}(t) - \frac{i}{2\pi}\bar{\alpha}_{k_p}\, g_m^*(k_p,k)b_m^\dagger(t), \tag{C.6}$$

$$\dot{b}_m(t) = \left(-i\Omega_m - \frac{\Gamma_m}{2}\right)b_m - i\bar{\alpha}_{k_p}\int \frac{\mathrm{d}k'}{2\pi} g_m^*(k_p,k')\bar{a}_{sk'}^\dagger(t) + f_{\text{ext}}(t), \tag{C.7}$$

where $\Delta(k) = -\omega_p + \omega_s(k)$ is the detuning between the pump and Stokes wave. $\bar{\alpha}_{k_p}$ is related to the input pump power incident on the crystal as [115]

$$P_p = \int \frac{\mathrm{d}k\mathrm{d}k'}{2\pi}\, \hbar\omega_p v_{gp} a_{pk'}^\dagger(t)a_{pk}(t)e^{i(k-k')z} = \frac{\hbar\omega_{pk}v_{gp}|\bar{\alpha}_{k_p}|^2}{2\pi}. \tag{C.8}$$

In the Fourier domain, using the the transformation $\bar{b}_m[\Omega] = \int_{-\infty}^{+\infty}\mathrm{d}t\; e^{i\Omega t}\bar{b}_m[t]$ and

$\bar{a}_{sk}[\Omega] = \int_{-\infty}^{+\infty} \mathrm{d}t\ e^{i\Omega t}\bar{a}_{sk}(t)$, we obtain

$$\bar{a}_{sk}[\Omega] = \frac{g_m^*(k_p,k)\bar{\alpha}_{k_p}}{2\pi}\frac{1}{\Omega - \Delta(k) + i\kappa/2}b_m^\dagger[\Omega]. \tag{C.9}$$

$$b_m[\Omega] = \frac{\bar{\alpha}_{k_p}}{\Omega - \Omega_m + i\Gamma_m/2}\int \frac{\mathrm{d}k'}{2\pi} g_m^*(k_p,k')\bar{a}_{sk'}^\dagger[\Omega] + \frac{1}{\Omega - \Omega_m + i\Gamma_m/2}f_{\mathrm{ext}}[\Omega] \tag{C.10}$$

Substituting Eq. (C.9) in Eq. (C.10) gives

$$b_m[\Omega] = \chi_{m,\mathrm{eff}}[\Omega]f_{\mathrm{ext}}[\Omega] \tag{C.11}$$

$$= \frac{1}{\Omega - \Omega_m + i\Gamma_m/2 + \sum(\Omega)}f_{\mathrm{ext}}[\Omega] \tag{C.12}$$

$$= \frac{1}{\Omega - (\Omega_m + \delta\omega[\Omega]) + i(\Gamma_m + \Gamma_{\mathrm{opt}}(\Omega))/2}f_{\mathrm{ext}}[\Omega], \tag{C.13}$$

where

$$\sum(\Omega) = -|\bar{\alpha}_{k_p}|^2 \int \tfrac{\mathrm{d}k'}{4\pi^2}\ |g_m(k_p,k')|^2 \left[\tfrac{\Omega-\Delta(k')}{(\Omega-\Delta(k'))^2+(\kappa/2)^2} + i\tfrac{\kappa/2}{(\Omega-\Delta(k'))^2+(\kappa/2)^2}\right]. \tag{C.14}$$

and the frequency dependent mechanical frequency $\delta\omega[\Omega] = -\mathrm{Re}\sum[\Omega]$ and the optical contribution to the damping is $\Gamma_{\mathrm{opt}}[\Omega] = 2\mathrm{Im}\sum[\Omega]$. We define the cooperativity in our system as the ratio of optical contribution to the phonon damping and the intrinsic phonon damping as $\mathcal{C}^{\mathrm{fs}} = \Gamma_{\mathrm{opt}}/\Gamma_m$. The optical contribution to the phonon damping is

$$\Gamma_{\mathrm{opt}}[\Omega] = 2\mathrm{Im}[\sum(\Omega)] = -2|\bar{\alpha}_{k_p}|^2 \int \tfrac{\mathrm{d}k'}{4\pi^2}\ \tfrac{\kappa/2}{(\Omega-\Delta(k'))^2+(\kappa/2)^2}|g_m(k_p,k')|^2. \tag{C.15}$$

$|g_m(k_p,k')|^2$, which is a sinc squared function, is peaked at the Stokes wavevector $k_s = -(\omega_p - \Omega)/v_s$. If we now take the limit of negligible optical loss (i.e. the limit where the sharply peaked Lorentzian in Eq.(C.15) samples the sinc squared function),

we obtain

$$\Gamma_{\text{opt}}[\Omega] \approx -2|\bar{\alpha}_{k_p}|^2|g_m(k_p,k_s)|^2 \int \frac{\mathrm{d}k'}{4\pi^2} \frac{\kappa/2}{(\Omega - v_s k' - v_p k_p)^2 + (\kappa/2)^2} \tag{C.16}$$

$$= -\frac{|\bar{\alpha}_{k_p}|^2}{2\pi v_{gs}}|g_m(k_p,k_s)|^2 \tag{C.17}$$

$$= -\frac{P_p}{\hbar\omega_p v_{gp} v_{gs}}|g_m(k_p,k_s)|^2. \tag{C.18}$$

When the frequency detuning between the pump and Stokes light matches the phonon mode frequency the cooperativity is given by

$$\mathcal{C}^{\text{fs}} = \frac{\Gamma_{\text{opt}}(\Omega_m)}{\Gamma_m} = \frac{P_p L^2 |g_0^m|^2}{\hbar\omega_p v_{gs} v_{gp} \Gamma_m}. \tag{C.19}$$

Appendix D

Derivation of Stability Criterion and anisotropy parameter

D.1 Anisotropy parameter and Stability Criterion

In this section, we derive the stability criterion for longitudinal acoustic modes in anisotropic crystalline medium along certain crystalline axes. We begin by considering a specific case of longitudinal modes propagating along x-cut silicon. We chose this specific crystalline cut because the dispersion surfaces are parabolic and symmetric along the propagation direction. We start with the Christoffel equation for elastic wave propagation in an anisotropic medium

$$\rho \frac{\partial^2 u_i}{\partial t^2} = c_{ijlm} \frac{\partial^2 u_m}{\partial x_j \partial x_l}, \tag{D.1}$$

where u_i is the i^{th} component of the acoustic displacement vector, c_{iklm} is the elastic constant tensor and ρ is the density of the medium. Using the symmetry property of

the elastic tensor in cubic crystal Eq. (D.1) reduces to

$$\rho\ddot{u}_1 = c_{11}u_{1,11} + c_{44}u_{1,22} + c_{44}u_{1,33} + (c_{12} + c_{44})(u_{2,12} + u_{3,13}), \tag{D.2}$$

$$\rho\ddot{u}_2 = c_{44}u_{2,11} + c_{11}u_{2,22} + c_{44}u_{2,33} + (c_{44} + c_{12})(u_{1,12} + u_{3,23}), \tag{D.3}$$

$$\rho\ddot{u}_3 = c_{44}u_{3,11} + c_{44}u_{3,22} + c_{11}u_{3,33} + (c_{12} + c_{44})(u_{1,13} + u_{2,23}), \tag{D.4}$$

where $c_{\alpha\beta}$ is the reduced elastic tensor coefficient, and $u_{m,jl} \equiv (\partial^2 u_m)/(\partial x_j \partial x_l)$. We see that the diffraction terms $(c_{44}u_{1,22}, c_{44}u_{1,33})$ for the longitudinal acoustic wave propagating along $\hat{x}$ is symmetric about x-axis. So for simplicity, we consider 2D acoustic beam propagation along $x - y$ plane (i.e. ignore terms related to the displacement u_3). This results in the following coupled differential equation for the acoustic displacement fields

$$\ddot{u}_x = v_l^2 u_{x,xx} + v_t^2 u_{x,yy} + \gamma_1^2 u_{y,xy}, \tag{D.5}$$

$$\ddot{u}_y = v_t^2 u_{y,xx} + v_l^2 u_{y,yy} + \gamma_1^2 u_{x,xy}, \tag{D.6}$$

where $v_l = \sqrt{c_{11}/\rho}, v_t = \sqrt{c_{44}/\rho}$, and $\gamma_1 = \sqrt{(c_{12} + c_{44})/\rho}$. We now consider a longitudinal wave propagating along x-direction i.e. $\mathbf{u}(\mathbf{r}, t) = \mathbf{A}(\mathbf{r})e^{-i(k_o x - \Omega t)}$, where $\mathbf{A}(\mathbf{r}) = A_x(x, y)\hat{x} + A_y(x, y)\hat{y}$, and $k_o = \Omega/v_l$. For paraxial beam propagation along x, we make the slowly varying envelope approximation (i.e. $\partial^2 A_i/\partial x^2 \ll ko^2 A_i, i = x, y$) to obtain the following coupled equations from Eqs. (D.5-D.6)

$$-k_o^2 v_l^2 A_x = -k_o^2 v_l^2 A_x - 2ik_o v_l^2 \frac{\partial A_x}{\partial x} + v_t^2 \frac{\partial^2 A_x}{\partial y^2} - i\gamma_1^2 k_o \frac{\partial A_y}{\partial y}, \tag{D.7}$$

$$-k_o^2 v_l^2 A_y = -k_o^2 v_t^2 A_y - 2ik_o v_t^2 \frac{\partial A_y}{\partial x} + v_l^2 \frac{\partial^2 A_y}{\partial y^2} - i\gamma_1^2 k_o \frac{\partial A_x}{\partial y}. \tag{D.8}$$

To solve these equations, we Fourier transform $\mathbf{A}(\mathbf{r})$ to k-space. So using $A_x(x, y) = 1/\sqrt{2\pi} \int dk_y \tilde{A}_x(x, k_y)e^{ik_y y}$ and $A_y(x, y) = 1/\sqrt{2\pi} \int dk_y \tilde{A}_y(x, k_y)e^{ik_y y}$, we get following

first order differential equations

$$\frac{\partial \tilde{A}_x}{\partial x} + ip\tilde{A}_x + iq\tilde{A}_y = 0, \tag{D.9}$$

$$\frac{\partial \tilde{A}_y}{\partial x} + ir\tilde{A}_y + is\tilde{A}_x = 0, \tag{D.10}$$

where $p = -(v_t^2 k_y^2)/(2v_l^2 k_o), q = \gamma_1^2 k_y/(2v_l^2), r = -(k_o^2(v_t^2 - v_l^2) + v_l^2 k_y^2)/(2v_l^2 k_o)$, and $s = \gamma_1^2 k_y/(2v_t^2)$. Applying $(\partial_x + ir)$ on Eq. (D.9) and making the paraxial approximation, we finally get

$$\frac{\partial \tilde{A}_x(x, k_y)}{\partial x} + i\frac{rp - qs}{p + r}\tilde{A}_x(x, k_y) = 0. \tag{D.11}$$

Assuming $k_y \ll k_o$ in the paraxial limit we get

$$\frac{rp - qs}{p + r} \simeq \frac{k_o(v_l^2 v_t^2 - v_t^4 + \gamma_1^4)}{-2v_l^2(v_l^2 - v_t^2)} \left(\frac{k_y}{k_o}\right)^2. \tag{D.12}$$

We can now re-write Eq. (D.11) as

$$2k' i\frac{\partial \tilde{A}_x}{\partial x} = -k_y^2 \tilde{A}_x, \tag{D.13}$$

where $k' = k_o\chi$, and the "anisotropy-parameter", χ is given by

$$\chi = \frac{v_l^2(v_l^2 - v_t^2)}{v_l^2 v_t^2 - v_t^4 + \gamma_1^4}. \tag{D.14}$$

Note that Eqn. (D.13) for acoustic wave propagation in the paraxial limit, is similar to the paraxial approximation to the scalar wave equation for electromagnetic field [181]. However, for the acoustic wave propagation in the paraxial limit there is an additional factor of χ in the propagation constant (i.e. $k' = k_o\chi$). While we have determined χ analytically, it is also possible to obtain χ numerically by fitting a quadratic function to the slowness surfaces [119]. It is well known from optics that Gaussian beams

satisfy the paraxial approximation to the wave equation [118]. Therefore, assuming acoustic field polarized along x (i.e. $\mathbf{u}(\mathbf{r},t) = A(x,y)e^{-i(k_o x - \Omega t)}\hat{x}$, with initial acoustic field at $x = 0$ as $A(x = 0, y) = A_o \exp(-y^2/w_o^2)$, we can solve Eq. (D.13) to get

$$\mathbf{u}(\mathbf{r},t) = A_o \hat{x} \frac{w_o}{w'(x)} \exp\left(-\frac{y^2}{w'(x)^2}\right) \exp\left(-ik_o \frac{y^2}{2R'(x)} + i\psi'(x)\right) \exp\left(-i(k_o x - \Omega t)\right), \tag{D.15}$$

where

$k' = k_o \chi = \dfrac{2\pi}{\lambda_{\text{ph}}} \chi$ for phonon with wavelength λ_{ph},

w_o is the acoustic waist radius at $x = 0$,

$w'(x) = w_o \sqrt{1 + \left(\dfrac{x}{x'_{\text{R}}}\right)^2}$ is the acoustic waist radius at x,

$x'_{\text{R}} = \dfrac{\pi w_o^2}{\lambda_{ph}} \chi$ is the acoustic Rayleigh length,

$R'(x) = \dfrac{1}{\chi}\left(x + \dfrac{{x'_{\text{R}}}^2}{x}\right)$ is the radius of curvature of the acoustic beam's wavefronts at x,

$\psi'(x) = \arctan\left(\dfrac{x}{x'_{\text{R}}}\right)$ is the acoustic Gouy phase at x.

Now that we have determined propagation equations for the Gaussian acoustic wave, we can perform stable Fabry-Pérot resonator analysis for the acoustic cavity similar to that for a two-mirror optical cavity [118]. For stimulate Given two surfaces with radius of curvatures R_1 and R_2 with spacing t between, we need to find a Gaussian beam that periodically refocuses upon each round trip. Let us assume that this Gaussian beam with an initially unknown spot size w_o is at an initially unknown location such that the reflecting surfaces are at distances x_1 and x_2 away (see Fig. D.1). For periodic refocusing, the acoustic beams' radius of curvatures $R'(x)$ need to

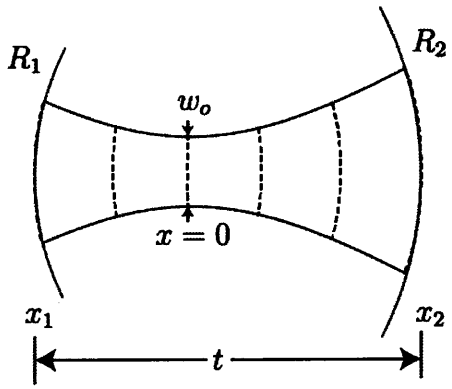

Figure D.1: **Acoustic resonator design.** Phonon cavity of length t with two surfaces with radii of curvature R_1 and R_2. Adapted from Ref. [108].

match with radius of curvatures of the two mirrors. This gives us three equations

$$R'(x_1) = \frac{1}{\chi}\left(x_1 + \frac{x\prime_{\mathrm{R}}^2}{x_1}\right) = R_1, \tag{D.16}$$

$$R'(x_2) = \frac{1}{\chi}\left(x_2 + \frac{x\prime_{\mathrm{R}}^2}{x_2}\right) = R_2, \tag{D.17}$$

$$t = x_2 - x_1. \tag{D.18}$$

We now invert Eqns. (D.16-D.18) to find the Gaussian beam parameters x'_{R}, x_1 and x_2 in terms of R_1, R_2 and t. So, if we define acoustic resonator "g-parameter" as follows

$$g_1 = 1 - \frac{t}{\chi R_1} \text{ and } g_2 = 1 - \frac{t}{\chi R_2}, \tag{D.19}$$

we can find the Gaussian beam parameters in terms of g_1, g_2 and t. The Rayleigh length for this trapped Gaussian beam is given by

$$x\prime_{\mathrm{R}}^2 = \frac{g_1 g_2(1 - g_1 g_2)}{(g_1 + g_2 - 2g_1 g_2)^2} t^2. \tag{D.20}$$

The locations of the curved surfaces with respect to the Gaussian beam waist are

$$x_1 = \frac{g_2(1-g_1)}{g_1+g_2-2g_1g_2}t, \tag{D.21}$$

$$x_2 = \frac{g_1(1-g_2)}{g_1+g_2-2g_2g_2}t. \tag{D.22}$$

From Eq. D.20 and the definition of the Rayleigh length derived earlier, we can obtain the Gaussian beam waist size at $x = 0$ and $x = t$

$$w_o^2 = \frac{t\lambda_{\text{ph}}}{\pi\chi}\sqrt{\frac{g_1g_2(1-g_1g_2)}{(g_1+g_2-2g_1g_2)^2}}, \tag{D.23}$$

$$w_2^2 = \frac{t\lambda_{\text{ph}}}{\pi\chi}\sqrt{\frac{g1}{g_2(1-g_1g_2)}}. \tag{D.24}$$

From equations (D.20) & (D.23) we see that for real and finite solutions to the Gaussian beam parameters and the beam waist size, we see that $0 \leq g_1g_2 \leq 1$. For a plano-convex phononic resonator discussed in this paper, $R_1 = \infty$ so, $g_1 = 1$ and $x_1 = 0$.

We can also analytically calculate the frequency spacing between the higher-order transverse modes, because in the paraxial limit higher order Hermite-Gaussian modes are also solutions to the paraxial equation in Eq. (D.13).

$$u_n(x,y) = A_o\hat{x}H_n\left(\frac{\sqrt{2}y}{w'(x)}\right)\times \tag{D.25}$$

$$\exp\left(-\frac{y^2}{w'(x)^2}\right)\exp\left(-ik_o\frac{y^2}{2R'(x)}+i(n+1/2)\psi'(x)\right)\exp\left(-ik_ox\right), \tag{D.26}$$

where H_ns are the Hermite polynomials of order n and are also solutions to Eq. (D.13). To calculate the higher order mode frequency spacing we look at the total round trip phase shift along the cavity axis (i.e. $y = 0$), which must be an integer

multiple of 2π. This gives us the following equation

$$-k_o t + (n + 1/2)(\psi'(t) - \psi'(0)) = \pi \tag{D.27}$$

$$\frac{-\Omega_n}{v_l} t + (n + 1/2)\psi'(t) = \pi \tag{D.28}$$

So the higher-order transverse mode spacing is given by

$$\Delta f = \frac{\Omega_n - \Omega_{n-1}}{2\pi} = \frac{1}{2\pi} \arctan\left(\frac{t}{x'_{\mathrm{R}}}\right) \frac{v_l}{t}, \tag{D.29}$$

with the Rayleigh length given by Eq. (D.20).

Appendix E

Derivation of the dissipative coupling term

To derive this additional term, H_{mn}, and how multimode strong coupling leads to interference of decay pathways, we begin by considering a simpler case of a single optical optical mode (a_2) coupled to two acoustic mode (b_1 and b_2). This derivation is also outlined in Ref. [112].

In the rotating frame of the pump, the undriven and linearized Hamiltonian for our system under the rotating wave approximation is given by

$$H^{\text{sys}} = \hbar\Delta a_2^\dagger a_2 + \sum_m \hbar\Omega_m b_m^\dagger b_m - \sum_m \hbar g_m (a^\dagger b_m + b_m^\dagger a). \tag{E.1}$$

As discussed in Ref. [111], the acoustic loss in our system is likely dominated by diffraction or a tilt of the crystal relative to the optical axis. Both of these effects can be viewed as a coupling of each resonator mode, whose transverse profile is determined by the optical cavity field, to the transverse modes of the entire crystal. Therefore, these extrinsic, geometric loss mechanisms are most accurately described using the input-output formalism for a resonator coupled to an external bath of modes [166] as seen in Fig. 6.10**a**. In our case, all of the acoustic modes b_m are coupled to a common

set of bath modes c_q at frequency ω_q with rates $f_{m,q}$, giving rise to the coupling Hamiltonian

$$H^{\mathrm{c}} = -i\hbar \sum_q \sum_m (f_{m,q} b_m^\dagger c_q - H.c.). \tag{E.2}$$

The Hamiltonian of the bath is given by

$$H^{\mathrm{bath}} = \sum_q \hbar\omega_q c_q^\dagger c_q, \tag{E.3}$$

and the Hamiltonian of the total system is given by

$$H = H^{\mathrm{sys}} + H^{\mathrm{bath}} + H^{\mathrm{c}}. \tag{E.4}$$

The coupled equations of motion (EOM) for the bath and resonator modes are then

$$\dot{c}_q = -i\omega_q c_q + \sum_m f_{m,q}^* b_m, \tag{E.5}$$

$$\dot{b}_m = \frac{i}{\hbar}[H^{\mathrm{sys}}, b_m] + \sum_q f_{m,q} c_q. \tag{E.6}$$

Following the analysis of Ref. [166], we solve for the EOM of the resonator modes and obtain

$$\dot{b}_m = \frac{i}{\hbar}[H^{\mathrm{sys}}, b_m] - \frac{\Gamma_{m,e}}{2} b_m - \sum_{n \neq m} \frac{\Gamma_{mn,e}}{2} b_n. \tag{E.7}$$

Here, we have made the usual Markov approximation and assumed that the coupling is independent of frequency so that $f_{m,q} = f_m$, which lets us introduce a decay rate $\Gamma_{m,e} = 2\pi |f_m|^2 \rho$, where $\rho = \sum_q \delta(\omega - \omega_q)$ is a constant density of bath states. Furthermore, since the resonator modes we are interested in are different longitudinal modes with the same transverse profile, it is fair to assume that all f_m are approxi-

mately equal. For now, we maintain a bit more generality and assume that they all have the same phase, which allows us to define $\Gamma_{mn} = \sqrt{\Gamma_{m,e}\Gamma_{n,e}}$. We emphasize, however, that the sign of the last term in Equation E.7 is in general determined by the relative phase of the bath coupling for different resonator modes.

In addition to the extrinsic dissipation we have considered so far, acoustic resonators also have intrinsic sources of dissipation such as scattering and absorption. Therefore, to be complete, we introduce an intrinsic decay rate $\Gamma_{m,i}$, so that the total dissipation rate for each acoustic made is $\Gamma_m = \Gamma_{m,e} + \Gamma_{m,i}$, corresponding to the linewidth extracted from OMIT spectra in the limit of weak optomechanical coupling. The final equations of motion for the optical and acoustic modes are then:

$$\begin{aligned}
\dot{a}_2 &= \frac{i}{\hbar}[H^{\text{sys}}, a] - \frac{\kappa}{2}a \\
&= -i\Delta a_2 - i\sum_m g_m b_m - \frac{\kappa}{2}a_2, \qquad \text{(E.8)} \\
\dot{b}_m &= \frac{i}{\hbar}[H^{\text{sys}}, b_m] - \frac{\Gamma_m}{2}b_m - \sum_{n\neq m}\frac{\Gamma_{mn}}{2}b_n \\
&= -i\Omega_m b_m - ig_m^* a - \frac{\Gamma_m}{2}b_m - \sum_{n\neq m}\frac{\Gamma_{mn}}{2}b_n. \qquad \text{(E.9)}
\end{aligned}$$

Therefore, we can obtain the additional term $-\sum_{n\neq m}\frac{\Gamma_{mn}}{2}b_n$ in Eqn. (E.9) resulting from acoustic modes decaying into a common bath by simply adding a "dissipative coupling" term $H_{mn} = -i(\Gamma_{mn}/2)b_m^\dagger b_n$ to H^{sys}.

Appendix F

Fabrication Details

In this appendix, we outline detailed fabrication steps used to make plano-convex resonators in a variety of crystalline substrates. We start with the solvent vapor reflow, which we have used successfully to create photoresist hemispheres on quartz, silicon, sapphire, and GaAs wafers.

F.1 Solvent Vapor Reflow

- Start with a double-sided polished wafer. Inspect the wafer to make sure the wafer is not contaminated. If the wafer has dust or other particulates, ultrasonic clean the wafer in NMP, acetone, and methanol solution, respectively, for 3 minutes each. Then clean the wafer using a piranha solution (3 parts of concentrated sulfuric acid and 1 part of 30% hydrogen peroxide solution) for 10 min to remove organic contaminates. Rinse the wafer in DI water for 1 minute and then blow dry with N_2 gas.

- Oxygen plasma clean the wafer for 3 min at RF-power of 150 W and a pressure of 300 mTorr. This helps eliminate the possibility of any organic contaminants as well as prepare the crystal surface for good resist adhesion.

- Spin coat a 5.5 um thick layer of photoresist (AZP 4620) on the wafer. Thinner photoresist such as AZP 4330 can also be used to obtain even thinner photoresist height of approximately 3 um. Please look up the appropriate resist spin curves to get the spinner speed and time. Typically, thinner photoresist height translates to shallower contact angle after reflow and hence larger radius of curvatures for the reflowed photoresist.

- After spinning, post-bake the AZP 4620 at 110 °C for 2 minutes. Note that since we care about both surfaces of the wafer being clean, do not directly put the wafer on the hotplate. Instead put a clean glass side on the hotplate, let it thermalize, and put the wafer on top of this clean glass slide. The AZP 4330 is post baked at 100 °C for 1 minute.

- A lithographic photomask was used to define circular structures and used during UV exposure of the positive photoresist (400mJ/cm^2 at 405 nm wavelength for AZP 4620 and 150 mJ/cm^2 at 405 nm wavelength for AZP 4330).

- Develop the exposed photoresist using 1:4 AZ400K:water developer solution. Development time is 5 min for AZP 4620 and 2 min for AZP 4330.

- Vapor prime the photoresist cylinders using resist adhesion promoter hexamethyldisilizane (HMDS) for 15 minutes. To do this, put a few drops of HMDS inside a closed chamber and then place the wafer inside it.

- To reflow the photoresist using solvent vapor, place the wafer upside down (not touching the liquid) inside the chamber that contains polypropylene glycol monomethyl ether acetate (PGMEA) solvent at 55 °C. The wafer itself is heated at 60 °C. Typically the photoresist cylinders reflow to form hemispherical surfaces completely within a few hours.

- After the reflow, bake the wafer at 90 °C for 1 minute and 110 °C for another 10 minutes to get rid of the solvent.

- Before reactive ion etching, ultrasonic clean the wafer in DI water for 3 minutes and heat the substrate in a hot plate to get ride of the moisture as well as harden the photoresist. For thicker photoresist AZP 4620 (AZP 4330), gradually increase the temperature from 125 °C (110 °C) to 170 °C (130 °C) over the course of 5 minutes to harden the photoresist.

The hemispherical patterns defined by the photoresist is transferred onto the substrate material by completely etching away the photoresist using reactive ion etching (RIE). We outline the etching recipes that we developed to etch various crystalline substrates, yielding plano-convex resonators with excellent surface quality.

F.2 Reactive ion etching

- Start by running a standard fluorine or chlorine based cleaning recipe based on which substrate you are etching (see below).

- Run a conditioning run with the following parameters based on the substrate material.

  - To etch single crystal quartz or fused silica substrates, we perform a slow reactive ion etch using SF_6 and Ar gases with 4 SCCM and 14 SCCM flow rates, respectively, at a low chamber pressure of 4 mTorr and a bias voltage of 370 V is used to etch away the photoresist completely.

  - To etch single crystal silicon, we use SF_6 and O_2 gases with 5 SCCM and 2 SCCM flow rates, respectively, at a chamber pressure of 10 mTorr and a bias voltage of 394 V.

- To etch single crystal GaAs, we perform RIE-ICP using BCl_3 and Ar gases with 5 SCCM and 10 SCCM flow rates, respectively, at a chamber pressure of 7 mTorr and a bias voltage of 444 V. RF power is set at 85 W and ICP power at 250 W and the etching is performed at 3 °C.
- To etch single crystal sapphire, we perform RIE-ICP using Cl_2 and BCl_3 gases with 6 SCCM and 24 SCCM flow rates, respectively, at a chamber pressure of 30 mTorr and a bias voltage of 406 V. RF power is set at 75 W and ICP power at 600 W and the etching is performed at 11 °C.

- After the etching is complete. Ultrasonic clean the wafer in DI water, NMP, acetone, and methanol for 3 minutes each.

- To passivate the surfaces of silicon after RIE, clean the wafer in piranha solution (3:1 mixtures of sulfuric acid and hydrogen peroxide) for 10 minutes. Then rinse in DI water for 1 minute.

- Dip the silicon substrate in diluted HF (5 parts DI water, 1 part 49% HF) for 1 minute to remove the native oxide layer. Finally, blow dry with N_2 gas.

Appendix G

Methods: Measurement of acousto-optic coupling

G.1 Stimulated Brillouin Scattering Measurements

For stimulated Brillouin scattering measurements, we use counterpropagating laser fields and measure the energy transfer from the higher frequency pump field to the lower frequency Stokes field. For such measurements, we not only want the laser fields to be co-linear but also need to ensure good overlap with the acoustic mode, which is defined by the plano-convex geometry. In what follows we outline the steps taken to align pump and Stokes laser fields to the plano-convex acoustic resonator.

- First, we remove the lenses (f)-(g) as well as the plano-convex crystal (DUT) from the setup seen in Fig. G.1 and use two pinholes to ensure that the pump and Stokes light are co-linear. In the setup show in Fig. G.1, the pump (Stokes) field impinges the crystal from the left (right).

- Turn off the Stokes light. Add the lens (f) so that the pump light is passing roughly through its center. The DUT is also placed in between the two lenses so that the pump light roughly passes through its center and the left surface of

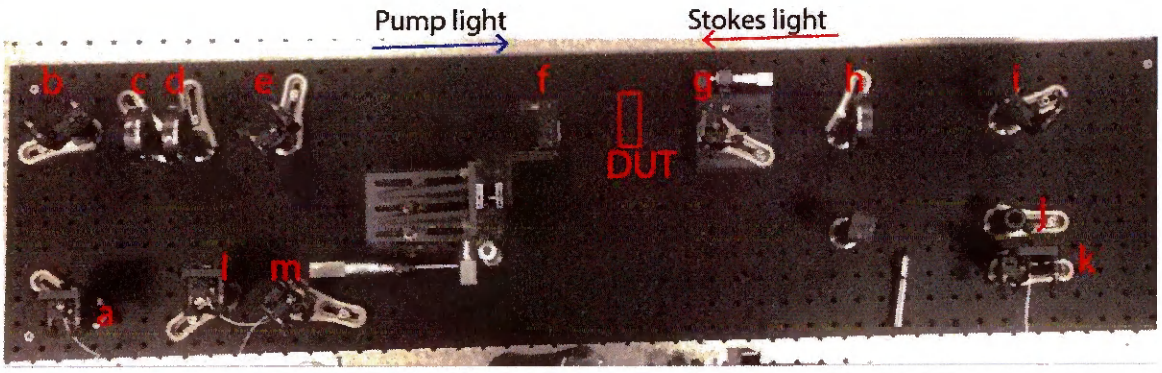

Figure G.1: **Setup used to measure coupling of bulk acoustic waves using free-space laser beams.** Free-space collimators: (a), (k), (l); Mirrors: (b), (j), (m); half-wave plate: (c), (h); quarter-wave plate: (d); 90:10 beam splitter: (e); lens: (f), (g); free-space isolator: (j).

the crystal is about a focal length away from the lens (f).

- Start by aligning the pump field normal to the surface of the crystal. To do this, adjust the mirror (b) and lens (f) so that the back-reflected light from the DUT goes back through the free-space collimator (a) first using a laser at 632 nm. Then, switch the laser source to 1550 nm, monitor the backscattered light, and maximize it to ensure the pump field is normal to the surface of the crystal.

- To align the laser light parallel to the crystal axis, sweep the wavelength of the laser and monitor the backreflection. Small reflections on the quartz-air interface means that you should see a modulated reflection spectrum when the two surfaces of the plano-convex crystal forms a low finesse optical cavity.

- Now add lens (g) and adjust (g) and (i) so that the pump light passes through the free-space collimator (k). By maximizing pump light transmitted through collimator (i) you ensure that the path of the counterpropagating optical beams are co-linear.

- Now turn on the probe light and align mirror (l) and collimator (m) so that ~10% of the Stokes light reflected from the beam-splitter (e) is coupled through

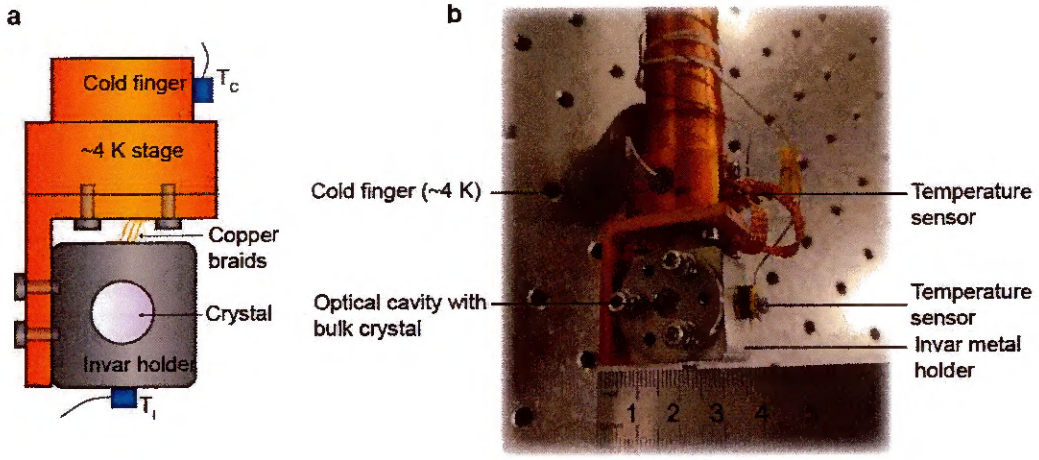

Figure G.2: **Optical cavity mounted in a Invar holder.** A schematic (a) and an actual picture (b) showing a monolithic Invar holder which consists of a bulk crystal placed inside a high-finesse optical cavity. Adapted from Ref. [112].

the free-space collimator (m).

- Ensure that the polarization of the pump and probe beam inside the crystal are colinear.

- Finally, place a free-space isolator (h) in the setup so prevent pump light from entering collimator (i). This ensures that the only stimulated Brillouin scattering we are measuring is from the free-space setup(i.e the crystal) and not from the optical fibers.

G.2 Coupling to a high-finesse optical cavity

In this section, we outline the steps to couple light into high-finesse optical cavity (see Fig. G.2). We begin by aligning the optical beam normal to the planar mirror.

- Start by removing the lens (d) and the polarizer (b) as seen in Fig. G.3.

- Do a very coarse alignment by adjusting both the mirror (c) and free-space collimator (a) such that the red laser (632 nm) is roughly at the center of the

optical cavity (e). Adjust (a) and (c) until the backreflection spot is overlapping with the light coming out of the free-space collimator (a).

- Switch the light source to 1550 nm. Now perform a fine alignment by monitoring the backreflected power and adjusting both (a) and (c) to maximize it.

- Add the lens (d) and translate it in x & y-direction such that the laser passes roughly through its center. At this point, the backreflection should already be close to the maximum.

- Readjust both (c) and (d) to maximize back-reflection.

- Translate the lens (d) in z-direction so that the optical cavity is at the focus and re-optimize both (c) and (d) to obtain maximum back-reflection.

We now outline the steps taken to center the beam on the optical axis.

- Switch the light source to a red laser (632 nm) and look at the light transmitted through the cavity. Translate the lens (d) in x and y direction so that multiple reflections coalesce into one 'blob'. Now, the beam should be pretty close to the optical axis.

- Switch the light source to 1550 nm and change the mirror (c) to maximize back-reflection. This way we fix the tilt misalignment that we introduced when we adjusted lens (d).

- Sweep the wavelength of the laser source continuously over several optical FSRs. Adjust the lens (d) as well as the mirror (c) to get large dip depths for the fundamental modes of the optical cavity.

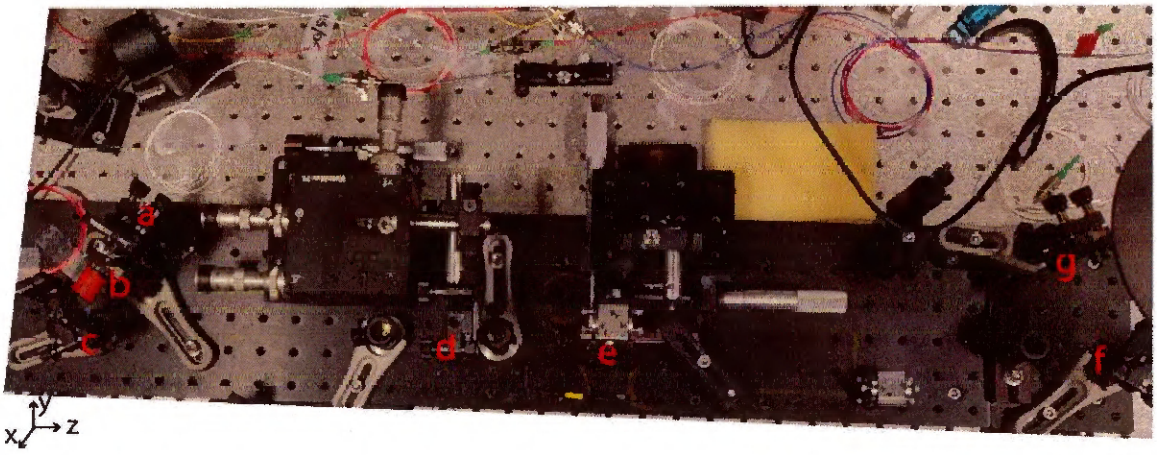

Figure G.3: **Free-space setup used to couple light into the high-finesse optical cavity.** Free-space collimator: (a); polarizer: (b); mirror: (c); lens: (d); optical cavity: (e).

Bibliography

[1] R. W. Boyd. *Nonlinear optics.* Elsevier, 2003.

[2] E. Hulburt. Explanation of the brightness and color of the sky, particularly the twilight sky. *JOSA*, 43(2):113–118, 1953.

[3] E. Garmire. Nonlinear optics in daily life. *Optics express*, 21(25):30532–30544, 2013.

[4] L. Brillouin. Diffusion de la lumière et des rayons x par un corps transparent homogène-influence de l'agitation thermique. In *Annales de physique*, volume 9, pages 88–122. EDP Sciences, 1922.

[5] L. Mandelstam. Light scattering by inhomogeneous media. *Zh. Russ. Fiz-Khim. Ova*, 58:381, 1926.

[6] P. Debye and F. Sears. On the scattering of light by supersonic waves. *Proceedings of the National Academy of Sciences of the United States of America*, 18(6):409, 1932.

[7] C. V. Raman. A new radiation. *Indian Journal of physics*, 2:387–398, 1928.

[8] C. V. Raman and K. S. Krishnan. A new type of secondary radiation. *Nature*, 121(3048):501, 1928.

[9] Meyer and Ramon. *Phys. Zeitschr.*, 33:270, 1932.

[10] R. Krishnan. The scattering of light in diamond and its raman spectrum. In *Proceedings of the Indian Academy of Sciences-Section A*, volume 26, page 399. Springer, 1947.

[11] R. Krishnan. Elastic constants of crystals from light scattering measurements. In *Proceedings of the Indian Academy of Sciences-Section A*, volume 41, pages 91–97. Springer, 1955.

[12] C. Venkateswaran. Interferometric studies of light scattering: Hypersonic velocities in liquids. In *Proceedings of the Indian Academy of Sciences-Section A*, volume 15, pages 371–375. Springer, 1942.

[13] A. Lawson and L. Meyer. Light scattering in liquid helium. *Physical Review*, 93(2):259, 1954.

[14] T. H. Maiman et al. Stimulated optical radiation in ruby. 1960.

[15] R. Chiao, C. Townes, and B. Stoicheff. Stimulated brillouin scattering and coherent generation of intense hypersonic waves. *Physical Review Letters*, 12(21):592, 1964.

[16] A. Laubereau, W. Englisch, and W. Kaiser. Hypersonic absorption of liquids determined from spontaneous and stimulated brillouin scattering. *IEEE Journal of Quantum Electronics*, 5(8):410–415, 1969.

[17] W. Heinicke, G. Winterling, and K. Dransfeld. Low-temperature measurement of the hypersonic absorption in fused quartz by stimulated brillouin scattering. *The Journal of the Acoustical Society of America*, 49(3C):954–958, 1971.

[18] H. Takuma and D. Jennings. Stimulated brillouin scattering in the off-axis resonator. *Applied Physics Letters*, 5(12):239–241, 1964.

[19] T. Ito and H. Takuma. On the threshold condition of the small and large angle stimulated brillouin scattering. *Journal of the Physical Society of Japan*, 24(4):965–965, 1968.

[20] K. Kao and G. A. Hockham. Dielectric-fibre surface waveguides for optical frequencies. In *Proceedings of the Institution of Electrical Engineers*, volume 113, pages 1151–1158. IET, 1966.

[21] T. Miya, Y. Terunuma, T. Hosaka, and T. Miyashita. Ultimate low-loss single-mode fibre at 1.55 μm. *Electronics Letters*, 15(4):106–108, 1979.

[22] E. Ippen and R. Stolen. Stimulated brillouin scattering in optical fibers. *Applied Physics Letters*, 21(11):539–541, 1972.

[23] R. Shelby, M. Levenson, and P. Bayer. Guided acoustic-wave brillouin scattering. *Physical Review B*, 31(8):5244, 1985.

[24] N. Shibata, Y. Azuma, T. Horiguchi, and M. Tateda. Identification of longitudinal acoustic modes guided in the core region of a single-mode optical fiber by brillouin gain spectra measurements. *Optics letters*, 13(7):595–597, 1988.

[25] R. G. Smith. Optical power handling capacity of low loss optical fibers as determined by stimulated raman and brillouin scattering. *Applied Optics*, 11(11):2489–2494, 1972.

[26] R. H. Stolen. Nonlinearity in fiber transmission. *Proceedings of the IEEE*, 68(10):1232–1236, 1980.

[27] N. Yoshizawa and T. Imai. Stimulated brillouin scattering suppression by means of applying strain distribution to fiber with cabling. *Journal of Lightwave Technology*, 11(10):1518–1522, 1993.

[28] V. I. Kovalev and R. G. Harrison. Waveguide-induced inhomogeneous spectral broadening of stimulated brillouin scattering in optical fiber. *Optics letters*, 27(22):2022–2024, 2002.

[29] P. D. Dragic, C.-H. Liu, G. C. Papen, and A. Galvanauskas. Optical fiber with an acoustic guiding layer for stimulated brillouin scattering suppression. In *Conference on Lasers and Electro-Optics*, page CThZ3. Optical Society of America, 2005.

[30] P. Dragic, T. Hawkins, P. Foy, S. Morris, and J. Ballato. Sapphire-derived all-glass optical fibres. *Nature Photonics*, 6(9):627, 2012.

[31] J. Ballato and P. Dragic. Rethinking optical fiber: new demands, old glasses. *Journal of the American Ceramic Society*, 96(9):2675–2692, 2013.

[32] K. Hill, B. Kawasaki, and D. Johnson. Cw brillouin laser. *Applied Physics Letters*, 28(10):608–609, 1976.

[33] D. R. Ponikvar and S. Ezekiel. Stabilized single-frequency stimulated brillouin fiber ring laser. *Optics letters*, 6(8):398–400, 1981.

[34] S. Smith, F. Zarinetchi, and S. Ezekiel. Narrow-linewidth stimulated brillouin fiber laser and applications. *Optics letters*, 16(6):393–395, 1991.

[35] R. Tkach and A. Chraplyvy. Fibre brillouin amplifiers. *Optical and quantum electronics*, 21(1):S105–S112, 1989.

[36] F. Zarinetchi, S. Smith, and S. Ezekiel. New developments in fiberoptic gyroscopes. In *Fiber Optic and Laser Sensors VII*, volume 1169, pages 300–304. International Society for Optics and Photonics, 1990.

[37] T. Horiguchi, K. Shimizu, T. Kurashima, M. Tateda, and Y. Koyamada. Development of a distributed sensing technique using brillouin scattering. *Journal of lightwave technology*, 13(7):1296–1302, 1995.

[38] M. Nikles, L. Thévenaz, and P. A. Robert. Simple distributed fiber sensor based on brillouin gain spectrum analysis. *Optics letters*, 21(10):758–760, 1996.

[39] K. Y. Song, W. Zou, Z. He, and K. Hotate. All-optical dynamic grating generation based on brillouin scattering in polarization-maintaining fiber. *Optics letters*, 33(9):926–928, 2008.

[40] J. Sancho, N. Primerov, S. Chin, Y. Antman, A. Zadok, S. Sales, and L. Thévenaz. Tunable and reconfigurable multi-tap microwave photonic filter based on dynamic brillouin gratings in fibers. *Optics express*, 20(6):6157–6162, 2012.

[41] D. T. Hon. Pulse compression by stimulated brillouin scattering. *Optics letters*, 5(12):516–518, 1980.

[42] K. Y. Song, K. Lee, and S. B. Lee. Tunable optical delays based on brillouin dynamic grating in optical fibers. *Optics express*, 17(12):10344–10349, 2009.

[43] L. Zou, X. Bao, and L. Chen. Brillouin scattering spectrum in photonic crystal fiber with a partially germanium-doped core. *Optics letters*, 28(21):2022–2024, 2003.

[44] P. Dainese, P. S. J. Russell, N. Joly, J. Knight, G. Wiederhecker, H. L. Fragnito, V. Laude, and A. Khelif. Stimulated brillouin scattering from multi-ghz-guided acoustic phonons in nanostructured photonic crystal fibres. *Nature Physics*, 2(6):388, 2006.

[45] M. S. Kang, A. Nazarkin, A. Brenn, and P. S. J. Russell. Tightly trapped acoustic phonons in photonic crystal fibres as highly nonlinear artificial raman oscillators. *Nature Physics*, 5(4):276, 2009.

[46] R. Pant, C. G. Poulton, D.-Y. Choi, H. Mcfarlane, S. Hile, E. Li, L. Thevenaz, B. Luther-Davies, S. J. Madden, and B. J. Eggleton. On-chip stimulated brillouin scattering. *Optics express*, 19(9):8285–8290, 2011.

[47] H. Lee, T. Chen, J. Li, K. Y. Yang, S. Jeon, O. Painter, and K. J. Vahala. Chemically etched ultrahigh-q wedge-resonator on a silicon chip. *Nature Photonics*, 6(6):369, 2012.

[48] H. Shin, W. Qiu, R. Jarecki, J. A. Cox, R. H. Olsson III, A. Starbuck, Z. Wang, and P. T. Rakich. Tailorable stimulated brillouin scattering in nanoscale silicon waveguides. *Nature communications*, 4:1944, 2013.

[49] P. T. Rakich, P. Davids, and Z. Wang. Tailoring optical forces in waveguides through radiation pressure and electrostrictive forces. *Optics express*, 18(14):14439–14453, 2010.

[50] P. T. Rakich, C. Reinke, R. Camacho, P. Davids, and Z. Wang. Giant enhancement of stimulated brillouin scattering in the subwavelength limit. *Physical Review X*, 2(1):011008, 2012.

[51] M. S. Kang, A. Butsch, and P. S. J. Russell. Reconfigurable light-driven opto-acoustic isolators in photonic crystal fibre. *Nature Photonics*, 5(9):549, 2011.

[52] D. B. Sohn, S. Kim, and G. Bahl. Time-reversal symmetry breaking with acoustic pumping of nanophotonic circuits. *Nature Photonics*, 12(2):91, 2018.

[53] C. G. Poulton, R. Pant, A. Byrnes, S. Fan, M. Steel, and B. J. Eggleton. Design for broadband on-chip isolator using stimulated brillouin scattering in

dispersion-engineered chalcogenide waveguides. *Optics express*, 20(19):21235–21246, 2012.

[54] E. A. Kittlaus, N. T. Otterstrom, P. Kharel, S. Gertler, and P. T. Rakich. Non-reciprocal interband brillouin modulation. *Nature Photonics*, 12(10):613, 2018.

[55] I. S. Grudinin, A. B. Matsko, and L. Maleki. Brillouin lasing with a caf 2 whispering gallery mode resonator. *Physical review letters*, 102(4):043902, 2009.

[56] I. V. Kabakova, R. Pant, D.-Y. Choi, S. Debbarma, B. Luther-Davies, S. J. Madden, and B. J. Eggleton. Narrow linewidth brillouin laser based on chalcogenide photonic chip. *Optics letters*, 38(17):3208–3211, 2013.

[57] J. Li, H. Lee, and K. J. Vahala. Low-noise brillouin laser on a chip at 1064 nm. *Optics letters*, 39(2):287–290, 2014.

[58] S. Gundavarapu, G. M. Brodnik, M. Puckett, T. Huffman, D. Bose, R. Behunin, J. Wu, T. Qiu, C. Pinho, N. Chauhan, et al. Sub-hertz fundamental linewidth photonic integrated brillouin laser. *Nat. Photon*, 13:60, 2018.

[59] J. Li, H. Lee, and K. J. Vahala. Microwave synthesizer using an on-chip brillouin oscillator. *Nature communications*, 4:2097, 2013.

[60] M. Merklein, B. Stiller, I. V. Kabakova, U. S. Mutugala, K. Vu, S. J. Madden, B. J. Eggleton, and R. Slavík. Widely tunable, low phase noise microwave source based on a photonic chip. *Optics letters*, 41(20):4633–4636, 2016.

[61] W. Zhang and R. A. Minasian. Widely tunable single-passband microwave photonic filter based on stimulated brillouin scattering. *IEEE Photonics Technology Letters*, 23(23):1775–1777, 2011.

[62] D. Marpaung, B. Morrison, M. Pagani, R. Pant, D.-Y. Choi, B. Luther-Davies, S. J. Madden, and B. J. Eggleton. Low-power, chip-based stimulated brillouin scattering microwave photonic filter with ultrahigh selectivity. *Optica*, 2(2):76–83, 2015.

[63] H. Shin, J. A. Cox, R. Jarecki, A. Starbuck, Z. Wang, and P. T. Rakich. Control of coherent information via on-chip photonic–phononic emitter–receivers. *Nature communications*, 6:6427, 2015.

[64] Y. A. Vlasov, M. O'boyle, H. F. Hamann, and S. J. McNab. Active control of slow light on a chip with photonic crystal waveguides. *nature*, 438(7064):65, 2005.

[65] M. Merklein, B. Stiller, K. Vu, S. J. Madden, and B. J. Eggleton. A chip-integrated coherent photonic-phononic memory. *Nature communications*, 8(1):574, 2017.

[66] J. Li, M.-G. Suh, and K. Vahala. Microresonator brillouin gyroscope. *Optica*, 4(3):346–348, 2017.

[67] R. Behunin, P. Kharel, W. Renninger, H. Shin, F. Carter, E. Kittlaus, and P. Rakich. Long-lived guided phonons in fiber by manipulating two-level systems. *arXiv preprint arXiv:1501.04248*, 2015.

[68] M. Nikles, L. Thevenaz, and P. A. Robert. Brillouin gain spectrum characterization in single-mode optical fibers. *Journal of Lightwave Technology*, 15(10):1842–1851, 1997.

[69] A. Fellay, L. Thévenaz, J. P. Garcia, M. Facchini, W. Scandale, and P. Robert. Brillouin-based temperature sensing in optical fibres down to 1 k. In *2002 15th Optical Fiber Sensors Conference Technical Digest. OFS 2002 (Cat. No. 02EX533)*, pages 301–304. IEEE, 2002.

[70] O. Anderson and H. Bömmel. Ultrasonic absorption in fused silica at low temperatures and high frequencies. *Journal of the American Ceramic Society*, 38(4):125–131, 1955.

[71] S. Le Floch and P. Cambon. Study of brillouin gain spectrum in standard single-mode optical fiber at low temperatures (1.4–370 k) and high hydrostatic pressures (1–250 bars). *Optics communications*, 219(1-6):395–410, 2003.

[72] W. Phillips. Tunneling states in amorphous solids. *Journal of Low Temperature Physics*, 7(3-4):351–360, 1972.

[73] S. Hunklinger and W. Arnold. Ultrasonic properties of glasses at low temperatures. *Physical Acoustics*, 12:155–215, 1976.

[74] H. J. Maris. On the mean free path of low energy phonons in single crystal quartz. *Philosophical Magazine*, 9(102):901–910, 1964.

[75] W. Liekens, L. Michiels, and A. De Bock. On the attenuation of 9.4 ghz longitudinal hypersonic waves in some trigonal crystals. *Journal of Physics C: Solid State Physics*, 4(10):1124, 1971.

[76] L. Landau and G. Rumer. Absorption of sound in solids. *Phys. Z. Sowjetunion*, 11(18), 1937.

[77] A. Akhieser. On the absorption of sound in solids. *J. Phys.(Ussr)*, 1:277, 1939.

[78] I. Pomeranchuck. Sound absorption in dielectrics. *J. Phys. USSR*, 4:529, 1941.

[79] A. N. Cleland. *Foundations of nanomechanics: from solid-state theory to device applications*. Springer Science & Business Media, 2013.

[80] H. Maris. The absorption of sound waves in perfect dielectric crystals. *Philosophical Magazine*, 12(115):89–106, 1965.

[81] S.-i. Tamura and H. Maris. Spontaneous decay of ta phonons. *Physical Review B*, 31(4):2595, 1985.

[82] P. Klemens. Decay of high-frequency longitudinal phonons. *Journal of Applied Physics*, 38(12):4573–4576, 1967.

[83] H. B. Huntington. Ultrasonic measurements on single crystals. *Physical Review*, 72(4):321, 1947.

[84] W. Price and H. Huntington. Acoustical properties of anisotropic materials. *The Journal of the Acoustical Society of America*, 22(1):32–37, 1950.

[85] H. Bömmel and K. Dransfeld. Excitation of very-high-frequency sound in quartz. *Physical Review Letters*, 1(7):234, 1958.

[86] E. Jacobsen. Piezoelectric production of microwave phonons. *Physical Review Letters*, 2(6):249, 1959.

[87] H. Bömmel and K. Dransfeld. Excitation and attenuation of hypersonic waves in quartz. *Physical Review*, 117(5):1245, 1960.

[88] H. Shaw, D. Winslow, A. Karp, and R. Wilson. Attenuation of hypersonic waves in sapphire and rutile at 2.8 gc/sec and room temperature. *Applied Physics Letters*, 4(2):28–30, 1964.

[89] R. Nava, R. Azrt, I. Ciccarello, and K. Dransfeld. Hypersonic absorption in quartz at temperatures below 30 k. *Physical Review*, 134(3A):A581, 1964.

[90] M. Pomerantz. Ultrasonic loss and gain mechanisms in semiconductors. *Proceedings of the IEEE*, 53(10):1438–1451, 1965.

[91] M. Pomerantz. Temperature dependence of microwave phonon attenuation. *Physical Review*, 139(2A):A501, 1965.

[92] J. Thaxter and P. Tannenwald. Phonon generation, propagation, and attenuation at 70 ghz. *IEEE Transactions on Sonics and Ultrasonics*, 13(2):61–68, 1966.

[93] M. Lewis and E. Patterson. Microwave phonon-attenuation measurements in quartz. *Physical Review*, 159(3):703, 1967.

[94] M. Lewis and E. Patterson. Microwave phonon attenuation in yttrium iron garnet. *Journal of Applied Physics*, 39(4):1932–1936, 1968.

[95] W. Liekens, L. Michiels, and A. De Bock. Microwave phonon attenuation in x-cut linbo3. *Physics Letters A*, 40(4):309–310, 1972.

[96] J. De Klerk, D. Bolef, and P. Klemens. " bottleneck" in the attenuation of hypersonic waves in quartz at low temperatures. *Physical Review Letters*, 10(4):127, 1963.

[97] C. Wilson. Vibration modes of at-cut convex quartz resonators. *Journal of Physics D: Applied Physics*, 7(18):2449, 1974.

[98] H. Tiersten and R. Smythe. An analysis of contoured crystal resonators operating in overtones of coupled thickness shear and thickness twist. *The Journal of the Acoustical Society of America*, 65(6):1455–1460, 1979.

[99] R. J. Besson, J.-J. Boy, and M. M. Mourey. Bva resonators and oscillators: a review. relation with space requirements and quartz material characterization. In *Proceedings of the 1995 IEEE International Frequency Control Symposium (49th Annual Symposium)*, pages 590–599. IEEE, 1995.

[100] S. Galliou, M. Goryachev, R. Bourquin, P. Abbé, J. P. Aubry, and M. E. Tobar. Extremely low loss phonon-trapping cryogenic acoustic cavities for future physical experiments. *Scientific reports*, 3:2132, 2013.

[101] S. Galliou, J. Imbaud, M. Goryachev, R. Bourquin, and P. Abbé. Losses in high quality quartz crystal resonators at cryogenic temperatures. *Applied Physics Letters*, 98(9):091911, 2011.

[102] A. Lo, P. Haslinger, E. Mizrachi, L. Anderegg, H. Müller, M. Hohensee, M. Goryachev, and M. E. Tobar. Acoustic tests of lorentz symmetry using quartz oscillators. *Physical Review X*, 6(1):011018, 2016.

[103] P. Bushev, J. Bourhill, M. Goryachev, N. Kukharchyk, E. Ivanov, S. Galliou, M. Tobar, and S. Danilishin. Testing of quantum gravity with sub-kilogram acoustic resonators. *arXiv preprint arXiv:1903.03346*, 2019.

[104] S. Ohno, T. Sonehara, E. Tatsu, A. Koreeda, and S. Saikan. khz stimulated brillouin spectroscopy. *Review of scientific instruments*, 77(12):123104, 2006.

[105] S. Ohno, T. Sonehara, E. Tatsu, A. Koreeda, and S. Saikan. Spectral shape of stimulated brillouin scattering in crystals. *Physical Review B*, 92(21):214105, 2015.

[106] W. Renninger, P. Kharel, R. Behunin, and P. Rakich. Bulk crystalline optomechanics. *Nature Physics*, 14(6):601, 2018.

[107] P. Kharel, R. Behunin, W. Renninger, and P. Rakich. Noise and dynamics in forward brillouin interactions. *Physical Review A*, 93(6):063806, 2016.

[108] P. Kharel, Y. Chu, M. Power, W. H. Renninger, R. J. Schoelkopf, and P. T. Rakich. Ultra-high-q phononic resonators on-chip at cryogenic temperatures. *APL Photonics*, 3(6):066101, 2018.

[109] Y. Chu, P. Kharel, W. H. Renninger, L. D. Burkhart, L. Frunzio, P. T. Rakich, and R. J. Schoelkopf. Quantum acoustics with superconducting qubits. *Science*, 358(6360):199–202, 2017.

[110] Y. Chu, P. Kharel, T. Yoon, L. Frunzio, P. T. Rakich, and R. J. Schoelkopf. Creation and control of multi-phonon fock states in a bulk acoustic-wave resonator. *Nature*, 563(7733):666, 2018.

[111] P. Kharel, G. I. Harris, E. A. Kittlaus, W. H. Renninger, N. T. Otterstrom, J. G. Harris, and P. T. Rakich. High-frequency cavity optomechanics using bulk acoustic phonons. *arXiv preprint arXiv:1809.04020*, 2018.

[112] P. Kharel, Y. Chu, E. A. Kittlaus, N. T. Otterstrom, S. Gertler, and P. T. Rakich. Multimode strong coupling in cavity optomechanics. *arXiv preprint arXiv:1812.06202*, 2018.

[113] T. Sonehara, Y. Konno, H. Kaminaga, S. Saikan, and S. Ohno. Frequency-modulated stimulated brillouin spectroscopy in crystals. *JOSA B*, 24(5):1193–1198, 2007.

[114] D. Royer and E. Dieulesaint. *Elastic waves in solids I: Free and guided propagation*. Springer Science & Business Media, 1999.

[115] J. Sipe and M. Steel. A hamiltonian treatment of stimulated brillouin scattering in nanoscale integrated waveguides. *New Journal of Physics*, 18(4):045004, 2016.

[116] K. Børkje and S. Girvin. Quantum optomechanics with a high-frequency dilational mode in thin dielectric membranes. *New Journal of Physics*, 14(8):085016, 2012.

[117] M. Aspelmeyer, T. J. Kippenberg, and F. Marquardt. Cavity optomechanics. *Reviews of Modern Physics*, 86(4):1391–1452, 2014.

[118] A. E. Siegman. Lasers university science books. *Mill Valley, CA*, 37:208, 1986.

[119] B. P. Newberry and R. B. Thompson. A paraxial theory for the propagation of ultrasonic beams in anisotropic solids. *The Journal of The Acoustical Society of America*, 85(6):2290–2300, 1989.

[120] B. A. Auld. *Acoustic fields and waves in solids.* , 1973.

[121] H. Kogelnik and T. Li. Laser beams and resonators. *Applied optics*, 5(10):1550–1567, 1966.

[122] I. Mason and E. Ash. Acoustic surface-wave beam diffraction on anisotropic substrates. *Journal of Applied Physics*, 42(13):5343–5351, 1971.

[123] R. Camley and A. Maradudin. Phonon focusing at surfaces. *Physical Review B*, 27(4):1959, 1983.

[124] A. G. Fox and T. Li. Resonant modes in a maser interferometer. *Bell System Technical Journal*, 40(2):453–488, 1961.

[125] A. Fox and T. Li. Modes in a maser interferometer with curved and tilted mirrors. *Proceedings of the IEEE*, 51(1):80–89, 1963.

[126] H. McSkimin, P. Andreatch Jr, and R. Thurston. Elastic moduli of quartz versus hydrostatic pressure at 25 and- 195.8 c. *Journal of Applied Physics*, 36(5):1624–1632, 1965.

[127] Y. Ohmachi and N. Uchida. Temperature dependence of elastic, dielectric, and piezoelectric constants in teo2 single crystals. *Journal of Applied Physics*, 41(6):2307–2311, 1970.

[128] I. S. Grudinin, H. Lee, O. Painter, and K. J. Vahala. Phonon laser action in a tunable two-level system. *Physical review letters*, 104(8):083901, 2010.

[129] M. Kervinen, I. Rissanen, and M. Sillanpää. Interfacing planar superconducting qubits with high overtone bulk acoustic phonons. *Physical Review B*, 97(20):205443, 2018.

[130] K. Satzinger, Y. Zhong, H.-S. Chang, G. Peairs, A. Bienfait, M.-H. Chou, A. Cleland, C. Conner, É. Dumur, J. Grebel, et al. Quantum control of surface acoustic-wave phonons. *Nature*, 563(7733):661, 2018.

[131] A. Kobyakov, M. Sauer, and D. Chowdhury. Stimulated brillouin scattering in optical fibers. *Advances in optics and photonics*, 2(1):1–59, 2010.

[132] T. Syau, B. J. Baliga, and R. W. Hamaker. Reactive ion etching of silicon trenches using sf 6/o 2 gas mixtures. *Journal of The Electrochemical Society*, 138(10):3076–3081, 1991.

[133] P. Savander. Microlens arrays etched into glass and silicon. *Optics and lasers in Engineering*, 20(2):97–107, 1994.

[134] M. Eisner and J. Schwider. Transferring resist microlenses into silicon by reactive ion etching. *Optical Engineering*, 35(10):2979–2983, 1996.

[135] L. Li, T. Abe, and M. Esashi. Smooth surface glass etching by deep reactive ion etching with sf 6 and xe gases. *Journal of Vacuum Science & Technology B: Microelectronics and Nanometer Structures Processing, Measurement, and Phenomena*, 21(6):2545–2549, 2003.

[136] N. Llombart, C. Lee, M. Alonso-delPino, G. Chattopadhyay, C. Jung-Kubiak, L. Jofre, and I. Mehdi. Silicon micromachined lens antenna for thz integrated heterodyne arrays. *IEEE Transactions on Terahertz Science and Technology*, 3(5):515–523, 2013.

[137] K. P. Larsen, J. T. Ravnkilde, and O. Hansen. Investigations of the isotropic etch of an icp source for silicon microlens mold fabrication. *Journal of Micromechanics and Microengineering*, 15(4):873, 2005.

[138] L. Erdmann and D. Efferenn. Technique for monolithic fabrication of silicon microlenses with selectable rim angles. *Optical Engineering*, 36(4):1094–1099, 1997.

[139] L. Li, M. Esashi, and T. Abe. A miniaturized biconvex quartz-crystal microbalance with large-radius spherical thickness distribution. *Applied physics letters*, 85(13):2652–2654, 2004.

[140] A. Emadi, H. Wu, S. Grabarnik, G. De Graaf, and R. Wolffenbuttel. Vertically tapered layers for optical applications fabricated using resist reflow. *Journal of Micromechanics and Microengineering*, 19(7):074014, 2009.

[141] R. Schnabel, N. Mavalvala, D. E. McClelland, and P. K. Lam. Quantum metrology for gravitational wave astronomy. *Nat. Commun.*, 1:121, 2010.

[142] S. Schreppler, N. Spethmann, N. Brahms, T. Botter, M. Barrios, and D. M. Stamper-Kurn. Optically measuring force near the standard quantum limit. *Science*, 344(6191):1486–1489, 2014.

[143] E. E. Wollman, C. Lei, A. Weinstein, J. Suh, A. Kronwald, F. Marquardt, A. Clerk, and K. Schwab. Quantum squeezing of motion in a mechanical resonator. *Science*, 349(6251):952–955, 2015.

[144] S. Hong, R. Riedinger, I. Marinković, A. Wallucks, S. G. Hofer, R. A. Norte, M. Aspelmeyer, and S. Gröblacher. Hanbury brown and twiss interferometry of single phonons from an optomechanical resonator. *Science*, 358(6360):203–206, 2017.

[145] R. Riedinger, A. Wallucks, I. Marinković, C. Löschnauer, M. Aspelmeyer, S. Hong, and S. Gröblacher. Remote quantum entanglement between two micromechanical oscillators. *Nature*, 556(7702):473, 2018.

[146] W. Yu, W. C. Jiang, Q. Lin, and T. Lu. Cavity optomechanical spring sensing of single molecules. *Nat. Commun.*, 7:12311, 2016.

[147] S. Barzanjeh, M. Abdi, G. J. Milburn, P. Tombesi, and D. Vitali. Reversible optical-to-microwave quantum interface. *Physical Review Letters*, 109(13):130503, 2012.

[148] J. Bochmann, A. Vainsencher, D. D. Awschalom, and A. N. Cleland. Nanomechanical coupling between microwave and optical photons. *Nature Physics*, 9(11):712, 2013.

[149] T. Bagci, A. Simonsen, S. Schmid, L. G. Villanueva, E. Zeuthen, J. Appel, J. M. Taylor, A. Sørensen, K. Usami, A. Schliesser, et al. Optical detection of radio waves through a nanomechanical transducer. *Nature*, 507(7490):81, 2014.

[150] R. W. Andrews, R. W. Peterson, T. P. Purdy, K. Cicak, R. W. Simmonds, C. A. Regal, and K. W. Lehnert. Bidirectional and efficient conversion between microwave and optical light. *Nature Physics*, 10(4):321, 2014.

[151] M. Eichenfield, J. Chan, R. M. Camacho, K. J. Vahala, and O. Painter. Optomechanical crystals. *Nature*, 462(7269):78, 2009.

[152] L. Ding, C. Baker, P. Senellart, A. Lemaitre, S. Ducci, G. Leo, and I. Favero. High frequency gaas nano-optomechanical disk resonator. *Physical review letters*, 105(26):263903, 2010.

[153] B. Khanaliloo, M. Mitchell, A. C. Hryciw, and P. E. Barclay. High-q/v monolithic diamond microdisks fabricated with quasi-isotropic etching. *Nano letters*, 15(8):5131–5136, 2015.

[154] S. Anguiano, A. Bruchhausen, B. Jusserand, I. Favero, F. Lamberti, L. Lanco, I. Sagnes, A. Lemaître, N. Lanzillotti-Kimura, P. Senellart, et al. Micropillar resonators for optomechanics in the extremely high 19–95-ghz frequency range. *Physical review letters*, 118(26):263901, 2017.

[155] J. Chan, T. M. Alegre, A. H. Safavi-Naeini, J. T. Hill, A. Krause, S. Gröblacher, M. Aspelmeyer, and O. Painter. Laser cooling of a nanomechanical oscillator into its quantum ground state. *Nature*, 478(7367):89, 2011.

[156] R. Riedinger, S. Hong, R. A. Norte, J. A. Slater, J. Shang, A. G. Krause, V. Anant, M. Aspelmeyer, and S. Gröblacher. Non-classical correlations between single photons and phonons from a mechanical oscillator. *Nature*, 530(7590):313, 2016.

[157] S. Weis, R. Rivière, S. Deléglise, E. Gavartin, O. Arcizet, A. Schliesser, and T. J. Kippenberg. Optomechanically induced transparency. *Science*, 330(6010):1520–1523, 2010.

[158] A. Kashkanova, A. Shkarin, C. Brown, N. Flowers-Jacobs, L. Childress, S. Hoch, L. Hohmann, K. Ott, J. Reichel, and J. Harris. Superfluid brillouin optomechanics. *Nature Physics*, 13(1):74, 2017.

[159] C.-H. Dong, Z. Shen, C.-L. Zou, Y.-L. Zhang, W. Fu, and G.-C. Guo. Brillouin-scattering-induced transparency and non-reciprocal light storage. *Nature communications*, 6:6193, 2015.

[160] A. Jayich, J. Sankey, B. Zwickl, C. Yang, J. Thompson, S. Girvin, A. Clerk, F. Marquardt, and J. Harris. Dispersive optomechanics: a membrane inside a cavity. *New Journal of Physics*, 10(9):095008, 2008.

[161] A. H. Safavi-Naeini, J. Chan, J. T. Hill, S. Gröblacher, H. Miao, Y. Chen, M. Aspelmeyer, and O. Painter. Laser noise in cavity-optomechanical cooling and thermometry. *New Journal of Physics*, 15(3):035007, 2013.

[162] G. Anetsberger, E. M. Weig, J. P. Kotthaus, and T. J. Kippenberg. Cavity optomechanics and cooling nanomechanical oscillators using microresonator enhanced evanescent near-field coupling. *Comptes Rendus Physique*, 12(9-10):800–816, 2011.

[163] M.-G. Suh, Q.-F. Yang, and K. J. Vahala. Phonon-limited-linewidth of brillouin lasers at cryogenic temperatures. *Physical review letters*, 119(14):143901, 2017.

[164] N. T. Otterstrom, R. O. Behunin, E. A. Kittlaus, Z. Wang, and P. T. Rakich. A silicon brillouin laser. *Science*, 360(6393):1113–1116, 2018.

[165] R. Kubo. The fluctuation-dissipation theorem. *Reports on progress in physics*, 29(1):255, 1966.

[166] A. A. Clerk, M. H. Devoret, S. M. Girvin, F. Marquardt, and R. J. Schoelkopf. Introduction to quantum noise, measurement, and amplification. *Reviews of Modern Physics*, 82(2):1155, 2010.

[167] S. Gröblacher, K. Hammerer, M. R. Vanner, and M. Aspelmeyer. Observation of strong coupling between a micromechanical resonator and an optical cavity field. *Nature*, 460(7256):724, 2009.

[168] E. Verhagen, S. Deléglise, S. Weis, A. Schliesser, and T. J. Kippenberg. Quantum-coherent coupling of a mechanical oscillator to an optical cavity mode. *Nature*, 482(7383):63, 2012.

[169] G. Enzian, M. Szczykulska, J. Silver, L. Del Bino, S. Zhang, I. A. Walmsley, P. DelHaye, and M. R. Vanner. Observation of brillouin optomechanical strong coupling with an 11 ghz mechanical mode. *Optica*, 6(1):7–14, 2019.

[170] J. Chan. *Laser cooling of an optomechanical crystal resonator to its quantum ground state of motion.* PhD thesis, California Institute of Technology, 2012.

[171] O. Arcizet, R. Rivière, A. Schliesser, G. Anetsberger, and T. J. Kippenberg. Cryogenic properties of optomechanical silica microcavities. *Phys. Rev. A*, 80(2):021803, 2009.

[172] F. Massel, S. U. Cho, J.-M. Pirkkalainen, P. J. Hakonen, T. T. Heikkilä, and M. A. Sillanpää. Multimode circuit optomechanics near the quantum limit. *Nature communications*, 3:987, 2012.

[173] A. Metelmann and A. A. Clerk. Nonreciprocal photon transmission and amplification via reservoir engineering. *Phys. Rev. X*, 5(2):021025, 2015.

[174] K. Fang, J. Luo, A. Metelmann, M. H. Matheny, F. Marquardt, A. A. Clerk, and O. Painter. Generalized non-reciprocity in an optomechanical circuit via synthetic magnetism and reservoir engineering. *Nat. Phys.*, 13(5):465–471, 2017.

[175] M. R. Vanner, I. Pikovski, and M. Kim. Towards optomechanical quantum state reconstruction of mechanical motion. *Annalen der Physik*, 527(1-2):15–26, 2015.

[176] E. MacQuarrie, T. Gosavi, A. Moehle, N. Jungwirth, S. Bhave, and G. Fuchs. Coherent control of a nitrogen-vacancy center spin ensemble with a diamond mechanical resonator. *Optica*, 2(3):233–238, 2015.

[177] X. Han, C.-L. Zou, and H. X. Tang. Multimode strong coupling in superconducting cavity piezoelectromechanics. *Phys. Rev. Lett.*, 117(12):123603, 2016.

[178] J. D. Cohen, S. M. Meenehan, G. S. MacCabe, S. Gröblacher, A. H. Safavi-Naeini, F. Marsili, M. D. Shaw, and O. Painter. Phonon counting and intensity interferometry of a nanomechanical resonator. *Nature*, 520(7548):522, 2015.

[179] P. Rakich and F. Marquardt. Quantum theory of continuum optomechanics. *New Journal of Physics*, 20(4):045005, 2018.

[180] M. Tomes, F. Marquardt, G. Bahl, and T. Carmon. Quantum-mechanical theory of optomechanical brillouin cooling. *Physical Review A*, 84(6):063806, 2011.

[181] B. E. Saleh and M. C. Teich. *Fundamentals of photonics*. John Wiley & Sons, 2019.